

Structure, Spectra and Dynamics of Alkali Cation Microhydration Clusters

Doctoral Thesis

submitted in partial fulfilment
of the requirements for the doctoral degree
“ Dr. rer. nat.”

to the Faculty of Mathematics and Natural Science
of the Christian-Albrechts-University of Kiel

submitted by

Franziska Schulz

Institute of Physical Chemistry

Kiel

2004

Referee

Co-Referee

Day Of The Exam

Authorised For Printing

Dean
.....

Abstract

The main focus of this work was the theoretical investigation of alkali cation microhydration clusters, i.e. $\text{Na}^+(\text{H}_2\text{O})_n$, $\text{K}^+(\text{H}_2\text{O})_n$, and $\text{Cs}^+(\text{H}_2\text{O})_n$ with $4 \leq n \leq 24$.

Structures were obtained applying global geometry optimisation, using a specialised version of genetic algorithms and the common TIP4P/OPLS model potential. The global and most important local minimum energy structures have been investigated and the results obtained constitute a first complete and systematic overview on structures of alkali cation microhydration clusters. By analysis of various interactions reasons for structural trends could be provided. The computed structures were investigated especially in terms of cage inclusion compounds (in particular a proposed dodecahedron cage structure for the case of $n = 20$) which were proposed to explain magic numbers found in related experimental studies. In case of $\text{M}^+(\text{H}_2\text{O})_{20}$ the question of the magic number is most intriguing: The proposed dodecahedron structure was found to be the global minimum for $\text{K}^+(\text{H}_2\text{O})_{20}$ and $\text{Cs}^+(\text{H}_2\text{O})_{20}$, but very close in energy to non-dodecahedron structures. Thus the static structures and energies alone are no adequate explanation for the magic number 20, and hence dynamic effects of the water network should be taken into account. Within the present model, dodecahedron shaped water networks do not occur in sodium microsolvation, in agreement with the absence of the magic number 20 for this system. A structural pattern all magic number cluster structures do have in common is that only three and/or four-coordinated water molecules can be observed.

Molecular dynamics simulations were applied to all global minimum energy cluster structures at different temperatures (canonical ensemble). Entropy effects and free energy surfaces were obtained using constrained dynamics on dissociating magic number clusters. It was found that indeed cluster structures containing only three and/or four-coordinated water molecules are more stable than others thus arriving at a possible explanation for the existence of magic number clusters. General structural trends and building patterns already observed for the static picture obtained by the global geometry optimisation are consistent with the dynamical behaviour in a canonical ensemble.

For a better understanding of these systems, and to provide data for direct comparison to the experiment, anharmonic infrared spectra for each global as well as some low-lying local minimum energy structures were calculated in the OH-stretch region within an empirical model. At the beginning of this investigation this model had been calibrated only for pure water clusters and ice, however, it was found to produce qualitatively correct data also for the present system. The spectra obtained with this model show characteristic correlations between cluster structures and certain spectral signatures which should make it possible to discern these cluster structures experimentally. It has been also shown that at temperatures up to 100 K global minimum structures (computed at 0 K) still dominate the spectra. Recently available experimental data, kindly provided by J.M. Lisy (University of Illinois) was used for a manual re-calibration of the empirical model. This provided almost perfect quantitative agreement with the experiment. Hence, it was possible for the first time to assign spectral peaks unambiguously to vibrational modes and deduce which isomers are present in the experiments. J.M. Lisy is currently extending this spectral measurements to larger clusters. In combination with our theoretical analysis, this will provide direct information on magic number cluster structures for the first time.

Kurzzusammenfassung

Der Schwerpunkt dieser Arbeit war die theoretische Untersuchung von Alkali-Kation-Mikrohydratationsclustern, d.h. $\text{Na}^+(\text{H}_2\text{O})_n$, $\text{K}^+(\text{H}_2\text{O})_n$ und $\text{Cs}^+(\text{H}_2\text{O})_n$, jeweils mit $4 \leq n \leq 24$.

Die Strukturen wurden mittels globaler Geometrieoptimierung bestimmt, unter Verwendung eines speziellen genetischen Algorithmus in Kombination mit dem TIP4P/OPLS Modellpotential. Die globalen sowie die wichtigsten lokalen Minimum-Strukturen wurden untersucht, wobei mit den erhaltenen Resultaten erstmals eine komplette, systematische Übersicht der Strukturen von Alkali-Kation-Mikrohydratationsclustern erstellt werden konnte. Dabei zu beobachtende strukturelle Trends konnten aufgrund einer Analyse verschiedener Wechselwirkungen erklärt werden. Die berechneten Strukturen wurden speziell auf Käfigstrukturen hin untersucht, die als eine mögliche Erklärung magischer Zahlen postuliert worden waren (wobei dem postulierten Dodekaederkäfig für die magische Zahl $n = 20$ ein besonderes Interesse zukam). Für $\text{M}^+(\text{H}_2\text{O})_{20}$ ist die Frage der magischen Zahlen besonders faszinierend: Die postulierten Dodekaederstrukturen wurden in der Tat als globales Optimum im Fall von $\text{K}^+(\text{H}_2\text{O})_{20}$ und $\text{Cs}^+(\text{H}_2\text{O})_{20}$ gefunden, allerdings energetisch dicht gefolgt von Nicht-Doedekaederstrukturen. Die statischen Strukturen und Energien alleine reichen also nicht als adäquate Erklärung für die magische Zahl $n = 20$ aus, weshalb auch dynamische Effekte des Wassernetzwerks berücksichtigt werden müssen. Mit dem hier verwendeten Modell findet man keine Dodekaederstrukturen für $\text{Na}^+(\text{H}_2\text{O})_{20}$, was in Übereinstimmung mit dem Experiment ist, in dem keine magischen Zahlen für $\text{Na}^+(\text{H}_2\text{O})_n$ beobachtet worden waren. Ein Strukturprinzip, das allerdings alle magischen Zahlen gemein haben, ist, daß sie lediglich aus drei- oder vierfach koordinierten Wassermolekülen bestehen.

Moleküldynamiksimulationen wurden für alle globalen Minimum-Strukturen und verschiedene Temperaturen (unter Verwendung eines kanonischen Ensembles) durchgeführt. Indem Strukturen magischer Zahlen erzwungenerweise dissoziiert wurden, konnten Entropieeffekte und Freie Energien erhalten werden. Dabei wurde beobachtet, daß tatsächlich Strukturen, die nur aus drei- oder vierfach koordinierten Wassermoleküle bestehen, stabiler sind als andere, weshalb dies durchaus eine mögliche Erklärung für die Existenz magischer Zahlen sein kann. Allgemeine strukturelle Trends und Aufbauprinzipien, die schon für die globale Geometrieoptimierung gefunden worden waren, wurden auch im dynamischen Verhalten der Strukturen in einem kanonischen Ensemble beobachtet.

Um ein besseres Verständnis dieser Systeme zu bekommen, und um Daten für einen Vergleich mit dem Experiment zu erhalten, wurden anharmonische Infrarotspektren für alle globalen sowie einige tiefliegende lokalen Minimum-Strukturen mit Hilfe eines empirischen Modells berechnet. Dieses Modell war zu Beginn der Untersuchungen auf reine Wassercluster und Eis kalibriert. Dennoch konnten qualitativ korrekte Daten für die hier vorliegenden Systeme erhalten werden. Die so berechneten Spektren zeigen eine charakteristische Wechselbeziehung zwischen den Clusterstrukturen und speziellen Merkmalen der Spektren, wodurch es möglich sein sollte, verschiedene Clusterstrukturen experimentell voneinander zu unterscheiden. Es konnte zudem gezeigt werden, daß für Temperaturen bis zu 100 K globale Minimum-Strukturen (die bei 0 K berechnet worden sind) die simulierten Spektren dominieren. Kürzlich erhältliche experimentelle Daten, die uns freundlicherweise von J.M.

Lisy (Universität Illinois) für unsere Untersuchungen zur Verfügung gestellt worden waren, konnten für eine Rekalibrierung des empirischen Modells verwendet werden. Dadurch konnte eine fast perfekte quantitative Übereinstimmung mit dem Experiment erhalten werden. So war es zum ersten Mal tatsächlich möglich, den einzelnen Peaks in den experimentellen Spektren Schwingungszustände zuzuordnen und daraus abzuleiten, welche Strukturen im Experiment tatsächlich vorliegen. Zur Zeit baut J.M. Lisy seine Untersuchungen auf größere Cluster aus, so daß schon bald mit Hilfe der Kombination Theorie/Experiment direkte Strukturinformationen über magische Zahlen erhalten werden können.

Contents

1. Introduction	1
1. Structural information on alkali cation microhydration clusters obtained from global geometry optimisation	5
2. Global geometry optimisation	7
2.1. Relevance of the global minimum	7
2.2. Global optimisation methods	8
2.2.1. Series of local optimisations	8
2.2.2. Simulated annealing	9
2.2.3. Basin-hopping	9
2.2.4. Genetic algorithms	9
3. Global optimisation of alkali cation microhydration clusters	11
3.1. Clathrates and magic numbers	11
3.2. Model potential	12
3.3. Phenotype algorithm	14
3.4. Water network dependent niching for $M^+(H_2O)_n$	18
4. Results and discussion	21
4.1. Pair interactions	21
4.2. Binding energy per water molecule as a function of cluster size	24
4.3. Remarks on the structure depicting program “xmakemol”	26
4.4. Structural trends for $M^+(H_2O)_n$ with $M = Na, K, Cs$ and $4 \leq n \leq 22$	27
4.5. Dodecahedral cage structures	33
4.5.1. Are magic numbers due to a special structural pattern?	38
5. Conclusions obtained from global geometry optimisation	43

II. Simulated infrared spectra of alkali cation microhydration clusters and comparison to experiment	45
6. Simulation of infrared spectra	47
6.1. The local mode approach	47
6.2. Frequency dependence	49
7. Results and discussion	51
7.1. Influence of the frequency vs. field curve on the spectral data	51
7.2. Overall trends in structure-spectra relations	52
7.3. Temperature dependence	60
8. Experimental data and peak assignment	65
8.1. $M^+(H_2O)$ with $M = Na, K, Cs$	68
8.2. Experimental infrared spectra of $Na^+(H_2O)_n / n = 3 - 4$	69
8.3. Experimental infrared spectra of $K^+(H_2O)_n / n = 3 - 5$	74
8.4. Experimental infrared spectra of $Cs^+(H_2O)_n / n = 3 - 6, 8$	79
9. Conclusions obtained from infrared spectra	89
III. Dynamics of alkali cation microhydration clusters	91
10. Molecular dynamics simulation	93
10.1. The concept of molecular dynamics	93
10.2. A basic structure of an MD-program	94
10.3. Molecular dynamics of alkali cation microhydration clusters	95
10.3.1. Molecular dynamics of molecules in general	95
10.3.2. Translational motion	97
10.3.3. Rotational motion	97
10.3.4. Force field	102
10.4. Molecular dynamics at constant temperature	102
10.4.1. Andersen thermostat	102
10.4.2. Nosé-Hoover thermostat	103
10.5. Constrained dynamics	104
10.5.1. The method of undetermined parameters	106
10.5.2. RATTLE or the method of undetermined parameters in combination with the velocity Verlet integration scheme	108
10.5.3. Application of RATTLE for constraining the distance between one wa- ter molecule and the central ion in alkali cation microhydration clusters	110

11. Results	113
11.1. Molecular dynamics program for alkali cation microhydration clusters	113
11.1.1. Quaternions	114
11.1.2. Velocities and kinetic energy	115
11.1.3. Checks on accuracy	115
11.1.4. Conservation laws	116
11.2. Canonical ensemble	119
11.2.1. Use of the Andersen thermostat	119
11.2.2. Dynamics of $M^+(H_2O)_n$ with $M = Na, K, Cs$ and $4 \leq n \leq 21$	120
11.2.3. Dynamics of dodecahedral cage structures	134
11.3. Constrained dynamics	137
12. Conclusions obtained from cluster dynamics	149
IV. Summary	151
13. Final conclusions and future prospects	153
V. Appendix	157
14. Excerpts from the molecular dynamics routine used in this work	159
14.1. double precision function gauss	159
14.2. subroutine andersen	160
14.3. subroutine randimp	161
15. Additional figures	167
15.1. Figures for constrained dynamics of $Cs^+(H_2O)_{19}$	167
15.2. Figures for constrained dynamics of $Cs^+(H_2O)_{21}$	172
15.3. Figures for constrained dynamics of $Cs^+(H_2O)_{20}$ DOD – dodecahedral	177
15.4. Figures for constrained dynamics of $Cs^+(H_2O)_{20}$ BND – non-dodecahedral	185
Bibliography	193
16. Acknowledgements	199
17. Curriculum Vitae	201
18. Erklärung	203

1. Introduction

Solvation is a universal phenomenon and has a large influence on a wide range of chemical and biochemical processes, especially those involving charged species. For example simple ions in solution, like alkali cations solvated in water, are essential for life on earth. And although there is plenty of literature on this topic, this delusory simple system is still difficult to investigate experimentally and/or simulate theoretically and therefore is still not completely understood.

A simplified approach are studies on alkali cation microsolvation clusters $M^+(H_2O)_n$ (with $M = Li, Na, K, Rb, Cs$, and $n = 1, 2, \dots$) in the gas phase [1, 2], since their reduced and controlled size promises an easier treatment. Indeed, they are accessible both experimentally (see the review articles [3–6] and references [7, 8]) as well as theoretically (on moderate ab-initio levels [9, 10] and with empirical potentials [11–13], see also further literature cited in these articles).

Studies on bulk solvation and solvated ions have shown that already little “droplets” of about 20 water molecules are a suitable medium for examining reactions in the liquid phase. From the early days of these experimental investigations, it was observed that clusters with certain values of n are “magic numbers” (in particular $n = 20$, but to a lesser degree also various smaller and larger values), i.e. they occur with increased abundance, compared to their immediate neighbours $n - 1$ and $n + 1$. The standard hypothesis to explain these magic numbers proposes the formation of cage inclusion compounds, in particular that of a dodecahedron of water molecules around the cation in the centre at $n = 20$. This hypothesis is often ascribed to Castleman [2] but definitely has a longer history (see citations in Kassner and Hagen [14]). Cage structures of this type, but typically with hydrophobic guest molecules, are well known in the extended solid state as clathrate hydrates. They occur in many natural and technological processes [15, 16] and hence are investigated both experimentally (see for example reference [17] and references therein) and theoretically (see for example [18] and references therein). Therefore, this explanation had a natural appeal and accordingly served as ad-hoc hypothesis in many contexts, from ab-initio calculations [19] and rationalisation of microsolvation experiments [2, 7, 20] up to attempts to understand solvation of hydrophobic groups in the gas phase [8] and in the liquid [21, 22].

In spite (or because) of this natural appeal, this explanation retained its hypothetical status, and it suffered from some shortcomings. Recently, Hodges and Wales [23] performed

a global optimisation study for the related special case $M = \text{H}_3\text{O}^+$ using empirical potentials. For $n = 20$, they actually found a dodecahedral cage structure as global minimum, but with the hydronium ion not in the centre but in the periphery, which is confirmed by ab-initio calculations at the MP2 level (see reference [24], which also gives a brief history of this particular point). Experiments were performed in which dangling OH, i.e. OH bonds which do not participate in the water network, were replaced by tri-methylamine groups, from which the actual number of dangling OH in the cluster structure could be deduced, namely 10 [25]. Assuming a dodecahedral structure for $n = 20$ leads to the same number of dangling OH as found in the experiment. And although this seems to favour the hypothesis of the magic number 20 being due to a dodecahedron shaped structure, this experiment does not give sufficient proof that this hypothesis is correct, as non-dodecahedron shaped cluster structures can contain the same number of dangling OH bonds. For other cations and other values of n the status of the clathrate hypothesis remained unclear. In particular, it cannot explain the common observation (see for example reference [7]) that $n = 20$ is a magic number for $M = \text{K}, \text{Rb}, \text{Cs}$, but not for $M = \text{Na}$. Actually, this does not seem to be an artifact of limited-size microsolvation clusters: Bulk solvation simulations also have shown characteristic differences between Na^+ and K^+ (reference [26] and references therein). Besides the attachment of labels like “structure-making” or “structure-breaking”, no detailed explanations for these differences seem to be available, although even biological systems like ion channels in cell membranes may rely on them.

None of the above mentioned theoretical studies is based on global optimisation methods, but rather *ad-hoc* generated cluster structures were taken and optimised locally. However, due to the fact that the number of local minima increases exponentially with respect to the cluster size, these approaches are extremely error-prone [27].

Methods which are commonly used for the global geometry optimisation of cluster structures are in general fairly expensive [28, 29]. A relatively new method for global geometry optimisation of cluster structures are genetic algorithms [27, 30–36]. Compared to the other global optimisation methods, genetic algorithms are very reliable in finding the global minimum while being fairly cheap.

Another advantage of some global geometry optimisation methods is that in practice they yield not just the global minimum energy structures, but also an extensive list of low-energy minimum structures. Nevertheless, they only yield a static picture at 0 K. Hence it is often argued that in principle global geometry optimisation of a system is irrelevant, as it is not directly comparable to experiment, as (1) experiments are performed above 0 K where a Boltzmann distribution of isomers exists and (2) no information on entropy and kinetic effects can be obtained by a plain geometry optimisation. Therefore a better approach would be a full, statistically complete, molecular dynamics or Monte Carlo simulation. Whereas it

is possible to gain pieces of information from single molecular dynamics or Monte Carlo trajectories, a study of statistically correct molecular dynamics or Monte Carlo simulation is still too expensive. One solution would be to combine global geometry optimisation with molecular dynamics simulation, and hence gain information on the important regions in configuration space which are likely to be most relevant for a dynamical simulation. In this way it is possible to get a relatively complete overview on the dynamics of these systems on a reasonable time-scale. This approach was chosen in this study.

As already mentioned above, experimental data on alkali cation microhydration clusters is accessible via mass spectrometry [7]. But while mass spectrometry yields information on stability and/or dissociation pathways as a function of the size of the clusters, it does not give any information about the actual structures. Recently it was also possible to obtain infrared spectra of alkali cation microhydration clusters [4]. These spectra could be used to gain more direct access to information about structural features of alkali cation microhydration clusters. Because peak positions strongly shift by unknown amounts depending on local neighbourhood, interpretation of spectra is difficult or impossible even for a single isomer. Using a local mode approach by Victoria Buch, it is possible to simulate anharmonic infrared spectra of microhydration clusters [37]. Hence a combination of both experimental and simulated spectral data might lead to the desired cluster structures, including reasons for magic numbers.

The aim of this work was to gain structural information about alkali cation microhydration clusters, i.e. $\text{Na}^+(\text{H}_2\text{O})_n$, $\text{K}^+(\text{H}_2\text{O})_n$, and $\text{Cs}^+(\text{H}_2\text{O})_n$ with $4 \leq n \leq 24$, both in general and also with a special focus on magic numbers and cage inclusion structures. The approach was to use a combination of global geometry optimisation, simulated anharmonic infrared spectra, and molecular dynamics simulation. According to the three different methods this work is divided into three parts. The first part will describe the global optimisation method and the results gained from the global optimisation. The results obtained by the global optimisation present the first unbiased complete and systematic overview about structural features of alkali cation microhydration clusters. These results were then used as input for the simulation of the infrared spectra as well as for the molecular dynamics simulations. The second part will focus on the simulated infrared spectra, assignment of the experimental spectra, and structural information which can be withdrawn from this combination of theory and experiment. The third part concentrates on molecular dynamics simulation, which was used to investigate dynamic effects of the water network and whether these are responsible for magic numbers. A final chapter will give an overview to which extent the three methods work together and whether additional conclusions can be drawn by using this combination.

Part I.

Structural information on alkali cation microhydration clusters obtained from global geometry optimisation

2. Global geometry optimisation

Clusters continue to challenge experimentalists and theorists alike. While experimentalists focus on basic questions such as changes of properties dependent on cluster size and magic numbers, they also link clusters to areas such as climatology [38] or nano-technology [39]. However, before theory can address such issues, it has to solve simpler problems, starting with the structure of clusters. Naively, one may assume that the cluster structure corresponding to the global minimum of the potential energy surface in the configuration space of the clusters is the one most likely to be found in the experiment. Actually in many experimental situations this appears to be true. In other situations it is likely that a mixture of thermodynamic and kinetic factors determines the cluster formation and structure [34, 40, 41]. Nevertheless cluster geometries corresponding to the global energy minimum or to low-energy local minima are not only likely candidates for the most probable structure, but they are also indispensable for the understanding of the most important features of the potential energy surface [42]. Furthermore, locating these minima should be less demanding than a microscopic simulation of possible cluster formation processes.

2.1. Relevance of the global minimum

This assumption, i.e. that the global minimum structure is actually the structure found in the experiment, is often used for underpinning the necessity of finding these structures [43]. On the other hand, it is often argued that in principle a global geometry optimisation of a system is irrelevant, as eventually the comparison to the experiment is what matters, where in turn one finds a Boltzmann distribution of many structures.

However, global geometry optimisation methods yield not just the global minimum energy structure in practice, but also extensive lists of low-energy local minimum structures. Hence, without expending the effort of full MD, one gets an impression of the regions in configuration space that are likely to be most relevant in dynamics studies.

Also, experimental evidence often indicates less structural variety than one may expect, and it also supports the usefulness of global geometry optimisation: For example, in experiments on small pure water clusters [40], only one structure is found, corresponding to the global minimum (possibly after zero-point energy correction, in the case of the hexamer cage vs.

prism structures [40]). From global geometry optimisations [34, 44], one knows the complete series of global and low-energy local minima, and hence it is possible to state that this is in agreement with the estimate of 5 K for the experimental temperature. In helium droplets, only the six-membered ring for the water hexamer was found [45]; again from global optimisations it is obvious that this is due to the influence of cluster formation kinetics. For slightly larger clusters $n = 6 - 10$, experimental spectra can be explained with just the one or two cluster structures lowest in energy [37]. Finally, for still larger systems and for heterogeneous clusters, the very occurrence of magic numbers [2, 7, 36] is a strong argument for structural influences not being washed out completely by dynamics covering extensive regions of configuration space.

2.2. Global optimisation methods

It has been shown that a discretised version of the problem of finding the global minimum structure of clusters belongs to the class of NP-hard problems [29, 46]. These proofs do not rely upon particular forms of the potential energy function. This suggests that the (computer) time needed to find an (exact) solution will increase exponentially with cluster size. Thus, it may seem that it is almost impossible to solve the global optimisation problem of clusters of any number of atoms or molecules relevant to physical or chemical applications. However, complexity proofs are typically general worst-case scenarios [29] and in special cases in practice one may arrive at solutions for NP-complete tasks in polynomial time. Several different exact deterministic methods (with a guarantee of finding the global optimum) exist [28]. Their practical application is limited to very small systems due to the NP-character of the problem and the implicit necessity to search the whole configuration space when using a deterministic method. However, if one is willing to sacrifice exactness or the guarantee of finding the global minimum, better scaling and shorter computer time is possible. These methods then will be non-exact and non-deterministic. However, they can be used for problems relevant to scientists.

Over the years, several different methods have been developed for global optimisation in all kinds of fields. As a comparison between these methods is not an integral part of this work, only a very short explanation of the most prominent methods shall be given. For detailed descriptions see the literature [28, 29] (and references therein).

2.2.1. Series of local optimisations

Successive local optimisations, excessively using external advance information, present the implicit standard procedure of theoretical chemistry. The choice of the starting points for the local optimisation can occur automatically in various ways [47]: simple random search,

systematic grid search, or a selection of points on classical trajectories. Alternatively or additionally an arbitrary amount of advance information can be included in the choice of the starting positions. In each case, this method will be a quasi-deterministic method provided that a sufficient number of starting points was selected. However, this presents more the theoretical point of view, as in reality this method often fails for clusters of relevant size due to the exponential scaling of search space. The danger of missing whole regions of the configuration space in practice is already very high for very small clusters [27].

2.2.2. Simulated annealing

The once very popular quasi-universal global optimisation method *simulated annealing* [48] is nowadays viewed more critically. The computational effort in comparison to the gained result (even ideally only the global minimum, no local minimum) is fairly high and above all the information gained during the computation of the momentary state of the system is not used at any later point. Also the determination of the optimal cooling curve proves to be quite problematic in practice.

2.2.3. Basin-hopping

A distant relative of simulated annealing is the so-called *basin hopping* [49]. The method basically employs a series of Monte-Carlo steps each followed by a local optimisation. This is equivalent to a Monte-Carlo method on a potential energy surface which has been transformed to a series of plateaus and steps thus showing considerably lower potential barriers. Due to the large number of local minimisations the effort involved is not inconsiderable.

2.2.4. Genetic algorithms

In contrast to the typically iterative improvement of single points in configuration space (here cluster geometries) without further exchange of information in the methods mentioned so far, evolutionary or genetic algorithms work with many trial solutions in parallel and exchange of information between them.

The general idea of genetic algorithms is global optimisation on the basis of the evolution of a species in an (in the majority of the cases chronologically constant) environment. Different variations of genetic algorithms have been applied in miscellaneous scientific areas over the past years, for example ranging from analytical chemistry [50], DNA- and protein-folding [51], and simulation of solvation models [52] up to cluster geometry optimisation [32, 33, 35, 53].

A basic genetic algorithm (or standard genetic algorithm) works as follows: All coordinates of a structure build up the genome of an individual and all n individuals together are called

the population. When mating, two individuals form a pair. Exactly $p/2$ pairs are selected according either to fitness parameters or at random. All selected pairs together form the so-called *mating pool*. For the actual reproduction each pair interchanges parts of its genes with its assigned partner, which is usually referred to as *cross-over* or *crossing-over*. This action represents the exchange of information between two individuals. In order to assure a full exploration of the configuration space, mutations are performed after the reproduction, i.e. a selected percentage of coordinates of a randomly chosen individual are changed at random. After reproduction and mutation the fittest individuals are selected according to a parameter of interest, for example the potential energy, to form the next generation. A detailed description of the actual genetic algorithm used in this work will be given in section 3.3. Due to the mixture of exploration, exchange of information and privileged reproduction of the best individuals the whole population will drift towards a low-lying minimum. By choosing adequate parameters (for example the rate of mutation, the population size etc.) one can in practice assure that this minimum is most likely the global minimum.

Compared to other global optimisation methods, such as simulated annealing [28, 29], genetic algorithms are very economic, as partial solutions i.e. short parts of the genome (so-called *building-blocks*), are tested in parallel: It could be shown in general for a standard genetic algorithm that the combination of *cross-over* and fitness-controlled reproduction leads to a preferred recombination of partial solutions which proved to be better than others and hence leads to an exponential augmentation of these building blocks in the next generations in favour of inferior partial solutions/building blocks.

Genetic algorithms are not only a general method, which is easy to program, but they are also quite robust when regarding the details of the actual implementation of a problem. Up to date, various variants have been applied with success [35, 36, 53–56].

3. Global optimisation of alkali cation microhydration clusters

As already mentioned in the introduction, the systems of interest for this work are alkali cation microhydration clusters with sodium, potassium and caesium as central ion, as experimentally found magic numbers for these clusters could not be explained yet (see section 3.1 below). In the following sections (see sections 3.2, 3.3, and 3.4) the method used for global geometry optimisation of these systems will be described in detail. A description of the method used and a selection of the results obtained have also been published in reference [57].

3.1. Clathrates and magic numbers

A special interest in research areas involving cluster physics and chemistry focuses on magic numbers, which correspond to clusters (composed of n atoms or molecules, detected in the experiment) that seem to exhibit a stronger stability than others, as they exist in increased quantity compared to their immediate neighbours ($n - 1$) and ($n + 1$). Figures 3.1, 3.2, and 3.3 depict typical mass spectra that were obtained for $\text{Na}^+(\text{H}_2\text{O})_n$, $\text{K}^+(\text{H}_2\text{O})_n$, and $\text{Cs}^+(\text{H}_2\text{O})_n$ -clusters, respectively,

using LILBID (laser induced liquid beam ionisation/desorption mass spectrometry) [7]. (Weak) magic numbers are indicated by arrows in these spectra. These numbers were also found using other techniques, such as for instance electro-spray [36], hence confirming the findings of LILBID.

From the beginning of these experimental investigations, it was found that $n = 20$ is possibly the most prominent magic number, but to a certain extent also various smaller and larger values were observed.

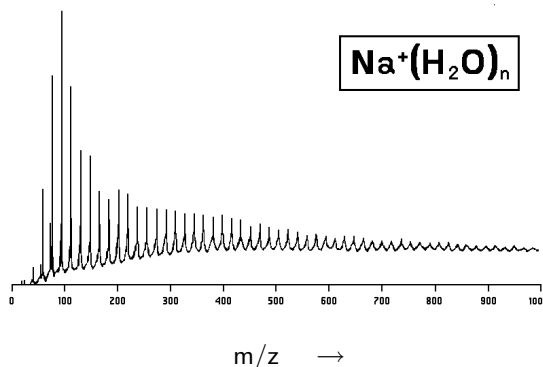


Figure 3.1.: Mass spectrum of $\text{Na}^+(\text{H}_2\text{O})_n$ clusters in the gas phase

As already mentioned in the introduction, the standard hypothesis which tries to explain these magic numbers proposes the formation of cage inclusion compounds, in particular that of a dodecahedron composed of 20 water molecules which surround the cation located in the centre [14, 58].

Cage inclusion compounds of this pattern, especially those containing a hydrophobic guest molecule, are well established as clathrate hydrates for the extended solid state. The dodecahedron hypothesis had some kind of natural appeal and for the related special case $M = \text{H}_3\text{O}^+$ a global optimisation search was performed using empirical potentials [23] and indeed a dodecahedral cage structure was found as global minimum, however with the hydronium ion not in the centre but in the periphery, which is confirmed by *ab-initio* calculations at the MP2 level [24]. And although these findings portray some weak support for the dodecahedron hypothesis in particular and for the clathrate hypothesis in general, in the case of alkali cation microhydration clusters the status of both remains unclear. Above all, these hypotheses fail to explain why $n = 20$ is a magic number for $M = \text{K}, \text{Rb}, \text{Cs}$, but not for $M = \text{Na}$ [7]. Hence, the aim of this work was to try and clarify this hypothesis by means of theoretical investigations.

3.2. Model potential

Due to the fact that calculations, especially global geometry optimisation of larger molecular clusters, i.e. clusters with $n \geq 10$, on *ab-initio* levels are to date still very difficult, methods which are based on empirical potentials still have to be used. To the best of our knowledge,

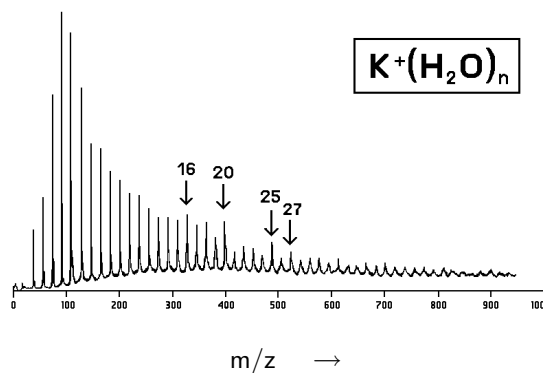


Figure 3.2.: Mass spectrum of $\text{K}^+(\text{H}_2\text{O})_n$ clusters in the gas phase

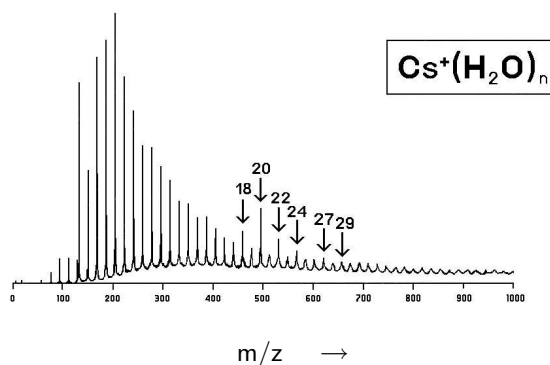


Figure 3.3.: Mass spectrum of $\text{Cs}^+(\text{H}_2\text{O})_n$ clusters in the gas phase

to date ab-initio data is only available for $\text{Na}^+(\text{H}_2\text{O})_n$ with $n \leq 10$ and $\text{K}^+(\text{H}_2\text{O})_n$ with $n \leq 8$ [9, 10], while no data on $\text{Cs}^+(\text{H}_2\text{O})_n$ could be found.

For water-water and water-ion interactions, the well-known TIP4P/OPLS model was used [59–61]. In this model, the water monomers are rigid. Interactions between two monomers m and n are described by a pair potential, see equation 3.1, consisting of a Lennard-Jones term between the locations of the oxygen atoms and of Coulomb terms between partial charges on the hydrogen atoms and on a dummy site Z on the HOH-angle bisector, somewhat off the oxygen atom (see figure 3.4). In equation 3.1 the labels m, n denote different water molecules, whereas the labels i, j denote different atoms or sites in these molecules.

$$v_{mn} = \sum_{i \in m} \sum_{j \in n} \frac{q_i q_j}{r_{ij}} + \frac{A_{ij}}{r_{OO}^{12}} - \frac{C_{ij}}{r_{OO}^6} \quad (3.1)$$

Water-cation interactions are modelled similarly, with the ion being treated like a water oxygen atom, except that it has a full charge of +1.0 assigned to its location.

The parameters for Na^+ , K^+ , and Cs^+ are taken from the literature [62, 63]. For completeness, all parameters used here are listed in Table 3.1. Note that the parameters given for water and the ions are for the pure interactions between like species, A_{ii} and C_{ii} . The actual mixed ion-water interaction parameters A_{ij} and C_{ij} are generated from these by the usual geometrical mean rule $P_{ij} = \sqrt{P_{ii}P_{jj}}$, for $P = A, C$.

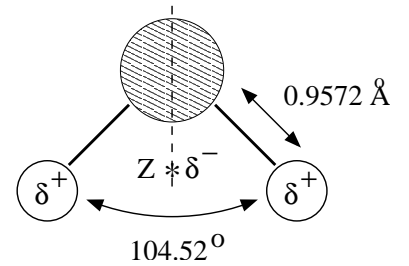


Figure 3.4.: TIP4P water molecule

The virtue of this choice of potential is in its common, widespread use in many fields, including biochemical studies. Certainly, one should not expect quantitative accuracy in absolute energy values for the clusters studied here, since the model has been parameterised largely for MD studies of bulk solvation and since explicit many-body terms and important terms for other types of physical interactions are missing, in particular polarisation of the water molecules.

However, all these effects as well as zero-point energy and finite temperature corrections enter via the parametrisation. Also, water and ion polarisation appears to be qualitatively essential for anion solvation [64] but only has small or negligible effects in cation solvation [65]. Therefore, it is not too surprising that qualitative cation microsolvation cluster structures and relative energy ordering of minima are reproduced very well by this model, compared to ab-initio calculations of small systems including such corrections, as already pointed out in reference [36]. Also TIP4P is known for its surprisingly good performance for small pure water clusters [66].

	H ₂ O	Na	K	Cs
charge q_Z	-1.04			
q_H	0.52			
q_O	0.0	1.0	1.0	1.0
A [\AA^{12} kJ/mol]	2510400.0	82006.0	1788175.0	86976837.0
C [\AA^6 kJ/mol]	2552.0	2615.0	11611.0	80973.0
r_{OH} [\AA]	0.9572			
r_{OZ} [\AA]	0.15			
$\angle(\text{HOH})$ [$^\circ$]	104.52			

Table 3.1.: TIP4P/OPLS parameters used in this work, see text

Finally, it should be pointed out that a largely electrostatic picture of the hydrogen bond in water, as provided by the TIP4P model, is not at all unreasonable, in contrast to the alleged covalent contributions strongly publicised recently [67], which were based on a misinterpretation of data [68].

3.3. Phenotype algorithm

The genetic algorithm used for this work is a so-called phenotype algorithm (named **phenix**), i.e. the program is based on a standard genetic algorithm [53–56] which has been modified significantly in some parts [31, 33]:

The algorithm does not use the otherwise common genetic coding of the geometries in so-called *strings* [56] but operates directly on the cluster geometry in three-dimensional space. Hence one circumvents the problem that a bad encoding of the string representation might make the global optimisation unnecessarily hard. Additionally this makes it easier to develop special operators and specific subroutines. For a graphical scheme of this genetic algorithm see figure 3.5.

Generation zero

The algorithm is initialised with locally optimised random cluster geometries, using a relatively small population size of about 30 individuals. This generation zero is produced by setting all coordinates of all cluster constituents to random numbers, followed by a local minimisation of each cluster structure. The local optimisations in this program are performed

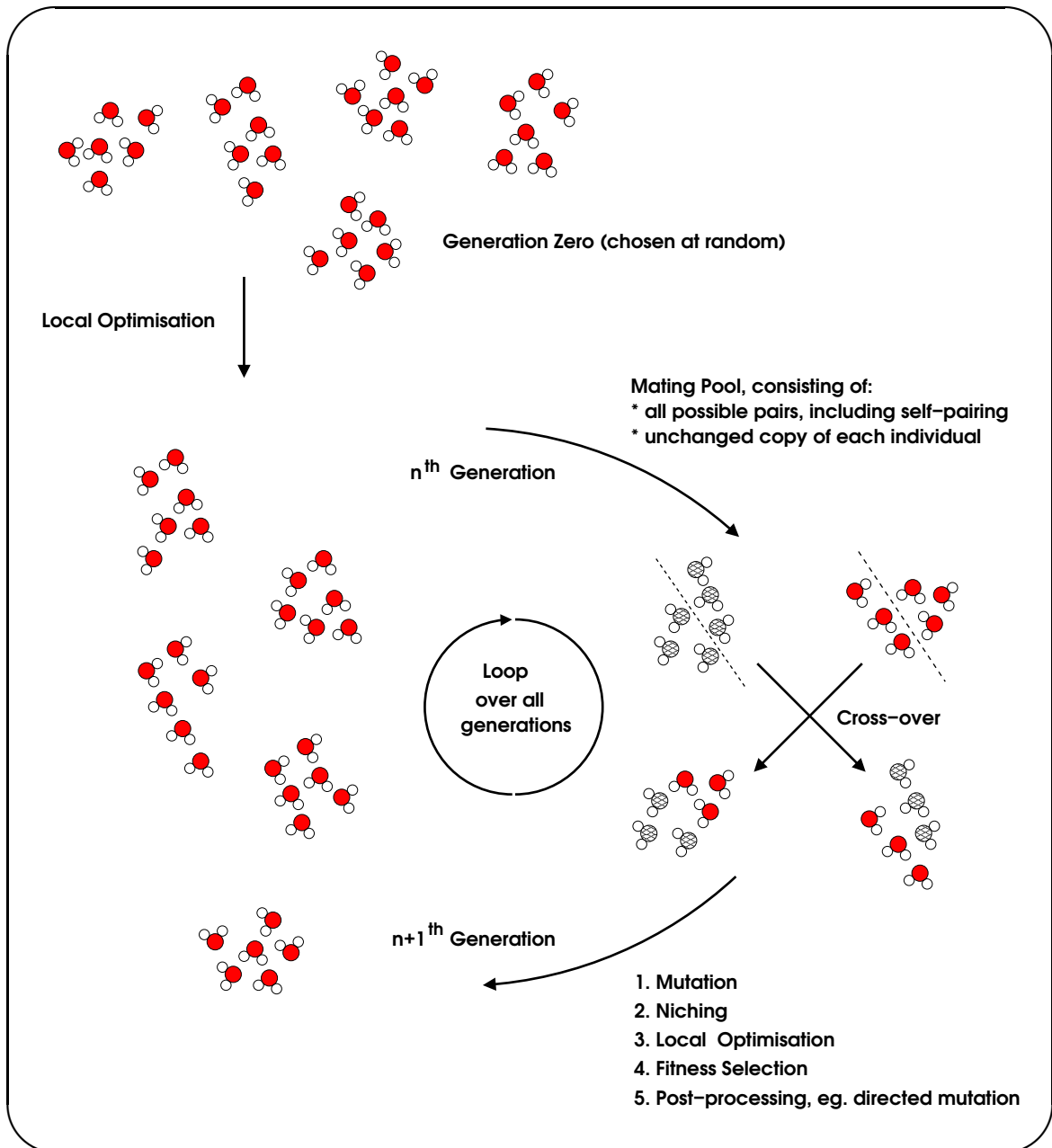


Figure 3.5.: Scheme of the evolutionary phenotype algorithm

using a quasi-Newton method. In order to avoid having to deal with clusters dissociated into many small bits and pieces (such configurations are very unlikely to lead to the global minimum structures in the case of alkali cation microhydration clusters) the random numbers are drawn only within a given coordinate range, thus placing some initial bias on compact structures. Also a minimum distance between the molecules is enforced in order to avoid numerical difficulties in the ensuing local minimisation, due to the typically steeply repulsive branches of most potential energy functions at close pair distance.

Reproduction – cross-over

In order to compensate for the size limitation of the population, instead of selecting $n/2$ parent pairs using some combination of fitness and random criteria, all possible pairs are created (including pseudo-pairs of each individual with a copy of itself). These pairs build up the *mating pool*. Applying a *cross-over* operator to the pairs, each pair produces two children. From this larger intermediate pool of children, n individuals are selected for the actual next generation using several criteria (see below).

The *cross-over*-operator divides the clusters by a plane into two parts of equal size. The cut proceeds through the origin (which contains the central ion). After recombining the cluster halves, their distance and relative orientation towards each other is optimised, before the full local minimisation is applied to the new cluster child.

Mutation

After the cross-over and before the local optimisation a small number of constituents (i.e. water molecules) of the clusters are chosen at random (typically not more than 30% total). Each of those is moved by a random distance in a random direction and rotated at random. However these moves are limited such that they must not place the moved constituent far away from the cluster or too close to another constituent.

Niching and selection of the fittest individuals

The selection of the actual next generation from the larger intermediate pool is done using two basic criteria: the usual fitness measure based on minimal potential energy and geometric diversity using niches (see below).

The whole pool is sorted by potential energy and in addition each cluster is assigned one (or several) numbers classifying its geometry. Starting from the clusters with the lowest potential energy, each cluster of the intermediate pool is inspected whether or not it is to be selected into a niche, and it is compared to clusters already selected into the next generation.

If its geometry classification number(s) deviate(s) more than a given difference from the corresponding classification number(s) of the already selected clusters, it is also selected, irrespective of its potential energy and constitutes a new geometrical niche of its own. If its geometry classification number(s) is (are) closer than a given difference to the one(s) of an already selected cluster (i.e. if it falls within an already established geometrical niche), it is selected only if the number of clusters in this niche does not exceed a given limit and if its potential energy differs from the other clusters in this niche by more than a given amount. This selection process continues until a total of n clusters has been selected (constant overall population size). To ensure a maximum of exploration there is also a niche for mutants, which is filled with clusters that were operated upon by the mutation operator; there are no other criteria for this niche, though the minimum energy difference criterion does still apply. Note that these geometrical niches differ from most usual ones in several respects: They exist only in the selection step (i.e. there is constant inter-breeding between niches); they are temporary and dynamic also in the sense that they are re-determined from scratch in each generation and then discarded again. And all user input needed for their determination is one measure characterising the clusters other than their potential energy. The general need for these niches as well as the choice of niche measures depends on the application under study.

Niching allows clusters to survive which would not have survived just because of their potential energy. This allows a larger diversity and hence a better exploration of the configuration space, as niching avoids that the population will finally drift into the catchment area of a local instead of the global minimum because no single structure can dominate the entire population [33].

Post-processing

After each new generation is established, it is subjected to a set of post-processing operators, applied in random selection to each cluster in turn in an attempt to further refine the selected clusters.

One obvious operator is a simple repetition of local minimisation but this time with a tighter threshold (this allows for the use of rather loose thresholds in the more numerous applications of local minimisations in the remainder of the algorithm).

Often the algorithm quickly converges to the vicinity of the correct global minimum solution but then takes a long time to move a very small number of misplaced molecules into their optimal places. This can be fixed using directed mutation operators: A very small number of the worst constituents is removed from the cluster and re-introduced into the most promising positions, discovered by a loose three-dimensional grid search over the whole surface and interior of the cluster. For molecular clusters also the optimal orientation is determined before the re-introduction.

For molecular clusters it is advantageous to treat the position and orientation coordinates not only together but also separately. Therefore, another important post-processing operator is a copy of the whole **phenix** algorithm operating solely on the orientation coordinates, with the position coordinates kept fixed at the values of the particular cluster under study.

3.4. Water network dependent niching for $M^+(H_2O)_n$

A suitable niching criterion for alkali cation microhydration clusters would be the number of rings formed by hydrogen bonds in the water network, as this way a greater diversity of different water networks is ensured. Hence a ring-count algorithm has been developed [57] in order to be able to implement such a niching criterion in the existent phenotype algorithm (**phenix**). This routine has also been partly described in reference [57] as well as the corresponding results.

As the ring-count routine proved to be more complicated to program than one might assume and in turn became rather complex it shall be described in a simplified version (see also figure 3.6 for a simplified flowchart). In a first step an adjacency matrix is computed for the water network, which contains all information regarding the number and direction of all hydrogen bonds formed by each water molecule. This adjacency matrix is then submitted to the actual ring-count routine. Now all one has to do is to step through the matrix and to extract the information needed to find and to count all present rings. As mostly four to seven-membered rings are present in the water networks, the size of the rings to be counted was reduced accordingly, which in turn made the routine both a little more concise and more efficient. When stepping through the matrix the routine will start from hydrogen bonds marked as such in the matrix. From this starting position the routine searches for an adjacent water molecule and proceeds from there looking for yet another adjacent water molecule and so on. The routine will proceed until either a ring is found which is easily recognised by again arriving at the starting position or a dead end is reached, which would be the case if the eighth adjacent water molecule in a row is not equal to the starting position. The restriction that a dead end is reached for the eighth water molecule is due to the limitation of ring sizes to $4 \leq n \leq 7$. In any case the routine will step back the same route to look for alternative branchings of the route as the same starting molecule can be present in more than one ring. In some cases the stepping back has to be performed several times before being able to advance to a new starting position as otherwise not all possibilities may have been accounted for, which again would lead to a miscount. While the stepping back assures that no possibility is missed and in turn all rings are accounted for at least once, it does not ensure that each ring is only counted once. Hence labels are assigned to each found and counted ring. Finally the routine was made more efficient such that once a ring was found, counted, and labelled, the routine would not step through the same ring again even if the possibility existed. The

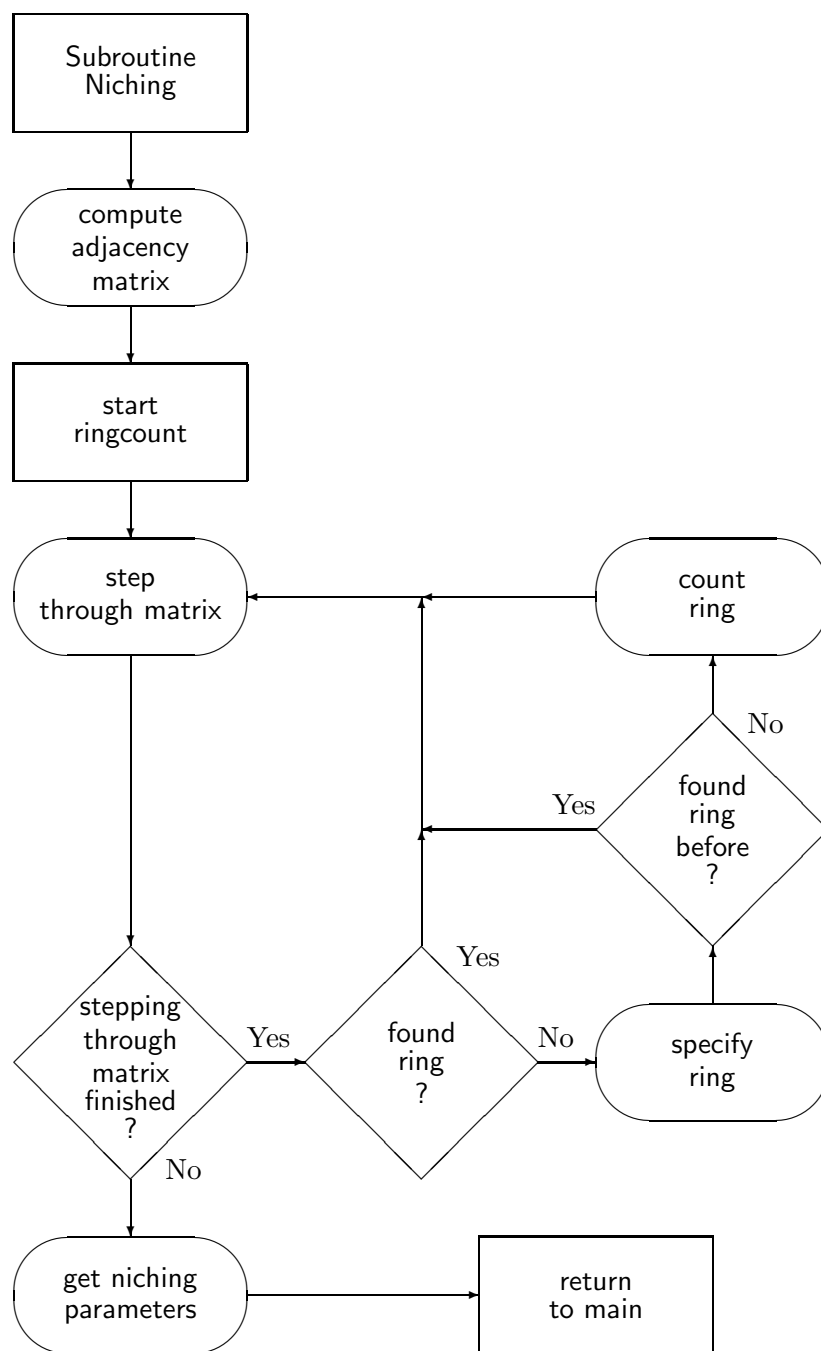


Figure 3.6.: Flowchart depicting a simplified version of the ring-count algorithm employed as niching criterion for alkali cation microhydration clusters

routine can also specify whether rings are homodromic, i.e. all hydrogen bonds in the ring are directed in the same way. These rings are supposed to be energetically more stable than cases in which the direction of the hydrogen bond differs. The information gained from the ring-count, i.e. type and number of rings, was then assigned to special parameters which were used for the actual niching.

4. Results and discussion

In order to gain more insight in solvation processes of alkali cations in water, microsolvation clusters $M^+(H_2O)_n$ (with $M = Na, K, Cs$, and $n = 4 \leq 24$) were investigated. These systems were globally optimised using **phenix** (for a detailed description of the algorithm see section 3.3). The structures found can be explained using the energy partitioning described in section 4.1 below. A selection of the results presented here has also been published in reference [57].

It should be mentioned again that the following results were obtained within the TIP4P/OPLS potential and therefore energy values should not be compared to the values obtainable from ab-initio calculations. For systems up to $n = 10$ ab-initio calculations are possible, however, structures obtained using the TIP4P/OPLS potential seem to be qualitatively correct. Hence, it can be assumed that also bigger systems are treated qualitatively correctly, thus allowing to make first assumptions about structural trends.

4.1. Pair interactions

Obviously, the most important gauge for the influence of an ion on the structure of a water network in its vicinity (i.e. for ion-water interactions) is the strength of the water dimer hydrogen bond (i.e. the water-water interaction). At optimal distance and relative orientation of the monomers in the water dimer, such a hydrogen bond yields an energy contribution of 26 kJ/mol, at the TIP4P level. It is tempting to compare this to the value of 20 kJ/mol to which high-level ab-initio treatments and experiment recently managed to converge [69]. But this misses the point entirely; as it has already been conceded in section 3.2 that TIP4P cannot be expected to give good absolute energy values but is nevertheless a reasonable model for our purposes. Thus, within the model to be used here, 26 kJ/mol is the valid number. Also, note that the dimer potential is comparatively flat: Moderate deformations (keeping the geometry within chemical reason) only cost a few kJ/mol and hence can be largely discounted. Therefore, the energy value of a (reasonably structured) water network can be approximated by the number of hydrogen bonds it contains.

Compared to the above 26 kJ/mol for a water-water interaction, ion-water interactions for Na^+ , K^+ and Cs^+ fare differently (see table 4.1): A single Na^+ -water interaction gains a maximum of 102.64 kJ/mol, within our model, at optimum distance (2.32 Å) and orientation.

ion-water distance [\AA]	optimal orientation	H	<i>flipped</i>	H	<i>flapped</i>	H
Na						
2.32	102.64	3.9	80.00	3.1	40.00	1.5
4.0	40.00	1.5	30.00	1.2	10.00	0.4
K						
2.68	79.59	3.1	60.00	2.3	30.00	1.1
5.0	25.00	1.0	20.00	0.8	8.00	0.3
Cs						
3.20	58.08	2.2	45.00	1.7	28.00	1.1
6.0	17.00	0.7	14.00	0.5	5.00	0.2

Table 4.1.: Energy contributions in kJ/mol and in comparison to the optimal water dimer hydrogen bond (columns marked “H”), for various ion-water interactions, see text

Thus, one such interaction can compensate four water-water interactions. In fact, since a single water molecule cannot have more than four hydrogen bonds (two as donor, two as acceptor), water-water interactions can never beat ion-water interactions, close to a sodium cation. In particular, in an ideal two-dimensional form (e.g. in a clathrate cage without surrounding water molecules), each water molecule participates in only three hydrogen bonds; therefore, we can expect that even at diameters larger than the 1st-shell distance such a cage structure will be less favourable than a three-dimensional distribution of water molecules in 1st and 2nd-shells around Na⁺. Due to the Coulomb part, the Na⁺-water potential is not only deep but also far-reaching: A water molecule 4 \AA away from a sodium cation (approximately corresponding to an average “2nd-shell” distance in our clusters) still gains 40 kJ/mol, or 1.5 hydrogen bonds. Also, the orienting power of Na⁺ is considerable: A water *flip* (see figure 4.1) at the optimal distance costs 23 kJ/mol, or one hydrogen bond. A water *flap* (see figure 4.2) costs a staggering 60 kJ/mol, or more than two hydrogen bonds. In small hydration clusters, this is difficult to compensate by hydrogen bonds, since almost all water molecules are at the cluster surface and hence most of them can participate only in at most three hydrogen bonds. At 2nd-shell distance (4 \AA), energy costs for these *flip* and *flap* angular motions are smaller (10 kJ/mol and 30 kJ/mol, respectively) but still very relevant on our scale. Thus, this simple consideration of a few representative interactions in a simple model potential leads to the expectation that a sodium cation should have a decisive re-structuring and re-ordering influence on surrounding water, extending beyond the first solvation shell. Interestingly, this “structure-breaking” effect is in perfect accord with observations deduced from expensive QM/MM simulations of bulk ion solvation [26]. This picture begins to change for the potassium cation: Within the OPLS model, it is simply larger than the sodium cation

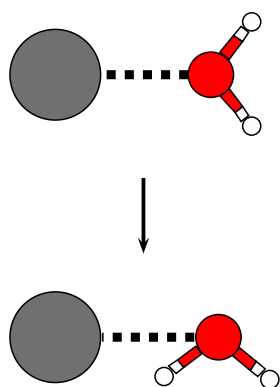


Figure 4.1.: *Flip* motion of a water molecule relative to an ion, starting from the equilibrium orientation (top) to the 90 degree position (bottom), see text.

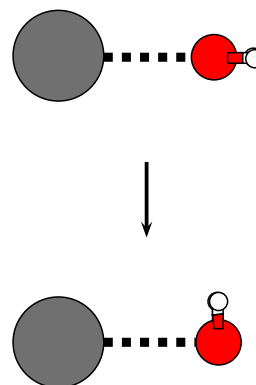


Figure 4.2.: *Flap* motion of a water molecule relative to an ion, starting from the equilibrium orientation (top) to the 90 degree position (bottom), see text.

via the Lennard-Jones term, hence the optimal ion-water distance is larger (2.68 \AA) and the attractive Coulomb contribution is smaller despite unchanged (partial) charges. Nevertheless, a water molecule at optimal distance and orientation towards K^+ still gains 79.59 kJ/mol , compensating three hydrogen bonds. Thus, following the above argument for sodium, one can expect to find a delicate balance between cage and non-cage structures for potassium. *Flip* and *flap* costs in the 1^{st} shell drop somewhat (18 and 50 kJ/mol , respectively) but not decisively. But at the average 2^{nd} -shell distance of 5 \AA one does see effects: Even in optimal orientation, one ion-water interaction does not gain us more than 25 kJ/mol or just one hydrogen bond. And, while a *flap* is still an important entry in the energy balance at this distance (costing 17 kJ/mol), a *flip* has become affordable since its cost ($4 - 5 \text{ kJ/mol}$) has dropped down from being comparable to full formation of a new hydrogen bond to being comparable to minor re-orientations within the hydrogen-bond network. Thus, the influence of K^+ on surrounding water is clearly less far-reaching than that of Na^+ , again in agreement with the QM/MM study [26] quoted above.

This trend continues for the case of the caesium cation: The largest possible contribution, that of a water molecule at optimal distance (3.20 \AA) and orientation, has dropped down to 58.08 kJ/mol , or just two hydrogen bonds. This can be compensated already by one-dimensional water networks, hence we can expect not only cage structures for the larger clusters but formation of ring structures already for the smallest clusters. *Flips* and *flaps*

within the 1st-shell (13 and 30 kJ/mol, respectively) are as cheap as in the 2nd-shell around Na⁺. In the 2nd-shell around Cs⁺ (at about 6 Å), optimal orientation of a water molecule yields at most 17 kJ/mol, and energy costs for *flaps* (12 kJ/mol) are not overly dramatic, while *flips* (3 kJ/mol) can be almost totally discounted. Therefore, the orienting power of caesium is small already at the optimal distance and diminishes further with increasing distance. Hence, formation of perfectly un-puckered cages (requiring a large amount of strongly *flipped* and *flapped* water molecules) can be expected to be least disfavoured in the case of caesium.

From this discussion, one can expect caesium cation microsolvation clusters to show markedly different structures compared to our findings for the sodium case [36], while potassium will take an intermediate position between these two. This is borne out and refined further by the actual structural findings in section 4.4.

4.2. Binding energy per water molecule as a function of cluster size

A possible tool often used to get a first impression on size-dependent trends is to plot the energy per water molecule vs. $n^{-1/3}$, i.e. the inverse cluster radius in the spherical droplet model, usually used to show trends in cluster properties [70, 71].

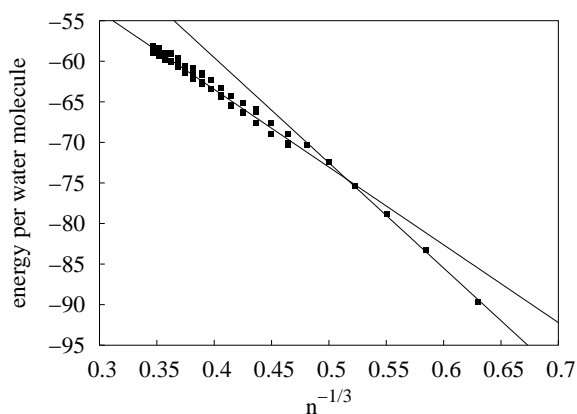


Figure 4.3.: Potential energy per water molecule (for Na⁺(H₂O)_n) vs. $n^{1/3} \equiv$ cluster size

In this section the plots of Na⁺(H₂O)_n, K⁺(H₂O)_n, and Cs⁺(H₂O)_n shall be briefly discussed.

When looking at the plot for Na⁺(H₂O)_n-clusters one can observe a change in the gradient around cluster sizes $9 \leq n \leq 11$ (see figure 4.3). As already mentioned a change in the gradient can indicate a transition region. Apart from this no point offset can be observed, suggesting the absence of magic numbers. In fact, there was a corresponding transition region found for these cluster sizes [36] where ion coordination patterns changed from trigonal bipyramidal

In case there are no exceptions in the build-up of the cluster structures with increasing n the result should be a smooth linear function. An indication of a structure transition could be a sudden change in gradient whereas single point offsets from the linear trend may point towards magic numbers. Thus inspection of these plots might indicate interesting size regions of the cluster structures. In the following part of this

to distorted octahedron-shaped. This is also in agreement with the mass spectral data (see section 3.1) as no magic numbers were found in the case of $\text{Na}^+(\text{H}_2\text{O})_n$ -clusters.

In the case of $\text{K}^+(\text{H}_2\text{O})_n$ -clusters deviations are not as obvious as for the case of $\text{Na}^+(\text{H}_2\text{O})_n$ -clusters. There might be a slight change in the gradient around cluster sizes with $9 \leq n \leq 11$ and also subtle point offsets from the linear trend are observable. Again this would be consistent with experiment (see section 3.1) which shows weak magic numbers. As it turns out, clusters with small $4 \leq n \leq 9$ tend to behave similarly to $\text{Na}^+(\text{H}_2\text{O})_n$ -clusters, whereas when the cluster become larger they show more of a $\text{Cs}^+(\text{H}_2\text{O})_n$ like behaviour (see following section).

The plot for $\text{Cs}^+(\text{H}_2\text{O})_n$ -clusters (see figure 4.5) differs from both the plots for $\text{Na}^+(\text{H}_2\text{O})_n$ and $\text{K}^+(\text{H}_2\text{O})_n$. No change in gradient is observable and the single points corresponding to $\text{Cs}^+(\text{H}_2\text{O})_{18}$ and $\text{Cs}^+(\text{H}_2\text{O})_{20}$ exhibit a strong offset from the linear trend, suggesting that these structures are magic number structures. This again is in good agreement with experiment as both $\text{Cs}^+(\text{H}_2\text{O})_{18}$ and $\text{Cs}^+(\text{H}_2\text{O})_{20}$ were found to be magic numbers experimentally. As $\text{Cs}^+(\text{H}_2\text{O})_{20}$ is a strong magic number and as there exists a special interest in the literature on the structure of this cluster (see section 3.1), this structure shall be focused on especially.

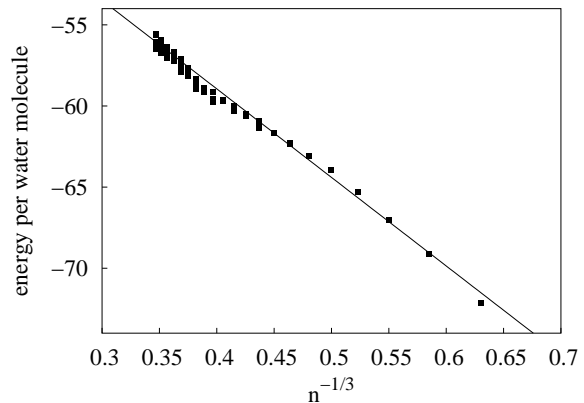


Figure 4.4.: Potential energy per water molecule (for $\text{K}^+(\text{H}_2\text{O})_n$) vs. $n^{1/3} \equiv$ cluster size

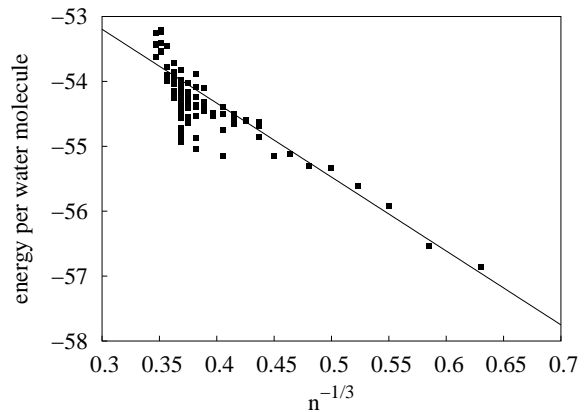


Figure 4.5.: Potential energy per water molecule (for $\text{Cs}^+(\text{H}_2\text{O})_n$) vs. $n^{1/3} \equiv$ cluster size

4.3. Remarks on the structure depicting program “*xmakemol*”

For displaying all cluster structures in this work the program *xmakemol* has been used (for an example cluster structure see figure 4.6). As *xmakemol* [72] has its own way to show interactions between particles some general remarks are in order, i.e. this program shows bonds for interactions between particles which should not always be mistaken for “real” bonds. In case of alkali cation microhydration clusters, these “bonds” concern water (oxygen) – cation and water (oxygen) – water (hydrogen), i.e. hydrogen bonds, interactions. The maximal length of these “bonds” can be manually adjusted by the user, however, the initial values the program uses are not at all unreasonable, hence these initial values were also adopted without further readjustment for depicting structures in this work.

The values for the water – cation “bond-lengths” are chosen such that one will see a “bond” for oxygen – sodium in case the distance between the two particles will be $\leq 2.5 \text{ \AA}$, whereas this “bond-length” is increased for oxygen – potassium to $\leq 3.0 \text{ \AA}$, according to the bigger size of the ion. This “bond-length” is increased even further for oxygen – caesium to $\leq 3.5 \text{ \AA}$. These “bonds-lengths” approximately correspond to the optimal distances between a water molecule and the central ion in the 1st-shell [9, 10] (see also section 4.1). Hence the number of “bonds” emanating from the central ion typically corresponds to its “actual” coordination number. For water – water interactions the case is somewhat similar. The optimal length of a hydrogen bond has been found to be approximately 2.0 \AA by ab-initio calculations [69]. *xmakemol* will show hydrogen bonds up to a length of $\leq 2.5 \text{ \AA}$ which is a reasonable length as the value of 2.0 \AA only describes the optimal distance which does not necessarily mean that this distance may not be elongated. Nevertheless, one always has to bear in mind that in any case no “bonds” are shown this does not mean that no interactions between these particles are present. The “bonds” shown by *xmakemol* merely function as guidance whether or not particles are within an approximate optimal distance with respect to their immediate neighbours.

In the course of this work the term “bond breaking” hence will refer to the bonds which are no longer depicted by *xmakemol* due to an increased distance between the two or more particles. Vice versa, if “bond formations” are mentioned this refers to a decreased distance between two or more particles.

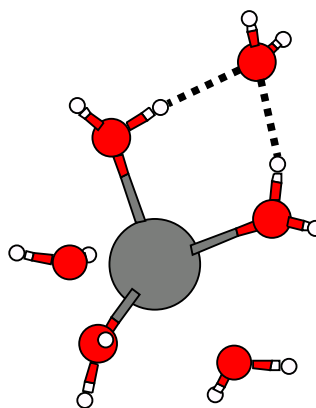


Figure 4.6.: Example structure for the structure depicting program *xmakemol*

4.4. Structural trends for $M^+(H_2O)_n$ with $M = Na, K, Cs$ and $4 \leq n \leq 22$

All cluster structures were computed employing a version of phenix where niching was applied. In comparison to reference [57] some structures were found to be better in energy and were replaced accordingly as global minimum. However, apart from $K^+(H_2O)_{20}$ only minor changes in structures and energy were observed. Hence there shall be no detailed description which cluster structures actually were improved using niching.

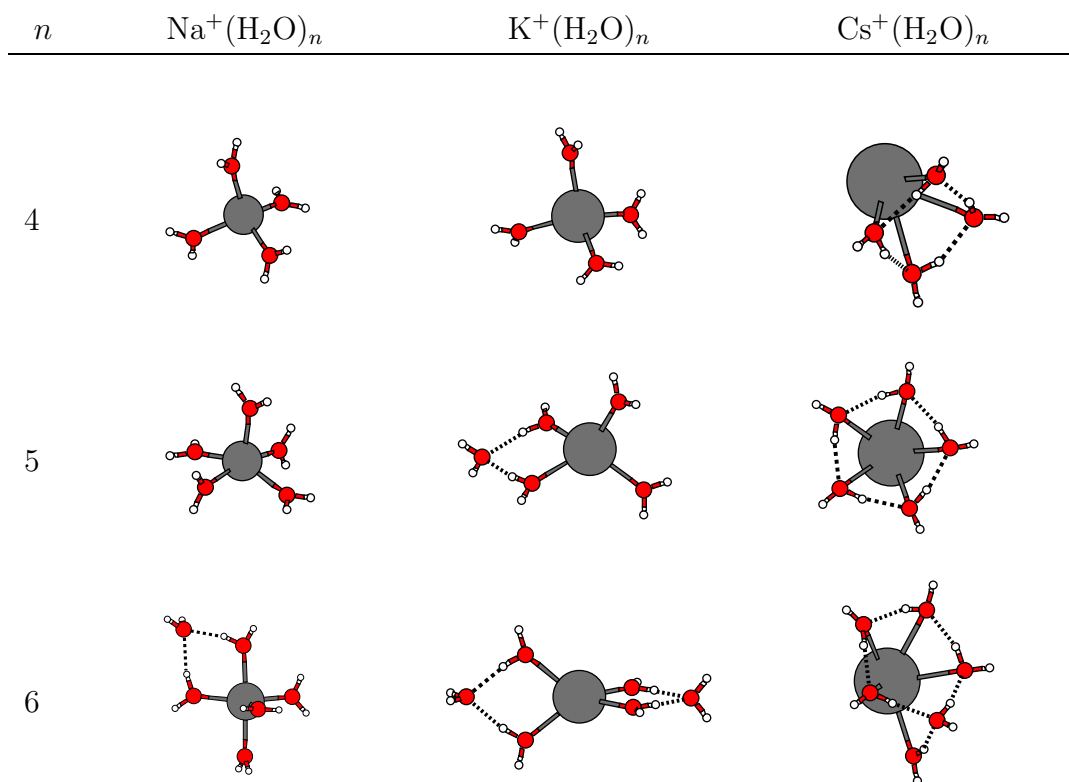


Figure 4.7.: Global minimum energy structures for $M^+(H_2O)_n$ with $M = Na, K, Cs$ and $n = 4, 5, 6$

Figure 4.7 shows global minimum structures of $M^+(H_2O)_n$ for $M = Na, K, Cs$ and $n = 4 - 6$. The general trends predicted in section 4.1 can be clearly observed: For $M = Na$, one can see the usual 1^{st} -shell coordination polyhedra, and the beginning of the buildup of a 2^{nd} -shell. There is no tendency whatsoever for 1^{st} -shell water molecules to aggregate and form hydrogen-bonded rings, since this would require strong *flips* or *flaps* and the energy costs for them are simply too high compared to the gain from the hydrogen bonds. For $M = Cs$, the situation is reversed: Hydrogen bond formation can overcompensate *flip/flap* costs, and therefore rings are formed from the start.

Finer structural details are also readily explained. As already discussed in reference [36], the $(5 + 1)$ isomer of $M = \text{Na}$ and $(n = 6)$ narrowly beats the $(6 + 0)$ isomer, due to 1^{st} -shell Na-water energy gains being reduced by crowding and to the 2^{nd} -shell Na-water energy gain still being relatively large. This balance can easily turn the other way upon slight changes:

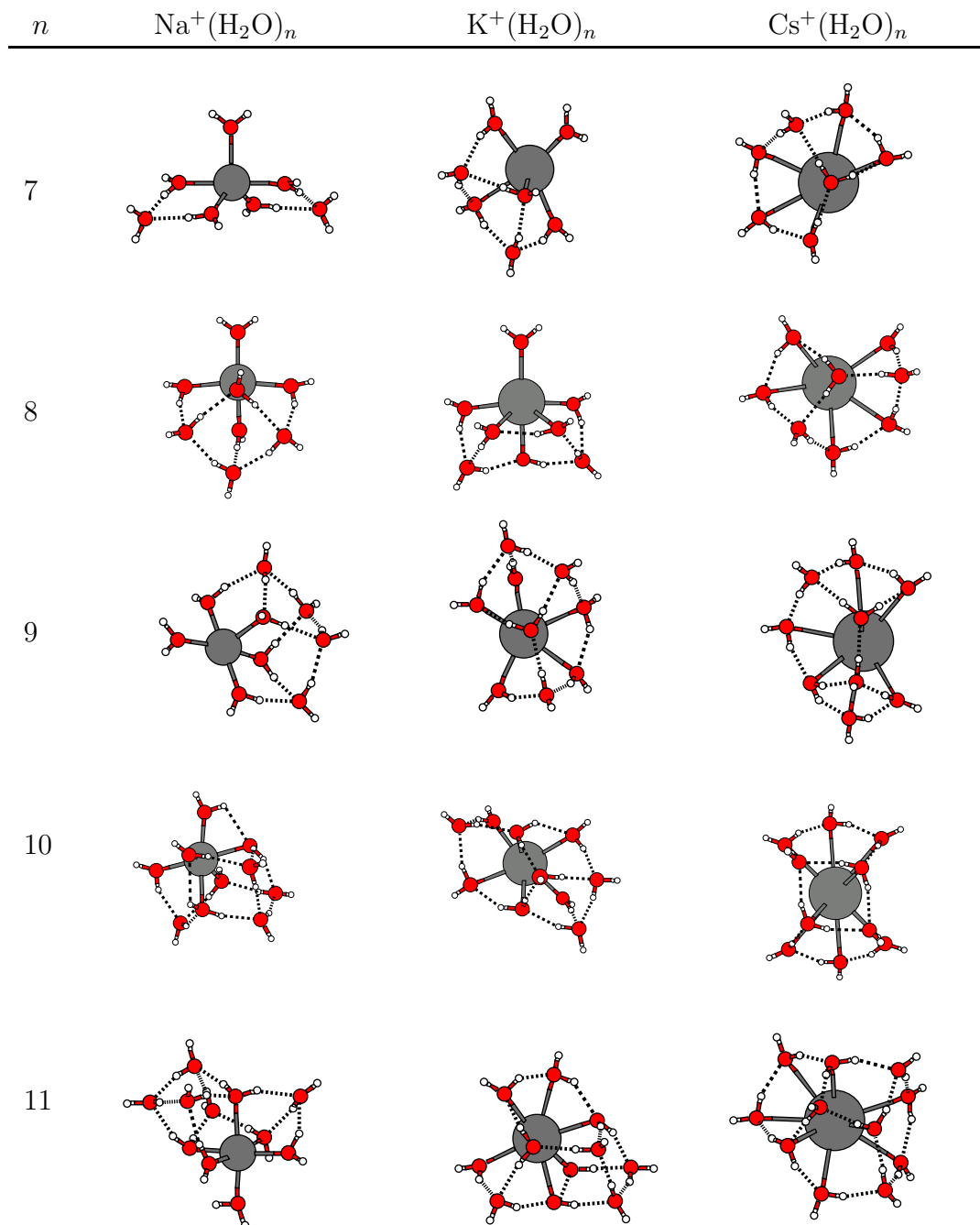


Figure 4.8.: Global minimum energy structures for $M^+(\text{H}_2\text{O})_n$ with $M = \text{Na}, \text{K}, \text{Cs}$ and $n = 7 - 11$

Although all the potassium structures shown in figure 4.7 are very similar in nature to the sodium structures, in the formation of 1^{st} -shell coordination polyhedra and 2^{nd} -shell bridges, the order of isomers is sometimes different. For $n = 5$, $(4 + 1)$ is better than $(5 + 0)$, and for $n = 6$ even $(4 + 2)$ is better than $(5 + 1)$. For these cluster sizes, ab-initio calculations are available [9, 10]; there, the order of these isomers depends upon inclusion of zero-point and finite temperature corrections.

With further increasing cluster sizes, the sodium clusters accumulate more 2^{nd} -shell bridges, and these can then further stabilise the structures by forming hydrogen bonds between themselves, starting beyond $n = 7$ (see figure 4.8). The caesium clusters, on the other hand, continue their ring growth pattern. As already observed for pure neutral water clusters [33, 35], four- and five-membered rings are preferred, offering the best compromise between strain reduction and maximising the number of hydrogen bonds per water molecule in the two-dimensional network. Three-membered rings are too strained, and six-membered rings are slightly less stable than two annealed four-membered rings (the “book” form of the neutral water hexamer). In fact, for caesium microhydration clusters, five-membered rings appear to be better than four-membered rings, since in all our global minimum cluster structures the number of five-membered rings is maximised. Extrapolation of this trend to larger clusters obviously leads directly to the dodecahedron at $n = 20$, consisting only of five-membered rings.

The corresponding potassium cases start to take an intermediate position between sodium and caesium, exhibiting features of both: For example, for $n = 9$ (see figure 4.8), the potassium cluster has an annealed four- and five-membered ring unit, similar to the caesium cluster, while such a feature is absent in the corresponding sodium cluster. For $n = 11$ (see figure 4.8), a caesium-like five-membered ring is actually combined with cuboid packings of 2^{nd} -shell bridges, characteristic for sodium.

All these trends continue towards larger clusters: The 2^{nd} -shell bridges start to enclose the 1^{st} -shell core in the sodium clusters and a distorted octahedron-shaped environment is favoured by the 1^{st} -shell water molecules over the trigonal bipyramidal environment found so far. As already mentioned, a signature of this was already visible in the plot of the energy per water molecule as a function of cluster size (see section 4.2). Potassium cluster structures seem to have an increased tendency towards structures similar to the corresponding caesium structures, i.e. the water molecules build a 1^{st} -shell around the ion consisting of annealed four-, five-, and six-membered rings (see figure 4.9). This is consistent with the observed slight change in gradient for plotting the energy as a function of cluster size (see section 4.2). Caesium clusters continue their trend to form annealed four-, five-, and six-membered rings and no change in build-up principles can be observed.

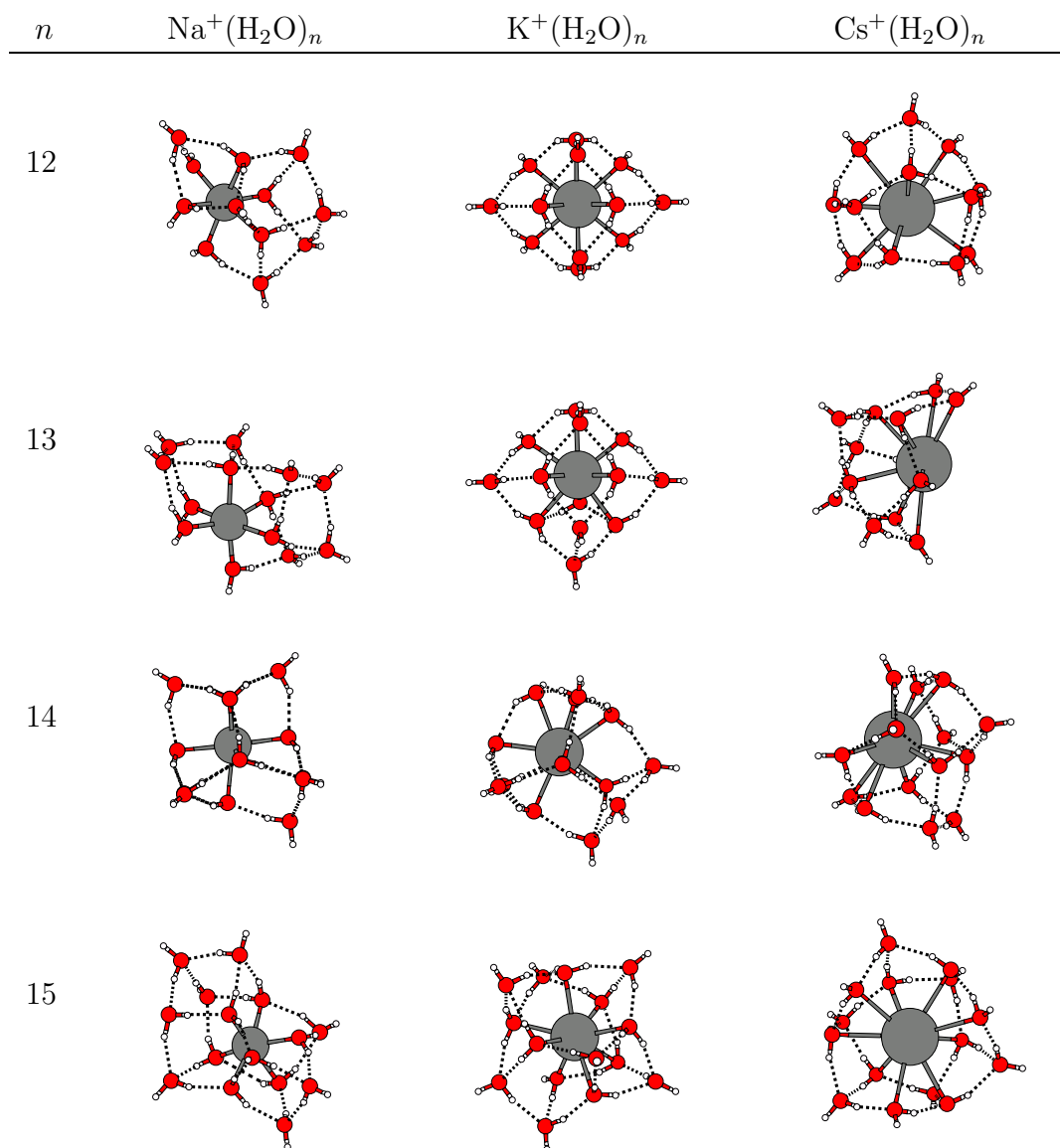


Figure 4.9.: Global minimum energy structures for $\text{M}^+(\text{H}_2\text{O})_n$ with $\text{M} = \text{Na}, \text{K}, \text{Cs}$ and $n = 12 - 15$

At still larger cluster sizes, new developments set in:

At $n = 16$, the water molecules manage to “close a shell” around the K^+ ion, in the sense that the water network encloses the cation from all sides and consists only of four-, five-, and six-membered rings (Figure 4.10). In smaller clusters, larger rings are present that can also be interpreted as holes in the shell since they bring the cation close to the surface of the cluster. The energy per water molecule as a function of $n^{-1/3}$ exhibits a maximum deviation from the overall trend at this cluster size $n = 16$ (Figure 4.11). At the same time, this cluster size corresponds to a (weak) magic number observed in several experiments (see section 3.1 and reference [7]). It is tempting to propose this shell closure as an explanation for this

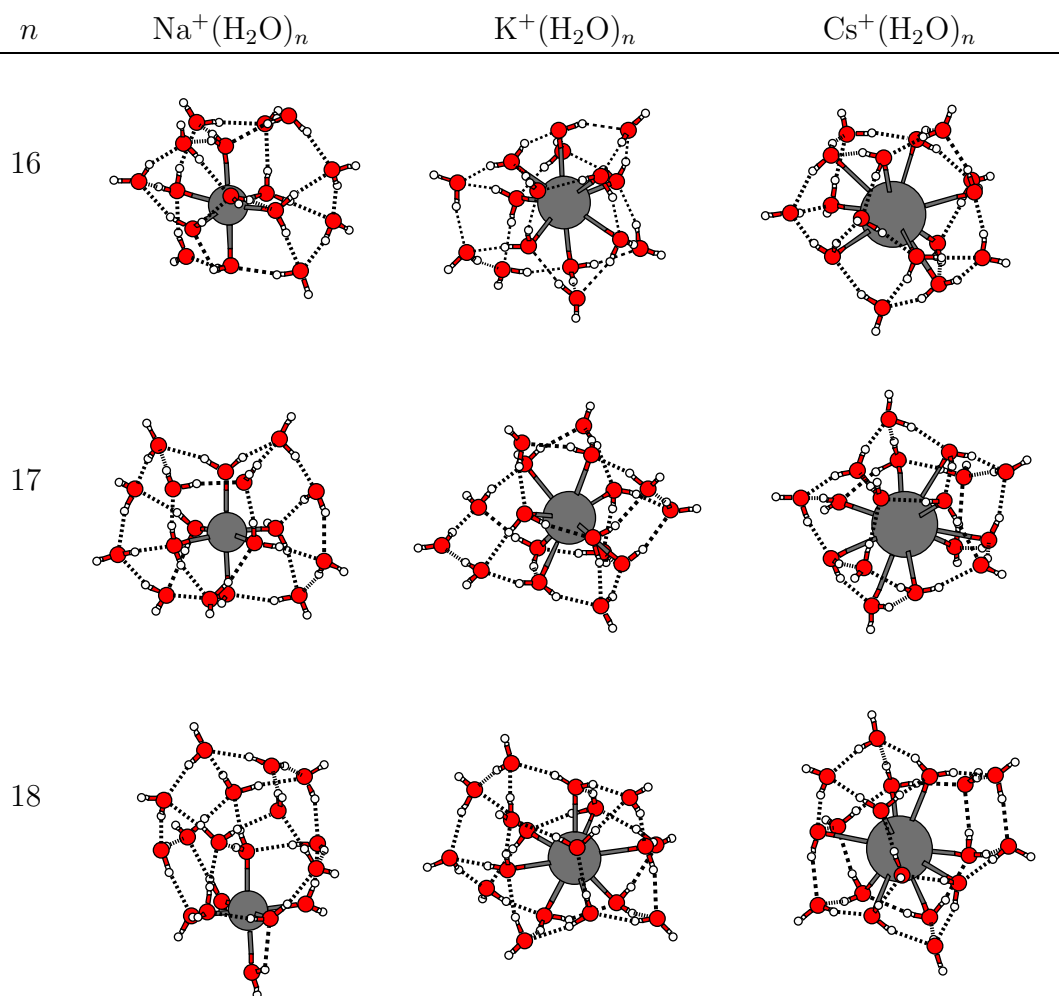


Figure 4.10.: Global minimum energy structures for $M^+(H_2O)_n$ with $M = Na, K, Cs$ and $n = 16, 17, 18$

observation. However, the global minimum energy structure of $K^+(H_2O)_{16}$ is far from “ideal” in that it is strongly puckered, with K^+ -water distances ranging from 2.7 Å to 4.2 Å, thus offering several obvious places for outside attacks, leading to further cluster growth or to partial dissociation. Nevertheless, the shell closure at this size may serve as a first working hypothesis for the magic number $n = 16$.

An analogous shell closure also happens for $Cs^+(H_2O)_n$, but only at $n = 18$, due to the larger size of the cation. Again, this corresponds conspicuously to the smallest clear magic number observed in various experiments (e.g. reference [7, 73]). Note that the structure we find (Figure 4.10) has not much in common with the structure tentatively proposed in reference [73]: They show a nicely smooth clathrate hull consisting of 2 squares, 8 pentagons and 1 hexagon, whereas we find a rather strongly puckered hull formed by 4 squares, 4 pentagons and 3 hexagons. Also, while the energy per molecule again deviates from the overall trend (Figure 4.12), the deviation is smaller than for $n = 19$ and $n = 20$. Therefore, again, shell

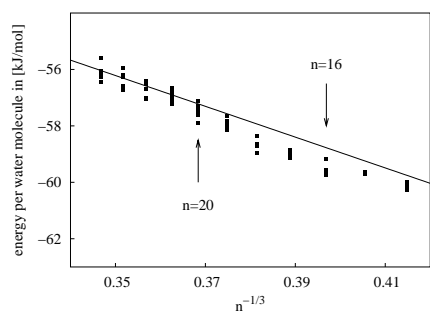


Figure 4.11.: Binding energy E [kJ/mol] per water molecule as a function of $n^{-1/3}$, for $\text{K}^+(\text{H}_2\text{O})_n$, in the range $n = 14 - 24$

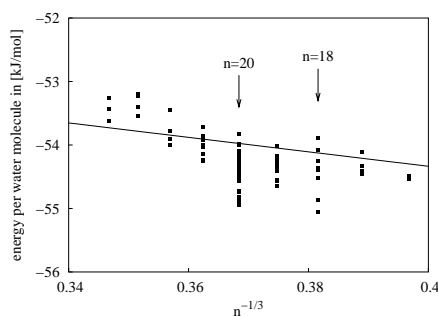


Figure 4.12.: Binding energy E [kJ/mol] per water molecule as a function of $n^{-1/3}$, for $\text{Cs}^+(\text{H}_2\text{O})_n$, in the range $n = 16 - 24$

closure may be the reason for the observed magic number at $n = 18$, but further investigations need to be done to confirm or refute this hypothesis.

As already explained in great detail in reference [36], for the case of Na^+ there is no shell closure, since the farther-reaching ordering influence of the sodium cation prevents clathrate-style ring formation of water molecules and lets two different structural principles compete instead (clusters with the cation centred and off-centre, respectively). Hence, one does not see a shell closure in either of them (neither in the size range $n = 16 - 18$ of Figure 4.10 nor below or above) but instead a structural transition from one principle to the other, between $n = 17$ and $n = 18$ (see figure 4.10). This explains the apparent absence of clear magic numbers in sodium cation microhydration experiments. Nevertheless, experiments with a sensitivity window suitably tuned to this size range [36] do observe at least a marked step in the data exactly at this position.

Figure 4.13 shows structural trends for $\text{M}^+(\text{H}_2\text{O})_n$ clusters in the size range $n = 20 - 24$. The famous case $n = 20$ will be discussed in detail in the following subsection 4.5. For $\text{M} = \text{Na}$ there are no dodecahedral structures, and the competition between centred structures and off-centre ones (with the second solvation shell shifted from the cation onto one of the water molecules of the first solvation shell) continues. For $\text{M} = \text{Cs}$, clathrate-like cage structures dominate. Additional water molecules beyond the actual formation of a dodecahedron at $n = 20$ are not really attached to its outside but rather are incorporated into an extending cage hull, leading again to a stronger puckering (while the shortest Cs-water distances stay approximately constant at 3.2 \AA , the longest distances vary as $4.55, 4.28, 4.33, 4.79, 4.89 \text{ \AA}$ for the series $n = 18, 19, 20, 21, 22$). For $\text{M} = \text{K}$, the structures exhibit again a mixture of Na- and Cs-characteristics: Clathrate-like cage formation with pronounced water rings is

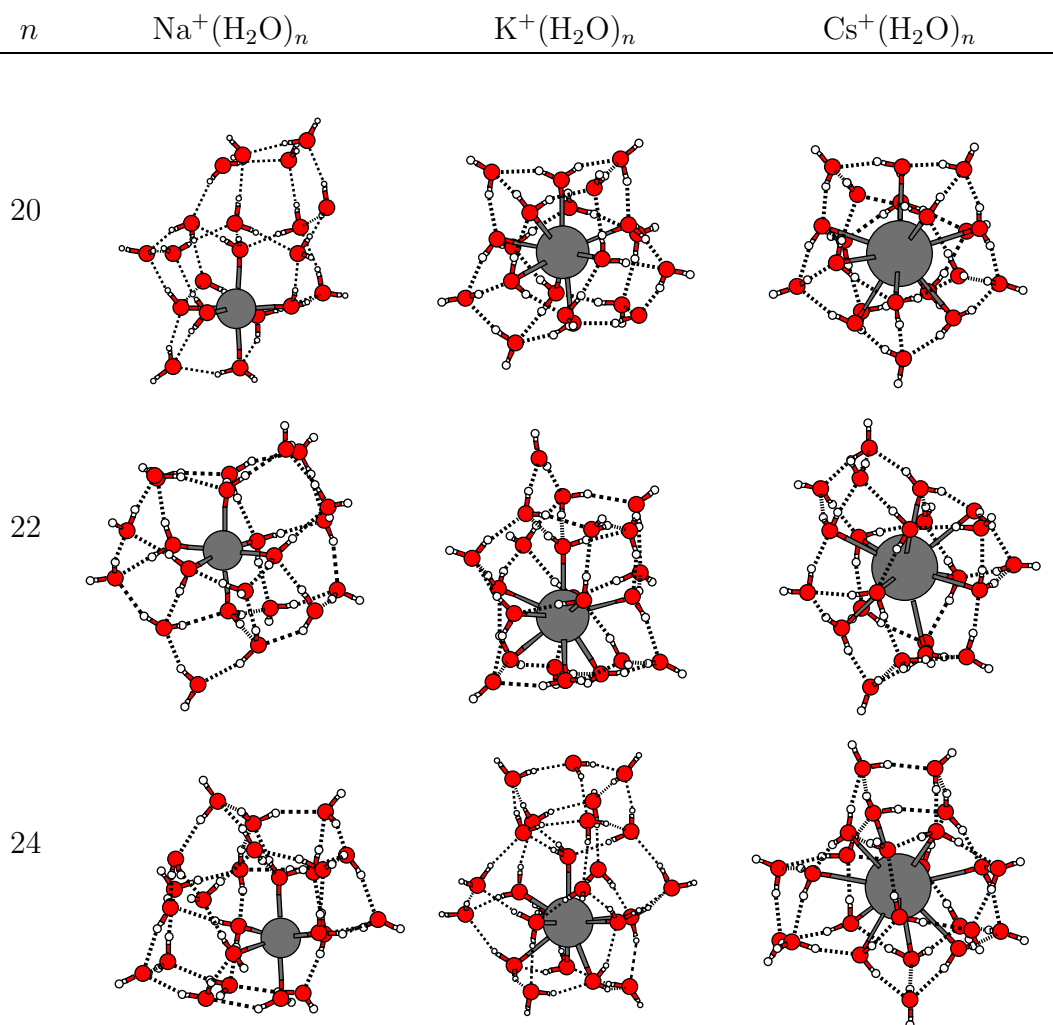


Figure 4.13.: Global minimum energy structures for $\text{M}^+(\text{H}_2\text{O})_n$ with $\text{M} = \text{Na}, \text{K}, \text{Cs}$ and $n = 20, 22, 24$

clearly present, in stark contrast to the Na case. However, the degree of puckering is much stronger than in the corresponding Cs clusters. Also, starting with $n = 21$, a water molecule is included into an elongated water hull, together with the cation, bearing a clear resemblance to the off-centre sodium cluster structures. However, at cluster sizes beyond $n = 20$, the limited computer time allocated for this study does not allow us the claim to have found the global minimum structures in all cases. Hence, there will not be a more extended discussion of these clusters or still larger ones here.

4.5. Dodecahedral cage structures

Since water clusters in the size range of $n = 20$ already pose a severe challenge to global geometry optimisation [35, 60], the global optimisation search was complemented by constructing

perfect dodecahedral structures (with various radii) for $M^+(H_2O)_n$ with $M = Na, K, Cs$ and $n = 20$, followed by a local optimisation of all degrees of freedom and a twice-repeated sequence of global optimisation of the orientational degrees of freedom only.

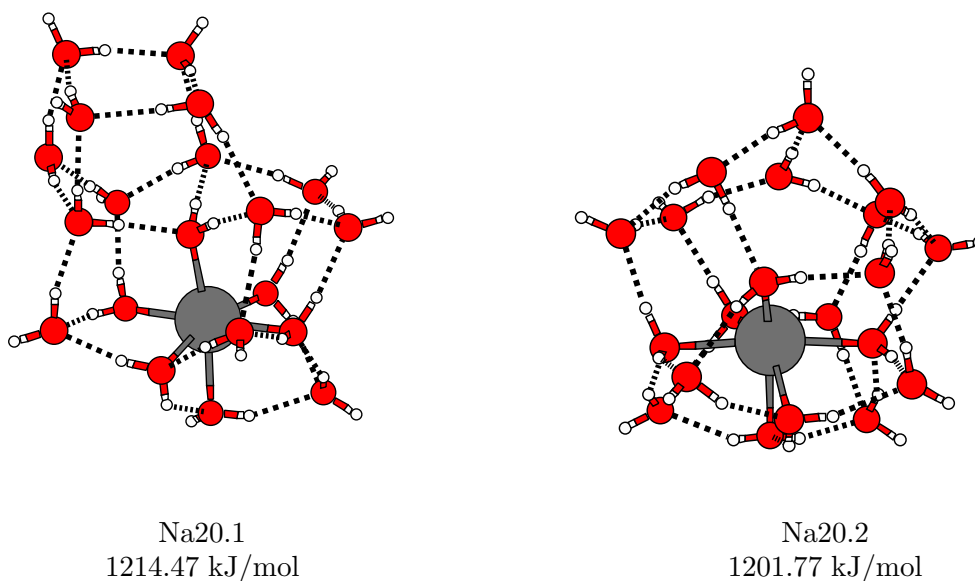


Figure 4.14.: $Na^+(H_2O)_{20}$: non-dodecahedral global minimum energy structure Na20.1, best dodecahedral structure Na20.2 (right)

For the case of $M = Na$, this scheme produced the desired dodecahedral cage structures. However, the best one of these, Na20.2 (Figure 4.14), turned out to have 13 kJ/mol less binding energy than the best structure found by our global optimisation routine, Na20.1, which belongs to the off-centre structural scheme mentioned above and clearly bears no relation to a dodecahedral cage form. Already the outer forms are totally different: Na20.1 is strongly elongated (the smallest moment of inertia is only 57% of the largest one), while Na20.2 is still very close to the perfect sphere of the dodecahedron (the smallest moment of inertia is 93% of the largest one). The most striking difference, however, is in the inner structure: In Na20.1, pair potential terms between the cation and all water molecules (the “cation embedding”) contribute 624.44 kJ/mol to the total binding energy of the cluster of 1214.47 kJ/mol. This is largely due to the optimally arranged first solvation shell, which is of prime importance for Na^+ , as explained in section 4.1. A true dodecahedral cage, however, is simply too large to be filled by the sodium cation. Its collapse would lead back to Na20.1 or a similar local minimum. Such a collapse was indeed found when performing a molecular dynamics simulation using a canonical distribution (see section 11.2.2). In the local minimum Na20.2 with retained dodecahedral cage, the sodium cation moves off-centre and attaches itself to the outer wall. Naturally, this leads to a worse cation embedding contribution of only 581.14 kJ/mol. This big difference in cation embedding is partially compensated by the better water-water interaction network in the dodecahedral hull of Na20.2, but a considerable final

difference of 13 kJ/mol remains. Therefore, a large number of non-dodecahedral local minima fall in-between these two structures, and hence it is unlikely that dodecahedral cage structures are of any importance for $\text{Na}^+(\text{H}_2\text{O})_{20}$. Together with the structural trends analysed above and in our earlier work [36], this provides a good candidate explanation why $n = 20$ is not magic for Na^+ : There is simply nothing special about the structure of $\text{Na}^+(\text{H}_2\text{O})_{20}$.

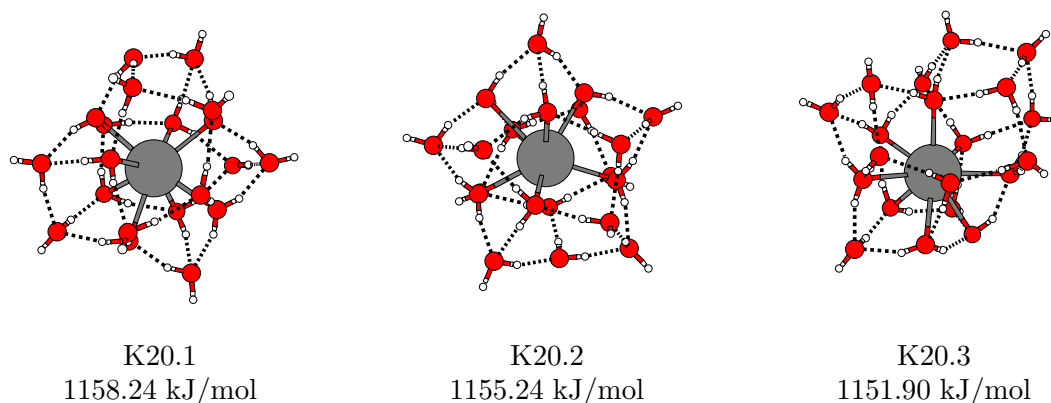


Figure 4.15.: $\text{K}^+(\text{H}_2\text{O})_{20}$: distorted dodecahedral global minimum energy structure K20.1 (left), distorted dodecahedral local minimum structure found by the direct dodecahedron construction scheme K20.2 (middle), non-dodecahedral local minimum structure K20.2 (right) and their binding energies in kJ/mol

As stated in reference [57], for the case $M = \text{K}$ a dodecahedron-shaped cluster structure K20.2 (see figure 4.15) was only found by a specially employed direct dodecahedron construction scheme, whereas global optimisation yielded a non-dodecahedron-shaped cluster structure K20.3, similar to Na20.1, using a version where no niching was applied. However employing a niching based global optimisation, the dodecahedron structure K20.1 for $M = \text{K}$ was found which is 3 kJ/mol better in energy than the cluster structure found by the direct dodecahedron construction scheme. Hence the niching seems to be very important in the case of $\text{K}^+(\text{H}_2\text{O})_{20}$ as otherwise the non-dodecahedron-shaped clusters dominate the populations. K20.3 is so strongly puckered that it resembles Na^+ cluster structures more than the Cs^+ ones. It contains 2 squares, 8 pentagons and 2 hexagons, and is quite non-spherical (although not as strongly as Na20.1: the smallest moment of inertia is 77% of the largest one). Again, there are similar differences in partial energy contributions as in the corresponding sodium cases: Cation embedding amounts to 520.25 kJ/mol for K20.1, 518.08 kJ/mol for K20.2, and 540.16 kJ/mol for K20.3. The difference between the embedding of the cation in the non-dodecahedron water network and that in the dodecahedron water network is smaller than that for sodium above. Hence it can just be over-compensated by the again better water network in the dodecahedron cage. Note, however, that both the dodecahedron-like cage structures K20.1 and K20.2 are quite far from the ideal dodecahedron which is sometimes depicted in

the literature: The puckering of the cage hull is so strong that cation-water distances vary between 2.73 and 4.43 Å (instead of being all alike). Bond angles in the five-membered rings vary between 70.3 and 128.9 degrees (instead of the abstract-geometrical ideal of 108 degrees which is almost realized in the free pure water pentamer five-membered ring cluster with the TIP4P potential). As a crude measure of off-planarity, dihedral angles within the five-membered rings reach 53.9 degrees (instead of the ideal zero degrees, or of the 1.6 to 29.5 degrees actually realized in the free TIP4P water pentamer).

All this somewhat diminishes the intuitive appeal of the dodecahedron as a natural explanation of the magic number $n = 20$. The failure of the corresponding binding energy to strongly deviate from the trend of its neighbours (see figure 4.11) is also not very convincing; but one does not want to overemphasise this finding since TIP4P/OPLS is likely not the best of all possible models for such an energy comparison. A water hull consisting only of five-membered rings may also have a kinetic advantage: It is speculated that sequential ring enlargement may be a preferred mode of water cluster growth, at least in the experimental environment of helium droplets [45]. On this route, the dodecahedron may form a natural culmination point. Again, cluster dynamics studies are necessary to further illuminate this possibility (see part III).

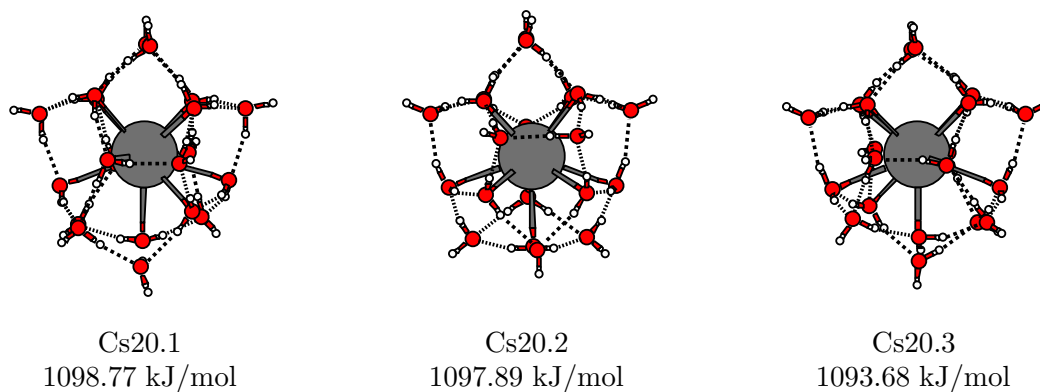


Figure 4.16.: $\text{Cs}^+(\text{H}_2\text{O})_{20}$: distorted dodecahedral global minimum energy structure Cs20.1 (left), non-dodecahedral local minimum structure Cs20.2 (middle) and dodecahedral local minimum structure Cs20.3 (right) and their binding energies in kJ/mol, for $\text{Cs}^+(\text{H}_2\text{O})_{20}$

Figure 4.16 depicts the global minimum Cs20.1 for $\text{Cs}^+(\text{H}_2\text{O})_{20}$ and two local minima Cs20.2 and Cs20.3. The first two structures were found by our global optimisation search, while the latter is the best one resulting from direct dodecahedron construction. In the perspective chosen here, all three structures appear to be very similar. This is also true of their gross overall form: The smallest moment of inertia is 87%, 83%, and 93% of the largest one, respectively; therefore all three are fairly close to spherical. However, only Cs20.1 and Cs20.3 are exclusively built from five-membered rings, whereas Cs20.2 contains 2 squares, 8 pentagons and 2 hexagons. Cation embedding differs again somewhat (399.65 kJ/mol,

403.29 kJ/mol and 395.78 kJ/mol, respectively) but not as much as in the potassium or sodium clusters presented above. Again, the water network contributions appear to be better for the dodecahedral-like cages of Cs20.1 and Cs20.3; this just barely over-compensates the better embedding in Cs20.2 to a final difference of not even 1 kJ/mol. The embedding difference between Cs20.1 and Cs20.3 seems to carry through to the difference in total energies, which may therefore be due to the small difference in deviations from a spherical form. Binding energies per molecule show a strong maximum in the deviation from the trend at $n = 20$ (Figure 4.12). Comparing Cs20.1 to the best structures for $n = 19$ and $n = 21$, shown in the same perspective in Figure 4.18, suggests that the Cs19.1 structure is simply the Cs20.1 structure with one water molecule missing, and that the Cs21.1 structure is simply the Cs20.1 structure with one additional water bridge attached to the outside (at the bottom left, in the given perspective). It is suggestive (but not strictly logically conclusive) that both changes do not improve the water network and hence the stability of the clusters.

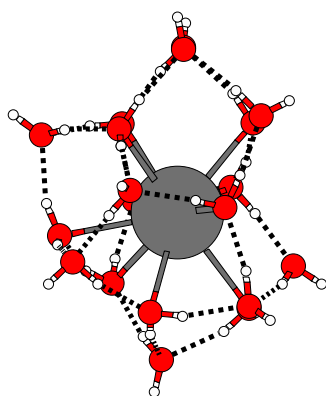


Figure 4.17.: Global minimum energy structure for $\text{Cs}^+(\text{H}_2\text{O})_{19}$

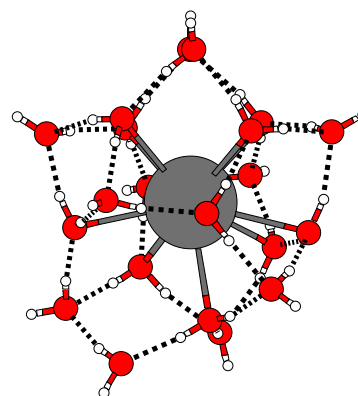


Figure 4.18.: Global minimum energy structure for $\text{Cs}^+(\text{H}_2\text{O})_{21}$

With these arguments it cannot be excluded that $\text{Cs}^+(\text{H}_2\text{O})_{20}$ may actually be magic because of a dodecahedral cage structure. But, again, the dodecahedral cage is a much less perfect rendering of the ideal platonic body than one may be tempted to believe: Cation-water distances range from 3.21 Å to 4.33 Å, and in the five-membered rings, bond angles vary between 78 and 138 degrees and dihedral angles reach values of 44 degrees (although deviations are admittedly smaller than in the K20.1 case; additionally, as noted at the end of section 4.4, $n = 20$ seems to be close to a “puckering minimum” for $M = \text{Cs}$). Perhaps more importantly, the structure Cs20.2 ends up with under 1 kJ/mol binding energy less than Cs20.1; at the crude modelling level used here, these two are effectively isoenergetic. But Cs20.2 is not a pure five-membered ring structure, it contains four- and six-membered rings. Nevertheless, it contains the same number (ten) of dangling OH bonds as Cs20.1 and as derived from experiments with tri-methylamine binding for $M = \text{H}_3\text{O}^+$ [25]. Therefore, although clathrate-like cage formation dominates the structures of $\text{Cs}^+(\text{H}_2\text{O})_n$ for all values of

n considered here, and although the global minimum for $n = 20$ has a (distorted) dodecahedral cage, the simple geometric elegance of the dodecahedron need not be the only explanation possible for the magic number $n = 20$; other cages may be just as good.

4.5.1. Are magic numbers due to a special structural pattern?

A structural pattern all magic number structures seem to have in common is that except for one global minimum structure none of the found global minimum cluster structures contain any water molecules which form three or four hydrogen bonds, i.e. only water molecules which either donate two hydrogen bridge bonds and accept one (DDA), or vice versa (DAA) are present. Generally the abbreviation D shall denote donor, i.e. one D for each donating OH bond per water molecule, and the abbreviation A is used for acceptor, i.e. one A for each accepted OH bond per water molecule, while single water molecules form no hydrogen bonds to any of the water molecules of the rest of the water network but are bound only to the central ion.

	single	A	D	DA	AA	DD	DDA	DAA	DDAA
$\text{Na}^+(\text{H}_2\text{O})_4$	4	–	–	–	–	–	–	–	–
$\text{Na}^+(\text{H}_2\text{O})_5$	5	–	–	–	–	–	–	–	–
$\text{Na}^+(\text{H}_2\text{O})_6$	–	–	4	–	2	–	–	–	–
$\text{Na}^+(\text{H}_2\text{O})_7$	1	–	4	–	1	–	–	–	–
$\text{Na}^+(\text{H}_2\text{O})_8$	1	–	3	1	–	–	–	3	–
$\text{Na}^+(\text{H}_2\text{O})_9$	1	–	2	1	–	–	1	4	–
$\text{Na}^+(\text{H}_2\text{O})_{10}$	–	–	2	2	–	–	2	4	–
$\text{Na}^+(\text{H}_2\text{O})_{11}$	1	–	2	1	–	1	1	5	–
$\text{Na}^+(\text{H}_2\text{O})_{12}$	–	–	2	1	–	1	2	6	–
$\text{Na}^+(\text{H}_2\text{O})_{13}$	–	–	–	1	–	2	3	7	–
$\text{Na}^+(\text{H}_2\text{O})_{14}$	–	–	–	–	–	–	7	7	–
$\text{Na}^+(\text{H}_2\text{O})_{15}$	–	–	–	1	–	2	4	8	–
$\text{Na}^+(\text{H}_2\text{O})_{16}$	–	–	–	1	–	1	6	8	–
$\text{Na}^+(\text{H}_2\text{O})_{17}$	–	–	–	1	–	2	5	9	–
$\text{Na}^+(\text{H}_2\text{O})_{18}$	–	–	–	1	–	2	4	8	3
$\text{Na}^+(\text{H}_2\text{O})_{19}$	–	–	–	2	–	2	4	8	3
$\text{Na}^+(\text{H}_2\text{O})_{20}$	–	–	–	1	–	2	5	9	3
$\text{Na}^+(\text{H}_2\text{O})_{21}$	–	–	2	–	–	1	4	9	4

Table 4.2.: Number and types of different molecules present in the global minimum structures of $\text{Na}^+(\text{H}_2\text{O})_n$

The three tables 4.2, 4.3, and 4.4 are a summary of the numbers and types of water molecules being present in global minimum structures for different cluster sizes for all three systems. Some explanations why special coordination numbers are preferred by which system has already been given in section 4.4. This chapter adds a few observations from yet another angle.

	single	A	D	DA	AA	DD	DDA	DAA	DDAA
$K^+(H_2O)_4$	4	–	–	–	–	–	–	–	–
$K^+(H_2O)_5$	2	–	–	2	1	–	–	–	–
$K^+(H_2O)_6$	–	–	–	4	2	–	–	–	–
$K^+(H_2O)_7$	1	–	2	2	–	–	–	2	–
$K^+(H_2O)_8$	1	–	2	3	–	–	–	2	–
$K^+(H_2O)_9$	–	–	2	3	–	–	1	3	–
$K^+(H_2O)_{10}$	–	–	2	2	–	–	2	4	–
$K^+(H_2O)_{11}$	–	–	1	3	–	–	3	4	–
$K^+(H_2O)_{12}$	–	–	–	4	–	–	4	4	–
$K^+(H_2O)_{13}$	–	–	–	3	–	–	5	5	–
$K^+(H_2O)_{14}$	–	–	–	–	–	–	7	7	–
$K^+(H_2O)_{15}$	–	–	–	1	–	–	7	7	–
$K^+(H_2O)_{16}$	–	–	–	–	–	–	8	8	–
$K^+(H_2O)_{17}$	–	–	–	1	–	–	8	8	–
$K^+(H_2O)_{18}$	–	–	–	–	–	–	9	9	–
$K^+(H_2O)_{19}$	–	–	–	1	–	–	9	9	–
$K^+(H_2O)_{20}$	–	–	–	–	–	–	10	10	–
$K^+(H_2O)_{21}$	–	–	–	–	–	–	9	11	1

Table 4.3.: Number and types of different molecules present in the global minimum structures of $K^+(H_2O)_n$

In table 4.2 the number and types of different molecules present in the global minimum structures of $Na^+(H_2O)_n$ are given. The structure found for $Na^+(H_2O)_{14}$ is the only structure found for $Na^+(H_2O)_n$ -clusters which fulfils the above mentioned criterion of three-coordinated molecules, however, this cluster size is not known to be a magic number. But then the mere presence of exclusively three-coordinated water molecules does not yet explain the presence of magic numbers. Nevertheless, one might argue that two-coordinated water molecules (and of course also one-coordinated or single water molecules) are less well bound to the water network and may hence be centres of dissociation or association. According to this assumption, four-coordinated water molecules would be even better than three-coordinated

ones. However, it is rather hard to build a cluster with four-coordinated water molecules if the total number of water molecules is small and if due to a four-coordinated water molecule other water molecules will have to be located in an unfavourable bonding situation or for that matter badly accommodate the central ion.

Looking at the corresponding table for $\text{K}^+(\text{H}_2\text{O})_n$ (see table 4.3) the picture becomes different. In contrast to smaller cluster sizes (which exhibit a similar bonding pattern as $\text{Na}^+(\text{H}_2\text{O})_n$, see section 4.4) medium and larger cluster sizes seem to prefer an equal number of DDA and DAA molecules for an even total number of water molecules, whereas odd total numbers of water molecules have an additional DA molecule starting from $n = 14$. Other experimental magic numbers for $\text{K}^+(\text{H}_2\text{O})_n$ are 16, 20, and 25.

	single	A	D	DA	AA	DD	DDA	DAA	DDAA
$\text{Cs}^+(\text{H}_2\text{O})_4$	–	–	–	4	–	–	–	–	–
$\text{Cs}^+(\text{H}_2\text{O})_5$	–	1	1	3	–	–	–	–	–
$\text{Cs}^+(\text{H}_2\text{O})_6$	2	–	–	4	–	–	–	–	–
$\text{Cs}^+(\text{H}_2\text{O})_7$	–	–	–	5	–	–	1	1	–
$\text{Cs}^+(\text{H}_2\text{O})_8$	–	–	1	5	–	–	1	1	–
$\text{Cs}^+(\text{H}_2\text{O})_9$	–	–	–	5	–	–	2	2	–
$\text{Cs}^+(\text{H}_2\text{O})_{10}$	–	–	–	6	–	–	2	2	–
$\text{Cs}^+(\text{H}_2\text{O})_{11}$	–	–	–	5	–	–	3	3	–
$\text{Cs}^+(\text{H}_2\text{O})_{12}$	–	–	–	4	–	–	4	4	–
$\text{Cs}^+(\text{H}_2\text{O})_{13}$	–	–	–	5	–	–	4	4	–
$\text{Cs}^+(\text{H}_2\text{O})_{14}$	–	–	–	4	–	–	5	5	–
$\text{Cs}^+(\text{H}_2\text{O})_{15}$	–	–	–	3	–	–	6	6	–
$\text{Cs}^+(\text{H}_2\text{O})_{16}$	–	–	–	2	–	–	7	7	–
$\text{Cs}^+(\text{H}_2\text{O})_{17}$	–	–	–	3	–	–	7	7	–
$\text{Cs}^+(\text{H}_2\text{O})_{18}$	–	–	–	–	–	–	9	9	–
$\text{Cs}^+(\text{H}_2\text{O})_{19}$	–	–	–	1	–	–	9	9	–
$\text{Cs}^+(\text{H}_2\text{O})_{20}$	–	–	–	–	–	–	10	10	–
$\text{Cs}^+(\text{H}_2\text{O})_{21}$	–	–	–	1	–	–	10	10	–
$\text{Cs}^+(\text{H}_2\text{O})_{22}$	–	–	–	–	–	–	11	11	–
$\text{Cs}^+(\text{H}_2\text{O})_{23}$	–	–	–	1	–	–	11	11	–
$\text{Cs}^+(\text{H}_2\text{O})_{24}$	–	–	–	–	–	–	11	11	2

Table 4.4.: Number and types of different molecules present in the global minimum structures of $\text{Cs}^+(\text{H}_2\text{O})_n$

For $\text{Cs}^+(\text{H}_2\text{O})_n$ -clusters the case is yet again a little different. While $\text{K}^+(\text{H}_2\text{O})_n$ -clusters start to show an equal number of DDA's and DAA's starting from medium sized clusters, $\text{Cs}^+(\text{H}_2\text{O})_n$ -clusters do this right from the beginning, where the first DDA and DAA molecules are present (see table 4.4). For smaller cluster sizes, DA molecules can be found in every structure, nevertheless, they start to disappear again for even numbers, starting from $n = 18$, which is also the first magic number for $\text{Cs}^+(\text{H}_2\text{O})_n$. In the experiment also 20, 22, 24 were found to be magic. In the case of $\text{Cs}^+(\text{H}_2\text{O})_n$ the categorisation of magic numbers being due to only DDA or DAA molecules being present in the structure at first sight seems to hold and also give a reason for magic numbers starting at 18.

For all three cations also the most important local minima were checked upon in view of this criterion, and it was found that the categorisation still holds. However no further information will be given in this work in order not to clutter it with too much data.

The exclusive presence of three-coordinated molecules may indeed be a good criterion for magic numbers in the size range under study. Exclusive three-coordination also is clearly linked to (bent) two-dimensional rather than one-dimensional or three-dimensional water networks, and hence to water cages around a central ion. However, three-coordinated water molecules can form many sorts of cages, not just those consisting of only five-membered rings, but also others containing also four- and six-membered rings. Therefore this criterion extends the dodecahedral clathrate hypothesis in a simple but effective way.

5. Conclusions obtained from global geometry optimisation

An extensive global geometry optimisation study has been performed for the alkali cation microsolvation clusters $M^+(H_2O)_n$, with $M = Na, K, Cs$, and reasons have been provided for the structural trends observed. The results suggest simple explanations for the absence of clearly discernible magic numbers for the sodium case, in particular for the missing magic number $n = 20$: Clathrate-like cage structures play no important role, and competition of two structural principles prevents obvious shell closures.

For $M = K$, the magic number $n = 16$ may be due to a shell closure. For $n = 20$, the global minimum appears to have a dodecahedral cage, but it is strongly distorted, and clearly non-dodecahedral minima are very close in energy.

$M = Cs$ exhibits a much clearer preference for water ring formation than the other two cases, leading naturally towards clathrate-like cage structures. In this case, the magic number $n = 18$ may be again a shell closure, analogous to $n = 16$ for potassium. Nevertheless, even here the dodecahedron does not dominate clearly for $n = 20$; other cages containing four- and six-membered rings are isoenergetic.

It was also found that magic numbers could exist due to an extremely simple categorisation as all magic number clusters seem to have one structural pattern in common: namely the absence of water molecules which are not at least three or four coordinated in the water network.

These results constitute a first complete and systematic overview on structures of alkali cation microhydration cluster $M^+(H_2O)_n$, with $M = Na, K, Cs$ and $4 \leq n \leq 24$, based on global optimisation studies. It is also the first unbiased check of the dodecahedron hypothesis. One might object that the results have been obtained using merely a model potential, however a complete and systematic overview would not have been possible using any ab-initio method. Nevertheless, in future studies the obtained results should be checked upon by using better model potentials also including polarisation, such as for example TTM2F (which unfortunately to date does not contain ion modelling). For better comparison the obtained structures should also be used as input geometries for both better model potentials and ab-initio calculations, such as for example DFT or MP2. However, results obtained from

DFT do not necessarily have to be more reliable than results obtained from model potentials, since DFT has known defects for long-range interactions. MP2/cc-pVTZ is generally accepted as minimum level for a quantitatively reliable description of such systems, however, this would be extremely expensive. Above all these calculations would not include zero point energy, temperatures different from 0 K, and/or dynamics. The first two items can be added a posteriori but only in the crude harmonic approximation. Also a more direct link to the experiment would be desirable instead of merely computing and comparing structures and corresponding potential energies and speculating about magic numbers in mass spectrometry. Hence, instead of going to more expensive calculations of energies, this work provides simulated anharmonic infrared spectra which can be compared directly to experimental data (see part II) and an extended molecular dynamics simulation study (see part III), including entropy and non-zero temperature and checking for possible dynamics reasons for magic numbers.

Part II.

Simulated infrared spectra of alkali cation microhydration clusters and comparison to experiment

6. Simulation of infrared spectra

As already mentioned in the introduction, mass spectra do not yield structural information. Hence a more direct link between theory and experiment is needed. The combination of experimental and theoretical infrared spectra proved to be stimulating for pure neutral water clusters [37]. The simulation technique is based on local modes and empirical parameters by V. Buch and it has been successful in reproducing the experimental infrared spectra of small pure neutral water clusters [37]. As pure water cluster behave at least to a certain extend similarly to alkali cation microhydration clusters, this model can also be used for the latter system. However it would have to be re-fitted. Unfortunately until very recently no experimental infrared spectra on alkali cation microhydration were available in the literature. Hence it was tested whether this model could be used without further re-fitting to provide a first overview, which turned out to be possible. The recently available experimental infrared spectra were obtained by J.M. Lisy and coworkers (Department of Chemistry, University of Illinois at Urbana Champaign, Illinois/USA), who kindly provided his data for the use of re-fitting the model potential of V. Buch and to obtain peak assignments and deductions on which structures are present in the experiments.

6.1. The local mode approach

As infrared spectra in the OH-stretch region are particularly sensitive to hydrogen bonding patterns one can expect to be able to differentiate between different cluster isomers by their OH-spectrum: A strong red shift occurs for the OH-stretch frequency of an OH-group involved in hydrogen bonding, but there is no red shift for a free OH-group.

Naturally, the ideal approach would be to compute anharmonic ab-initio infrared spectra. However, quantitative reproduction of OH stretch spectra of water clusters would require correlated ab-initio calculations on a level which is very high for systems of the size of clusters presented in this paper [9]. These calculations would be very challenging but still possible, however the exact calculation of excited vibrational wave functions cannot be done in reasonable time. Even harmonic infrared spectra of large alkali cation water clusters are difficult and computationally challenging, though it can be realized to compute spectra for small pure neutral water clusters [9, 10, 74].

Hence as a first step the empirical local mode approach toward the OH-stretch spectra by V. Buch was favoured as it proved to be successful for pure water clusters, ice and phenol water clusters [37, 75–77].

In contrast to ab-initio methods the empirical approach makes it possible to calculate even anharmonic OH-stretch spectra within less than one second even for clusters containing 30 water molecules. The approach has already been applied to large pure water clusters of the size $n = 1000$ [78] as well as ice [79] by V. Buch. However, the disadvantage all empirical methods have in common is the dependence on experimental data for fitting, and the local mode approach is no exception (see also section 6.2). Therefore it is not possible to transfer the approach to chemically different systems without re-fitting.

Another approach to obtain infrared stretch spectra is via molecular dynamics, but this requires much longer CPU times and also depends on the quality of the interaction potential used. One could circumvent the latter disadvantage by direct ab-initio MD but obviously this increases the necessary CPU time by several orders of magnitude.

Method

In brief, the OH-stretch spectrum is computed from a collection of coupled local Morse oscillators representing the OH-stretch coordinate. Each local mode is described by a Morse potential v_{Morse} :

$$h(r) = -\frac{1}{2} \frac{\partial^2}{\partial r^2} + v_{Morse} \quad (6.1)$$

Excited states are computed by expansion in an exciton basis:

$$\Psi = \sum_i c_i |\psi_0^{(1)} \psi_0^{(2)} \psi_0^{(3)} \dots \psi_1^{(i)} \dots \psi_0^{(n)}\rangle \quad (6.2)$$

In the product state $|\psi_0^{(1)} \psi_0^{(2)} \psi_0^{(3)} \dots \psi_1^{(i)} \dots \psi_0^{(n)}\rangle$ there is one quantum of energy in bond i and zero quanta in the remaining bonds. The bond strength can be expressed in terms of an electric field component $E_{||}$, parallel to the bond vector at the bond. The dependence of the Morse bond parameters or OH-stretch frequency, respectively, on the electric field component $E_{||}$ is essential for constructing the Hamiltonian matrix. This correlation can be understood as a modelling of the OH-mode with vibrating partial charges on the H-site in an electrostatic field.

Given a function $\nu(E_{||})$ for the local OH-stretch frequency, the un-coupled OH-stretch frequencies of the water cluster network can be computed by analysis of the electric field at each OH-group due to the partial charges and induced dipoles from other molecules.

After calculating the Morse potential v_{Morse} and the ground state eigenfunctions for each un-coupled OH-group, the OH-bonds are coupled via intra- and intermolecular couplings and

the coupled Hamiltonian can be constructed.

$$H = \sum_k h(r_k) + P_{intra} + V_{intra} + V_{inter} \quad (6.3)$$

The intramolecular coupling is a sum of the momentum coupling term

$$P_{intra} = \sum \hat{p}_1 \hat{p}_2 \cos \frac{(\angle HOH)}{m_O}, \quad (6.4)$$

describing the coupling between two OH-bonds sharing an O-atom with the mass m_O , and the potential coupling term

$$V_{intra} = k_{intra} \delta r_1 \delta r_2, \quad (6.5)$$

with δr describing the displacement from the equilibrium bond distance. The intermolecular coupling term is modelled with an oscillating dipole-dipole interaction with a constant OH-bond dipole derivative μ' where the vectors e_1 and e_2 depict the unit vectors along the OH-bonds and the distance vector e_r denotes the unit vector connecting the bond equilibria.

$$V_{inter} = k_{dd} \delta r_1 \delta r_2 \quad \text{with} \quad k_{dd} = \mu' \frac{(e_1 e_2) - 3(e_1 e_r)(e_2 e_r)}{r^3} \quad (6.6)$$

All the terms and their parameterisation, such as the OH-bond dipole derivative μ' , for water clusters are described more closely in reference [37].

The evaluation of the Morse matrix elements $\langle \psi_0 | p_i | \psi_1 \rangle$ and $\langle \psi_0 | \delta r_i | \psi_1 \rangle$ necessary for the computation of the Hamiltonian matrix is specified in reference [80]. After the diagonalisation of the Hamilton matrix the stick spectrum can be obtained directly from the eigenvalues and it is then folded by Lorentzians to approximate the infrared spectrum. The infrared absorption intensities are calculated from the transition probabilities as in reference [37].

So far the method can merely be used for pure water clusters. The additional alkali cation is simply treated as an extra positive charge. There was no radius assigned, as the clusters are not altered in their geometry while computing the spectra, and no polarisability was assumed, as it can be neglected for cations though not for anions.

6.2. Frequency dependence

As already mentioned, the local mode approach is empirical, i.e. the frequency dependence is fitted to the experiment. However, there were no experiments on alkali cation microhydration clusters at this point of the investigation, hence a correct frequency vs. field curve could not be obtained for these systems (see section 7.1 for further details).

For ion-water systems, it was suggested [81] that the frequency vs. field curve shows a parabolic form. This idea was generalised [37] for pure water clusters and ice, assuming

that the OH-stretch frequency $\nu(E_{||})$ is some not necessarily parabolic function of $E_{||}$, where a certain parameterisation will best reproduce the measured spectral data for pure water clusters. The function is then constructed such as to interpolate between the bond frequencies of gaseous water and the experimental values for the frequencies of hydrogen-bonded OH-in cyclic water clusters, $(\text{H}_2\text{O})_n$ ($N = 1 - 5$). For the water network of the alkali cation microhydration clusters the frequency dependence is adopted from reference [37] employing the non-parabolic frequency vs. field curve. This approach would be correct if it were used for pure water clusters, however the systems to be used here are ion-water systems and the ion would be unaccounted for in the frequency dependence. M. Probst [81] suggested a parabolic form for $\text{Mg}^+(\text{H}_2\text{O})_n$ systems, however the frequency dependences given in his paper are size and structure dependent whereas the frequency dependence given by V. Buch can be applied to all cluster structures and sizes. It was claimed [77] that the spectra depend strongly on the frequency vs. field curve so the first step was to alter the frequency vs. field curve and test the sensitivity of the spectral data. It was found that although the resulting spectral data changed quantitatively, the qualitative overall peak pattern remained the same which made it possible to interpret the spectral data within these boundaries. The results will be discussed in more detail in section 7.

7. Results and discussion

7.1. Influence of the frequency vs. field curve on the spectral data

As already mentioned in section 6.2 the frequency vs. field curves were altered in order to test the dependence of the infrared stretch spectra on this curve. It can be seen easily from the equations used (for further information see reference [37]) that shifts by $\Delta\nu$ result in no changes in the spectral data. Shifting the curve by ΔE_{\parallel} though resulted in changes: The shifted curves are depicted in figure 7.1. The resulting spectra are shown in figure 7.4. For ΔE_{\parallel} values of -10% no changes in the spectral data could be observed, whereas a shift by 50% resulted in an expansion of the spectrum towards lower wave numbers. The peak pattern for larger wave numbers is not expanded as much as the peak pattern for lower wave numbers. For ΔE_{\parallel} values of 10% the spectrum is compressed, with peaks located in lower wave number areas experiencing a stronger shift towards higher wave numbers than peaks in the higher wave number area. Almost identical effects as for positive ΔE_{\parallel} shifts can be observed for the alteration of the frequency dependence towards parabolic shapes as in reference [81] (see figure 7.2 and figure 7.3). Peak patterns in lower wave number regions are compressed and shifted to higher wave number regions. The effect on peak patterns in higher wave number regions is basically the same, though not as strong.

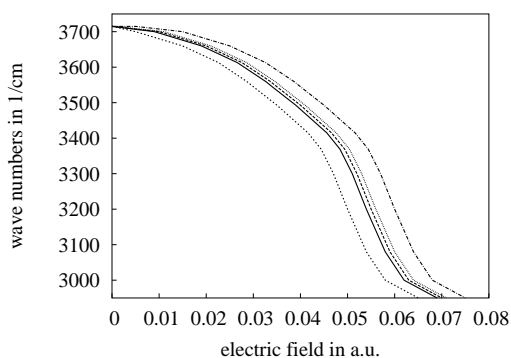


Figure 7.1.: Frequency vs. field curve of V. Buch with respect to shifts in ΔE_{\parallel} direction (from left to right): $\Delta E_{\parallel} = -0.005, -0.001, 0.0, 0.001, 0.005$

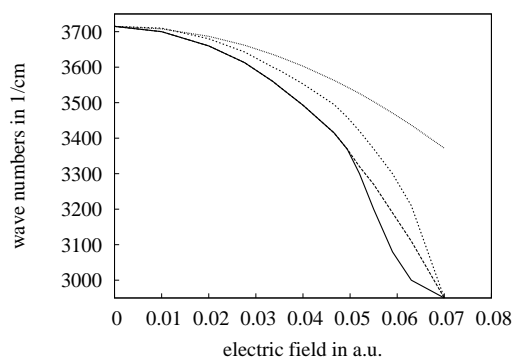


Figure 7.2.: Deformation of the frequency vs. field curve of V. Buch [37] (solid line) towards the parabolic form, suggested by M. Probst [81]; (from left to right: (norm), (p1), (p2), (p3))

For all alterations it was found that although the resulting spectral data changed quantitatively, the qualitative overall peak pattern remained the same. While peaks may be shifted onto each other using changed frequency dependences, thus creating a double peak or even a single peak, no change in the relative ordering of the peaks could be observed. Therefore one can use the frequency vs. field curve from reference [37] unchanged. Once the correct curve is known from fits to experimental data, it should be possible to easily transform the results found here towards the correct spectral data. At this stage of this work, this merely is a first step to gain insight in anharmonic infrared spectra on alkali cation water clusters. Hence this approach seemed to be legitimate, even if it might produce no quantitatively correct spectral data. Therefore, in sections 7.2 and 7.3, qualitative results with the unchanged curve are shown. A fit to the recently available experimental data and quantitative results follow in section 8.

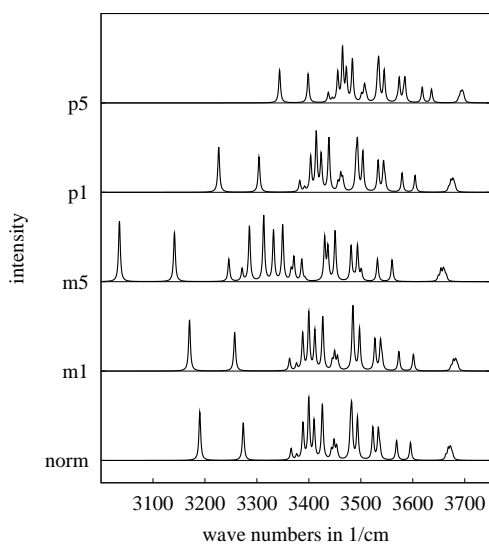


Figure 7.3.: Spectral data (intensity in arbitrary units) corresponding to changes in the frequency dependence; (norm): spectrum correlating to the frequency vs. field of V. Buch [37]; (p3): spectrum correlating to the curve suggested by M. Probst [81]; for (p1), (p2) see figure 7.2

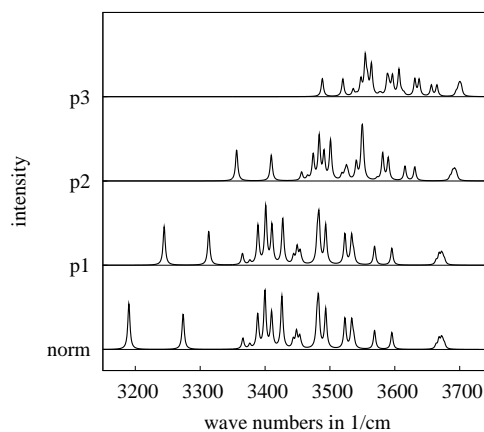


Figure 7.4.: Spectral data (intensity in arbitrary units) corresponding to changes in the frequency dependence (see figure 7.1); (norm): spectrum correlating to the frequency vs. field of V. Buch [37]; (m1): $\Delta E_{||} = -0.001$ [a.u.]; (m5): $\Delta E_{||} = -0.005$ [a.u.]; (p1): $\Delta E_{||} = 0.001$ [a.u.]; (p5): $\Delta E_{||} = 0.005$ [a.u.]

7.2. Overall trends in structure-spectra relations

Infrared spectra have been calculated for all global minimum cluster structures of the systems $M^+(\text{H}_2\text{O})_n$ for $M = \text{Na}, \text{K},$ and Cs and for each value of n in the range of $4 \leq n \leq 22$ (see also reference [82]).

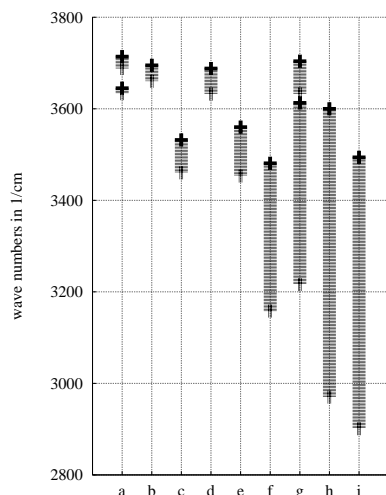


Figure 7.5.: Distribution of peaks with respect to wave numbers and coordination of the water molecules for $\text{Na}^+(\text{H}_2\text{O})_n$: (a): single H_2O ; (b): dangling OH; (c): D; (d): AA; (e): DD; (f): DDAA; (g): DA; (h): DDA; (i): DAA

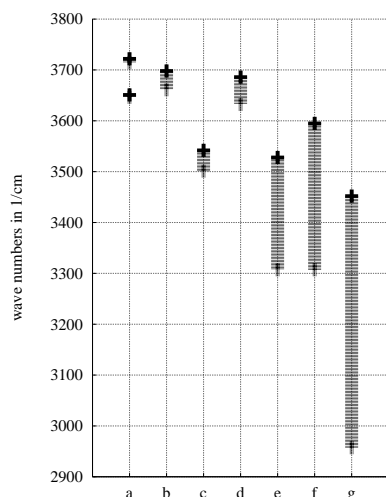


Figure 7.6.: Distribution of peaks with respect to wave numbers and coordination of the water molecules for $\text{K}^+(\text{H}_2\text{O})_n$: (a): single H_2O ; (b): dangling OH; (c): D; (d): AA; (e): DA; (f): DDA; (g): DAA

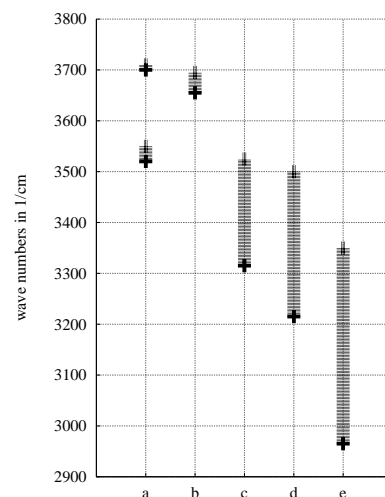


Figure 7.7.: Distribution of peaks with respect to wave numbers and coordination of the water molecules for $\text{Cs}^+(\text{H}_2\text{O})_n$: (a): single H_2O ; (b): dangling OH; (c): DA; (d): DDA; (e): DAA

The cluster structures used for the investigation of infrared spectra are mainly global minimum structures. Only a few interesting low-lying minimum structures were also studied. Hence any structural remarks made in the following sections refer only to global minima cluster structures unless stated otherwise. Generally the abbreviation D shall denote donor, i.e. one D for each donating OH bond per water molecule, and the abbreviation A is used for acceptor, i.e. one A for each accepted OH bond per water molecule. OH bonds which stick out are usually referred to as dangling OH, while single water molecules form no hydrogen bonds to any of the water molecules of the rest of the water network but are bound only to the central ion.

The main structural units in most of the cluster structures of $M^+(\text{H}_2\text{O})_n$ are three-coordinated molecules of two varieties: double donor – single acceptor (DDA) and single donor – double acceptor (DAA). Hydrogen atoms of DDA molecules form relatively weak hydrogen bonds, whereas DAA molecules form relatively strong hydrogen bonds [37, 74, 76, 83].

The peak distributions, i.e. certain H-bonds lead to peaks in certain regions which cannot be found anywhere else, of these typical H-bond arrangements for the global minima cluster structures of $M^+(\text{H}_2\text{O})_n$ ($M = \text{Na}, \text{K}, \text{Cs}$ and $4 \leq n \leq 20$) are depicted in figures 7.5, 7.6, and 7.7. Looking at peak distribution is a first step of assigning peak patterns as it gives a better overview on the overall situation: In general the peak distributions for $\text{Cs}^+(\text{H}_2\text{O})_n$ and $\text{K}^+(\text{H}_2\text{O})_n$ are quite similar though the peak patterns for $\text{K}^+(\text{H}_2\text{O})_n$ experience a small blue-shift compared to $\text{Cs}^+(\text{H}_2\text{O})_n$. The distributions for $\text{Na}^+(\text{H}_2\text{O})_n$ show some similar features, however the peaks are generally closer together, i.e. the blue-shift found for $\text{K}^+(\text{H}_2\text{O})_n$ is even stronger here. In addition there are more different three-dimensional coordinations found for the water molecules in $\text{Na}^+(\text{H}_2\text{O})_n$ clusters and hence the overlap of peak areas is a lot stronger than for the peak patterns found for $\text{K}^+(\text{H}_2\text{O})_n$ and $\text{Cs}^+(\text{H}_2\text{O})_n$ cluster structures.

Single water

Single water molecules show two distinctive peaks which correspond to the symmetric and antisymmetric stretch frequencies of the isolated water molecule. The peaks for single water molecules of $\text{K}^+(\text{H}_2\text{O})_n$ and $\text{Cs}^+(\text{H}_2\text{O})_n$ clusters can typically be found in distinct regions, which are well distinguishable from other regions. Thus the peaks found in that region can be assigned reliably to these molecules. The area for $\text{K}^+(\text{H}_2\text{O})_n$ is found generally at approximately 3650 cm^{-1} and 3720 cm^{-1} . For $\text{Cs}^+(\text{H}_2\text{O})_n$ these peaks can be found around approximately 3520 cm^{-1} and 3710 cm^{-1} . In smaller $\text{Na}^+(\text{H}_2\text{O})_n$ clusters these peaks are also observable and for $n \leq 11$ they are rather distinct. In some cases an overlap can occur with peaks from DA molecules, though only for the region around 3635 cm^{-1} . For wave numbers between $3690 - 3720 \text{ cm}^{-1}$ only single waters could be assigned. Even though there might be some overlap for $\text{Na}^+(\text{H}_2\text{O})_n$ these molecules can be assigned very reliable, in all three systems.

For example the cluster structure of $\text{K}^+(\text{H}_2\text{O})_5$ exhibits two single water molecules and a total of four dangling OH (see the following section; for the cluster structure see figure 7.8 and for the corresponding spectrum see figure 7.9). The peaks of the single water molecules appear at 3717 cm^{-1} and at 3647 cm^{-1} . The peaks at wave numbers $> 3700 \text{ cm}^{-1}$ are well separated from the dangling OH peaks. AA molecules can yield peaks around 3650 cm^{-1} as well. In the example of $\text{K}^+(\text{H}_2\text{O})_5$ the AA peak can be found at 3633 cm^{-1} , hence in this case it does not overlap the peak of the single waters.

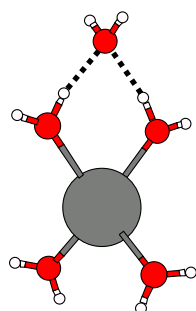


Figure 7.8.: Global minimum structure of $K^+(H_2O)_5$

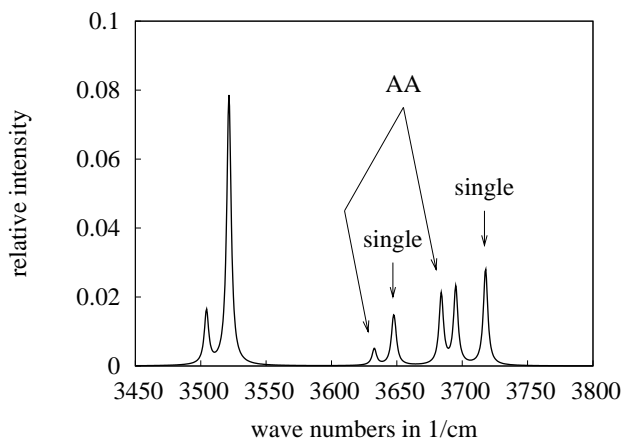


Figure 7.9.: Infrared spectrum of $K^+(H_2O)_5$

Dangling OH

Dangling OH bond peaks occur between $3660 - 3695 \text{ cm}^{-1}$ for $Na^+(H_2O)_n$, $3660 - 3700 \text{ cm}^{-1}$ for $K^+(H_2O)_n$, and $3655 - 3695 \text{ cm}^{-1}$ for $Cs^+(H_2O)_n$, respectively, forming a dense peak multiplet (see figure 7.10). Hence they do not contribute much to structure assignment, especially as there is no cluster without dangling OH bonds.

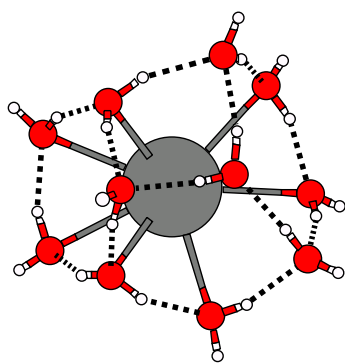


Figure 7.10.: Global minimum structure of $Cs^+(H_2O)_{11}$

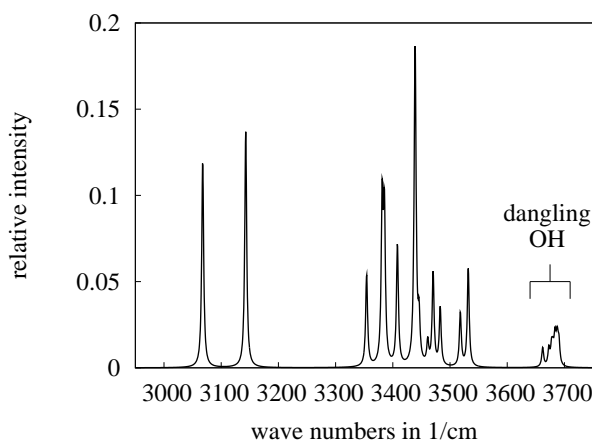


Figure 7.11.: Infrared spectrum of $Cs^+(H_2O)_{11}$

Double acceptors – AA

Molecules accepting two hydrogen bonds and donating none can only be found for $Na^+(H_2O)_n$ and $K^+(H_2O)_n$ and some low energy structures of $Cs^+(H_2O)_n$ with small n ($4 \leq n \leq 8$). In

some but not all of these clusters these peaks are fairly distinct.

In the example of $\text{K}^+(\text{H}_2\text{O})_5$ (for the cluster structure see figure 7.8 and for the corresponding spectrum see figure 7.9), the AA peak is very close to one peak of the single water molecules. However the peaks of the single water molecules usually do not appear outside the region of $3645 - 3655 \text{ cm}^{-1}$.

So peaks in this region, at least for smaller cluster structures with $n \leq 10$, in combination with missing peaks at wave numbers $> 3700 \text{ cm}^{-1}$, allow a relatively reliable assumption of AA molecules being present in a structure.

Double donors – DD

DD molecules just donate hydrogen bonds and cannot accept them for geometrical reasons. Those molecules are mostly found in $\text{Na}^+(\text{H}_2\text{O})_n$ clusters. Similar to single-donators they can be found at the edge of the water network (see figure 7.12 and figure 7.14). The peaks corresponding to DD molecules can usually be found between $3450 - 3560 \text{ cm}^{-1}$.

The DD region of $\text{Na}^+(\text{H}_2\text{O})_{13}$ (see figure 7.13) lies between $3508 - 3549 \text{ cm}^{-1}$. Only one peak corresponding to DDA can be found in that region at 3528 cm^{-1} , similar in intensity to the DD peaks. As DD molecules are usually very close to the central ion they have actually a similar electronic environment as DDA: Two donating hydrogen atoms and accepting one hydrogen bond from another water molecule vs. donating two hydrogen atoms and 'accepting' the positive charge of the close central ion. Hence it is not surprising that the peaks for DD molecules appear in a similar range as the DDA molecules.

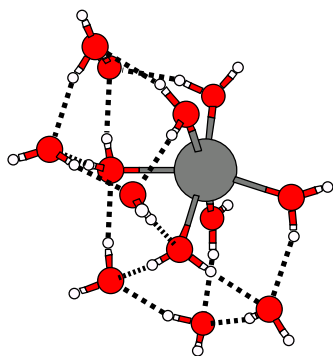


Figure 7.12.: Global minimum structure of $\text{Na}^+(\text{H}_2\text{O})_{13}$

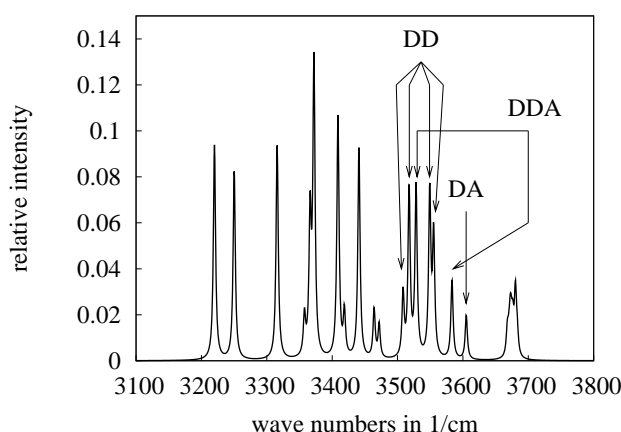


Figure 7.13.: Infrared spectrum of $\text{Na}^+(\text{H}_2\text{O})_{13}$

For smaller cluster structures $n \leq 13$ the areas between DD and DDA coincide only a little, with DD molecules tending to yield peaks in higher wave number regions from $3480 -$

3560 cm^{-1} than DDA molecules approximately from $3330 - 3530\text{ cm}^{-1}$. Hence this is no exclusion criterion, though finding peaks in the area of $3480 - 3560\text{ cm}^{-1}$ can lead to a first assumption that the cluster structure most possibly contains one or more DD molecules.

Single donor single acceptor – DA

DA molecules accepting one bond and donating one can be found throughout all cluster sizes, though not for magic numbers. But as peaks corresponding to DA molecules more or less coincide with both DDA and DAA peaks, assignments in experiments would have to rely heavily on theoretical data.

For example, both $\text{Na}^+(\text{H}_2\text{O})_{13}$ and $\text{Na}^+(\text{H}_2\text{O})_{20}$ each have one DA water molecule in their cluster structure (see figures 7.12, 7.14 for cluster structures and figures 7.13, 7.15 for the corresponding spectra). With 3605 cm^{-1} the DA peak in the spectrum of $\text{Na}^+(\text{H}_2\text{O})_{13}$ is somewhat isolated from the other peaks; neighbouring peaks at higher wave numbers are dangling OH, found at $3668 - 3683\text{ cm}^{-1}$, and the next neighbour in the direction of lower wave numbers is a DDA peak at 3583 cm^{-1} . For $\text{Na}^+(\text{H}_2\text{O})_{20}$, however, the DA peak is found at 3441 cm^{-1} , surrounded and overlapped by peaks corresponding to DDA and DD molecules.

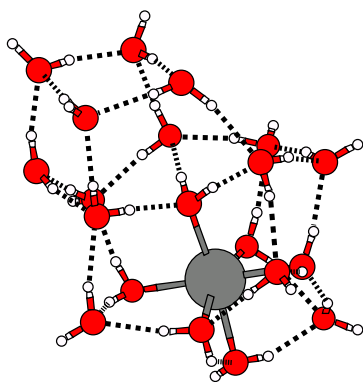


Figure 7.14.: Global minimum structure of $\text{Na}^+(\text{H}_2\text{O})_{20}$

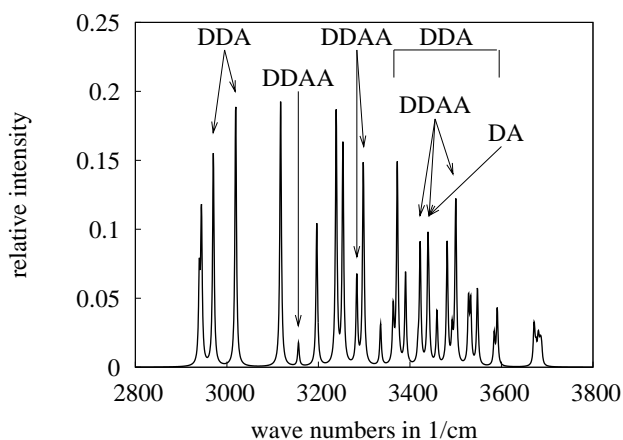


Figure 7.15.: Infrared spectrum of $\text{Na}^+(\text{H}_2\text{O})_{20}$

Double donor single acceptor – DDA and double donor double acceptor – DDAA

The area correlating to DDA molecules would probably be difficult for experimentalists, too, as there are usually many peaks which are very close together, in addition to the overlap by both DA and DD molecules. DDAA molecules are only found in $\text{Na}^+(\text{H}_2\text{O})_n$ structures

($n \geq 18$). They can also be found in the DDA region, though most of the DDAA peaks are very isolated.

In the example spectrum of $\text{Na}^+(\text{H}_2\text{O})_{20}$ (see figure 7.15, with the corresponding structure shown in figure 7.14) the DDAA peaks can be found at 3492 cm^{-1} , 3442 cm^{-1} , 3422 cm^{-1} , 3299 cm^{-1} , 3284 cm^{-1} , and 3156 cm^{-1} . The DDAA peaks are usually very high in intensity. In that area from $3492\text{ cm}^{-1} - 3156\text{ cm}^{-1}$, also DD, DA, DDA, and DAA peaks can be found. The DAA peaks concentrate around the lower wave numbers $3492 - 3336\text{ cm}^{-1}$, whereas DA and DD peaks are found in higher wave number regions of the DDAA area: $3481 - 3459\text{ cm}^{-1}$. DDA peaks are found throughout that DDAA region. As there is in general a large overlap of peak areas in cluster structures with a large n ($n \geq 18$), theoretical data would be essential for assigning peaks correctly.

Single donor double acceptor – DAA

DAA molecules show peaks in the lower wave number area of the spectrum. They are usually well separated from the DD/DDA/DDAA region for $n \leq 14$. For larger n the separation can still be observed for symmetric cluster structures which exhibit a sparser peak pattern than non-symmetric ones (see also section 7.2). However, the wave number area where overlaps can be observed is relatively narrow.

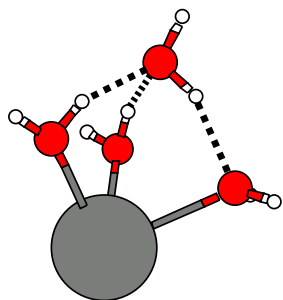


Figure 7.16.: Example of a DAA molecule (topmost water molecule)

DAA molecules showing the most distinctive peaks have one structural feature in common. They exhibit an angle $\angle HOM^+$ between 70° and 100° (where the angle is measured between the central ion M^+ and the oxygen atom of the DAA water molecule and the donating hydrogen atom of the DAA water molecule) while the dangling OH bond points away from the central ion (see figure 7.16). The water molecules donating the hydrogen bonds towards the DAA are quite close to the central ion, while the DAA is a little farther away. The number of the distinct peaks found for DAA molecules corresponds in more than 95% of the cases to the number of DAA molecules in the cluster. Therefore these peaks contribute much to the possibility of gaining more structural insight in alkali cation microhydration clusters via infrared spectroscopy.

As mentioned in section 7.1 the frequency vs. field curve used for the computation of the spectral data does not produce quantitatively correct results. The peaks affected most by the alteration of the frequency dependence are the DAA peaks. However even for large changes in the frequency vs. field curve the peaks are still very distinct. Reaching the parabolic form

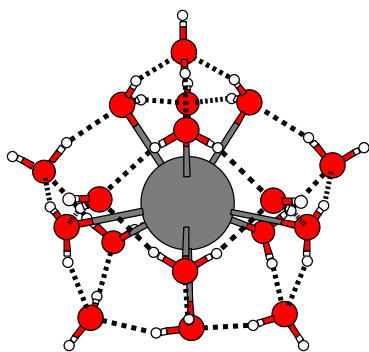


Figure 7.17.: Global minimum structure of $\text{Cs}^+(\text{H}_2\text{O})_{18}$

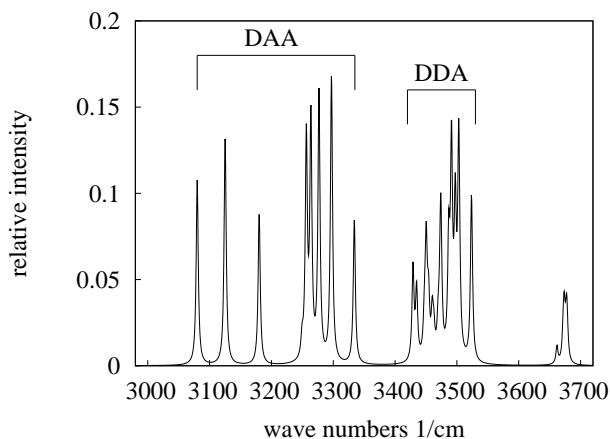


Figure 7.18.: Infrared spectrum of $\text{Cs}^+(\text{H}_2\text{O})_{18}$

of the curve the gap between the DDA and DAA becomes very small but is still visible. But as most probably the real frequency vs. field curve will be in between the two extremes, the DAA peaks should still lead to a better understanding of cluster structures in the experiment.

As an example $\text{Cs}^+(\text{H}_2\text{O})_{18}$ was chosen. The cluster structure is depicted in figure 7.17 and the corresponding spectrum is depicted in figure 7.18. The cluster structure consists only of DAA and DDA water molecules, 9 each. In the spectrum the areas corresponding to both these water molecules are well separated. The DAA region ranges from $3080 - 3334 \text{ cm}^{-1}$ and the DDA region ranges from $3429 - 3524 \text{ cm}^{-1}$. There are nine DAA peaks: 3334 cm^{-1} , 3297 cm^{-1} , 3277 cm^{-1} , 3264 cm^{-1} , 3256 cm^{-1} , 3250 cm^{-1} , 3180 cm^{-1} , 3125 cm^{-1} , and 3080 cm^{-1} corresponding to the nine water molecules. Compared to the DDA region the peaks are better separated and in general higher in intensity. So far no regularity with respect to the peak order of the DAA peaks, for example distance towards the central ion, could be found.

Symmetry effects

Cluster structures showing special symmetry or pseudo-symmetry, such as the dodecahedron, are quite rare. However the spectral data corresponding to these kind of cluster structures is very distinct.

The spectra exhibit large gaps between peak areas corresponding to different water molecules. The number of peaks is decreased and their intensity is increased compared to spectral data of cluster structures of the same size with no symmetry, as symmetry related water molecules contribute to the same peak. An example of a cluster featuring high symmetry is $\text{K}^+(\text{H}_2\text{O})_{12}$, see figure 7.19 for the structure and figure 7.20 for the corresponding spectrum. (For the

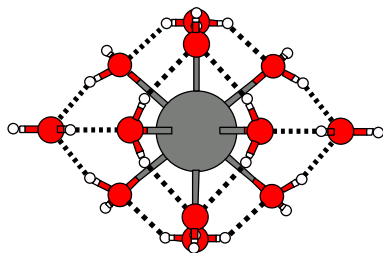


Figure 7.19.: Global minimum structure of $K^+(H_2O)_{12}$; *Inner circle:* four-membered-ring consisting of two DAA and two DDA water molecules; *Outer circle:* the water molecules in the figure forming a ring around the inner circle

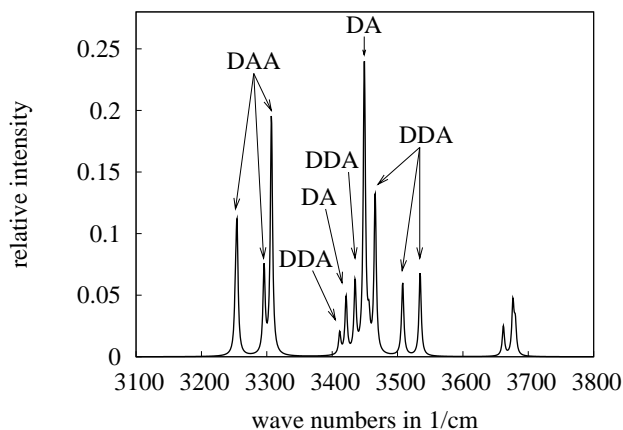


Figure 7.20.: Infrared spectrum of $K^+(H_2O)_{12}$

dodecahedral case which exhibits a pseudo-symmetry, see section 7.3 for the cluster structure and corresponding spectral data of $Cs^+(H_2O)_{20}$).

The structure of $K^+(H_2O)_{12}$ consists of DA-, DDA-, and DAA-water-molecules, 4 each. In the spectrum of $K^+(H_2O)_{12}$ the DAA peaks are well separated from the rest of the spectrum, and though there are 4 DAA water molecules only three peaks are observed, due to symmetry. The main peak corresponding to the DA molecules is found at 3449 cm^{-1} , with each of the 4 DA water molecules contributing the same amount. The two peaks at 3507 cm^{-1} and 3535 cm^{-1} correspond to the two DDA molecules belonging to the five-membered rings. The DDA peaks located around the DA peak correlate with the DDA molecules of the four-membered ring.

7.3. Temperature dependence

To simulate experimental data, the Boltzmann probability distribution of $Cs^+(H_2O)_{20}$ with 1400 available local minima was computed at $T > 0\text{ K}$.

In the case of $Cs^+(H_2O)_{20}$ the global minimum is represented by a dodecahedron shaped clathrate-like water network with a binding energy of 1098.7731 kJ/mol . The local minima close to the global minimum either show minimally distorted dodecahedral shape or water networks exhibiting four-membered and six-membered rings arranged such that the cluster hull

maintains a quasi-clathrate form. The best non-dodecahedral cluster structure has a binding energy of 1097.8913 kJ/mol. Lower in energy, the dodecahedron-shaped cluster structures become more distorted than the non-dodecahedron cluster structures. In figure 7.21 two representative cluster structures, dodecahedral vs. non-dodecahedral, are depicted. For the corresponding spectra see figure 7.22. Spectra were simulated for distributions corresponding to different temperatures: 0 – 15 K, 50 K, 80 K, 120 K, 150 K, and 273 K. For completeness spectra were simulated also for room temperature and 373 K, however, the results are not depicted in this work.

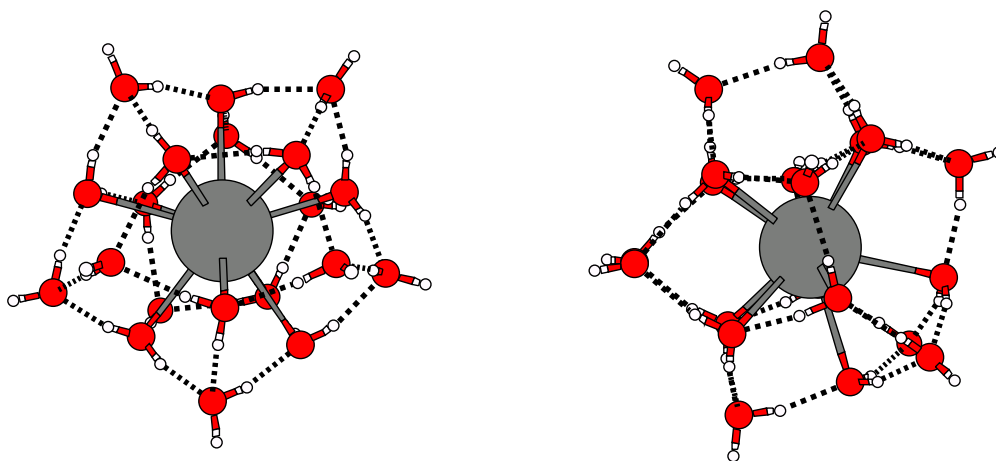


Figure 7.21.: Global minimum structure of $\text{Cs}^+(\text{H}_2\text{O})_{20}$ – dodecahedron (left) and local minimum structure of $\text{Cs}^+(\text{H}_2\text{O})_{20}$ – best non-dodecahedron (right)

Cluster structures with a probability less than 10^{-3} were neglected. Temperatures in typical cluster beam experiments are hard to determine; in different settings, estimates range from 5 K to 150 K. In figure 7.22, the bottom graph corresponds to the spectrum of the best non-dodecahedral cluster structure, followed by the reference spectrum of the global minimum, above which the spectra increasing in temperature are displayed.

Between 0 K and 15 K no change with regard to the reference spectrum was found, though more than one cluster structure was accounted for in the distribution, each with a relative contribution of $> 97\%$. Since the first six cluster structures in the distribution are dodecahedral and almost degenerate in energy ($1098.7731 \text{ kJ mol}^{-1} - 1098.7729 \text{ kJ mol}^{-1}$), even at 0 K all these structures have to be accounted for. But even when the temperature increases to about 80 K the noise generated by cluster structures significantly different from the global minimum is more or less negligible. The noise observed for spectra around 80 K grows into peaks as the temperature rises. By temperatures above 120 K the noise peaks have reached the size of the smaller peaks of the spectrum. They belong mostly to the structures showing a moderate deviation in the cluster geometry with respect to both the global minimum and the best non-dodecahedron. This can easily be shown by computing the spectral data for each

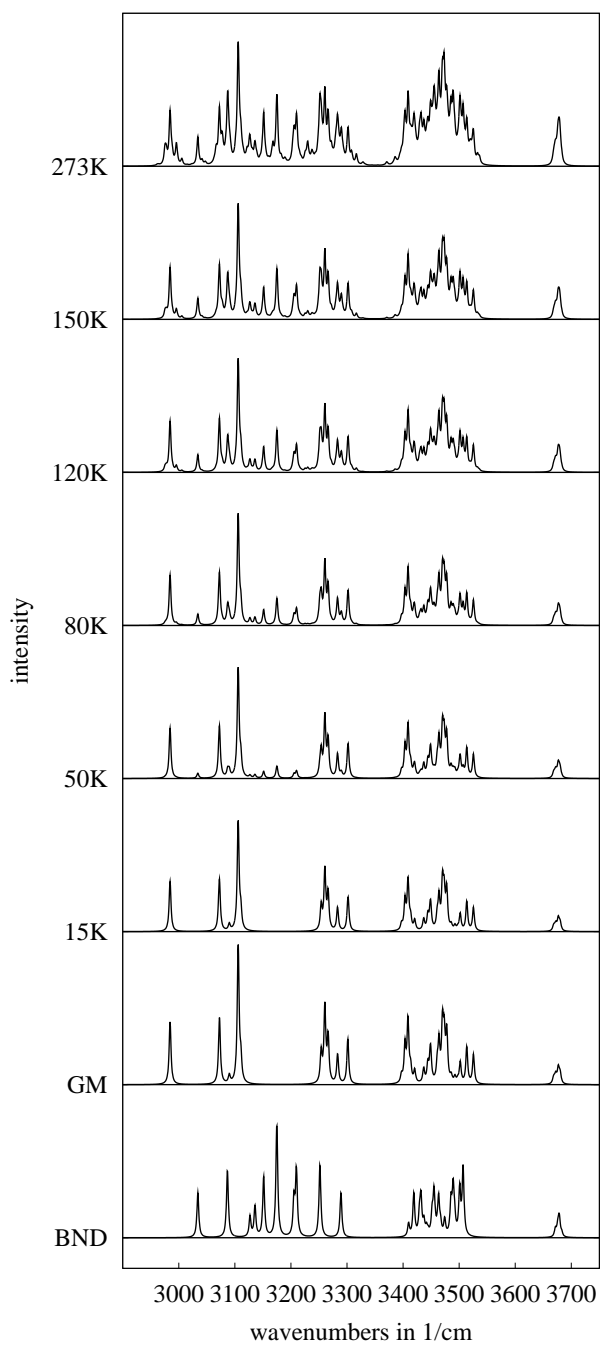


Figure 7.22.: Spectra of $\text{Cs}^+(\text{H}_2\text{O})_{20}$ with respect to temperature and Boltzmann probability distribution (intensity in arbitrary units); BND: reference spectrum of the best non-dodecahedral cluster structure of $\text{Cs}^+(\text{H}_2\text{O})_{20}$; GM: reference spectrum of the dodecahedral cluster structure of the global minimum of $\text{Cs}^+(\text{H}_2\text{O})_{20}$

structure separately. For minor changes with respect to the global minimum and the best non-dodecahedron, respectively, only the peak pattern in the DAA region is slightly altered, whereas for stronger distortions, destroying the approximate symmetry, the peak patterns resemble that of non-symmetric clusters, i.e. there are less distinct peaks and no separated peak areas. For $\text{Cs}^+(\text{H}_2\text{O})_n$ and within the limitations of both the TIP4P/OPLS model and the empirical spectra simulation, one therefore expects that experiments in the low-temperature region (< 50 K) should be able to discern structural preferences unambiguously and to decide even between the closely related species of the dodecahedron (only five-membered rings) and cages which contain four-, five-, and six-membered rings.

Noise from different structures becomes visible only above 120 K. Therefore, at lower temperatures, it may be possible to disentangle the experimental spectra into major contributions from just a few structural species by comparison to theory.

8. Experimental data and peak assignment

As already mentioned in section 7.1, the frequency vs. field curve fitted for pure water clusters could also be used for alkali cation microhydration clusters, as it still produced qualitatively correct data. In order to be able to obtain quantitatively correct data, the curve would have to be re-fitted for each of the three systems $\text{Na}^+(\text{H}_2\text{O})_n$, $\text{K}^+(\text{H}_2\text{O})_n$, and $\text{Cs}^+(\text{H}_2\text{O})_n$ separately. As experimental data on infrared spectra was not available until very recently and only on small cluster sizes [84], it was not yet possible to fit these curves using an optimisation routine. Instead they were fitted manually in a first attempt. Nevertheless, excellent quantitative agreement between experiment and theory could be achieved, allowing first structural assignments which would not have been possible without theory.

As experimental infrared spectra of alkali cation microhydration clusters will not just show signatures of only one structure but of a distribution of structures depending on temperature, fitting and assignment are not possible using merely the global minimum structures, instead a Boltzmann distribution of all computed structures per cluster size as a function of the potential energy and temperature has to be used. When computing a spectrum of Boltzmann distributed structures, the intensity of the peaks of each cluster structure can then be assigned according to the Boltzmann weight of this structure. As the temperature at which the infrared spectra were measured experimentally ranges approximately around $T = 100$ K [84], the Boltzmann distribution was computed using this temperature.

It is worth mentioning that for the fitting procedure mainly one experimental spectrum per system and its corresponding theoretical spectrum were used. For example in the case of $\text{Cs}^+(\text{H}_2\text{O})_n$ the spectrum used for the fitting procedure was the experimental spectrum of $\text{Cs}^+(\text{H}_2\text{O})_5$ as it already provides a rather large abundance of peaks compared to its smaller neighbours and the peaks are still assignable to peaks in the theoretical spectrum unlike for the spectra for larger cluster sizes, such as for example $n = 6, 8$. After fitting the theoretical spectrum of $\text{Cs}^+(\text{H}_2\text{O})_5$ to its corresponding experimental spectrum, a frequency vs. field curve was obtained, which was optimally fitted for this spectrum (see figure 8.1 for the fit and figure 8.2 for the corresponding spectrum). When using this “pre-fitted” curve for the simulation of theoretical spectra of other cluster sizes, both smaller and larger, one also already obtains very good agreement between theory and experiment (see also figure 8.2).

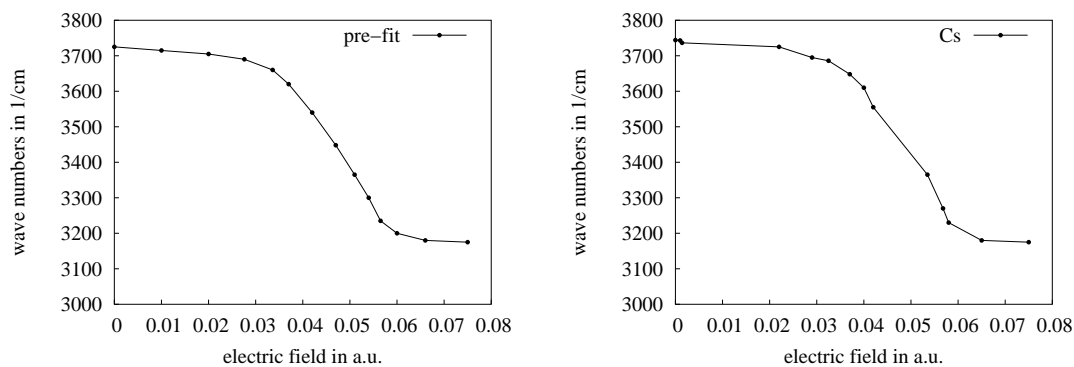


Figure 8.1.: Frequency vs. field curves: (pre-fit) pre-fitted curve for $\text{Cs}^+(\text{H}_2\text{O})_5$ (left), (Cs) manually re-fitted curve for $\text{Cs}^+(\text{H}_2\text{O})_n$ (right), for the latter see also figure 8.3

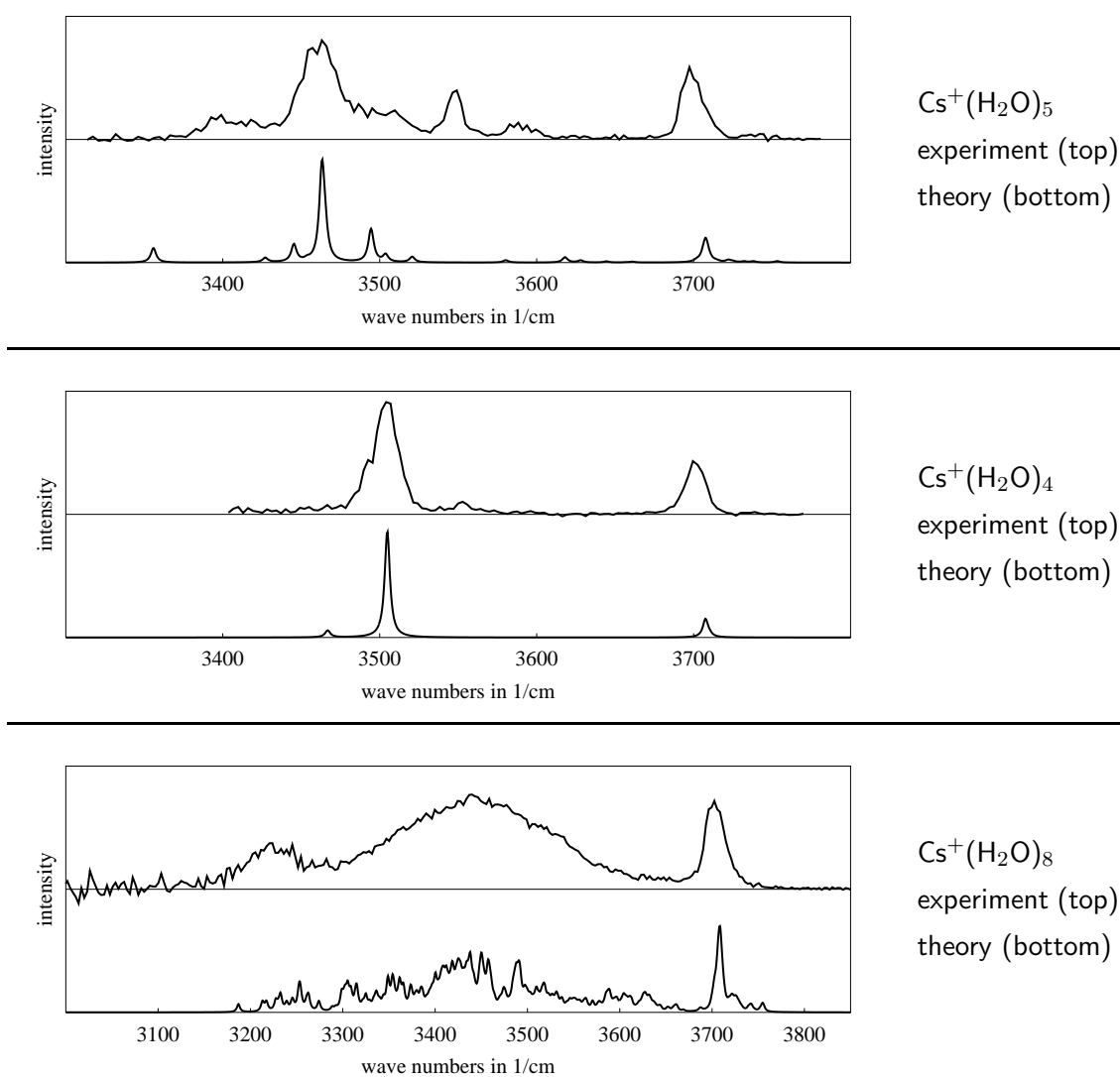


Figure 8.2.: Experimental and theoretical infrared spectra (using a manually fitted frequency vs. field curve which was solely fitted and optimised for $\text{Cs}^+(\text{H}_2\text{O})_5$ – see figure 8.1) of $\text{Cs}^+(\text{H}_2\text{O})_5$ (top), $\text{Cs}^+(\text{H}_2\text{O})_4$ (middle), and $\text{Cs}^+(\text{H}_2\text{O})_8$ (bottom), respectively, intensity in arbitrary units

	Experimental		Theoretical	
	symmetric	antisymmetric	symmetric	antisymmetric
$\text{Cs}^+(\text{H}_2\text{O})$	$3635.5 \pm 5 \text{ cm}^{-1}$	$3711.5 \pm 5 \text{ cm}^{-1}$	3660.5 cm^{-1}	3751.6 cm^{-1}

Table 8.1.: Frequencies for $\text{Cs}^+(\text{H}_2\text{O})$, both experimental and theoretical, using the manually fitted frequency vs. field curve which was solely fitted and optimised for $\text{Cs}^+(\text{H}_2\text{O})_5$ (see figure 8.1)

Nevertheless, although the overall trends are already in very good agreement for the comparison between theory and experiment for simulated theoretical spectra using a frequency vs. field curve solely fitted for the spectrum of $\text{Cs}^+(\text{H}_2\text{O})_5$, the agreement for all other cluster sizes can still be improved somewhat applying further subtle changes to the frequency vs. field curve. One obvious case are single water molecules (see table 8.1 for values obtained in the experiment and for theoretical values using the frequency vs. field curve for $\text{Cs}^+(\text{H}_2\text{O})_5$) as they still showed a rather large offset compared to the experimental values. Also peak regions which were not represented in the spectrum of $\text{Cs}^+(\text{H}_2\text{O})_5$ but can be found for cluster sizes of $n \geq 7$ could be improved by a “re-fit”. However the changes applied were only very subtle as can be seen in figure 8.1.

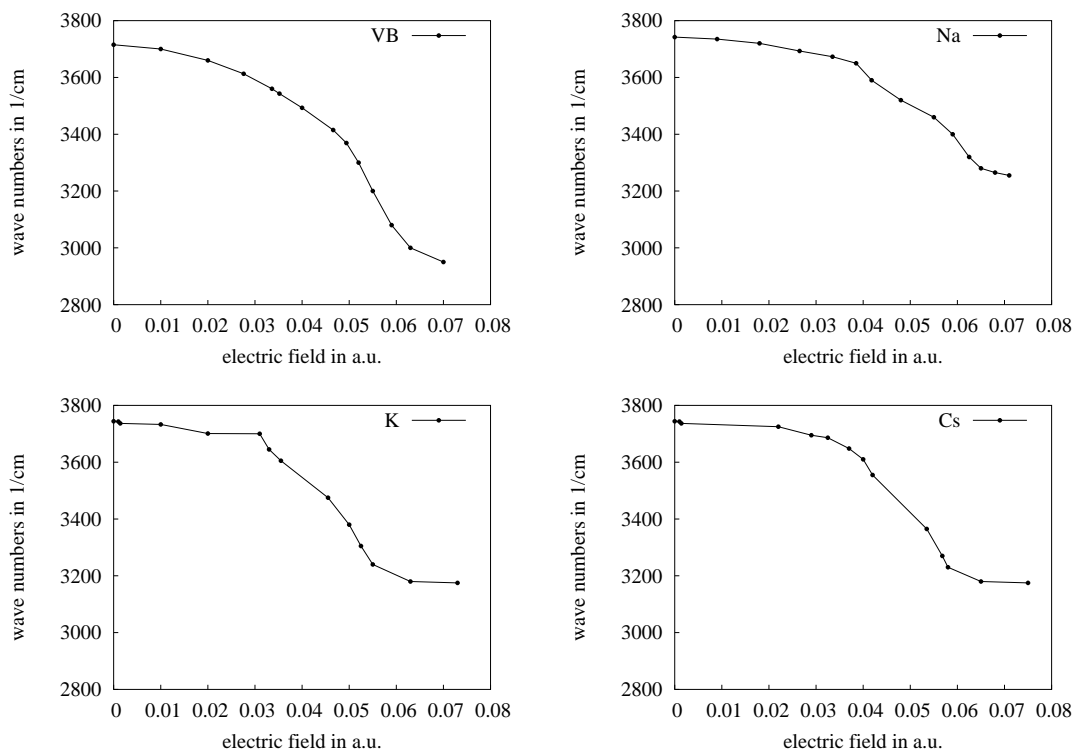


Figure 8.3.: Frequency vs. field curves: (VB) curve of Victoria Buch for pure water clusters originally used also for alkali cation microhydration clusters (left top), (Na) manually re-fitted curve for $\text{Na}^+(\text{H}_2\text{O})_n$ -clusters (right top), (K) manually re-fitted curve for $\text{K}^+(\text{H}_2\text{O})_n$ -clusters (left bottom), (Cs) manually re-fitted curve for $\text{Cs}^+(\text{H}_2\text{O})_n$ -clusters (right bottom)

The final fit of the frequency vs. field curve for $\text{Cs}^+(\text{H}_2\text{O})_n$ (depicted in figure 8.1) was then used for the simulation of all theoretical spectra without applying further changes (see below and following sections). For this final fit, all experimental spectra so far available for $\text{Cs}^+(\text{H}_2\text{O})_n$, i.e. $n = 3 - 6, 8$ were taken into account in order to fine-tune the curves obtained in the “pre-fit”. This procedure was also used for re-fitting the frequency vs. field curves for $\text{Na}^+(\text{H}_2\text{O})_n$ and $\text{K}^+(\text{H}_2\text{O})_n$. For $\text{Na}^+(\text{H}_2\text{O})_n$ only the experimental spectra of $n = 3, 4$ could be used for the fine tuning as so far only these two were available, whereas for $\text{K}^+(\text{H}_2\text{O})_n$ three experimental spectra could be used, namely $n = 3, 4, 5$. It was found that the final fits of the frequency vs. field curves for all three systems do not differ much from the original curve for neutral water clusters by V. Buch. Plots of all four curves are depicted in figure 8.3. As already said in the case of $\text{Cs}^+(\text{H}_2\text{O})_n$, the curves depicted in figure 8.3 for the case of $\text{Na}^+(\text{H}_2\text{O})_n$ and $\text{K}^+(\text{H}_2\text{O})_n$ were then applied for the simulation of all further spectra (see below and following sections) without further re-adjustment. In an ongoing collaboration with us, Jim Lisy is extending his infrared spectra measurements towards larger clusters. We are confident to be able to use the spectra simulations fitted here to the spectra of a few smaller clusters without further changes to assign and explain those spectra of larger clusters. Together with the simulated spectra this will then produce a much more detailed insight into the structures than hitherto possible and may lead to a better understanding of magic numbers.

8.1. $\text{M}^+(\text{H}_2\text{O})$ with $\text{M} = \text{Na}, \text{K}, \text{Cs}$

As the infrared spectra of one single water molecule with an ion, i.e. spectra of $\text{Na}(\text{H}_2\text{O})$, $\text{K}(\text{H}_2\text{O})$, and $\text{Cs}(\text{H}_2\text{O})$, respectively, are obviously fairly easy to assign both experimentally and theoretically, these peaks can be used for fitting. In table 8.2, the wave numbers found in the experiment are displayed vs. the wave numbers obtained by the theoretical model approach using the manually re-fitted frequency vs. field curves displayed in figure 8.3. As one can see, both experiment and theory are already in very good agreement. Especially the theoretical antisymmetric frequencies are within the given error margin for the experimental values, whereas the theoretical symmetric frequencies still are a little too high compared to their experimental equivalents. Again, it should be mentioned that these values were obtained using manually re-fitted curves. Hence one can assume that by using an optimisation procedure for the fitting even better results should be obtainable.

In the following sections, the results for assigning peaks and structures to the experimental data for $\text{Na}^+(\text{H}_2\text{O})_n$, $\text{K}^+(\text{H}_2\text{O})_n$, and $\text{Cs}^+(\text{H}_2\text{O})_n$, respectively, are described. For each experimental spectrum, one overall theoretical spectrum including all local minima according to their statistical weight and the most important structures contributing to this overall

	Experimental		Theoretical	
	symmetric	antisymmetric	symmetric	antisymmetric
$\text{Na}^+(\text{H}_2\text{O})$	$3634.5 \pm 5 \text{ cm}^{-1}$	$3707.0 \pm 5 \text{ cm}^{-1}$	3643.2 cm^{-1}	3707.5 cm^{-1}
$\text{K}^+(\text{H}_2\text{O})$	$3636.0 \pm 5 \text{ cm}^{-1}$	$3710.0 \pm 5 \text{ cm}^{-1}$	3644.1 cm^{-1}	3709.4 cm^{-1}
$\text{Cs}^+(\text{H}_2\text{O})$	$3635.5 \pm 5 \text{ cm}^{-1}$	$3711.5 \pm 5 \text{ cm}^{-1}$	3647.4 cm^{-1}	3716.7 cm^{-1}

Table 8.2.: Frequencies for single water molecules, experimental and theoretical (using the respective manually re-fitted frequency vs. field curves of figure 8.3).

spectrum are presented (exceptions are described in the corresponding sections). In addition the theoretical spectra and corresponding cluster structures are displayed separately. The actual fitting will not be discussed, but rather the re-fitted curves are used to deduce which structures are present in the experiments. All theoretical spectra displayed were computed applying the manually re-fitted frequency vs. field curves of figure 8.3.

8.2. Experimental infrared spectra of $\text{Na}^+(\text{H}_2\text{O})_n / n = 3 - 4$

$\text{Na}^+(\text{H}_2\text{O})_3$

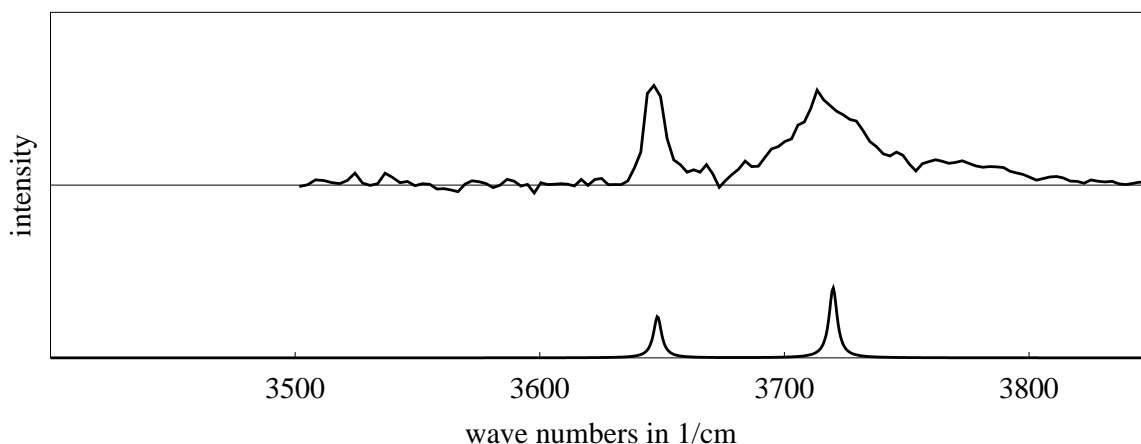


Figure 8.4.: Experimental infrared spectrum of $\text{Na}^+(\text{H}_2\text{O})_3$ (top spectrum), and computed infrared spectrum (bottom spectrum) using a re-fitted frequency vs. field curve for $\text{Na}^+(\text{H}_2\text{O})_n$ -clusters, intensity in arbitrary units

The global minimum structure of $\text{Na}^+(\text{H}_2\text{O})_3$ is trigonal planar. Hence all three water molecules are single water molecules. According to table 8.2 for single water molecules in $\text{Na}^+(\text{H}_2\text{O})$ two peaks should be found in the experimental spectrum if the assumed trigonal planar structure contributes to the spectrum. Indeed two peaks are visible in the experimental spectrum which is depicted in figure 8.4: the first peak is located at 3646 cm^{-1} whereas

the second one is found at 3713 cm^{-1} . However, according to table 8.2 these wave numbers do not seem to correspond to single water molecules, as these are found at $3634.5 \pm 5\text{ cm}^{-1}$ and $3707.0 \pm 5\text{ cm}^{-1}$ for $\text{Na}^+(\text{H}_2\text{O})$, thus suggesting that the global minimum found for $\text{Na}^+(\text{H}_2\text{O})_3$ does not give the main contribution to the experimental spectrum.

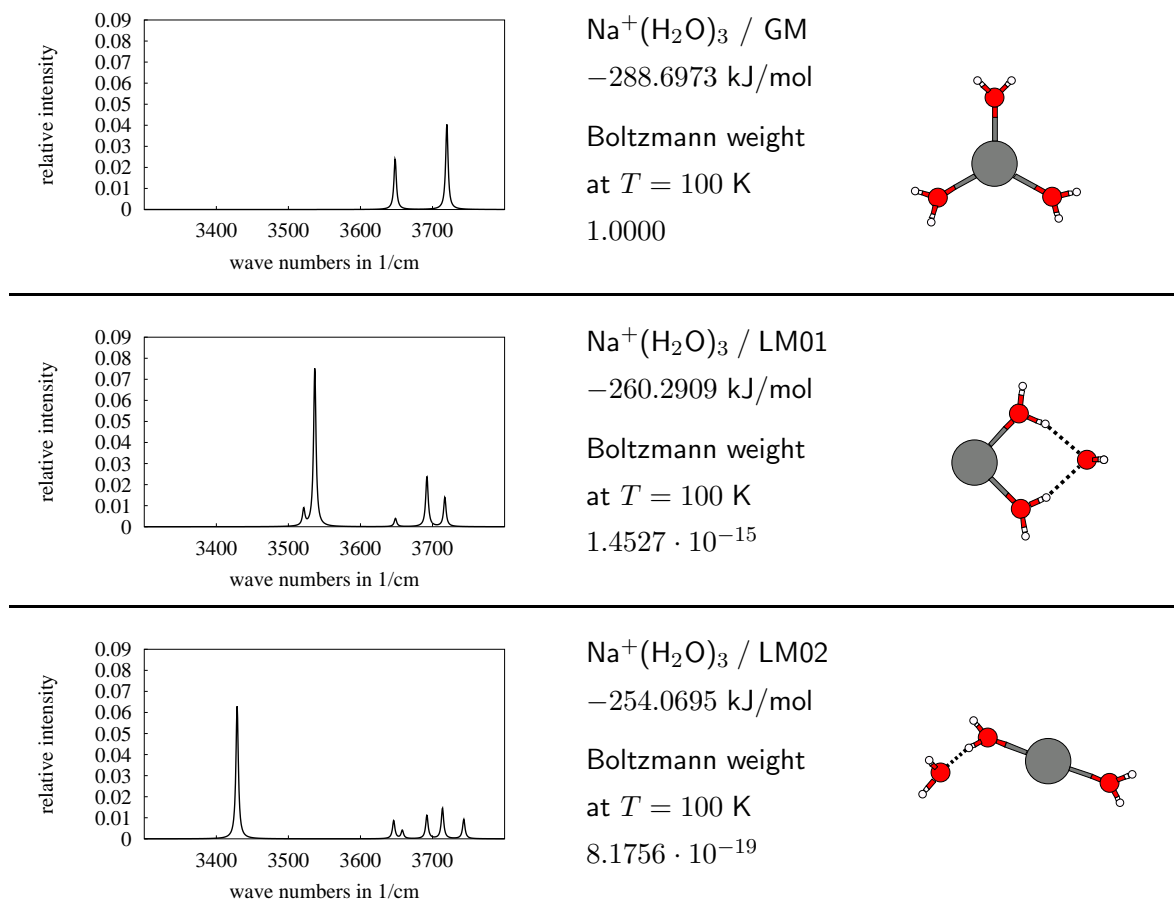


Figure 8.5.: Spectra and geometries of $\text{Na}^+(\text{H}_2\text{O})_3$ in energetical order and their Boltzmann weights

Using the re-fitted frequency vs. field curve to simulate the spectrum of the global minimum structure (as for a Boltzmann distribution of all $\text{Na}^+(\text{H}_2\text{O})_3$ structures at $T = 100\text{ K}$ all local minimum structures have a Boltzmann weight of zero) two major peaks were obtained in the theoretical spectrum: the first at 3648 cm^{-1} and the second 3720 cm^{-1} (see figure 8.5). In figure 8.5 and also all following figures in this chapter the abbreviation GM denotes the global minimum whereas LM# denote the local minimum structures, numbered in the energetical order obtained using the TIP4P/OPLS potential. Looking at the separate spectrum of the global minimum structure for $\text{Na}^+(\text{H}_2\text{O})_3$, two peaks corresponding to the three single water molecules can be observed: the first at 3647 cm^{-1} and the second at 3718 cm^{-1} . This is in excellent agreement with the experimental spectrum and suggests that indeed the structure is trigonal planar and the frequencies in the experimental spectrum are somewhat shifted to higher wave numbers compared to the experimental spectrum of $\text{Na}^+(\text{H}_2\text{O})$ (see table

8.2). Comparing the energies and corresponding Boltzmann weights of the local minimum structures with the global minimum, this again is in good agreement, as the potential energy of the best local minimum is about 28 kJ/mol worse than the potential energy of the global minimum and thus should not contribute at all to a superposed spectrum. Hence one can draw the conclusion that for the case of $\text{Na}^+(\text{H}_2\text{O})_3$ the structure observed in the experimental spectrum is trigonal planar. It should also be emphasised that the re-fitted curve for $\text{Na}^+(\text{H}_2\text{O})_n$ also correctly yields the blue-shift for peaks of single water molecules comparing the theoretical spectra of $\text{Na}^+(\text{H}_2\text{O})$ and $\text{Na}^+(\text{H}_2\text{O})_3$.

$\text{Na}^+(\text{H}_2\text{O})_4$

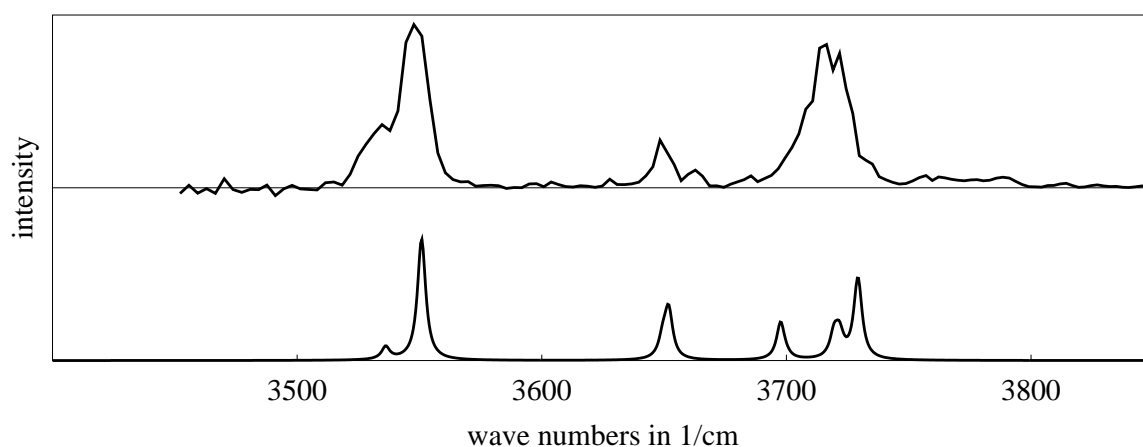


Figure 8.6.: Experimental infrared spectrum of $\text{Na}^+(\text{H}_2\text{O})_4$ (top spectrum), and superposed theoretical infrared spectrum (bottom spectrum) of structures GM and LM01 (see figure 8.7) with respective Boltzmann weights of 1.0 (see text), using the manually re-fitted frequency vs. field curve for $\text{Na}^+(\text{H}_2\text{O})_n$ -clusters, intensity in arbitrary units

Similar to the global minimum structure of $\text{Na}^+(\text{H}_2\text{O})_3$, the global minimum structure of $\text{Na}^+(\text{H}_2\text{O})_4$ contains four equivalent single water molecules which compose a tetrahedron. Hence one should expect two peaks in the experimental spectrum comparable to the peaks found in the experimental spectrum of $\text{Na}^+(\text{H}_2\text{O})_3$, i.e. peaks corresponding to single water molecules exhibiting a small blue-shift. However in the experimental spectrum more than these two peaks are observable (see figure 8.6). The peaks for the experimental spectrum are found at 3531 cm^{-1} , 3547 cm^{-1} , 3651 cm^{-1} , 3659 cm^{-1} , 3682 cm^{-1} , 3716 cm^{-1} , and 3721 cm^{-1} , respectively. Two of the four peaks found at $3651\text{ cm}^{-1}/3659\text{ cm}^{-1}$ and at $3716\text{ cm}^{-1}/3721\text{ cm}^{-1}$ should correspond to single water molecules according to the results obtained for the experimental spectra of $\text{Na}^+(\text{H}_2\text{O})$ and $\text{Na}^+(\text{H}_2\text{O})_3$. In case two of the peaks do correspond to single water molecules, they would in any case also experience a small blue-shift as already observed for the spectrum of $\text{Na}^+(\text{H}_2\text{O})_3$, hence showing consistency.

However, it has yet to be clarified which of the four peaks can actually be assigned to the single water molecules. The other peaks visible in the experimental spectrum obviously have to correspond to other structures (in theory according to the Boltzmann distribution of the global and local minimum structures, see figure 8.7).

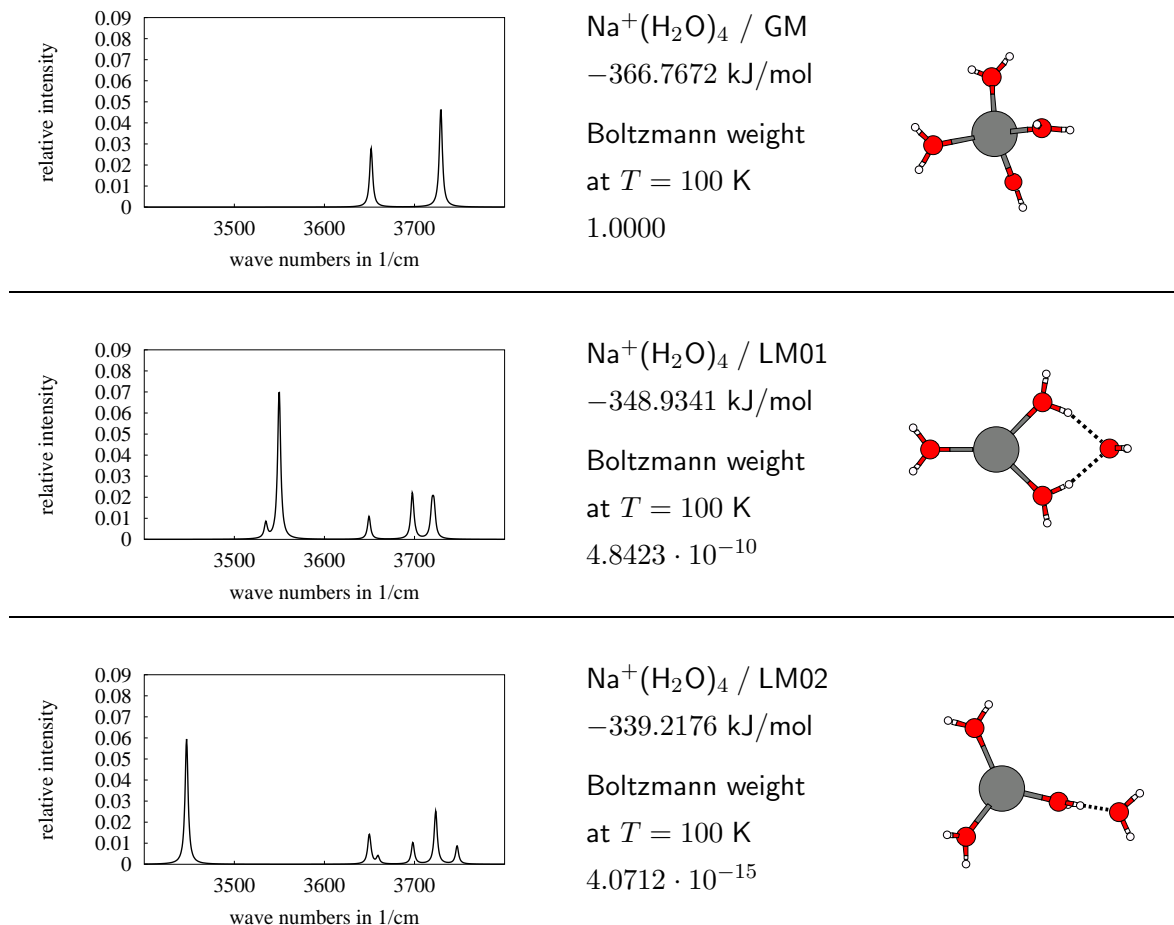


Figure 8.7.: Spectra and geometries of $\text{Na}^+(\text{H}_2\text{O})_4$ in energetical order and their Boltzmann weights

However, according to the Boltzmann weights of the different structures (see figure 8.7), only the peaks of the tetrahedron should be visible in the experimental spectrum which obviously is incorrect. When using the TIP4P/OPLS potential for global geometry optimisation of alkali cation microhydration clusters, one has to bear in mind that although the energetical order of the obtained structures and the obtained structures themselves are produced correctly with high probability, energies differences are sometimes incorrect [36, 57]. Errors in energy differences were found to be larger for smaller cluster structures while it can be assumed that for larger systems they become smaller, as TIP4P/OPLS was originally designed for larger systems. Hence, superposed theoretical spectra (using the Boltzmann weights obtained with TIP4P/OPLS potential energies) not always contain contributions from all structures found in the experiment. Hence as a first step one should successively check the simulated spectra of

all local minimum structures in full intensity and compare them to the experiment. However, this way only peak positions can be compared, not intensities. Therefore, one should fully discard the Boltzmann distribution obtained from the TIP4P/OPLS energies and assign new Boltzmann weights according to the intensities of the peaks found in the experiment. Thus, converting adjusted Boltzmann weights back to energy differences, one also gets an impression of the errors in the potential energies produced by TIP4P/OPLS. In the case of $\text{Na}^+(\text{H}_2\text{O})_n$ so far only the experimental spectra of $\text{Na}^+(\text{H}_2\text{O})_3$ and $\text{Na}^+(\text{H}_2\text{O})_4$ were available for re-fitting the frequency vs. field curve. The experimental spectra only show peaks in the higher wave number regions, hence only these regions can be incorporated in the fit, thus so far neglecting other wave number regions, especially those which are typical for higher coordinated water molecules. For the cases of $\text{K}^+(\text{H}_2\text{O})_n$ and $\text{Cs}^+(\text{H}_2\text{O})_n$ it was found that fitting the lower wave number regions also had a large impact on the intensity of the peaks in higher wave number regions. As mentioned above, discarding the current Boltzmann weights (see figure 8.7) and assigning each local minimum a Boltzmann weight of one would only be a first step as that way only peak positions can be assigned whereas it would be more logical to also re-adjust the Boltzmann weights according to the intensities in the spectrum. However, the intensities of the peaks in the wave number region of $< 3600 \text{ cm}^{-1}$ are most probably produced incorrectly. Hence, instead of assigning new Boltzmann weights according to the intensities of the peaks to the structures for the case of $\text{Na}^+(\text{H}_2\text{O})_4$, the spectra of GM and LM01 were both computed using a Boltzmann weight of 1.0 (see figure 8.6). In figure 8.7 the most important structures for $\text{Na}^+(\text{H}_2\text{O})_4$ are depicted. Only the top two structures, namely GM and LM01, display peaks in the wave number regions also occupied in the experiment, whereas the structure LM02 features two peaks which are beyond these wave number regions. Under the assumption that not all wave number regions are yet fitted correctly due to the lack of sufficient experimental data, structure LM02 will not be used in the superposed spectrum, although its actual Boltzmann weight according to the experiment (not theory) might be significant. Hence only the structures GM and LM01 are used for peak assignment in the experimental spectrum.

In the theoretical spectrum the structure GM exhibits two peaks, the first at 3651 cm^{-1} and the second at 3729 cm^{-1} . Both peaks correspond to the four single water molecules. The peaks of the single water molecules in the theoretical spectrum of structure LM01 are found at 3649 cm^{-1} and 3721 cm^{-1} , respectively. The spectrum of LM01 also shows two other peaks in this region, namely 3649 cm^{-1} and 3719 cm^{-1} , corresponding to the AA molecule. Two peaks, 3534 cm^{-1} and 3549 cm^{-1} , correlate with the DA molecules in LM01, whereas the peak found at 3697 cm^{-1} arises from the dangling OH. When comparing the peaks found in the experimental spectrum with the ones obtained for the theoretical spectrum of LM01, the DA molecules are the most easy to assign: $3534/3549 \text{ cm}^{-1}$ for the theoretical spectrum and $3531/3547 \text{ cm}^{-1}$, respectively, for the experimental spectrum, as these values are already

in very good agreement. When looking at the frequencies of the single water molecules, there is a slight difference in the values between the two theoretical spectra GM and LM01 which however is negligible: $3651/3729\text{ cm}^{-1}$ and $3649/3721\text{ cm}^{-1}$. There exists a set of similar peaks in the experimental spectrum $3651/3659\text{ cm}^{-1}$ and $3716/3721\text{ cm}^{-1}$. However, in this region there are also peaks corresponding to the AA molecule of the structure LM01 assumed to be present: 3649 cm^{-1} and 3719 cm^{-1} . In other words the peaks are too close together to presently allow an unambiguous assignment. Nevertheless, these two structures can already be assigned with certainty to the experimental spectrum which is a substantial progress.

8.3. Experimental infrared spectra of $\text{K}^+(\text{H}_2\text{O})_n / n = 3 - 5$

$\text{K}^+(\text{H}_2\text{O})_3$

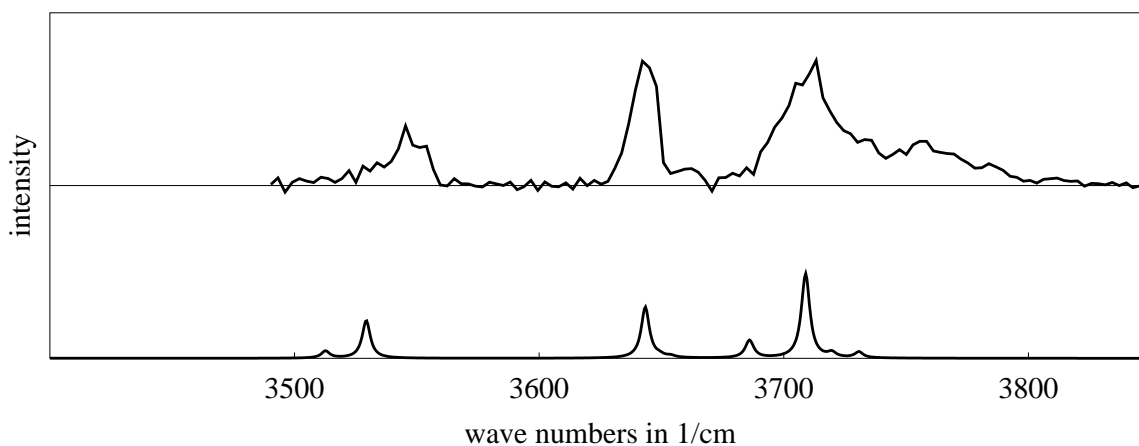


Figure 8.8.: Experimental infrared spectrum of $\text{K}^+(\text{H}_2\text{O})_3$ (top spectrum), and superposed theoretical infrared spectrum (bottom spectrum) of structures GM, LM01, and partly LM02 (see figure 8.9) with Boltzmann weights of 1.0, 0.3, and 0.2, respectively (see text), using the manually re-fitted frequency vs. field curve for $\text{K}^+(\text{H}_2\text{O})_n$ -clusters, intensity in arbitrary units

Unlike the experimental spectrum of $\text{Na}^+(\text{H}_2\text{O})_3$ which exhibited merely two peaks corresponding to single water molecules thus showing only one structural species, the spectrum of $\text{K}^+(\text{H}_2\text{O})_3$ shows six important peaks, however very broad, thus indicating the presence of more than just one structure (see figure 8.8): 3545 cm^{-1} , 3642 cm^{-1} , 3656 cm^{-1} , 3710 cm^{-1} , 3730 cm^{-1} , and 3752 cm^{-1} . Whereas the experimental spectrum clearly shows the presence of more than one species, the superposed theoretical spectrum according to the Boltzmann weights given in figure 8.9 would only exhibit two distinct peaks in the region of single water molecules, corresponding to the global minimum structure which is trigonal planar, thus consisting of three equivalent single water molecules. So again the question arises which of the other local minimum structures participate in the experimental spectrum although according to their Boltzmann weight obtained from the TIP4P/OPLS energies they should not. Similar

to the case of $\text{Na}^+(\text{H}_2\text{O})_4$, only the spectra corresponding to the structures GM and LM01 can be fully taken into account, as for LM02 the wave number region in which the largest peak is found outside of the fitted wave number region for $\text{K}^+(\text{H}_2\text{O})_n$ (see figure 8.9). However, this structure cannot be excluded totally as in the experimental spectrum there is a broad band of peaks in the range of $3700 \text{ cm}^{-1} - 3800 \text{ cm}^{-1}$ which would fit all other peaks found in the theoretical spectrum of LM02. Hence this structure will partly be taken into account such that only the fitted wave number region around 3700 cm^{-1} of this spectrum is displayed in figure 8.8, thus excluding the largest peak for LM02. Nevertheless, in contrast to $\text{Na}^+(\text{H}_2\text{O})_n$, the wave number region which could be fitted for $\text{K}^+(\text{H}_2\text{O})_n$ is somewhat broader. Hence, one can assume with great certainty that the intensities of peaks in the region of $3500 \text{ cm}^{-1} - 3800 \text{ cm}^{-1}$ are reproduced correctly. It was found that Boltzmann weights for GM, LM01, and LM02 of the rate $1.0 : 0.3 : 0.2$, respectively, seem to best reproduce the intensity ratio in the experimental spectrum (see figure 8.8). This ratio would decrease the energy difference between GM and LM01 from $\Delta E = 12 \text{ kJ/mol}$ to $\Delta E = 1 \text{ kJ/mol}$, which would make both structures close to iso-energetic at 100 K. The Boltzmann weight for LM02 was arbitrarily chosen to be 0.2 as to still fit the energetical order obtained by TIP4P/OPLS and because this structures seems to be very close in energy to LM01. However, as this Boltzmann weight is chosen arbitrarily, the structure shall not be compared to GM.

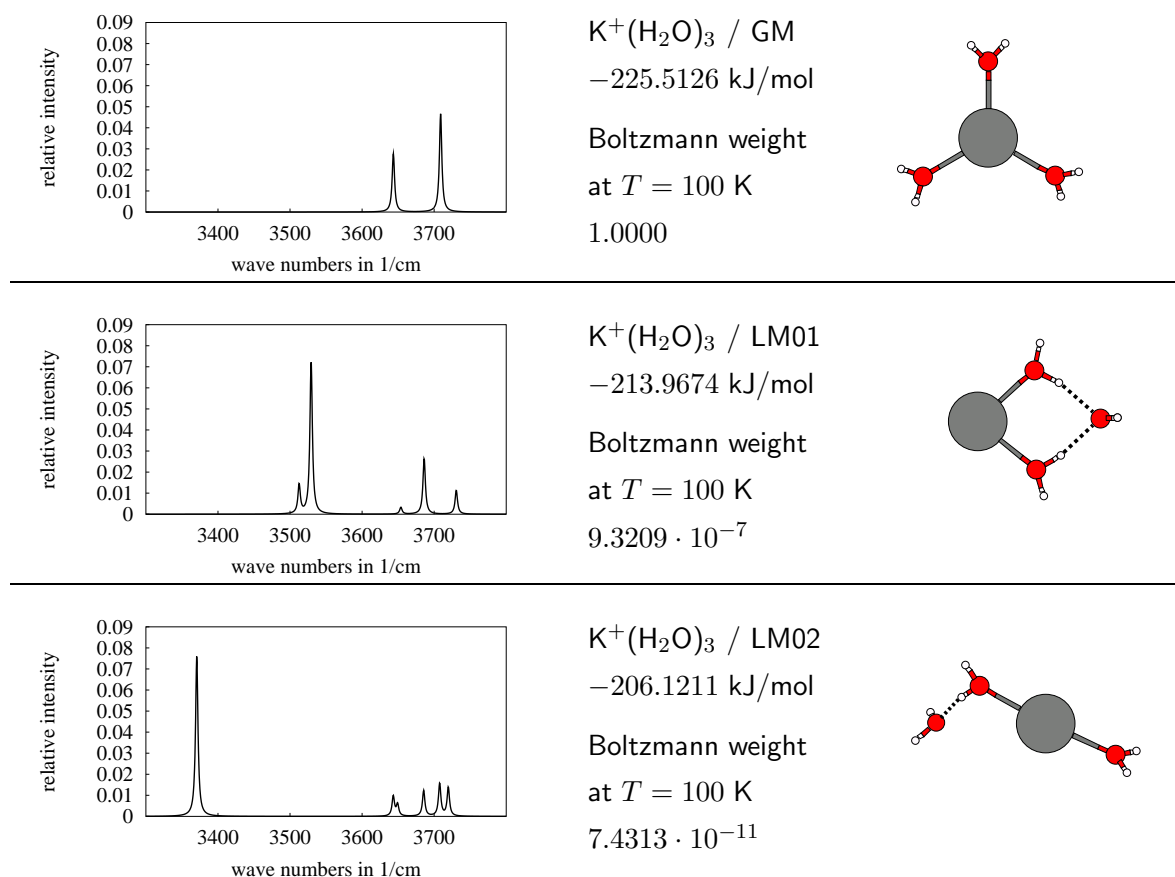


Figure 8.9.: Spectra and geometries of $\text{K}^+(\text{H}_2\text{O})_3$ in energetical order and their Boltzmann weights

Peaks contributed by the structure GM (see figure 8.9) can be found at 3643 cm^{-1} and 3709 cm^{-1} , respectively. Looking at structure LM01, five important peaks are observable: 3512 cm^{-1} (DA), 3529 cm^{-1} (DA), 3653 cm^{-1} (AA), 3686 cm^{-1} (dangling OH from DA), and 3730 cm^{-1} (dangling OH from AA). Assuming that the fitted frequency vs. field curve is producing almost correct spectral data, the two peaks of the single water molecules would be easy to assign: $3643/3709\text{ cm}^{-1}$ (theoretical) vs. $3642/3710\text{ cm}^{-1}$ (experimental). As for the peaks of structure LM01 it becomes more difficult. The peaks corresponding to the AA molecule $3653/3730\text{ cm}^{-1}$ (theoretical) seem to match $3656/3730\text{ cm}^{-1}$ (experimental), whereas the peaks found in the experimental spectrum at 3545 cm^{-1} and 3656 cm^{-1} could correspond to the DA of LM01, which shows peaks at 3512 cm^{-1} and 3529 cm^{-1} . This shift would indicate that the curve is not fitted correctly for that region or that even an altogether different structure contributes peaks to this wave number region in the spectrum. It is assumed that both cases are true, i.e. that indeed the peaks found at 3545 cm^{-1} and 3656 cm^{-1} in the experimental spectrum can be assigned to the DA, as this would be consistent with the results for $\text{K}^+(\text{H}_2\text{O})_4$ (see following section), but also other structures are present in the spectrum also contributing peaks in this wave number region, as for example structure LM02. The peak found at 3370 cm^{-1} may well move towards the region around 3500 cm^{-1} after fine-tuning the frequency vs. field curve once more experimental data is available. Nevertheless, again two structures could be assigned with great certainty which again is a great progress.

$\text{K}^+(\text{H}_2\text{O})_4$

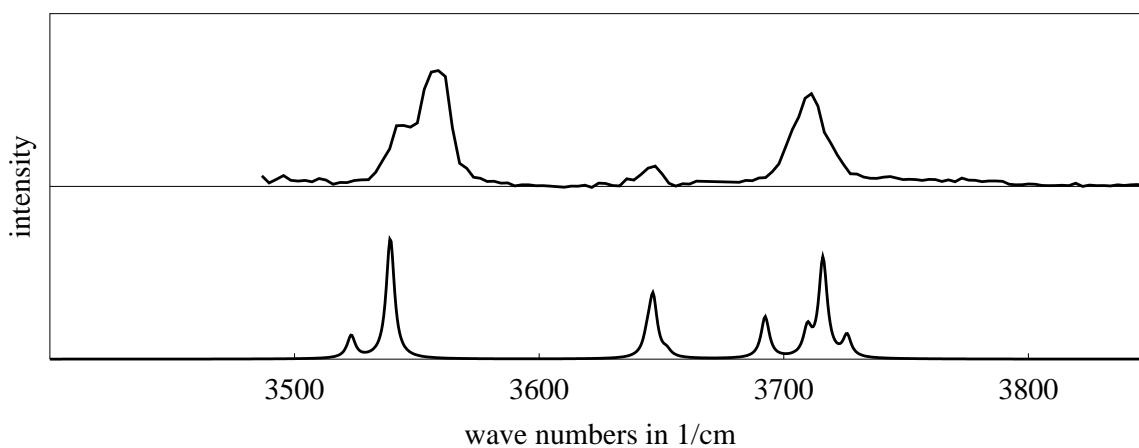


Figure 8.10.: Experimental infrared spectrum of $\text{K}^+(\text{H}_2\text{O})_4$ (top spectrum), and superposed theoretical infrared spectrum (bottom spectrum) of structures GM, LM01, and LM02 (see figure 8.11) with respective Boltzmann weights of 1.0 (see text), using the manually re-fitted frequency vs. field curve for $\text{K}^+(\text{H}_2\text{O})_n$ -clusters, intensity in arbitrary units

The experimental spectrum of $\text{K}^+(\text{H}_2\text{O})_4$ (see figure 8.10) looks very similar to that of $\text{Na}^+(\text{H}_2\text{O})_4$ (see figure 8.6). Therefore the structures present might be similar to those present for the case of $\text{Na}^+(\text{H}_2\text{O})_4$. The important peaks in the experimental spectrum can

be found at: 3541 cm^{-1} , 3558 cm^{-1} , 3644 cm^{-1} , and 3711 cm^{-1} . Comparing the experimental values with the theoretical ones for the three most prominent structures (see figure 8.11), these structures seem to be indeed responsible for the experimental spectrum. The part of the frequency vs. field curve correlating with the lower wave number regions of DA peaks could be readjusted further to produce even better quantitative agreement. Judging from the experimental spectrum of $K^+(H_2O)_4$ one should assume a tetrahedron and a third (3+1) structure to be present in the experiment as for the case of $Na^+(H_2O)_4$. The three most important structures found by global geometry optimisation (see figure 8.11) are firstly, a tetrahedron, secondly a quadratic planar structure, and thirdly a (3 + 1) geometry.

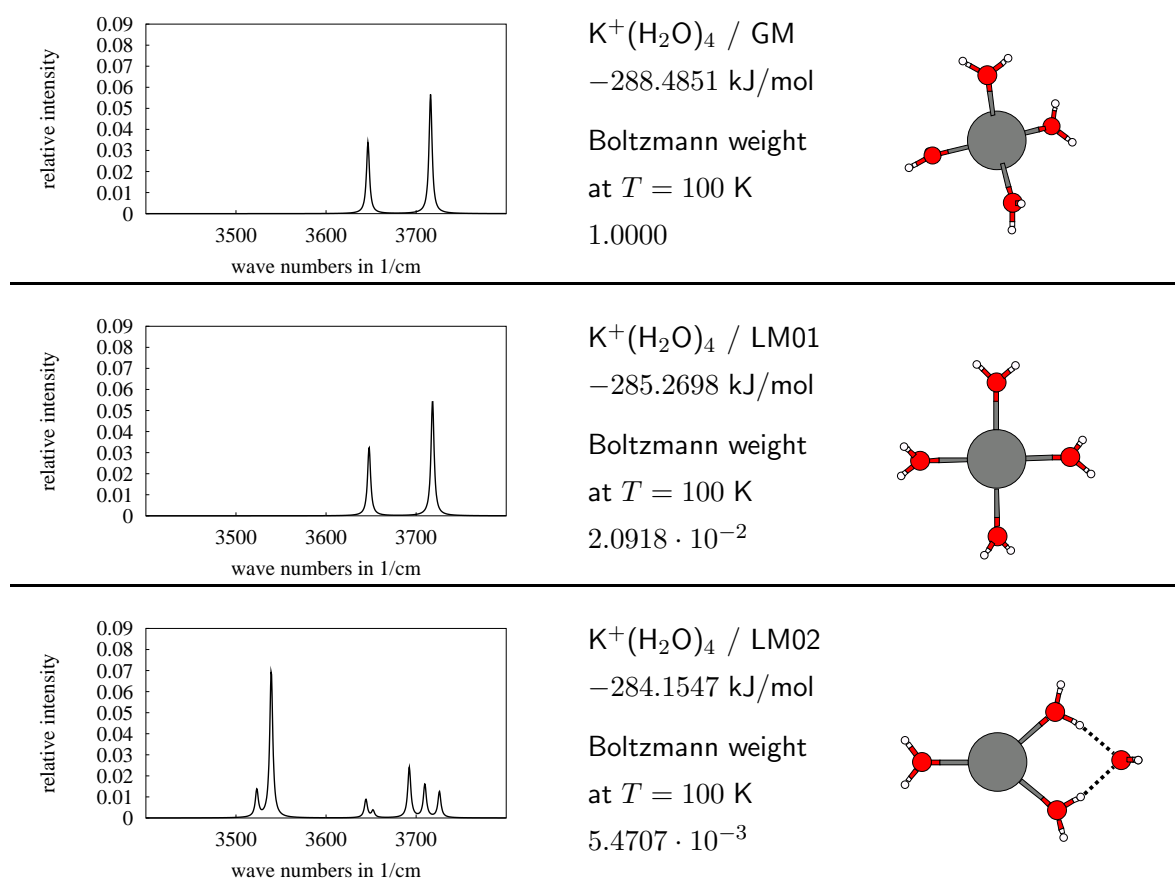


Figure 8.11.: Spectra and geometries of $K^+(H_2O)_4$ in energetical order and their Boltzmann weights

As both the tetrahedron and the planar structure consist only of equivalent single water molecules they result in almost identical peaks: $3646/3716\text{ cm}^{-1}$ for the tetrahedron and $3647/3718\text{ cm}^{-1}$ for the quadratic planar structure, respectively. As for the (3 + 1) structure seven important peaks are observed: 3523 cm^{-1} (DA), 3539 cm^{-1} (DA), 3644 cm^{-1} (single), 3652 cm^{-1} (AA), 3692 cm^{-1} (dangling OH of DA), 3709 cm^{-1} (single), and 3725 cm^{-1} (AA). Hence, as already found for the case of $Na^+(H_2O)_4$, the peaks found in the experimental

spectrum can respectively be assigned to the single water molecules found in GM, LM01 and LM02, as well as to the DA and AA molecules in LM02. However, again the Boltzmann weights obtained when using the TIP4P/OPLS energies had to be discarded for reproducing the experimental spectrum. As both structures GM and LM01 contribute to the same peaks it is impossible to deduce Boltzmann weights for them from the experimental spectrum, hence both structures were assigned a Boltzmann weight of 1.0 (see figure 8.10). As already mentioned in the previous section, it is assumed that the intensities of the peaks in the simulated spectra are reproduced correctly within the region of $3500\text{ cm}^{-1} - 3800\text{ cm}^{-1}$. To best reproduce the intensity ratio of the peaks in the experimental spectrum, structure LM02 was also assigned a Boltzmann weight of 1.0 (see also figure 8.10). This completely overrides any energetical differences between the structures and makes them iso-energetic. Nevertheless, the decrease in energy difference is less staggering than for the case of $\text{K}^+(\text{H}_2\text{O})_3$, the maximum decrease is about 6 kJ/mol .

$\text{K}^+(\text{H}_2\text{O})_5$

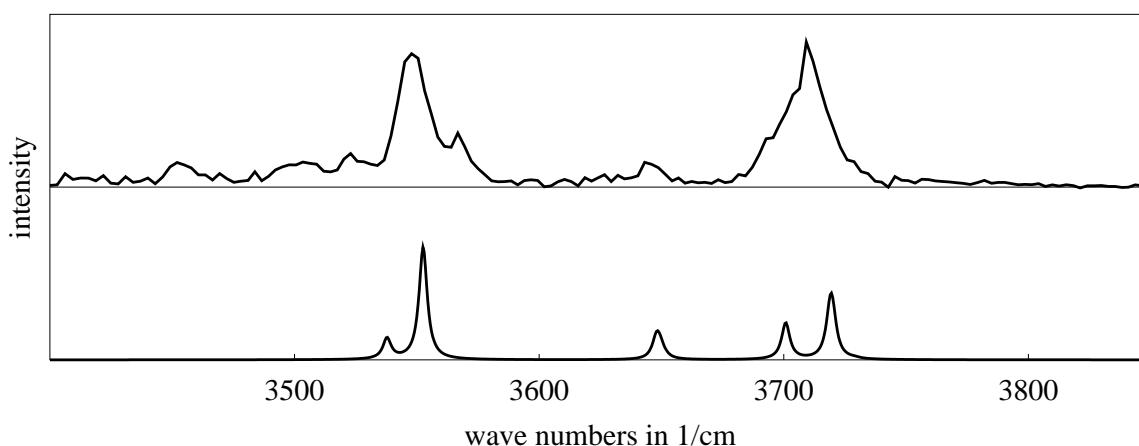


Figure 8.12.: Experimental infrared spectrum of $\text{K}^+(\text{H}_2\text{O})_5$ (top spectrum), and computed infrared spectrum (bottom spectrum) using the manually re-fitted frequency vs. field curve for $\text{K}^+(\text{H}_2\text{O})_n$ -clusters, intensity in arbitrary units

Comparing the experimental spectra of $\text{K}^+(\text{H}_2\text{O})_4$ and $\text{K}^+(\text{H}_2\text{O})_5$, one observes that they are very similar (see figures 8.10 and 8.12, respectively). Hence it can be assumed that even now five water molecules surround the ion, the structures of $\text{K}^+(\text{H}_2\text{O})_5$ have to be similar to those of $\text{K}^+(\text{H}_2\text{O})_4$. And indeed, when looking at the structures for $\text{K}^+(\text{H}_2\text{O})_5$ (see figure 8.13) one finds that the global minimum corresponds to a (3+2) structure and the first local minimum to a tetragonal pyramid. The peaks for the (3 + 2) structure can be observed at: 3537 cm^{-1} (DA), 3552 cm^{-1} (DA), 3649 cm^{-1} (single), 3650 cm^{-1} (AA),

3700 cm^{-1} (dangling OH of DA), 3719 cm^{-1} (single), and 3720 cm^{-1} (AA). The tetragonal pyramid contributes at: 3652 cm^{-1} and 3728 cm^{-1} . The experimental spectrum shows the following peaks: 3452 cm^{-1} , 3503 cm^{-1} , 3522 cm^{-1} , 3547 cm^{-1} , 3564 cm^{-1} , 3645 cm^{-1} , and 3709 cm^{-1} . Comparing these values leads to the conclusion that indeed the most important peaks in the experimental spectrum correspond to the structure GM and possibly also to the structures LM01. However, as the peaks for the single molecules of both structures contribute to the same peaks the actual energy difference cannot be evaluated according to the experimental peak intensities as for some other cases.

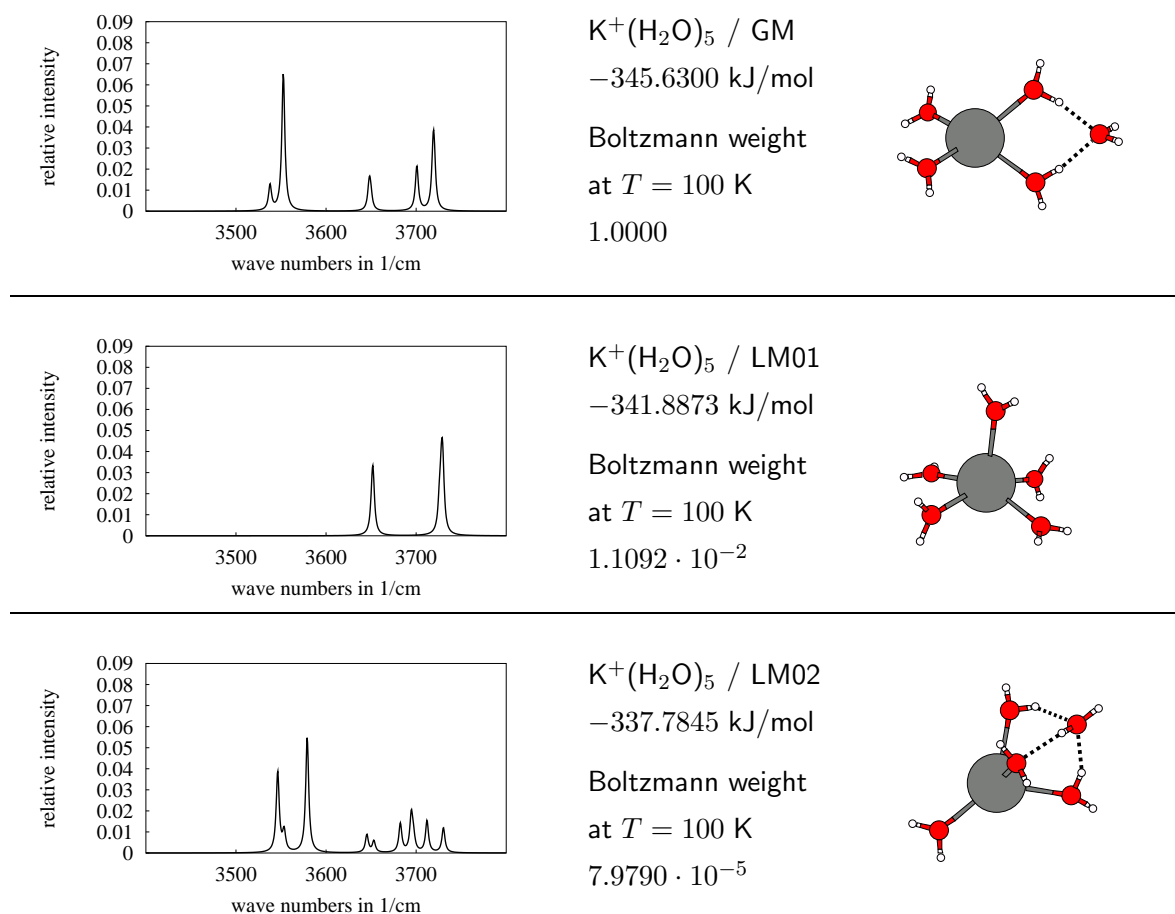


Figure 8.13.: Spectra and geometries of $\text{K}^+(\text{H}_2\text{O})_5$ in energetical order and their Boltzmann weights

8.4. Experimental infrared spectra of $\text{Cs}^+(\text{H}_2\text{O})_n / n = 3 - 6, 8$

$\text{Cs}^+(\text{H}_2\text{O})_3$

Surprisingly the experimental spectrum of $\text{Cs}^+(\text{H}_2\text{O})_3$ shows different peaks compared to both $\text{Na}^+(\text{H}_2\text{O})_3$ and $\text{K}^+(\text{H}_2\text{O})_3$ as no peaks possibly corresponding to any single water

molecule are visible (see figure 8.14), provided that there is no strong shift compared to the values given in table 8.2. Instead peaks are found at: 3512 cm^{-1} , 3529 cm^{-1} , and 3704 cm^{-1} . While the peak at 3704 cm^{-1} might still correspond to the asymmetric stretch frequency of a single water molecule, the peak for the symmetric frequency would be totally missing. Looking at the energetically most favourable structures obtained from the global optimisation and their corresponding spectra, at first none of the most prominent structure/spectra seem to fit the experimental spectrum (see figure 8.15). However, it appears that a low-lying local minimum does fit (see structure LM05 in figure 8.15). The structure contributes to peaks at: 3515 cm^{-1} (AA), 3546 cm^{-1} (AA), 3640 cm^{-1} (DA), and 3699 cm^{-1} (dangling OH from DA). Comparing these peaks with the experimental values shows fairly good agreement: 3512 cm^{-1} (experimental) and 3515 cm^{-1} (AA, theoretical); 3529 cm^{-1} (experimental) and 3546 cm^{-1} (AA, theoretical); 3704 cm^{-1} and 3699 cm^{-1} (dangling OH from DA, theoretical). The theoretically found peak at 3640 cm^{-1} (DA) does not seem to have an experimental equivalent, although there seems to be a small elevation in the experimental spectrum in this region. In contrast to the spectral data obtained for $\text{Na}^+(\text{H}_2\text{O})_3$ and $\text{K}^+(\text{H}_2\text{O})_3$, the peaks corresponding to the AA molecules have shifted considerably towards lower wave numbers for $\text{Cs}^+(\text{H}_2\text{O})_3$.

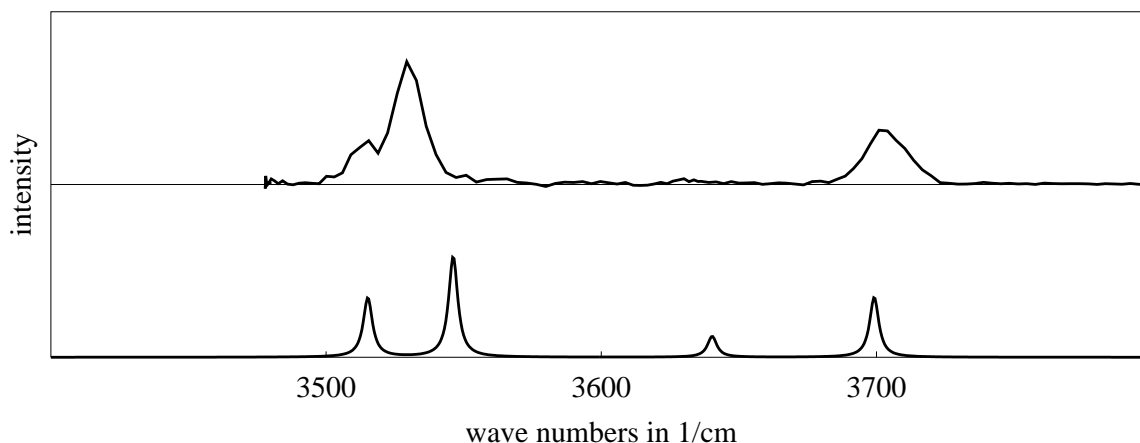


Figure 8.14. Experimental infrared spectrum of $\text{Cs}^+(\text{H}_2\text{O})_3$ (top spectrum), and computed infrared spectrum (bottom spectrum) using the manually re-fitted frequency vs. field curve for $\text{Cs}^+(\text{H}_2\text{O})_n$ -clusters and the structure LM05 from figure 8.15 as main contributing structure, which has been re-assigned a Boltzmann weight of 1.0 (see text). Intensity in arbitrary units.

At first it might seem unreasonable that instead of energetically more favourable structures only one of the energetically worse local minimum structures solely can be assigned to the experimental spectrum. However, this is not at all unreasonable. As already mentioned in the previous sections the energy differences produced by TIP4P/OPLS can be incorrect, especially for smaller cases, as TIP4P/OPLS was designed for larger systems and hence is better in reproducing correct energy differences for the latter.

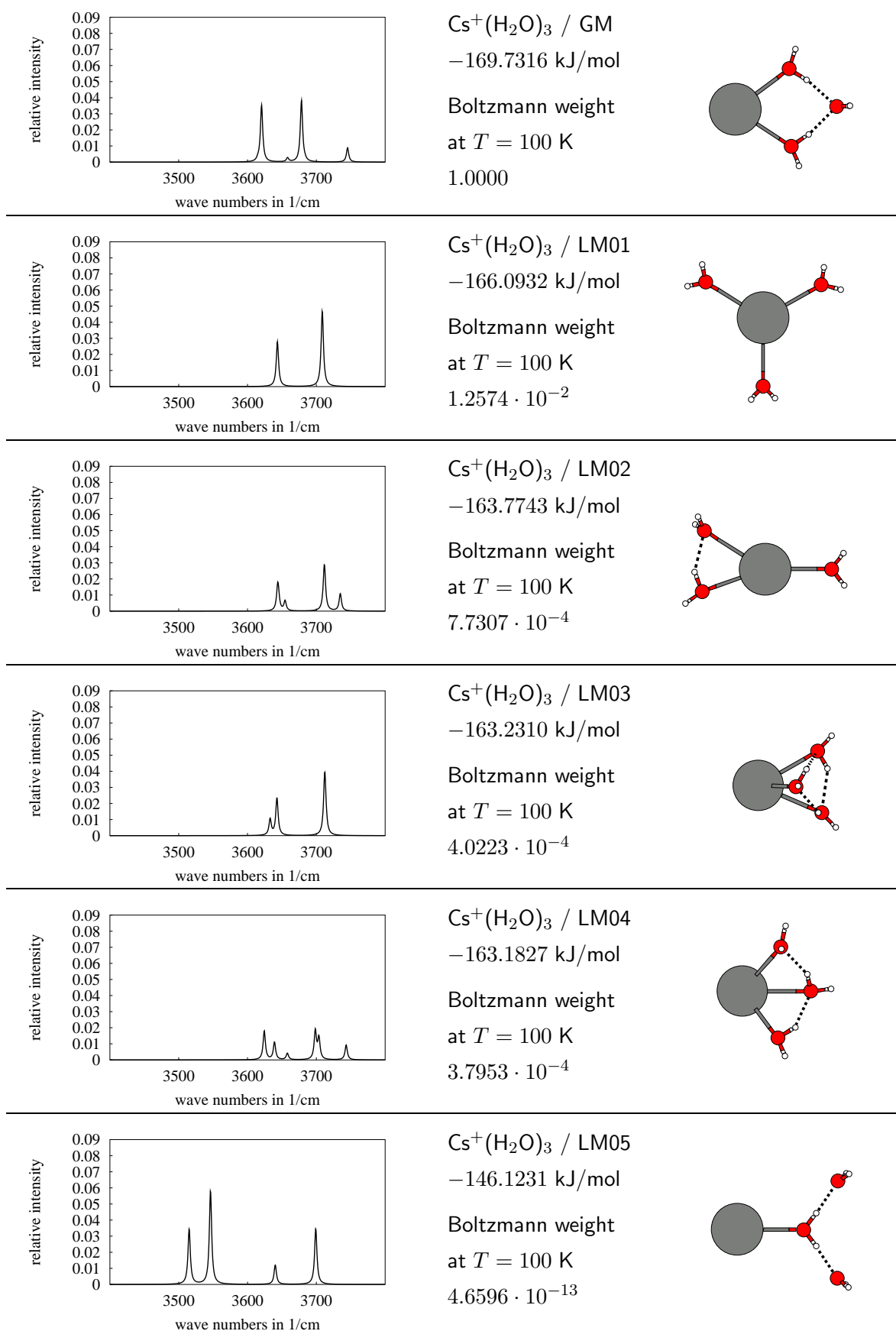


Figure 8.15.: Spectra and geometries of $\text{Cs}^+(\text{H}_2\text{O})_4$ in energetical order and their Boltzmann weights

Hence the structure of LM05 might not be as bad in energy as it first appears. Also entropy effects have to be taken into account as the experiment is performed above 0 K, thus resulting in a possible energetical reordering of the cluster structures. And indeed it seems that LM05 has far more possibilities to arrange its water molecules without suffering energy penalties, for example the two attached (A) water molecules have considerable rotational freedom. While the moieties in the other clusters also can move around the central ion without dissociating, even small rotations would lead to an increase in the potential energy.

$\text{Cs}^+(\text{H}_2\text{O})_4$

As already stated in section 4.4, small $\text{Cs}^+(\text{H}_2\text{O})_n$ clusters behave differently from $\text{Na}^+(\text{H}_2\text{O})_n$ and $\text{K}^+(\text{H}_2\text{O})_n$ clusters by their tendency to building rings right from the start. Looking at the experimental spectrum of $\text{Cs}^+(\text{H}_2\text{O})_4$, three major peaks can be observed (see figure 8.16), which are not in the wave number regions of single water molecules (compare values given for $\text{Cs}^+(\text{H}_2\text{O})$ in table 8.2): 3504 cm^{-1} , 3549 cm^{-1} , and 3702 cm^{-1} . As only three peaks are present in the experimental spectrum one can make a first assumption that either only one structure or a couple of very similar structures contribute to the spectrum.

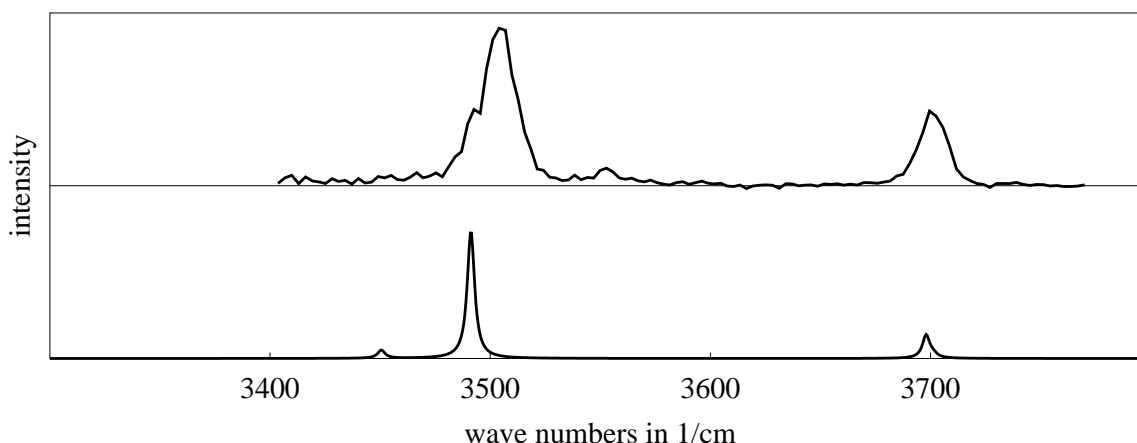


Figure 8.16.: Experimental infrared spectrum of $\text{Cs}^+(\text{H}_2\text{O})_4$ (top spectrum), and computed infrared spectrum (bottom spectrum) using the manually re-fitted frequency vs. field curve for $\text{Cs}^+(\text{H}_2\text{O})_n$ -clusters, intensity in arbitrary units

Looking at the global optimisation structures (see figure 8.17) one finds that the most prominent structures are not very similar. Looking at the peaks of structure GM – 3450 cm^{-1} (DA), 3491 cm^{-1} (DA), and 3698 cm^{-1} (dangling OH from DA), respectively – and comparing these values to those of the experimental spectrum one finds very good agreement for two peaks: 3491 cm^{-1} (theoretical, DA) vs. 3549 cm^{-1} (experimental) and 3491 cm^{-1} (theoretical, DA) vs. 3702 cm^{-1} (experimental). The third peak in the theoretical spectrum seems to be on the wrong side of the DA peak at 3491 cm^{-1} .

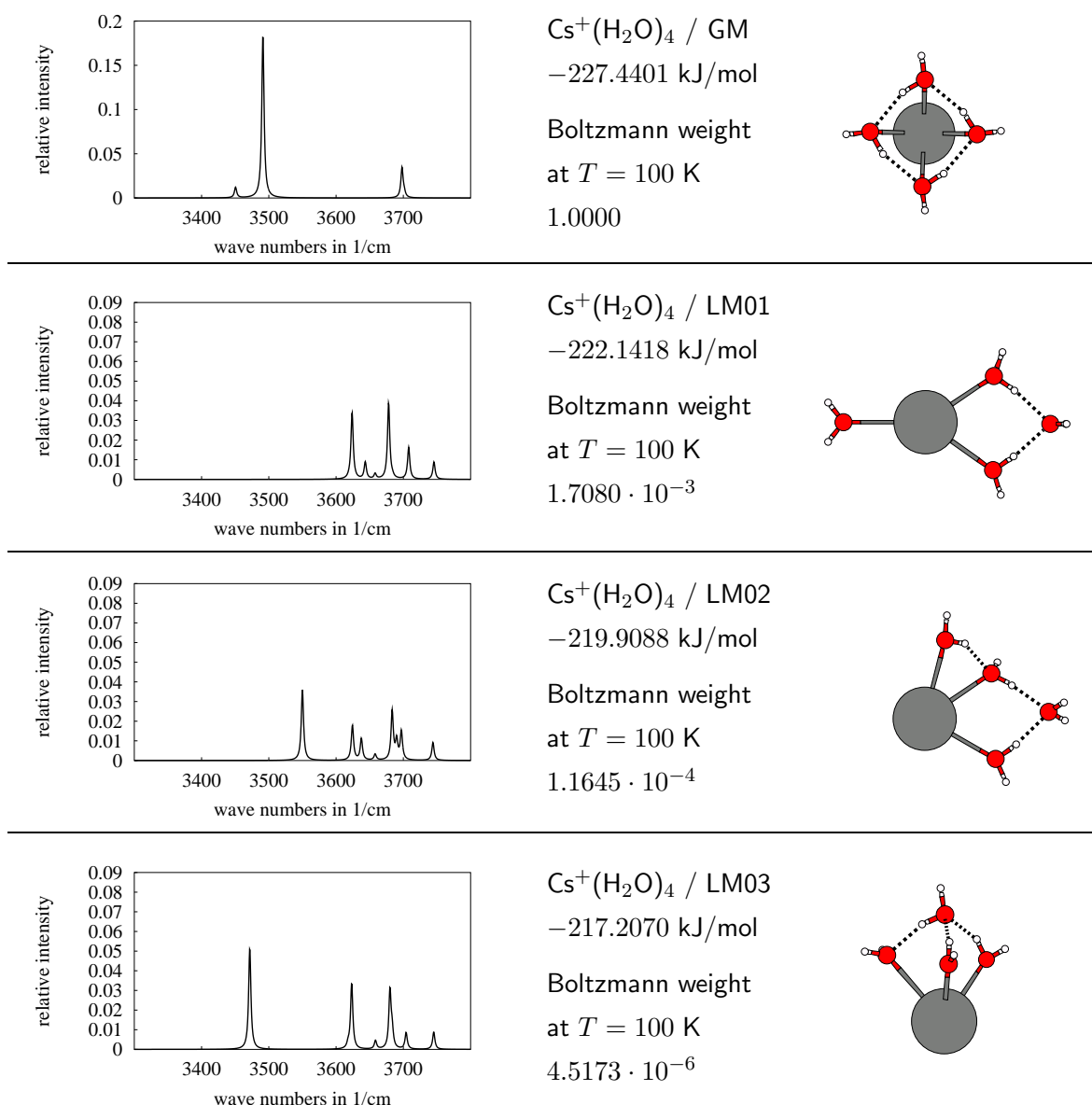


Figure 8.17.: Spectra and geometries of $\text{Cs}^+(\text{H}_2\text{O})_4$ in energetical order and their Boltzmann weights

As the model for computing theoretical infrared spectra is a very simple though still potent model, it might still suffer from some shortcomings and hence one can assume that the peaks 3491 cm^{-1} (theoretical, DA) vs. 3549 cm^{-1} (experimental) actually are equivalent. Furthermore, the spectra of all the LM# structures in figure 8.17 exhibit many more peaks than visible in the experimental spectrum. It is very unlikely that the spectra simulation model produces qualitative errors in this respect. Hence the assumption that only one structure is present in the experimental spectrum seems to be correct and it also seems to prove that at least for $\text{Cs}^+(\text{H}_2\text{O})_4$ the global optimisation results obtained using the TIP4P/OPLS potential seem to be correct.

Cs⁺(H₂O)₅

Comparing the experimental spectra of Cs⁺(H₂O)₄ and Cs⁺(H₂O)₅ one observes that the three prominent peaks already found for Cs⁺(H₂O)₄ are also present for the case of Cs⁺(H₂O)₅, however the bands are broader and a couple of more peaks are visible (see figure 8.18): 3395 cm⁻¹, 3460 cm⁻¹, 3506 cm⁻¹, 3546 cm⁻¹, 3585 cm⁻¹, and 3697 cm⁻¹.

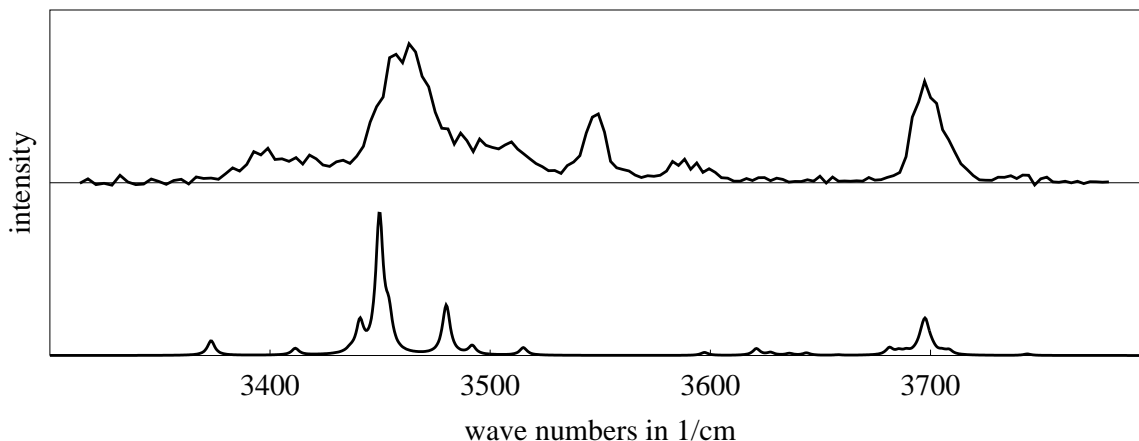


Figure 8.18.: Experimental infrared spectrum of Cs⁺(H₂O)₅ (top spectrum), and computed infrared spectrum (bottom spectrum) using the manually re-fitted frequency vs. field curve for Cs⁺(H₂O)_n-clusters and re-assigned Boltzmann weights (see text). Intensity in arbitrary units.

Bearing in mind the results for Cs⁺(H₂O)₄ and looking at the structures for Cs⁺(H₂O)₅ (see figure 8.19) one finds that the global minimum has the structure of a five-membered ring attached to the central ion which should indeed yield very similar peaks as the four-membered ring found for Cs⁺(H₂O)₄ (see figure 8.17). Comparing the peaks of Cs⁺(H₂O)₅ (GM) of the theoretical spectrum – 3411 cm⁻¹ (DA), 3449 cm⁻¹ (DA), and 3697 cm⁻¹ (dangling OH from DA) – to the experimental values and the corresponding results from Cs⁺(H₂O)₄ one can easily see that the five-membered ring structure contributes as a main structure to the experimental spectrum. Similar to the findings for Cs⁺(H₂O)₄ the smaller peak of the two peaks corresponding to the DA molecule is on the wrong side of the main peak.

While assigning the peaks in the experimental spectrum corresponding to Cs⁺(H₂O)₅ (GM) was fairly simple, the remaining peaks pose more difficulties. In superposing all spectra of all local minimum structures up to LM09 (as no specific information could be gained from investigating the additional spectra of LM04 – LM09 no structures and spectra are depicted in this work) one finds that all structures seem to contribute to the spectrum. The superposed spectrum depicted in figure 8.18 was computed with re-assigned Boltzmann weights of 0.7, 0.5, and 0.3 for the structures LM01, LM02, and LM03, respectively. The structures LM01, LM02, and LM03 depicted in figure 8.19 are already very close in energy, nevertheless the re-assignment of the Boltzmann weight decreases the energy differences even further. It is

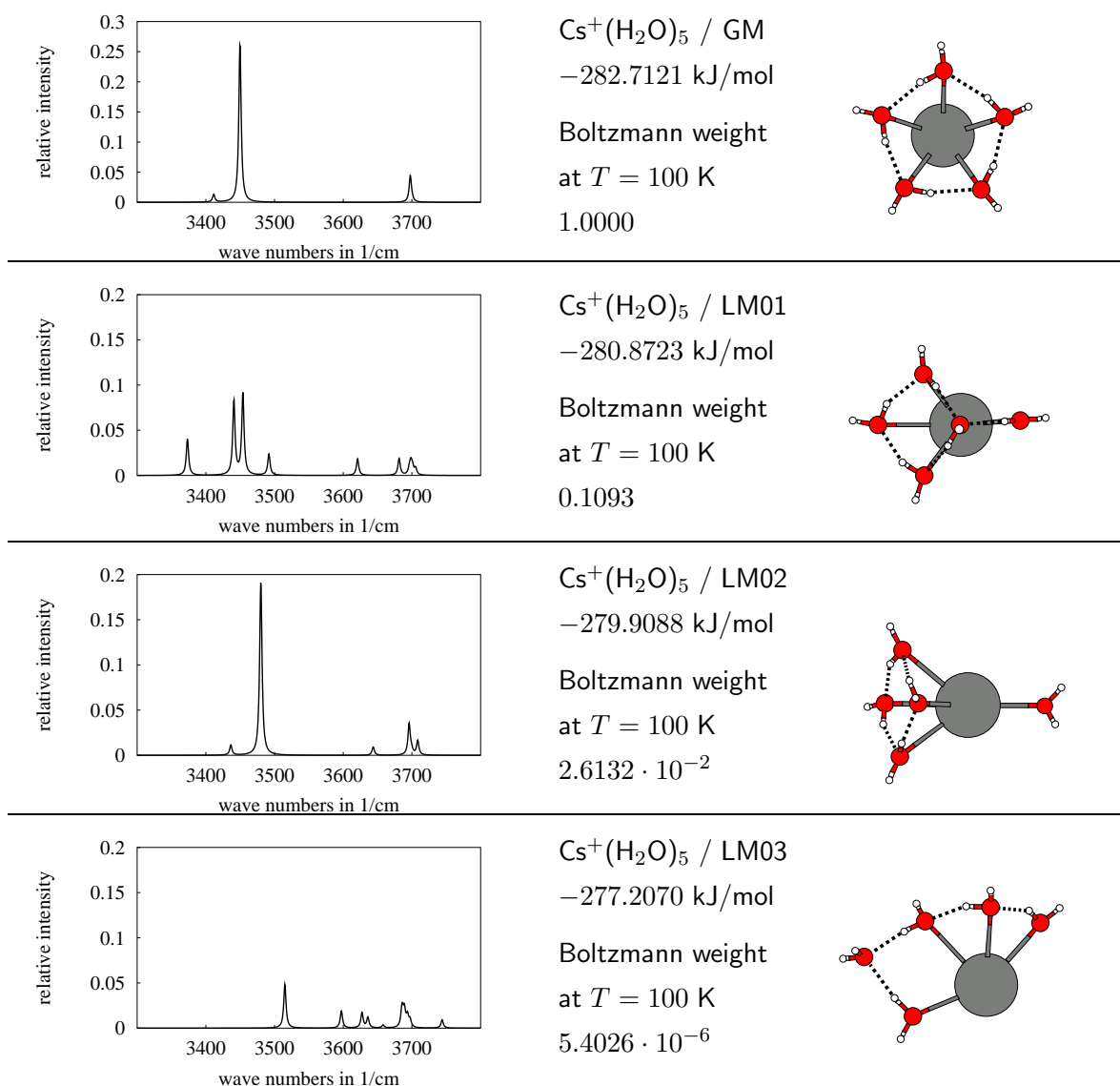


Figure 8.19.: Spectra and geometries of $\text{Cs}^+(\text{H}_2\text{O})_5$ in energetical order and their Boltzmann weights

assumed that at least the new Boltzmann weight for LM01 is approximately correct, leading to a new energy difference $\Delta E = 0.3$ kJ/mol instead of $\Delta E = 2.7$ kJ/mol. As for all other structures, including LM02 and LM03, it is only certain that they indeed have a larger Boltzmann weight than that obtained using TIP4P/OPLS, however, it is not possible yet to distinguish which peaks in the experimental spectrum belong to which peaks in the theoretical spectra, and therefore also to which structures, with enough confidence. Therefore, it is so far impossible to assign this spectrum further. Nevertheless, a considerable amount of structural information could be produced also in this case by comparison of the experiment and theory.

Cs⁺(H₂O)₆ and Cs⁺(H₂O)₈

As already for the case of Cs⁺(H₂O)₅, the experimental spectra of Cs⁺(H₂O)₆ (see figure 8.20 and 8.22) and Cs⁺(H₂O)₈ (see figure 8.20 and 8.23), respectively, become less distinct and only very broad bands of peaks are visible. However these spectra could still be used to show that at least the overall trend in the theoretical spectra using the re-fitted curve seems to be correct also for these cluster sizes. Although these spectra shall not be discussed any further with respect to assigning structures to the peaks, the structures and corresponding separate spectra are depicted for completeness and to show that the agreement between theory and experiment is still very good (see figure 8.22 for Cs⁺(H₂O)₆ and figure 8.23 for Cs⁺(H₂O)₈; the theoretical spectra were obtained using TIP4P/OPLS Boltzmann weights).

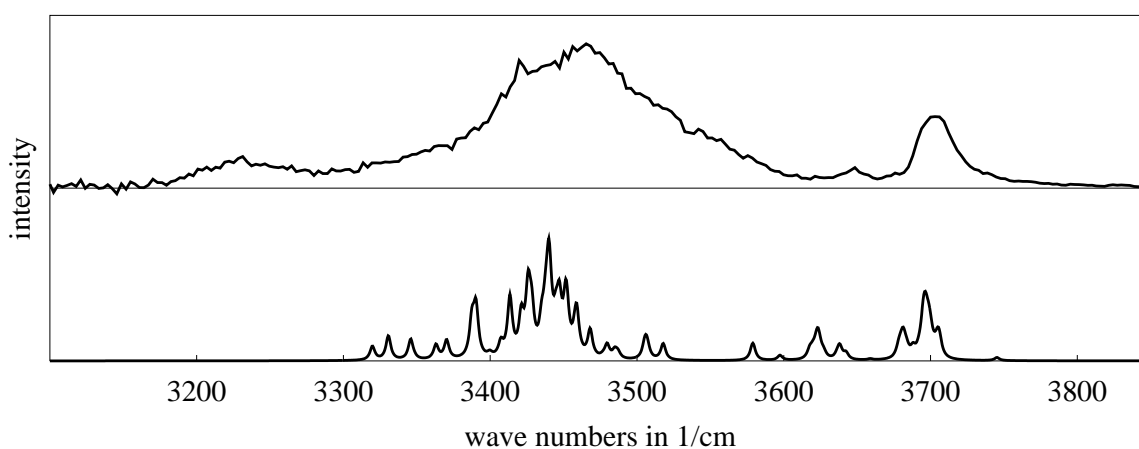


Figure 8.20.: Experimental infrared spectrum of Cs⁺(H₂O)₆ (top spectrum), and computed infrared spectrum (bottom spectrum) using the manually re-fitted frequency vs. field curve for Cs⁺(H₂O)_n-clusters, intensity in arbitrary units

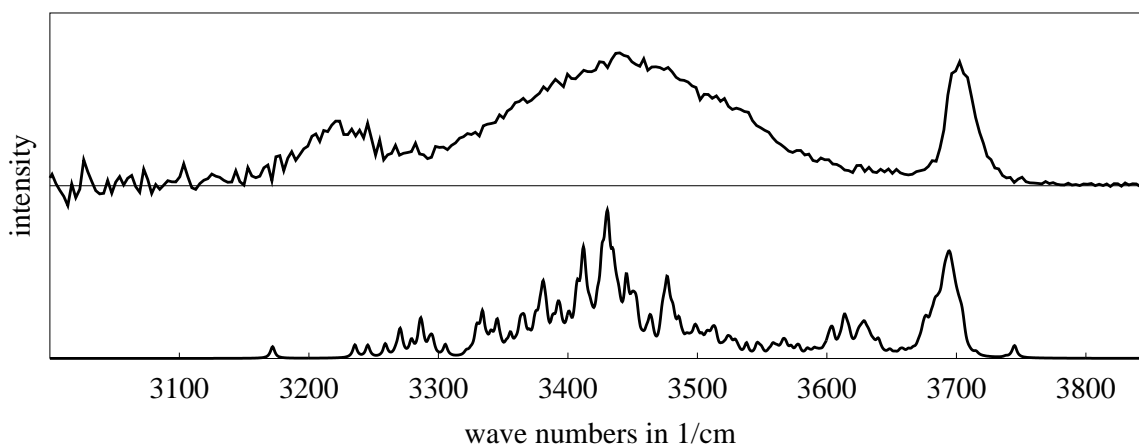


Figure 8.21.: Experimental infrared spectrum of Cs⁺(H₂O)₈ (top spectrum), and computed infrared spectrum (bottom spectrum) using the manually re-fitted frequency vs. field curve for Cs⁺(H₂O)_n-clusters, intensity in arbitrary units

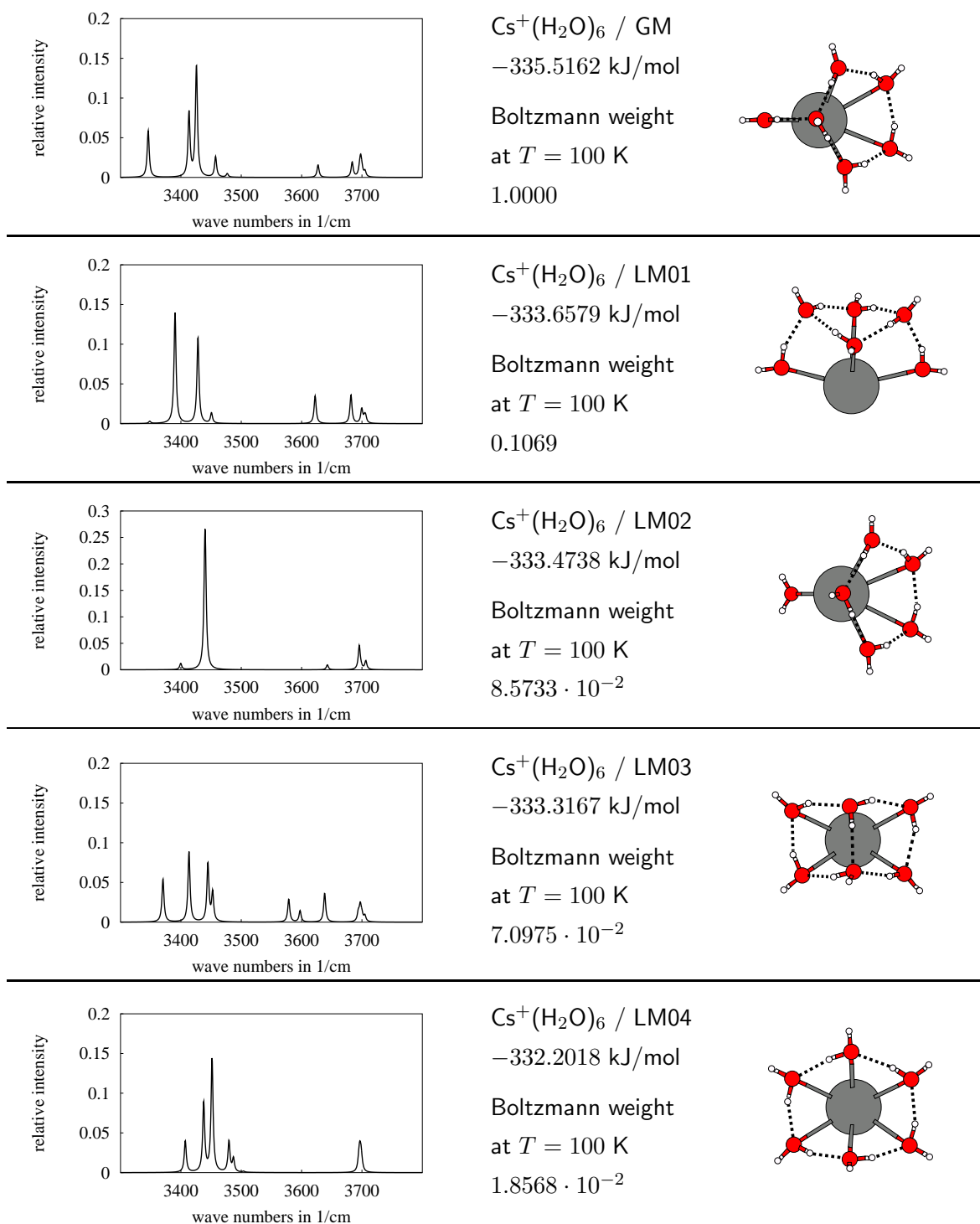


Figure 8.22.: Spectra and geometries of $\text{Cs}^+(\text{H}_2\text{O})_6$ in energetical order and their Boltzmann weights

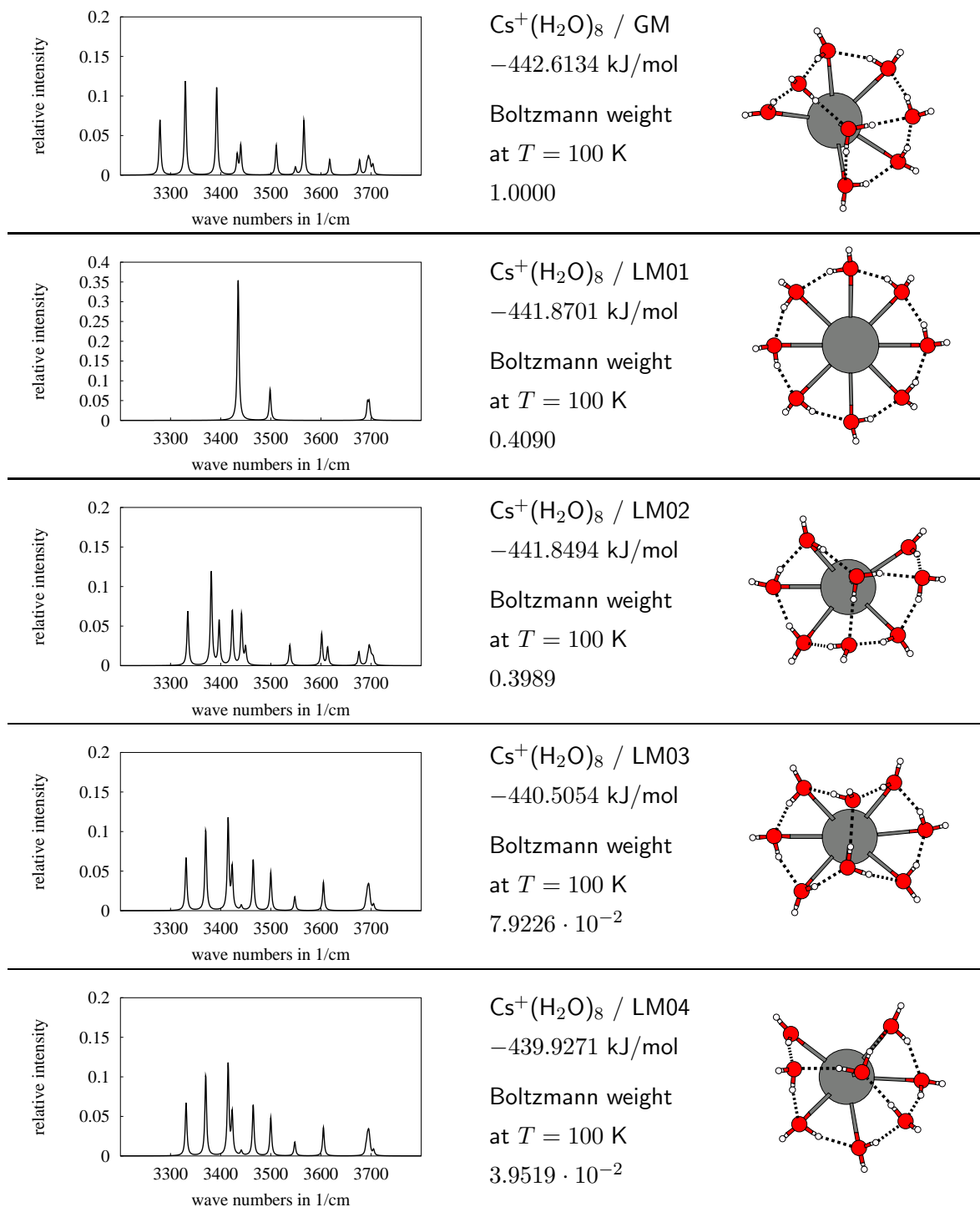


Figure 8.23.: Spectra and geometries of $\text{Cs}^+(\text{H}_2\text{O})_8$ in energetical order and their Boltzmann weights

9. Conclusions obtained from infrared spectra

An extensive study computing anharmonic infrared spectra of alkali cation microhydration clusters $M^+(H_2O)_n$, with $M = Na, K,$ and Cs and $4 \leq n \leq 22$, has been carried out.

It was found that some peak patterns are fairly distinct which will presumably allow experimentalists to directly withdraw at least some structural information from experimental spectral data. Other peak patterns, though prominent for smaller cluster sizes of $n \leq 13$, are usually too congested or superposed with too many other patterns for larger cluster structures, as to allow direct extraction of structural information from experimental spectra. However, for most of the more complicated spectra, structural information can still be gained by the combination of theoretical and experimental data.

This is an encouraging result, as the most interesting cases are not cluster structures with small but large n , such as magic numbers, for example $n = 20$. So far larger alkali cation microhydration clusters have been investigated mostly by mass spectrometry, yielding preferred cluster sizes, i.e. magic numbers, but no structural information. It has been shown that infrared spectra can contribute to obtaining structural information, even in the presence of several cluster isomers at non-zero temperatures.

Recently available experimental data, kindly provided by J.M. Lisy and coworkers (Department of Chemistry, University of Illinois at Urbana Champaign, Illinois/USA, personal correspondence), could be used for re-fitting the frequency vs. field curves for all three systems $M^+(H_2O)_n$, with $M = Na, K,$ and Cs , respectively, which is essential for obtaining quantitatively correct data. However, due to time constraints, this refit could so far only be done manually, though still leading to an already very good agreement between theory and experiment. Starting from the manually re-fitted frequency vs. field curves, use of an optimisation routine will make it possible to generate an automatic and even better fit. However, to be able to do this, more experimental data is needed to first be able to obtain a correct peak assignment for more structures than already available. One would also need the experimental spectra of bigger cluster sizes to control the fitting procedure and to see whether or not different curves are needed for smaller and bigger cluster sizes, as with increasing size the water molecules are further away from the central ion and hence feel less of its presence but more of their immediate neighbours. Nevertheless, even at this early stage of this investigation, it has been possible for the first time to assign structures to all experimental spectra

of smaller cluster structures up to $n = 5$. For these assignments, Boltzmann distributions at $T = 100$ K, obtained using the TIP4P/OPLS energies from the global optimisation results, have been computed to simulate superposed theoretical spectra which would best correspond to the experiment. However, it turned out that in some though not all cases for smaller cluster structures the energetical order for the local minima obtained by using TIP4P/OPLS did not correspond to the observations made in the experiment. This is by no means surprising as TIP4P/OPLS has been designed for larger systems and hence is known to encounter difficulties in correctly reproducing energy differences for smaller cluster structures of $n \leq 8$. Nevertheless, there are reasons to assume that for $n \geq 9$ TIP4P/OPLS becomes more reliable. Also, entropy effects have to be taken into account for temperatures larger than 0 K which were also neglected in the treatment shown so far. Nevertheless, the obtained results for structure assignment in the experiment are still very encouraging indeed, as they show that both theory and experiment can learn and gain from each other. This gives us some confidence that it will be possible to extend this study to larger systems, which may then lead to direct structural information on clusters in the size region of magic numbers.

The final step to be taken was to further elucidate the system of alkali cation microhydration clusters using MD calculations to investigate if the magic number status of certain cluster sizes is also influenced by build-up dynamics or size-specific resistance to dissociation.

Part III.

Dynamics of alkali cation microhydration clusters

10. Molecular dynamics simulation

Molecular dynamics (MD) simulation is a method for calculating the equilibrium and transport properties of a classical many-body system, in which the term classical in this context denotes that the nuclear motion of the individual particles follows the laws of classical mechanics. For a wide range of materials this proves to be an excellent approximation. Exceptions would be, for instance, the translational and rotational motion of very light atoms and molecules, such as He or H₂, where quantum effects would have to be taken into account. A good overview of molecular dynamics simulation can be found in references [85, 86].

10.1. The concept of molecular dynamics

In many ways molecular dynamics simulations indeed match real experiments. When a real experiment is performed, the procedure is as follows: A sample is prepared and the property of interest is measured in a certain interval of time with an appropriate instrument. In case the property of interest is subject to statistical noise, then a longer average will produce more accurate results. The approach followed in a molecular dynamics simulation is exactly the same. First a sample is prepared, i.e. a model system consisting of N particles is selected and Newton's equations of motion are solved for this system until the properties are equilibrated, or in other words, the system no longer undergoes changes with time. After the equilibration the actual measurement is executed. Mistakes which can be made in real experiments are comparable to the mistakes that can be made when conducting a computer experiment. For example, the sample is not prepared correctly, the measurement is too short, the system experiences an irreversible alteration in due course of the investigation or one simply does not determine what one expects. In order to determine an observable quantity in a molecular dynamics simulation the observable has to be expressed as a function of the positions and momenta of the particles in the system. For instance, making use of equipartition of energy over all degrees of freedom which enter quadratically in the Hamiltonian of the system provides a convenient definition of the temperature in a classical many-body-system.

10.2. A basic structure of an MD-program

A simple molecular dynamics program would be constructed as follows:

- (1) First, the parameters which specify the conditions of the run (such as initial temperature, number of particles, density, time step and various others) are read.
- (2) The system is initialised (i.e. the velocities are selected at random).
- (3) In the main loop first the forces are determined which is followed by the integration of Newton's equations of motion for a time interval Δt . These two steps are repeated until the desired length of time of the simulation has been reached.
- (5) After completion of the central loop the averages of measured quantities are determined and printed out.

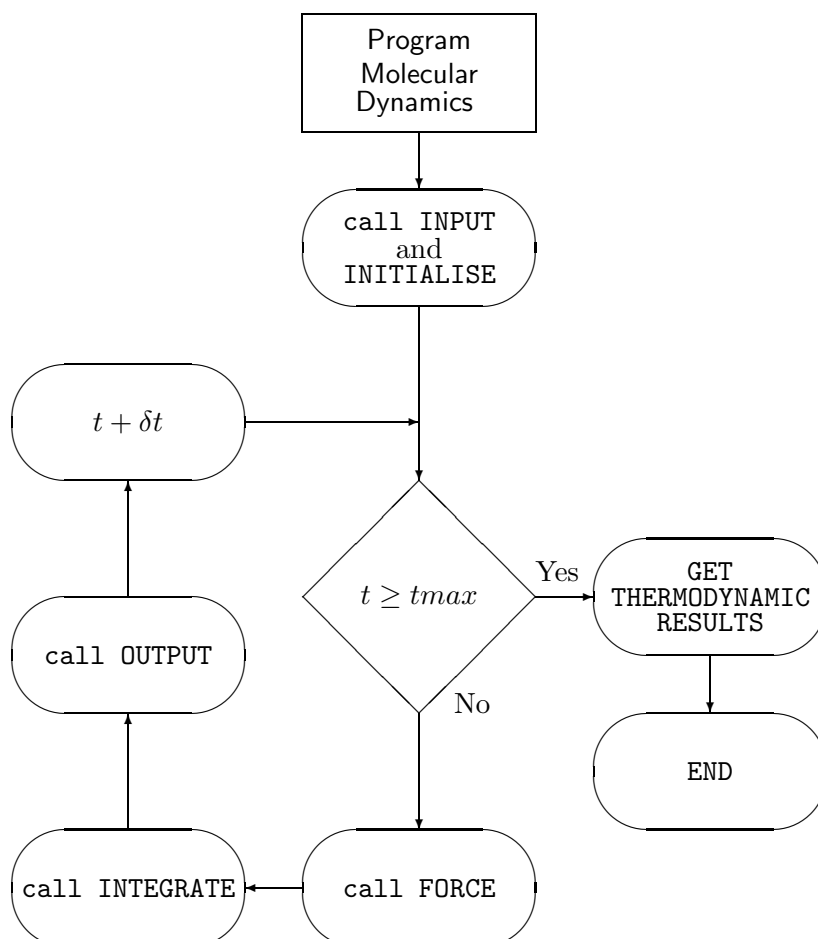


Figure 10.1.: A sample molecular dynamics program

A sample flowchart is displayed in figure 10.1 which would carry out a molecular dynamics simulation for a simple atomic system.

Details regarding molecular dynamics simulation of water and alkali cation microhydration clusters in particular, such as for example the use of the force field or the integration of the equations of motion, will be further explained in the following section.

10.3. Molecular dynamics of alkali cation microhydration clusters

10.3.1. Molecular dynamics of molecules in general

Any molecular system consists of particles interacting via intra- and intermolecular forces. Basically there should be no distinction between these forces, however, the intramolecular forces are at least one order of magnitude greater than the intermolecular forces. In other words, molecular bond vibrations occur so rapidly that an extremely short time step would be required to solve the equations of motion. The usual solution is to take the intramolecular bonds as well as the angles for small molecules, such as water, to be of fixed value. This is by no means an inconsequential step, as at normal temperatures the amplitude of vibration (classical or quantum) is fairly small compared with molecular dimensions.

With all intramolecular degrees of freedom frozen, the molecular motion can be divided into a translational motion of the centre of mass and a rotational motion of the molecule about its centre of mass.

Calculating the centre of mass trajectories involves solving either a system of $3N$ second-order differential equations with the Cartesian coordinates \mathbf{r}_i where m_i is the mass of the i^{th} particle and \mathbf{f}_i the total force acting on that particle

$$\sum_i m_i \ddot{\mathbf{r}}_i = \sum_i \mathbf{f}_i \quad (10.1)$$

or an equivalent set of $6N$ first-order differential equations (for much more details see reference [86]) where \mathbf{p}_i is the generalised momentum and \mathcal{V} the potential function.

$$\sum_i \dot{\mathbf{r}}_i = \sum_i \frac{\mathbf{p}_i}{m_i} \quad (10.2)$$

$$\sum_i \dot{\mathbf{p}}_i = - \sum_i \nabla_{\mathbf{r}_i} \cdot \mathcal{V} = \sum_i \mathbf{f}_i \quad (10.3)$$

A common method for solving these ordinary differential equations, such as equations 10.1 and 10.2/10.3 is the finite difference approach which works as follows: The attempt is to obtain the positions, velocities and other dynamic information at a later time than time t , i.e. $(t + \Delta t)$ to a satisfactory degree of exactitude using the molecular positions, velocities and

other dynamic information at time t . In order to be able to do this the differential quotients (dx/dt) is approximated by differences ($\Delta x/\Delta t$). The equations can be solved using a step-by-step method with the choice of the time interval Δt regulated by the chosen method. In any case Δt must be considerably smaller than the time commonly needed by a molecule to travel its own length. Several different algorithms satisfy the criteria of the general finite pattern. For an overview see reference [86] and references therein.

A summary of desirable qualities for a successful simulation would be as follows:

- (1) The algorithm should be fast and require little memory
- (2) The algorithm should duplicate the classical trajectory as closely as possible
- (3) The algorithm should permit the use of a long time step Δt
- (4) The algorithm should be time-reversible and satisfy the known conservation laws for energy
- (5) The algorithm should be simple in form and easy to program

Not all of the above points are similarly significant for molecular dynamics simulation. The crude speed of the integration method is not critical compared with the rather time consuming force calculation which has to be performed at every time step. Hence the ability to employ a long time step Δt actually is most important, as this allows to compute a simulation with given total time in a modest number of integration steps. Obviously for larger time steps Δt the solution will follow the exact classical trajectory less accurately. Above all no integration scheme will supply a substantially accurate solution for a very long simulation time. Fortunately this is not required anyway, as molecular dynamics serves two roles:

- Firstly, substantially accurate solutions of the equations of motion are needed only for times which can be compared with the correlation times of interest, so that time correlation functions can be computed accurately.
- Secondly, the method is used to generate states sampled from the microcanonical ensemble. No exact classical trajectories are needed, when the energy is conserved.

For the second case, particle trajectories are required to stay on the appropriate constant-energy hypersurface in phase space as otherwise correct ensembles will not be generated. Energy conservation becomes less good as the time step is increased, hence all simulations involve a compromise between economy and accuracy, i.e. a good algorithm permits a relatively large time step to be used while preserving the energy in the microcanonical ensemble within acceptable error boundaries.

10.3.2. Translational motion

Several standard algorithms exist for integrating the translational equations of motion [85, 86]. One of the most commonly used methods in the past probably was the method which was initially adopted by Verlet [85, 87]. The method presents a direct solution of the second-order equations 10.1 and it is based on positions $\mathbf{r}(t)$, accelerations $\mathbf{a}(t)$ and the positions from the preceding time step $\mathbf{r}(t - \Delta t)$. The positions are advanced according to the following equation:

$$\mathbf{r}(t + \Delta t) = 2 \cdot \mathbf{r}(t) - \mathbf{r}(t - \Delta t) + \mathbf{a}(t) \cdot \Delta t^2 \quad (10.4)$$

The velocities $\mathbf{v}(t)$ do not appear at all as they are not needed to compute the trajectory. However, they are needed for estimating the kinetic energy (and hence the total energy). Therefore the velocities have to be obtained separately, according to

$$\mathbf{v}(t) = \frac{\mathbf{r}(t + \Delta t) - \mathbf{r}(t - \Delta t)}{2 \cdot \Delta t} \quad (10.5)$$

Whereas advancing the positions is correct except for errors of the order \mathcal{O}^4 computing the velocities is subject to errors of the order \mathcal{O}^2 .

A Verlet-equivalent algorithm which stores positions, velocities and accelerations at the same time t and above all minimises the round-off error is the so-called *velocity-Verlet*-algorithm [88].

$$\mathbf{r}(t + \Delta t) = \mathbf{r}(t) + \mathbf{v}(t) \cdot \Delta t + \mathbf{a}(t) \cdot \frac{\Delta t^2}{2} + \mathcal{O}(\Delta t^3) \quad (10.6)$$

$$\mathbf{v}(t + \Delta t) = \mathbf{v}(t) + [\mathbf{a}(t) + \mathbf{a}(t + \Delta t)] \cdot \frac{\Delta t}{2} + \mathcal{O}(\Delta t^3) \quad (10.7)$$

By eliminating the velocities the Verlet algorithm can be recovered. The velocity-Verlet-algorithm seems to be the most popular algorithm used nowadays, due to its numerical stability, convenience and simplicity. For these reasons the velocity-Verlet-algorithm has been chosen for this work.

10.3.3. Rotational motion

Rotational motion is dominated by the torque $\boldsymbol{\tau}(t)$ about the centre of mass. The torque enters the rotational equations of motions just as the force enters the translational equations of motion. However the character of orientation in space is a guarantee that the equations of rotational motion will fare less simple to program as the translational ones.

The orientation of a rigid body in space specifies the relation between an axis system fixed with respect to the space (laboratory frame \mathcal{L}) and one fixed with respect to the rigid body (molecular frame \mathcal{M}), i.e. the "principal" body-fixed system, in which the moment of inertia tensor is diagonal. Any unit vector \mathbf{e} may be expressed in terms of components in the molecular or laboratory frames which are related by a rotation matrix:

$$\mathbf{e}^{\mathcal{M}} = \mathbf{E} \cdot \mathbf{e}^{\mathcal{L}} \quad (10.8)$$

The nine components of the rotation matrix are defined by three angles, commonly known as *Euler*-angles ϕ, θ, ψ . Unfortunately, several conventions exist for these angles [89]. Unless stated otherwise, all equations used in this work refer to the so-called *x*-convention [89].

The rotation matrix \mathbf{E} referring to the *x*-convention reads:

$$\mathbf{E}(\phi, \theta, \psi) = \begin{pmatrix} \cos \psi \cos \phi - \cos \theta \sin \phi \sin \psi & \cos \psi \sin \phi + \cos \theta \cos \phi \sin \psi & \sin \psi \sin \theta \\ -\sin \psi \cos \phi - \cos \theta \sin \phi \cos \psi & -\sin \psi \sin \phi + \cos \theta \cos \phi \cos \psi & \cos \psi \cos \theta \\ \sin \theta \sin \phi & -\sin \theta \cos \phi & \cos \theta \end{pmatrix} \quad (10.9)$$

The angular velocities determine the orientation of the molecule within time. The time derivative of the angular velocity $\boldsymbol{\omega}$ is governed by the torque acting on the molecule. For molecular dynamics simulation it is convenient to express the torque $\boldsymbol{\tau}$ in terms of the angular velocity and the moment of inertia tensor in the molecular frame $\mathbf{I}^{\mathcal{M}}$, where it is diagonal.

$$\dot{\mathbf{I}}^{\mathcal{L}} = \boldsymbol{\tau}^{\mathcal{L}} \quad (10.10)$$

$$\dot{\mathbf{I}}^{\mathcal{M}} + \boldsymbol{\omega}^{\mathcal{M}} \times \mathbf{I}^{\mathcal{M}} = \boldsymbol{\tau}^{\mathcal{M}} \quad (10.11)$$

The resulting equations for the components of $\boldsymbol{\omega}$ in the molecular frame become:

$$\dot{\omega}_x^{\mathcal{M}} = \frac{\tau_x^{\mathcal{M}}}{I_x} + \left(\frac{I_y - I_z}{I_x} \right) \omega_y^{\mathcal{M}} \omega_z^{\mathcal{M}} \quad (10.12)$$

$$\dot{\omega}_y^{\mathcal{M}} = \frac{\tau_y^{\mathcal{M}}}{I_y} + \left(\frac{I_z - I_x}{I_y} \right) \omega_z^{\mathcal{M}} \omega_x^{\mathcal{M}} \quad (10.13)$$

$$\dot{\omega}_z^{\mathcal{M}} = \frac{\tau_z^{\mathcal{M}}}{I_z} + \left(\frac{I_x - I_y}{I_z} \right) \omega_x^{\mathcal{M}} \omega_y^{\mathcal{M}} \quad (10.14)$$

where I_x, I_y, I_z are the three principal moments of inertia.

From this the equations of motion for the Euler angles themselves can be derived:

$$\dot{\phi} = -\frac{\sin \phi \cos \theta}{\sin \theta} \cdot \omega_x^{\mathcal{L}} + \frac{\cos \phi \cos \theta}{\sin \theta} \cdot \omega_y^{\mathcal{L}} + \omega_z^{\mathcal{L}} \quad (10.15)$$

$$\dot{\theta} = \cos \phi \cdot \omega_x^{\mathcal{L}} + \sin \phi \cdot \omega_y^{\mathcal{L}} \quad (10.16)$$

$$\dot{\psi} = \frac{\sin \phi}{\sin \theta} \cdot \omega_x^{\mathcal{L}} - \frac{\cos \phi}{\sin \theta} \cdot \omega_y^{\mathcal{L}} \quad (10.17)$$

In principle equations 10.12/10.13/10.14 and 10.15/10.16/10.17 can also be solved in a step-by-step fashion, just as for the translational case. Unfortunately these equations suffer a major drawback: they become singular whenever $\theta \rightarrow 0$ or $\theta \rightarrow \pi$, respectively. The molecular motion remains unaffected in case this occurs however, because of the definition of the Euler angles and the choice of axes the angles ϕ and ψ become degenerate. Hence the equations of motion presented in this form are inadequate.

A singularity-free description of the equations of motion however, cannot be obtained in terms of three independent variables whereas the use of four quaternion parameters as generalised coordinates [86, 89–91] fulfil the requirement of well-behaved rotational equations of motion. The quaternions satisfy the normalisation constraint:

$$q_0^2 + q_1^2 + q_2^2 + q_3^2 = 1 \quad (10.18)$$

In the Euler angle convention the quaternions are defined as follows,

$$q_0 = \cos\left(\frac{\theta}{2}\right) \cos\left(\frac{\phi + \psi}{2}\right) \quad (10.19)$$

$$q_1 = \sin\left(\frac{\theta}{2}\right) \cos\left(\frac{\phi - \psi}{2}\right) \quad (10.20)$$

$$q_2 = \sin\left(\frac{\theta}{2}\right) \sin\left(\frac{\phi - \psi}{2}\right) \quad (10.21)$$

$$q_3 = \cos\left(\frac{\theta}{2}\right) \sin\left(\frac{\phi + \psi}{2}\right) \quad (10.22)$$

and the rotation matrix becomes

$$\mathbf{E}(q_0, q_1, q_2, q_3) = \begin{pmatrix} q_0^2 + q_1^2 - q_2^2 - q_3^2 & 2 \cdot (q_1 q_2 + q_0 q_3) & 2 \cdot (q_1 q_3 - q_0 q_2) \\ 2 \cdot (q_1 q_2 - q_0 q_3) & q_0^2 - q_1^2 + q_2^2 - q_3^2 & 2 \cdot (q_2 q_3 + q_0 q_1) \\ 2 \cdot (q_1 q_3 + q_0 q_2) & 2 \cdot (q_2 q_3 - q_0 q_1) & q_0^2 - q_1^2 - q_2^2 + q_3^2 \end{pmatrix} \quad (10.23)$$

The equations of motion for each molecule in terms of quaternions read as follows

$$\begin{pmatrix} \dot{q}_0 \\ \dot{q}_1 \\ \dot{q}_2 \\ \dot{q}_3 \end{pmatrix} = \frac{1}{2} \begin{pmatrix} q_0 & -q_1 & -q_2 & -q_3 \\ q_1 & q_0 & -q_3 & q_2 \\ q_2 & q_3 & q_0 & -q_1 \\ q_3 & -q_2 & q_1 & q_0 \end{pmatrix} \begin{pmatrix} 0 \\ \omega_x^{\mathcal{M}} \\ \omega_y^{\mathcal{M}} \\ \omega_z^{\mathcal{M}} \end{pmatrix} \quad (10.24)$$

which can be written in an abbreviated form

$$\dot{\mathbf{q}} = \frac{1}{2} \cdot \mathbf{Q}(q_0, q_1, q_2, q_3) \cdot \boldsymbol{\omega}^{\mathcal{M}} \quad (10.25)$$

Velocity-Verlet-like rotational integrator

In the literature the rotational *leap-frog-like-algorithm* is almost exclusively used for integrating the rotational equations of motion [85, 86]. While the leap-frog-algorithm yields the

positions	$\mathbf{r}(t)$	\rightarrow	$\mathbf{r}(t + \Delta t)$
velocities	$\mathbf{v}(t)$	\rightarrow	$\mathbf{v}(t + \Delta t)$
forces	$\mathbf{a}(t)$	\rightarrow	$\mathbf{a}(t + \Delta t)$
torques	$\boldsymbol{\tau}^{\mathcal{M}}(t)$	\rightarrow	$\boldsymbol{\tau}^{\mathcal{M}}(t + \Delta t)$
angular velocities	$\boldsymbol{\omega}^{\mathcal{M}}(t)$	$\boldsymbol{\omega}^{\mathcal{M}}(t + \frac{1}{2} \Delta t)$	$\boldsymbol{\omega}^{\mathcal{M}}(t + \Delta t)$
angular momentum	$\mathbf{L}^{\mathcal{M}}(t)$	$\mathbf{L}^{\mathcal{M}}(t + \frac{1}{2} \Delta t)$	$\mathbf{L}^{\mathcal{M}}(t + \Delta t)$
quaternions	$\mathbf{q}(t)$	$\mathbf{q}(t + \frac{1}{2} \Delta t)$	$\mathbf{q}(t + \Delta t)$
quaternion derivatives	$\dot{\mathbf{q}}(t)$	$\dot{\mathbf{q}}(t + \frac{1}{2} \Delta t)$	$\dot{\mathbf{q}}(t + \Delta t)$

Figure 10.2.: Overview over advancing the coordinates, velocities, etc. using the Velocity-Verlet-like rotational integrator

positions and accelerations at time $(t + \Delta t)$, the velocities can only be obtained for mid-steps, i.e. $(t - \Delta t/2)$ and $(t + \Delta t/2)$. Using the velocities at mid-step the velocities at time t , though not $(t + \Delta t)$, can be constructed. The great advantage of velocity-Verlet-algorithm over the leap-frog-algorithm is that all information, i.e. positions, accelerations, and velocities, can be obtained directly for $(t + \Delta t)$ at each time step.

To the best of our knowledge a velocity-Verlet-like rotational integrator has been proposed and so far been used only by Gaberoglio [92].

Equivalent to the translational velocity-Verlet-algorithm all quantities are needed at time t (see figure 10.3.3) for the velocity-Verlet-like rotational integrator. Though not directly belonging to the rotational equations of motion, the first step is to compute and save the forces $\mathbf{a}(t)$ (or accelerations, respectively) and then to perform the first step of the translational velocity-Verlet in order to advance the positions from $\mathbf{r}(t) \rightarrow \mathbf{r}(t + \Delta t)$.

$$\mathbf{r}(t + \Delta t) = \mathbf{r}(t) + \mathbf{v}(t) \cdot \Delta t + \mathbf{a}(t) \cdot \frac{\Delta t^2}{2} + \mathcal{O}(\Delta t^3) \quad (10.26)$$

Using the knowledge of the principal moments of inertia (computed in the molecular frame), the rotation matrix, and the linear momentum, one can evaluate the angular velocities $\omega_x^{\mathcal{M}}(t), \omega_y^{\mathcal{M}}(t), \omega_z^{\mathcal{M}}(t)$ at the time t according to the following equation

$$\boldsymbol{\omega}^{\mathcal{M}}(t) = \mathbf{I}^{-1} \cdot \mathbf{E}(q_0(t), q_1(t), q_2(t), q_3(t)) \cdot \mathbf{L}^{\mathcal{L}}(t) \quad (10.27)$$

Having the angular velocities $\boldsymbol{\omega}^{\mathcal{M}}(t)$ at time t , the quaternion derivative $\dot{\mathbf{q}}(t)$ at time t can be calculated according to the equations of motion (see equation 10.24)

$$\dot{\mathbf{q}}(t) = \frac{1}{2} \cdot \mathbf{Q}(q_0(t), q_1(t), q_2(t), q_3(t)) \cdot \boldsymbol{\omega}^{\mathcal{M}}(t) \quad (10.28)$$

Based on both the quaternion derivative $\dot{\mathbf{q}}(t)$ and the quaternions $\mathbf{q}(t)$ at time t , the quaternions at mid-step $\mathbf{q}(t + \frac{1}{2} \Delta t)$ can be evaluated

$$\mathbf{q}(t + \frac{\Delta t}{2}) = \mathbf{q}(t) + \dot{\mathbf{q}}(t) \cdot \frac{\Delta t}{2} \quad (10.29)$$

In order to obtain the quaternion derivative at mid-step $\dot{\mathbf{q}}(t + \frac{1}{2} \Delta t)$, which will be needed to fully advance the quaternions from $\mathbf{q}(t + \frac{1}{2} \Delta t) \rightarrow \mathbf{q}(t + \Delta t)$ the angular momentum has to be advanced to mid-step first using the torques $\boldsymbol{\tau}^{\mathcal{L}}$ at time t

$$\mathbf{L}^{\mathcal{L}}(t + \frac{\Delta t}{2}) = \mathbf{L}^{\mathcal{L}}(t) + \boldsymbol{\tau}^{\mathcal{L}}(t) \cdot \frac{\Delta t}{2} \quad (10.30)$$

with which the angular velocity at mid-step can be computed.

$$\boldsymbol{\omega}^{\mathcal{M}}(t + \frac{\Delta t}{2}) = \mathbf{I}^{-1} \cdot \mathbf{E} \left(q_0(t + \frac{\Delta t}{2}), q_1(t + \frac{\Delta t}{2}), q_2(t + \frac{\Delta t}{2}), q_3(t + \frac{\Delta t}{2}) \right) \cdot \mathbf{L}^{\mathcal{L}}(t + \frac{\Delta t}{2}) \quad (10.31)$$

Now, the quaternion derivative at mid-step can be obtained according to $\dot{\mathbf{q}}(t + \frac{1}{2} \Delta t)$ (see equation 10.24)

$$\dot{\mathbf{q}}(t + \frac{\Delta t}{2}) = \frac{1}{2} \cdot \mathbf{Q} \left(q_0(t + \frac{\Delta t}{2}), q_1(t + \frac{\Delta t}{2}), q_2(t + \frac{\Delta t}{2}), q_3(t + \frac{\Delta t}{2}) \right) \cdot \boldsymbol{\omega}^{\mathcal{M}}(t + \frac{\Delta t}{2}) \quad (10.32)$$

Finally, the quaternions at time $(t + \Delta t)$ are available

$$\begin{aligned} \mathbf{q}(t + \Delta t) &= \mathbf{q}(t) + \dot{\mathbf{q}}(t) \cdot \Delta t + \ddot{\mathbf{q}}(t) \cdot \frac{\Delta t^2}{2} + \mathcal{O}(\Delta t^3) \\ &= \mathbf{q}(t) + \dot{\mathbf{q}}(t + \frac{\Delta t}{2}) \cdot \Delta t + \mathcal{O}(\Delta t^3) \end{aligned} \quad (10.33)$$

The final step of the velocity-Verlet-like rotational integrator is to recompute the forces, as now $\mathbf{r}(t + \Delta t)$ and $\mathbf{q}(t + \Delta t)$ have been computed, which is essentially all to sufficiently describe the orientation of a molecule in space.

For completion and before being able to run through the velocity-Verlet-like rotational integrator again, the angular momenta have to be updated from $\mathbf{L}^{\mathcal{L}}(t + \frac{1}{2} \Delta t) \rightarrow \mathbf{L}^{\mathcal{L}}(t + \Delta t)$ according to

$$\begin{aligned} \mathbf{L}^{\mathcal{L}}(t + \Delta t) &= \mathbf{L}^{\mathcal{L}}(t) + \boldsymbol{\tau}^{\mathcal{L}}(t) \cdot \Delta t + \dot{\boldsymbol{\tau}}^{\mathcal{L}}(t) \cdot \frac{\Delta t^2}{2} + \mathcal{O}(\Delta t^3) \\ &= \mathbf{L}^{\mathcal{L}}(t) + (\boldsymbol{\tau}^{\mathcal{L}}(t) + \boldsymbol{\tau}^{\mathcal{L}}(t + \Delta t)) \cdot \frac{\Delta t^2}{2} \\ &= \mathbf{L}^{\mathcal{L}}(t + \frac{\Delta t}{2}) + \boldsymbol{\tau}^{\mathcal{L}}(t + \Delta t) \cdot \frac{\Delta t^2}{2} \end{aligned} \quad (10.34)$$

and of course also the linear velocities (using equation 10.7 of the translational Verlet).

$$\mathbf{v}(t + \Delta t) = \mathbf{v}(t) + \frac{\Delta t}{2} \cdot [\mathbf{a}(t) + \mathbf{a}(t + \Delta t)] + \mathcal{O}(\Delta t^3) \quad (10.35)$$

10.3.4. Force field

As already mentioned in section 10.3, the force calculation is the most time-consuming part of all molecular dynamics simulations. Hence the choice of the force field is crucial for the time performance of the algorithm.

Because the model potential TIP4P/OPLS (for a detailed description of the model potential and its advantages and disadvantages see section 3.2) has already been used for the global geometry optimisation and because it has been optimised for molecular dynamics simulation it seemed a fair choice not only resulting in reasonable CPU-simulation-time but also making it possible to directly compare the results from the molecular dynamics simulation with the results obtained by the global geometry optimisation.

10.4. Molecular dynamics at constant temperature

The molecular dynamics method described in section 10.3.1 et seqq is a procedure for investigating natural time evolution of a classical system of N particles in the volume V and the total energy E being a constant of motion. Provided that the time averages are equivalent to ensemble averages, the (time) averages derived from a conventional MD simulation are equivalent to ensemble averages in the microcanonical (constant NVE) ensemble. However, it is often more convenient to perform simulations in other ensembles, such as for example NVT . In the following two sections two different approaches to realise an NVT ensemble are outlined.

10.4.1. Andersen thermostat

In the constant-temperature method proposed by Andersen [93] the system is coupled to a heat bath which dictates the desired temperature. The coupling to the heat bath is described by stochastic impulsive forces acting infrequently on particles selected at random. Between the collisions, the system evolves at constant energy corresponding to the normal Newtonian equations of motion. The stochastic collisions guarantee that all accessible constant energy shells are frequented analogous to their Boltzmann weight.

Before beginning a constant-temperature simulation the first step is to select the strength of the coupling with the heat bath. This coupling strength is accounted for by the frequency ν of stochastic collisions.

A constant-temperature simulation using the Andersen thermostat is comprised of the following steps:

- (1) Begin with an initial set of positions and momenta and integrate the equations of motion for time Δt .
- (2) Particles are chosen to be subjected to a collision with the heat bath. The probability that a particle is selected in a time step of length Δt is equal to $(\nu \cdot \Delta t)$.
- (3) In case particle i has been chosen to be subjected to a collision, its new velocity will be drawn from a Maxwell-Boltzmann distribution according to the adapted temperature T . Apart from particle i no other particles are affected by this collision.

Combining Newtonian Dynamics with stochastic collisions turns the molecular dynamics simulation into a Markov process [94]. However a canonical distribution in phase space is invariant under consecutive applications of the Andersen algorithm, as shown in reference [93]. As the Markov chain is also irreducible and aperiodic [93, 95, 96] the Andersen algorithm indeed produces a canonical ensemble.

In practise, it is important to choose the collision frequency ν such that energy fluctuations in a system embedded in an infinite heat bath are comparable to the decay rate of the energy fluctuations in the simulation of a system of equal size [93]. Nevertheless it should be mentioned that one should always keep in mind that applying the Andersen thermostat for simulating dynamical properties can be quite risky as it is unphysical. However, all static properties, such as potential energy or pressure are completely independent of the stochastic collision frequency and hence simulated accurately.

10.4.2. Nosé-Hoover thermostat

As just described in section 10.4.1 constant temperature dynamics in the Andersen approach is achieved using stochastic collisions with a heat bath. Whereas Nosé has shown that deterministic molecular dynamics can also be performed at constant temperature [97, 98]. This deterministic approach is based on the use of an extended Lagrangian, i.e. a Lagrangian which contains additional, artificial coordinates and velocities. The extended Lagrangian approach finds its origin in constant-pressure molecular dynamics simulation [93] introduced by Andersen. Nowadays it is more common to use the Nosé scheme in the formulation of Hoover [99, 100], the so-called Nosé-Hoover thermostat. For details regarding the equations of motion and their implementation see reference [85].

For a system in which there are no external forces (such as constraints) and the centre of mass remains fixed, the Nosé-Hoover thermostat will generate a canonical distribution. However, even though there are systems with external forces for which the Nosé-Hoover thermostat generates a correct canonical ensemble, there exist exceptions in which the expected behaviour is not reproduced. In other words, the Nosé-Hoover thermostat only produces an accurate

canonical ensemble for molecular systems in which merely one quantity is conserved or for the case that there are no external forces and the centre of mass remains fixed. The last condition can be fulfilled in most practical systems by simply initialising the system with a zero centre of mass velocity. Nevertheless in order to be able to simulate more general systems one cannot rely on the Nosé-Hoover algorithm. At this point, it should be mentioned that the Andersen thermostat does not suffer from any of these shortcomings, though its dynamics are less realistic.

To obtain a Nosé-Hoover thermostat where these restriction do not apply, a scheme was proposed in which the Nosé-Hoover thermostat is coupled to another thermostat, or if necessary to a whole chain of thermostats [101]. These chains regard additional conservation laws and it was shown that this generalisation of the original Nosé-Hoover thermostat, provided that it is ergodic, still produces a canonical ensemble [101]. A detailed description of the corresponding equations of motion and their implementation is given in reference [85].

Due to these shortcomings and the fact that the Andersen thermostat actually computes static properties in a correct manner, it has been favoured in this work over the Nosé-Hoover thermostat and Nosé-Hoover chains, respectively, especially in view of saving a considerable amount of CPU-time.

10.5. Constrained dynamics

Sometimes one might get the impression that all problems in mechanics can be reduced to solving the following set of differential equations

$$\sum_i m_i \ddot{\mathbf{r}} = \sum_i \left(\mathbf{F}_i^{(E)} + \sum_j \mathbf{F}_{ij}^{(I)} \right) \quad (10.36)$$

with the external forces $\mathbf{F}^{(E)}$ acting on the particles due to sources outside the system and the internal forces $\mathbf{F}^{(I)}$ on for example the particle i due to all other particles in the system. In other words, one just exchanges the various forces acting upon the particles of the system, turns the mathematical crank, and grinds out the answers. However, this view is an oversimplification even from a purely physical point of view, as sometimes it is necessary to take into account constraints that limit the motion of the system.

Constraints may be classified in various ways [89]. The classification most often used is as follows:

In case the conditions of the constraint are expressible as equations connecting the coordinates of the particles (and possibly the time) having the form

$$0 = f(\mathbf{r}_1, \mathbf{r}_2, \mathbf{r}_3, \dots, t) \quad (10.37)$$

then the constraints are said to be *holonomic*. The two most simple examples of holonomic constraints are, the rigid body, where the constraints are expressed by equations of the form

$$0 = (\mathbf{r}_i - \mathbf{r}_j)^2 - d_{ij}^2, \quad (10.38)$$

and particles constrained to moving along a curve or on a given surface (such as a sphere), with the equations defining the curve or surface acting as the equations of constraint. Constraints that cannot be expressed in this fashion are termed *non-holonomic*, as for example the constraint involving gas molecules trapped in a container.

Account for a system of N interacting particles and l general holonomic constraints which are given according to

$$0 = \sigma_k(\{\mathbf{r}(t)\}) \quad \text{with} \quad k = 1, \dots, l \quad (10.39)$$

where $\{\mathbf{r}(t)\}$ represents the subset of coordinates of the N particles which participate in the particular constraint σ_k at time t . The equations of motion of the particles become after generalising them to l independent constraints,

$$\sum_i^N m_i \ddot{\mathbf{r}} = \sum_i^N (\mathbf{F}_i(t) + \mathbf{G}_i(t)) = \sum_i^N \left(-\nabla_i E_{pot}(t) - \sum_k^l \lambda_k(t) \nabla_i \sigma_k \right) \quad (10.40)$$

where E_{pot} is the potential energy of the system, $\lambda_k(t)$ is the Lagrangian multiplier corresponding to the constraint σ_k , and $\mathbf{F}_i(t)$ and $\mathbf{G}_i(t)$ accounting for the potential energy forces and constraint forces on site i , respectively. Through the coordinates, the forces $\mathbf{F}_i(t)$ and $\mathbf{G}_i(t)$ implicitly depend on time.

The basic constraint dynamics methods commonly applied are the analytical method and the method of undetermined parameters [102], respectively. The analytical method comprises first the selection of an integration method (such as for instance the basic Verlet or the velocity Verlet to mention only two) requiring the total forces and their derivatives with respect to time up to the order s_{max} as input. The forces of constraints and their derivatives can then be calculated and combined with the potential energy forces in the used integration scheme to produce the constrained coordinates. However, without the adaptation of a correction scheme, the analytical method yields constrained degrees of freedom deviating with time from their constrained value due to the error brought in by the unavoidable numerical integration of the equations of motion.

The method of undetermined parameters is essentially equivalent to the analytical method, however modified such that it is ensured that the constraints are satisfied accurately at each time step. Basically, the modification requires replacing the highest derivative with respect to time of the Lagrangian multiplier by a set of undetermined parameters with values to be computed such that the constraints are satisfied at each time step. This method does

not introduce any additional numerical errors worse than the error caused by the integration scheme itself.

The method of undetermined parameters is fairly common though it is very difficult to get hold of a documentation. Hence a short summary shall be given here.

10.5.1. The method of undetermined parameters

A truncated Taylor series solution of

$$\sum_i^N m_i \ddot{\mathbf{r}}_i = \sum_i^N [\mathbf{F}_i(t) + \mathbf{G}_i(t)] = \sum_i^N \left[-\nabla_i E_{pot}(t) - \sum_k^l \lambda_k(t) \nabla_i \sigma_k \right] \quad (10.41)$$

produces the time derivatives of the coordinates of any order $n \geq 2$ with respect to the forces $\{\mathbf{F}(t)\}$ and their derivatives and the unknown Lagrangian multipliers $\{\lambda(t)\}$ and their derivatives:

$$\begin{aligned} \mathbf{r}_i(t + \Delta t, \{\lambda^{(p)}(t)\}) &= \mathbf{r}_i(t) + \mathbf{v}_i(t) + \sum_{n=2}^{s_{max}+2} \frac{1}{m_i} \cdot \mathbf{F}_i^{(n-2)}(t) \cdot \frac{\Delta t^n}{n!} \\ &+ \sum_{n=2}^{s_{max}+2} \frac{1}{m_i} \left[\binom{n-2}{p} \lambda_k^{(p)}(t) [\nabla_i \sigma_k]^{n-p-2}(t) \right] \frac{\Delta t^n}{n!} \end{aligned} \quad (10.42)$$

This can be rearranged such, that terms with the same order of $\{\lambda^{(p)}(t)\}$ appear together:

$$\begin{aligned} \mathbf{r}_i(t + \Delta t, \{\lambda^{(p)}(t)\}) &= \mathbf{r}_i(t) + \mathbf{v}_i(t) + \sum_{n=2}^{s_{max}+2} \frac{1}{m_i} \cdot \mathbf{F}_i^{(n-2)}(t) \cdot \frac{\Delta t^n}{n!} \\ &+ \delta \mathbf{r}_i(t + \Delta t, \{\lambda^{(0)}(t)\}) \\ &+ \delta \mathbf{r}_i(t + \Delta t, \{\lambda^{(1)}(t)\}) \\ &+ \delta \mathbf{r}_i(t + \Delta t, \{\lambda^{(2)}(t)\}) \\ &+ \dots \\ &+ \delta \mathbf{r}_i(t + \Delta t, \{\lambda^{(s_{max}-1)}(t)\}) \\ &+ \delta \mathbf{r}_i(t + \Delta t, \{\lambda^{(s_{max})}(t)\}) \\ &\text{with } i = 1, \dots, N \end{aligned} \quad (10.43)$$

where $\delta \mathbf{r}_i(t + \Delta t, \{\lambda^{(0)}(t)\})$ contains s_{max} terms that are linear in $\{\lambda^{(0)}(t)\}$ whereas $\delta \mathbf{r}_i(t + \Delta t, \{\lambda^{(1)}(t)\})$ contains $s_{max}-1$ terms linear in $\{\lambda^{(1)}(t)\}$ and so on. Finally, $\delta \mathbf{r}_i(t + \Delta t, \{\lambda^{(s_{max})}(t)\})$ contains a single term that is linear in $\{\lambda^{(s_{max})}(t)\}$; and the equation can be rearranged as follows:

$$\begin{aligned} \mathbf{r}_i(t + \Delta t, \{\lambda^{(0)}(t), \dots, \lambda^{(s_{max})}(t)\}) &= \mathbf{r}'_i(t + \Delta t, \{\lambda^{(0)}(t), \dots, \lambda^{(s_{max}-1)}(t)\}) \\ &+ \mathbf{r}_i(t + \Delta t, \{\lambda^{(s_{max})}(t)\}) \\ &\text{with } i = 1, \dots, N \end{aligned} \quad (10.44)$$

where the partially constrained position vector $\mathbf{r}'_i(t + \Delta t, \{\lambda^{(0)}(t), \dots, \lambda^{(s_{max}-1)}(t)\})$ is defined as the sum of all terms except for the last one depicted in equation 10.43. The first step of the method of undetermined parameters is to evaluate the set of $\mathbf{r}'_i(t + \Delta t, \{\lambda^{(0)}(t), \dots, \lambda^{(s_{max}-1)}(t)\})$ by computing only $\{\lambda^{(p)}(t)\}$, where $p = 0, 1, \dots, (s_{max} - 1)$, and proceed by integrating the equations of motion. The second step is to choose the set $\{\delta\mathbf{r}\}$ to enforce the exact satisfaction of the constraints at every time step. In other words, the set of $\{\lambda^{(s_{max})}(t)\}$ is substituted by a new set of parameters $\{\gamma\}$:

$$\begin{aligned} \mathbf{r}_i(t + \Delta t, \{\lambda^{(0)}(t), \dots, \lambda^{(s_{max}-1)}(t), \gamma\}) &= \mathbf{r}'_i(t + \Delta t, \{\lambda^{(0)}(t), \dots, \lambda^{(s_{max}-1)}(t)\}) \\ &+ \delta\mathbf{r}_i(t + \Delta t, \{\gamma\}) \\ &\text{with } i = 1, \dots, N \end{aligned} \quad (10.45)$$

The parameters $\{\gamma\}$ are required to be of such values as to fulfil

$$\begin{aligned} 0 &= \sigma_k(\{\mathbf{r}_i(t + \Delta t, \{\lambda^{(0)}(t), \dots, \lambda^{(s_{max}-1)}(t), \gamma\})\}) \\ &\text{with } k = 1, \dots, l \end{aligned} \quad (10.46)$$

Replacing $\{\lambda^{(s_{max})}(t)\}$ by $\{\gamma\}$ in the expression for $\delta\mathbf{r}_i(t + \Delta t, \{\lambda^{(s_{max})}(t)\})$, $\delta\mathbf{r}_i(t + \Delta t, \{\gamma\})$ can be obtained.

The comparison of equation 10.42 and equation 10.43 leads to:

$$\begin{aligned} \delta\mathbf{r}_i(t + \Delta t, \{\gamma\}) &= -\frac{1}{m_i} \cdot \frac{\Delta t^{s_{max}+2}}{(s_{max} + 2)!} \sum_{k=1}^l \gamma_k \nabla_i \sigma_k(t) \\ &\text{with } i = 1, \dots, N \end{aligned} \quad (10.47)$$

namely, the general expression for the displacements required to fulfil the constraints. Adoption of a desired integration algorithm and desired forms of holonomic constraints determines the value of s_{max} and the functional dependence of $\delta\mathbf{r}_i(t + \Delta t, \{\gamma\})$ on $\{\mathbf{r}(t)\}$, respectively. By means of equation 10.47, equation 10.45 becomes:

$$\begin{aligned} \mathbf{r}_i(t + \Delta t, \{\lambda^{(0)}(t), \dots, \lambda^{(s_{max}-1)}(t), \gamma\}) &= \mathbf{r}'_i(t + \Delta t, \{\lambda^{(0)}(t), \dots, \lambda^{(s_{max}-1)}(t)\}) \\ &+ \delta\mathbf{r}_i(t + \Delta t, \{\gamma\}) \\ &- \frac{1}{m_i} \cdot \frac{\Delta t^{s_{max}+2}}{(s_{max} + 2)!} \sum_{k=1}^l \gamma_k \nabla_i \sigma_k(t) \\ &\text{with } i = 1, \dots, N \end{aligned} \quad (10.48)$$

10.5.2. RATTLE or the method of undetermined parameters in combination with the velocity Verlet integration scheme

The general formalism consists of two steps:

- (1) The computation of the partially constrained coordinates and
- (2) the calculation of the undetermined parameters and constrained coordinates.

The coordinate equations of the method of undetermined parameters using the velocity Verlet scheme are (which follows from equation 10.48 with $s_{max} = 0$):

$$\mathbf{r}_i(t + \Delta t, \{\gamma\}) = \mathbf{r}'_i(t + \Delta t) - \frac{\Delta t}{2m_i} \sum_{k=1}^l \gamma_k \nabla_i \sigma_k(t) \quad (10.49)$$

The purely unconstrained position vector $\mathbf{r}'_i(t + \Delta t)$ is given by:

$$\mathbf{r}'_i(t + \Delta t) - \frac{\Delta t}{2m_i} = \mathbf{r}_i(t) + \mathbf{v}_i(t) \cdot \Delta t + \mathbf{a}(t) \cdot \frac{\Delta t^2}{2} \quad (10.50)$$

Given that the coordinates at time $(t + \Delta t)$ satisfy the constraint equations the parameters $\{\gamma\}$ are determined accordingly. The new velocities at time $(t + \Delta t)$ are

$$\mathbf{v}_i(t + \Delta t, \{\eta\}) = \mathbf{v}'_i(t + \Delta t, \{\eta\}) - \frac{\Delta t}{2m_i} \sum_{k=1}^l \eta_k \nabla_i \sigma_k(t + \Delta t) \quad (10.51)$$

Again given that the velocities at time $(t + \Delta t)$ satisfy the constraint equations the parameters $\{\eta\}$ are chosen accordingly. Combining the first derivatives with respect to time of the constraint equation for $\sigma_k(\{\mathbf{r}(t + \Delta t)\})$ with the chain rule one obtains

$$\begin{aligned} 0 &= \frac{d}{\Delta t} \sigma_k(\{\mathbf{r}(t + \Delta t)\}) \\ &= \sum_{i=1}^{n_k} \mathbf{v}_i(t + \Delta t) \cdot \nabla_i \sigma_k(\{\mathbf{r}(t + \Delta t)\}) \end{aligned} \quad (10.52)$$

In order to solve this set of l linear equations for $\{\eta\}$ either a matrix inversion technique [102] or the SHAKE approach [86] may be used. The SHAKE procedure has been developed for the basic Verlet integration algorithm and consists of finding incrementally the displacement a particle needs to successively satisfy all constraints adopted. The solution for $\{\gamma\}$ and $\{\eta\}$ using the velocity Verlet integration scheme in combination with SHAKE is called RATTLE [103].

The first part of RATTLE is analogous to SHAKE. The new positions of the particles $\{\mathbf{r}(t + \Delta t)\}$ obtained for the current iteration are equal to:

$$\mathbf{r}_i(t + \Delta t, \{\gamma\}) = \mathbf{r}'_i(t + \Delta t) - \frac{\Delta t}{2m_i} \sum_{k=1}^l \gamma_k \nabla_i \sigma_k(t) \quad (10.53)$$

with $i = 1, \dots, n_k$

where the starting value of $\mathbf{r}'_i(t + \Delta t)$ is given by the unconstrained position vector

$$\mathbf{r}'_i(t + \Delta t) = \mathbf{r}_i(t) + \mathbf{v}_i(t) \cdot \Delta t + \mathbf{a}(t) \cdot \frac{\Delta t^2}{2} \quad (10.54)$$

The new positions should satisfy the constraint equation for σ_k

$$\begin{aligned} 0 &= \sigma_k(\{\mathbf{r}(t + \Delta t)\}) \\ &= \sigma_k\left(\{\mathbf{r}'(t + \Delta t)\} - \left\{\frac{\Delta t^2}{m} \gamma_k \nabla \sigma_k(t)\right\}\right) \end{aligned} \quad (10.55)$$

Generally equation 10.55 is non-linear in γ_k . After applying a Taylor expansion to each holonomic constraint $\sigma_k(\{\mathbf{r}(t + \Delta t)\})$ around $\sigma_k(\{\mathbf{r}'(t + \Delta t)\})$, equation 10.55 becomes:

$$\begin{aligned} 0 &= \sigma_k\left(\{\mathbf{r}'(t + \Delta t)\} - \left\{\frac{\Delta t^2}{m} \gamma_k \nabla \sigma_k(t)\right\}\right) \\ &= \sigma_k(\{\mathbf{r}'(t + \Delta t)\}) - \sum_{i=1}^{n_k} \frac{\Delta t^2}{m_i} \gamma_k \nabla_i \sigma_k(t) \cdot \nabla_i \sigma_k(\{\mathbf{r}'(t + \Delta t)\}) + \dots \end{aligned} \quad (10.56)$$

where the non-linear terms are not depicted explicitly. The domain of validity of the Taylor representation in equation 10.56 has to be cautiously established for every single form of holonomic constraint.

As the iterative procedure over constraints ensures obtaining the solution in this manner satisfying the non-linear part of equation 10.56 all terms higher than first order in equation 10.56 are neglected in favour of computationally efficiency. Solving equation 10.56 for γ_k yields:

$$\gamma_k = \frac{1}{\Delta t^2} \frac{\sigma_k(\{\mathbf{r}'(t + \Delta t)\})}{\sum_{i=1}^{n_k} \frac{1}{2m_i} \nabla_i \sigma_k(t) \cdot \nabla_i \sigma_k(\{\mathbf{r}'(t + \Delta t)\})} \quad (10.57)$$

However the validity of being able to neglect all non-linear terms in equation 10.56 must be carefully determined for each holonomic constraint σ_k respectively, as the larger the non-linearity inherent in the constraint σ_k becomes, the smaller becomes the allowed range of the constraint corrections to justify the negligence of the non-linear terms.

Iterations over the constraints proceed until all constraints are satisfied, within a given tolerance. In case all constraints are satisfied and the coordinates at $(t + \Delta t)$ are available, the forces $\{\mathbf{F}(t + \Delta t)\}$ can be calculated in order to continue with the second stage of RATTLE. In the second stage, the promoted velocities of the particles $\{\mathbf{v}(t + \Delta t)\}$ obtained in the current iteration are

$$\begin{aligned} \mathbf{v}_i(t + \Delta t) &= \mathbf{v}'_i(t + \Delta t) - \frac{\Delta t}{2m_i} \eta_k \nabla_i \sigma_k(t + \Delta t) \\ &\text{with } i = 1, \dots, n_k \end{aligned} \quad (10.58)$$

where the starting value of $\mathbf{v}'_i(t + \Delta t)$ is given according to

$$\mathbf{v}'_i(t + \Delta t) = \mathbf{v}_i(t) + \frac{\Delta t}{2m_i} \left(\mathbf{F}_i(t) - \sum_{k=1}^l \nabla_i \sigma_k(t) + \mathbf{F}_i(t + \Delta t) \right) \quad (10.59)$$

The new velocities need to satisfy the derivative with respect to time of the constraint equation. Inserting equation 10.59 in equation 10.55 leads to

$$\begin{aligned} 0 &= \sum_{i=1}^{n_k} \mathbf{v}'(t + \Delta t) \cdot \nabla_i \sigma_k(\{\mathbf{r}(t + \Delta t)\}) \\ &\quad - \eta_k \sum_{i=1}^{n_k} \frac{\Delta t}{2m_i} \nabla_i \sigma_k(\{\mathbf{r}(t + \Delta t)\}) \cdot \nabla_i \sigma_k(\{\mathbf{r}(t + \Delta t)\}) \end{aligned} \quad (10.60)$$

The solution of this linear equation for η_k is

$$\eta_k = \frac{\sum_{i=1}^{n_k} \mathbf{v}'_i(t + \Delta t) \cdot \nabla_i \sigma_k(\{\mathbf{r}(t + \Delta t)\})}{\Delta t \cdot \sum_{i=1}^{n_k} \frac{1}{2m_i} \nabla_i \sigma_k(\{\mathbf{r}(t + \Delta t)\}) \cdot \nabla_i \sigma_k(\{\mathbf{r}(t + \Delta t)\})} \quad (10.61)$$

Again, iterations over all constraints proceed until the constraints on the velocities have been satisfied within a given tolerance. The entire procedure is repeated for each time step.

10.5.3. Application of RATTLE for constraining the distance between one water molecule and the central ion in alkali cation microhydration clusters

Consider an alkali cation microhydration cluster where the distance between the central ion and the centre of mass coordinates of a selected water molecule of the water network has to be constrained. The general holonomic constraint equation (see equation 10.37) then takes the special form

$$0 = \sigma(\{\mathbf{r}\}) = (\mathbf{r}_{Ion}(t) - \mathbf{r}_{H_2O}(t))^2 - d_{Ion/H_2O}^2 \quad (10.62)$$

For this particular constraint, the first stage of RATTLE yields

$$\mathbf{r}_{Ion}(t + \Delta t) = \mathbf{r}'_{Ion}(t + \Delta t) - \frac{1}{m_{Ion}} \cdot \Delta t^2 \cdot \gamma \cdot (\mathbf{r}_{Ion}(t) - \mathbf{r}_{H_2O}(t)) \quad (10.63)$$

$$\mathbf{r}_{H_2O}(t + \Delta t) = \mathbf{r}'_{H_2O}(t + \Delta t) - \frac{1}{m_{H_2O}} \cdot \Delta t^2 \cdot \gamma \cdot (\mathbf{r}_{H_2O}(t) - \mathbf{r}_{Ion}(t)) \quad (10.64)$$

And equation 10.57 is reduced to:

$$\gamma = \frac{(\mathbf{r}'_{Ion}(t + \Delta t) - \mathbf{r}'_{H_2O}(t + \Delta t))^2 - d_{Ion/H_2O}^2}{2 \cdot \Delta t^2 \cdot \left(\frac{1}{m_{Ion}} - \frac{1}{m_{H_2O}} \right) \cdot (\mathbf{r}_{Ion}(t) - \mathbf{r}_{H_2O}(t)) \cdot (\mathbf{r}'_{Ion}(t + \Delta t) - \mathbf{r}'_{H_2O}(t + \Delta t))} \quad (10.65)$$

For the second stage of RATTLE equation 10.58 becomes:

$$\mathbf{v}_{Ion}(t + \Delta t) = \mathbf{v}'_{Ion}(t + \Delta t) - \frac{1}{m_{Ion}} \cdot \Delta t \cdot \eta \cdot (\mathbf{r}_{Ion}(t + \Delta t) - \mathbf{r}_{H_2O}(t + \Delta t)) \quad (10.66)$$

$$\mathbf{v}_{H_2O}(t + \Delta t) = \mathbf{v}'_{H_2O}(t + \Delta t) - \frac{1}{m_{H_2O}} \cdot \Delta t \cdot \eta \cdot (\mathbf{r}_{H_2O}(t + \Delta t) - \mathbf{r}_{Ion}(t + \Delta t)) \quad (10.67)$$

where $\mathbf{r}_{Ion}(t + \Delta t)$ and $\mathbf{r}_{H_2O}(t + \Delta t)$ are the constrained coordinates. And equation 10.61 reduces to:

$$\eta = \frac{(\mathbf{r}_{Ion}(t + \Delta t) - \mathbf{r}_{H_2O}(t + \Delta t)) \cdot (\mathbf{v}'_{Ion}(t + \Delta t) - \mathbf{v}'_{H_2O}(t + \Delta t))}{\Delta t \cdot \left(\frac{1}{m_{Ion}} - \frac{1}{m_{H_2O}} \right) \cdot (\mathbf{r}_{Ion}(t + \Delta t) - \mathbf{r}_{H_2O}(t + \Delta t))^2} \quad (10.68)$$

11. Results

There already exist several commercial molecular dynamics routines that can be used for different systems, applying various model or ab-initio potentials. These commercial routines also comprise special features such as for example different kind of ensembles or constraints too mention only two examples. However, none of the commercial routines had the features needed for this work all at once and, at the same time, the potential used elsewhere in this work. Hence, a molecular dynamics routine was written from scratch for alkali cation microhydration clusters employing all special features wanted.

11.1. Molecular dynamics program for alkali cation microhydration clusters

The most simple ensemble to program is the microcanonical ensemble or constant NVE , respectively, as it is a scheme for studying natural time evolution of a classical system of N particles in the volume V and only the classical equations of motion apply leading to constant energy. When setting up a new molecular dynamics program from scratch, it is very useful to first program a microcanonical distribution, as its conservation laws, such as the energy conservation or centre of mass conservation, are very helpful for checking the accuracy of the algorithm. Hence the first step was to design a microcanonical ensemble for alkali cation microhydration clusters and proceed from there.

As a molecular dynamics routine for simulating molecular systems is rather difficult to start with from scratch compared to atomic systems, a routine was written for ordinary atomic clusters employing the Lennard-Jones potential, thus having a basis routine which could be extended to molecular systems. After ensuring that this basis routine worked accurately, by scrutinising the compliance with the conservation laws, it was expanded onto alkali cation microhydration clusters using the TIP4P/OPLS potential. This was done such that the routine can be used for different alkali cation systems, defining the system via input parameters. The first obstacle in extending the atomic systems to molecular systems was to derive the quaternions from the available Cartesian coordinates of the geometries obtained by global geometry optimisation (see section 11.1.1 for the derivation of the quaternions). Having correct quaternions, the actual heart of the molecular dynamics routine could be implemented,

namely, the integration scheme. The velocity-Verlet was used for translational motion and a velocity-Verlet-like rotational integrator (described in section 10.3.3) was applied to the rotational motion. This program now presented an algorithm which could be used for the simulation of a microcanonical distribution, the accuracy of which was tested again (see section 11.1.3). Now a basis algorithm was available. This basis was then extended to also be able to generate a canonical ensemble which was obtained using the Andersen thermostat (see sections 10.4.1 and 11.2.1). A further extension constrained single water molecules to a fixed distance from the central ion in order to obtain free energies of dissociation of these water molecules (for detailed explanations see section 11.3).

11.1.1. Quaternions

Starting from the known geometries obtained from global optimisation given in either x, y, z (Cartesian) coordinates for each atom, or centre of mass x, y, z (Cartesian/COM) coordinates and Euler angles in the y -convention [89], respectively, a geometry in centre of mass x, y, z (Cartesian COM) coordinates and quaternions in the x -convention had to be derived as the integration scheme was given for this convention. It is no problem at all switching between Euler angles in y -convention and Euler angles in x -convention. However quaternions available using either Euler angles in x -convention or y -convention proved to suffer from the shortcoming that it was not possible to re-invert the coordinates unambiguously, i.e. going from Euler angles to quaternions and back to Euler angles. As it was inevitable to have a working transformation procedure, as the potential energy and its derivatives were not obtainable using quaternions, the quaternions were derived directly from the x, y, z (Cartesian) coordinates which seems to be unconventional or maybe even too trivial, as this has so far not been found in the literature.

A known reference geometry was mapped on the geometry the coordinates of which were to be transformed using a rotation matrix. The matrix elements needed for this mapping could then be derived using the common `lapack` routine for solving systems of linear equations. It is important to note, that due to singularities in the linear equation system, this method only works when the geometries are not symmetric, hence the geometries had to be distorted. The rotation matrix of the quaternions in the x -convention is given by:

$$\begin{aligned} \mathbf{E}(q_0, q_1, q_2, q_3) &= \begin{pmatrix} q_0^2 + q_1^2 - q_2^2 - q_3^2 & 2 \cdot (q_1 q_2 + q_0 q_3) & 2 \cdot (q_1 q_3 - q_0 q_2) \\ 2 \cdot (q_1 q_2 - q_0 q_3) & q_0^2 - q_1^2 + q_2^2 - q_3^2 & 2 \cdot (q_2 q_3 + q_0 q_1) \\ 2 \cdot (q_1 q_3 + q_0 q_2) & 2 \cdot (q_2 q_3 - q_0 q_1) & q_0^2 - q_1^2 - q_2^2 + q_3^2 \end{pmatrix} \\ &= \begin{pmatrix} E_{11} & E_{12} & E_{13} \\ E_{21} & E_{22} & E_{23} \\ E_{31} & E_{32} & E_{33} \end{pmatrix} \end{aligned} \quad (11.1)$$

from which the quaternions could then be obtained directly via:

$$q_0^2 = \frac{1}{4}(1 + E_{11} + E_{22} + E_{33}) \quad (11.2)$$

$$q_1^2 = \frac{1}{4}(1 + E_{11} - E_{22} - E_{33}) \quad (11.3)$$

$$q_2^2 = \frac{1}{4}(1 - E_{11} + E_{22} - E_{33}) \quad (11.4)$$

$$q_3^2 = \frac{1}{4}(1 - E_{11} - E_{22} + E_{33}) \quad (11.5)$$

The sign of the quaternions is not uniquely defined, with a total of 16 possibilities. The number of these possibilities may be reduced, however the CPU-time needed to compare the 16 possibilities to the rotation matrix gained from mapping the two geometries onto each other can be neglected. Once having the correct quaternions it is no problem converting between quaternions and Euler angles, as long as one is staying in the same convention.

11.1.2. Velocities and kinetic energy

In order to obtain different starting conditions for a statistic of many molecular simulations of the same system, the initial velocities are drawn at random. The initial set of coordinates of the particles are obtained from the structures obtained by global geometry optimisation and transformed to x, y, z (Cartesian/COM) coordinates and quaternions, see above. For this work the total angular momentum in x, y, z direction, respectively, was set to zero. Hence it was not possible to draw all velocities at random. Also it had to be taken into account that different masses are present, namely for the ion and the water molecules. Therefore, linear momenta \vec{p} were randomly chosen instead. To ensure that the total angular momentum is equal to zero in all three directions in space, for N particles $N - 3$ linear momenta were drawn at random, whereas the rest was calculated according to the constraint. For the corresponding subroutine see appendix section 14.3. As the temperature is directly linked to the velocities via the kinetic energy, a factor was introduced with which the velocities could be scaled after the initial selection according to the desired temperature. See also appendix section 14.3.

11.1.3. Checks on accuracy

Is the algorithm working accurately? This is the first question one should ask after the simulation has been run for the first time. Unfortunately the answer almost always is *no*. What can be done to ensure that the algorithm yields reliable results?

The first check is whether or not the conservation laws are obeyed properly, in particular the total energy should be constant. For a simple Lennard-Jones system, for instance, fluctuations of 1 part in 10^4 in the total energy are generally considered to be within an acceptable

error margin. In case of observed energy fluctuations, these may be reduced by decreasing the time step. Due to limited accuracy of representation of numbers on the computer, errors increase again for time-steps that become too small. Also small time-steps prevent reaching significant or desirable total propagation times, not just because of investing computational expense but also because in any discretised numerical representation each time-step introduces an error, hence the number of time-steps cannot go to “infinity”. A slow up-drift in energy may simply be due to a time step that is too long. However, it can, but does not necessarily have to, indicate a serious program error. The possibility of time step errors can be eliminated by running several simulations using different time steps and then comparing the errors in the energy fluctuation [86]. When simulating molecular systems, errors more easily creep into the program compared to the rather simple atomic case. Energy conservation should hold just as for atomic simulations, although to achieve this for small molecules sometimes a rather short time step is needed, as rotational motion occurs extremely rapidly compared to the translational motion. In case non-conservation is a problem caused by a time step that is too large, this can be checked by freezing out the rotation, i.e. the rotational algorithm is disengaged which would physically correspond to giving the molecules an infinite moment of inertia and zero angular velocity. The total energy should be conserved under these conditions. Vice versa, the angular motion can be tested by temporarily omitting the translational motion, thus fixing the molecular centres of mass at their present positions.

11.1.4. Conservation laws

The conservation laws, i.e. energy conservation and centre of mass conservation, have been checked thoroughly, using different cluster sizes and cluster systems, i.e. $M = \text{Na}, \text{K}, \text{Cs}$, as input and running several simulations with different starting conditions per used system. To show the accuracy of the implemented algorithm, the results obtained for one example system at two different temperatures are described in the following two paragraphs. As input geometry for the examples shown here the global minimum structure of $\text{Cs}^+(\text{H}_2\text{O})_{20}$ and temperatures of $T = 40 \text{ K}$ and $T = 150 \text{ K}$ were chosen. The total simulation time was set to 10 ps using a time step of 0.1 fs, hence arriving at a total of 10^6 time steps.

Centre of mass

The absolute value of deviation of the centre of mass coordinates at $T = 40 \text{ K}$ and $T = 150 \text{ K}$ for $\text{Cs}^+(\text{H}_2\text{O})_{20}$ for all three directions of space are depicted in table 11.1. The absolute values of deviation found are within the numerical error margin for both temperatures and hence the conservation law for the centre of mass can be considered to be obeyed very accurately. The deviation for other systems was within the same range as the one for the example system.

	deviation in x -direction	deviation in y -direction	deviation in z -direction
$T = 40$ K	$2.1233 \cdot 10^{-12}$	$4.9625 \cdot 10^{-14}$	$7.2492 \cdot 10^{-13}$
$T = 150$ K	$1.4532 \cdot 10^{-12}$	$1.8799 \cdot 10^{-12}$	$3.8782 \cdot 10^{-12}$

Table 11.1.: Deviations in the centre of mass coordinates at $T = 40$ K and $T = 150$ K (absolute values) for all three directions of space, respectively

Total energy

The conservation of the total energy is probably the most important conservation law, as it shows that the integration of the equations of motion and the potential are both implemented correctly.

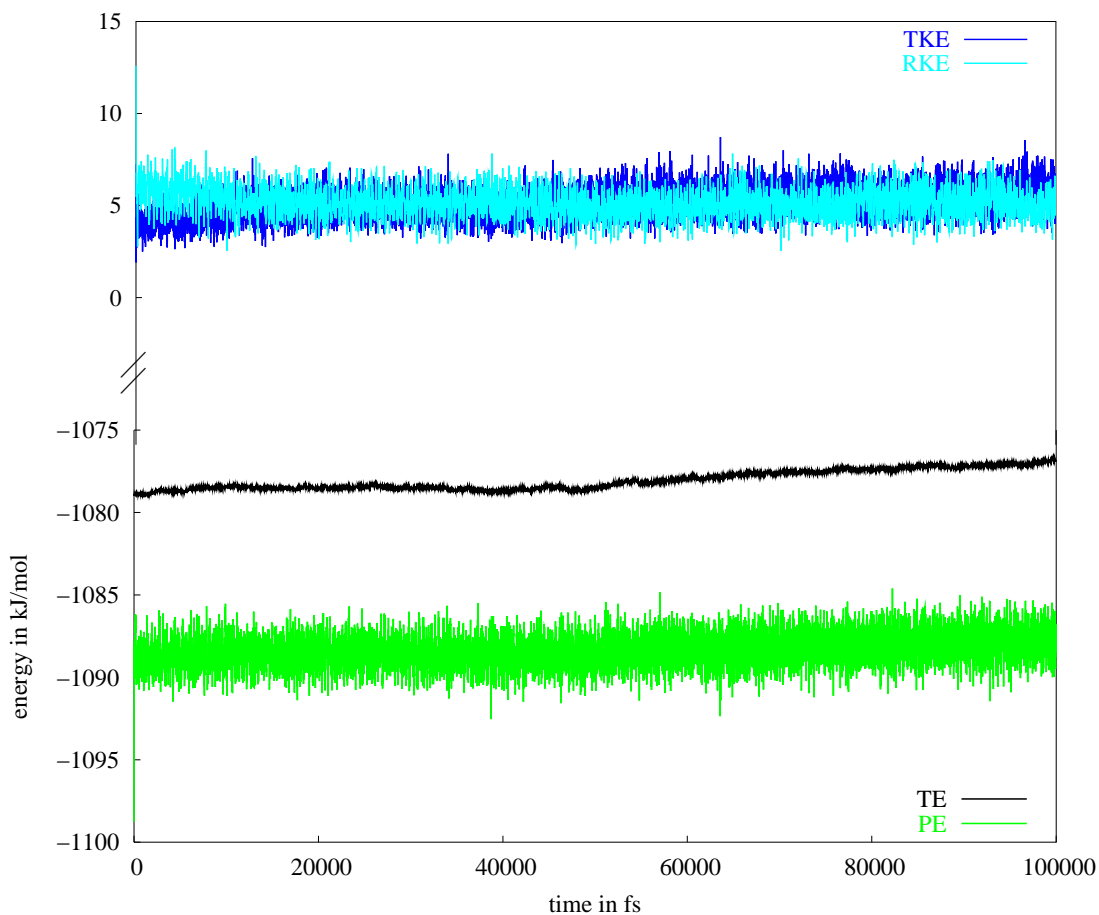


Figure 11.1.: Energy [in kJ/mol] conservation of $\text{Cs}^+(\text{H}_2\text{O})_{20}$ at $T = 40$ K over a total simulation time of 100000 fs, where TKE stands for translational kinetic energy, RKE for rotational kinetic energy, PE for potential energy, and TE for total energy

The energy conservation is usually no problem when simulating atomic systems, however

it can become difficult to fulfil when looking at molecular systems, as already mentioned above. The time step for the examples given here was set to 0.1 fs with a total simulation time of 10 ps thus arriving at 10^6 time-steps total. As the integration of the equations of motion cannot be performed without introducing a numerical error, more time steps will result in non-observance of the energy conservation, i.e. the energy will drift. As energy drifts are most often due to a time step which is too long, a time-step range of 10^{-6} fs up to 1 fs were investigated. A time step of 1 fs was clearly too high, whereas almost no difference was observable in the range of 10^{-6} fs up to 10^{-1} fs. Hence the largest possible time step was chosen in order to save as much computer time as possible and arriving at a longer overall simulation time. Also, as explained above, translational motion and rotational motion were tested separately.

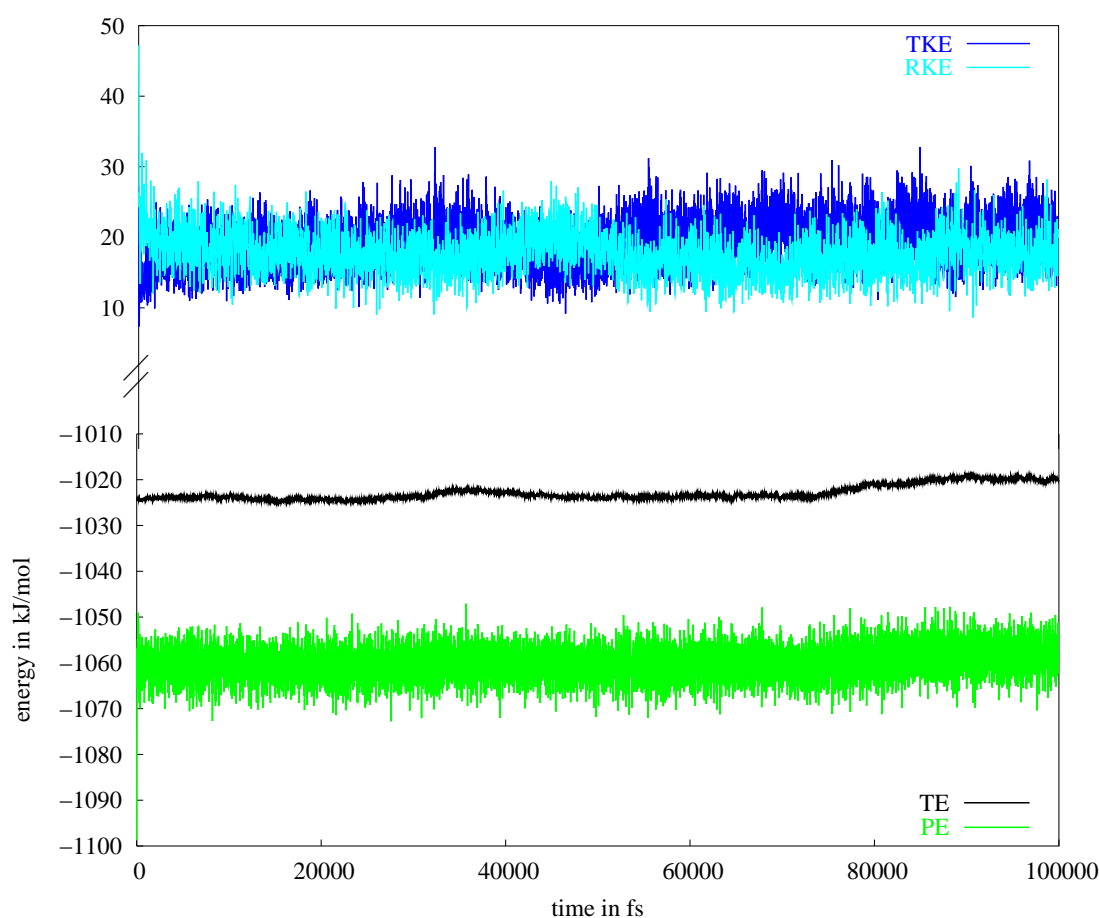


Figure 11.2.: Energy [in kJ/mol] conservation of $\text{Cs}^+(\text{H}_2\text{O})_{20}$ at $T = 150$ K over a total simulation time of 100000 fs, where TKE stands for translational kinetic energy, RKE for rotational kinetic energy, PE for potential energy, and TE for total energy

At $T = 40$ K the total energy is found to be increased by 2.00 kJ/mol from -1078.93 kJ/mol to -1076.93 kJ/mol (see also figure 11.1) which is within an acceptable error margin.

At $T = 150$ K the total energy is increased by 4.34 kJ/mol during the simulation from -1024.39 kJ/mol to -1020.05 kJ/mol (see also figure 11.2). As for higher temperatures the rotations become even faster, this was considered to be accurate as test simulations using smaller time-steps did not yield any improvement. A separate test of translational and rotational motion yielded an excellent energy conservation with an error margin of fluctuations of less than 1 part in 10^5 .

As the algorithm indeed obeys the energy conservation to a sufficient degree it could be extended to the next step, i.e. implementing the Andersen thermostat to obtain a canonical distribution and finally a constraint to be able to compute the free energy of the dissociation of water molecules in the water network.

11.2. Canonical ensemble

As most experiments are performed at constant N, V, T rather than at N, V, E , it is more convenient to run molecular dynamics simulation at constant temperature. As already explained in section 10.4.1, a thermostat is needed in order to keep the temperature fixed. Due to the shortcomings explained in section 10.4.2, the Andersen thermostat was favoured over the Nosé-Hoover Chains, although it behaves unphysical in some respects.

11.2.1. Use of the Andersen thermostat

In order to simulate the experimental conditions as closely as possible, the simulations were performed at different temperatures. The Andersen thermostat was chosen, which has been described in detail in section 10.4.1. As already mentioned the Andersen thermostat simulates the thermal bath via instantaneous stochastic collisions that affect the momentum of the particles. The collisions occur according to a Gauss distribution. The times at which the particles suffer collisions are statistically uncorrelated. The subroutine for the Andersen thermostat and the Gauss function used in this work are given in the appendix sections 14.1 and 14.2, respectively.

For the Andersen thermostat to work most efficiently, the collision frequency ν had to be chosen adequately. The choice of the frequency ν must be made by taking into account two opposite requirements: The frequency has to be high enough in order to yield an efficient thermostat but it must not be too large as the thermostat must not influence the diffusive properties. A choice of a collision frequency ν in the range between $1 \cdot 10^{11}$ and $5 \cdot 10^{11} \text{ s}^{-1}$ seems to satisfy both conditions [85, 104].

11.2.2. Dynamics of $M^+(\text{H}_2\text{O})_n$ with $M = \text{Na}, \text{K}, \text{Cs}$ and $4 \leq n \leq 21$

For all three systems, i.e. $M^+(\text{H}_2\text{O})_n$ with $M = \text{Na}, \text{K}, \text{Cs}$ and $4 \leq n \leq 21$, molecular dynamics simulations were run using a canonical ensemble at four different temperatures: $T = 40$ K, $T = 80$ K, $T = 120$ K, and $T = 150$ K, respectively. These temperatures were selected since experiments such as mass spectrometry and infrared spectroscopy are assumed to be within this temperature region. As already explained in section 2.1, global geometry optimisation methods yield not just the global minimum structure in practice, but also extensive lists of low-energy local minimum structures, which gives an impression of the regions in configuration space that are likely to be most relevant in dynamics studies, without expending the effort of full MD. However due to time constraints, merely global minimum structures were used as input geometries and just six runs (with a total simulation time of 10 ps and a time-step of 0.1 fs each) per structure and temperature could be performed. This does by no means represent a sufficient statistic, especially as no runs with local minimum structures as input were computed, except for the special case of $n = 20$ (see section 11.2.3). Nevertheless, the obtained results still serve as a first guidance concerning trends in the dynamics of the water network.

$\text{Na}^+(\text{H}_2\text{O})_n$

As expected, with rising temperature the movement of the molecules becomes stronger. At $T = 40$ K, mostly hindered rotational motion of molecules is observable and only small hindered translational movements for some water molecules, mostly those sitting on the edge of a water network, thus being not as tightly “bound” by other water molecules. The picture starts to change slightly for $T = 80$ K. The rotational motion still is more intense than the translational motion, though the translational motion becomes stronger. Due to the more intense movements, in some of the medium to larger sized cluster structures hydrogen bonds in the water network start to open up, but are closed again almost instantly. See section 4.6 for labels such as “bond breaking” and “bond formation” used in the following sections for explanations of structural changes observed in the animations obtained from the MD-simulations. Also in the larger clusters, water molecules which are on the edge of the water network start to move back and forth between their original position and a position from where they can participate more strongly in the water network. All these movements still happen rather slowly. Hence no examples shall be depicted for these temperatures.

There is a qualitative change in behaviour between the temperatures $T = 80$ K and $T = 120$ K, as at $T = 120$ K the motion of the water molecules becomes a lot stronger and some cluster structures, mostly smaller sized ones, start to change. The larger clusters are less affected by the temperature rise, as most of the water molecules take part in an optimised

and rather cohesive water network which hinders both their translational and rotational motion. Also, more simply, the total kinetic energy is disturbed over many more degrees of freedom, resulting in less energy available in each of them. Similar to the case of $T = 80$ K, the water molecules at the edge of the water network of medium and large sized clusters try to join the water network. However for larger systems the temperature is not high enough as to produce fundamental changes in the structures examined (some examples are described in more detail below). It should be mentioned again that the cluster structures used as input geometries are global minimum structures, hence they are supposed to be already quite stable compared to local minimum structures. Hence this could lead to the comparatively little changes observed for medium to larger sized structures. This is somewhat underpinned by the fact that a sodium local minimum dodecahedron cage structure (with a potential energy deviating by more than 10 kJ/mol from the global optimum), the dynamics of which was investigated in the course of testing the dodecahedron hypothesis, exhibits rather strong changes for temperatures of $T = 80$ K, and larger as the dodecahedron structure collapsed to a structure similar to that of the global minimum (for further detail see section 11.2.3). Combined with the fact that almost no changes are observable at $T = 40$ K, this strongly suggests that global geometry optimisation indeed produces structures which are relevant in the experiment.

Upon increasing the temperature to $T = 150$ K, the trend already observed for $T = 120$ K becomes more pronounced. Smaller clusters now readily change their structure and also some larger cluster structures open up, although the tendency to exhibit a more or less compact water network still prevails. For more detailed examples see below.

In the case of $\text{Na}^+(\text{H}_2\text{O})_4$, no change in structure, apart from differently distorted tetrahedra, can be observed for any of the temperatures used in the simulation. This does not necessarily imply that other structures are not possible in MD simulations for $\text{Na}^+(\text{H}_2\text{O})_4$. It rather connotes that maybe the total simulation time is too small, or for that matter also the statistic, which is most likely as crossing activation barriers in MD is a rare event. Also a further increase in temperature might lead to structural changes which would imply that the activation barrier for structural changes in $\text{Na}^+(\text{H}_2\text{O})_4$ is too high for temperatures $T \leq 150$ K.

The case of $\text{Na}^+(\text{H}_2\text{O})_5$ is quite similar for temperatures up to $T = 120$ K, i.e. the structure stays basically a more or less distorted pyramid. For $T = 150$ K the pyramid starts to break up (see figure 11.3), changing between pyramidal and other structures. As there are still only five water molecules present, the variety of different cluster structures is still comparatively small. This structural variety increases a lot, when going for instance to $n = 6$ (see figure 11.4) or $n = 8$ (see figure 11.5).

$\text{Na}^+(\text{H}_2\text{O})_6$ already shows significant structural changes at $T = 120$ K. The rate of these

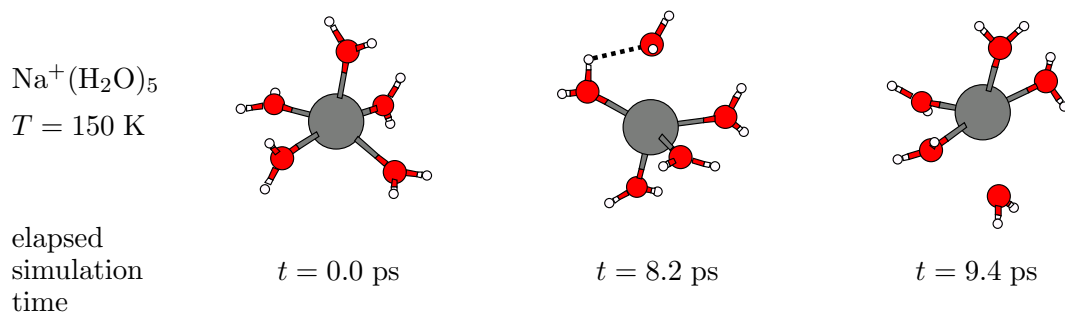


Figure 11.3.: Snapshots from the molecular dynamics simulation of $\text{Na}^+(\text{H}_2\text{O})_5$, using a canonical ensemble, at $T = 150 \text{ K}$

changes increases for $T = 150 \text{ K}$. In figure 11.4, snapshots of both temperatures are depicted. When looking at the actual movie at $T = 150 \text{ K}$, the water molecules seem to wander around the ion, thus participating in somewhat similar or even equivalent structures at another position than before.

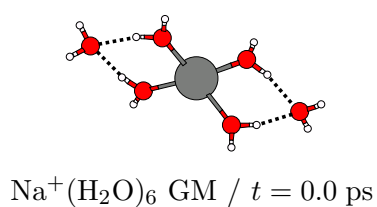
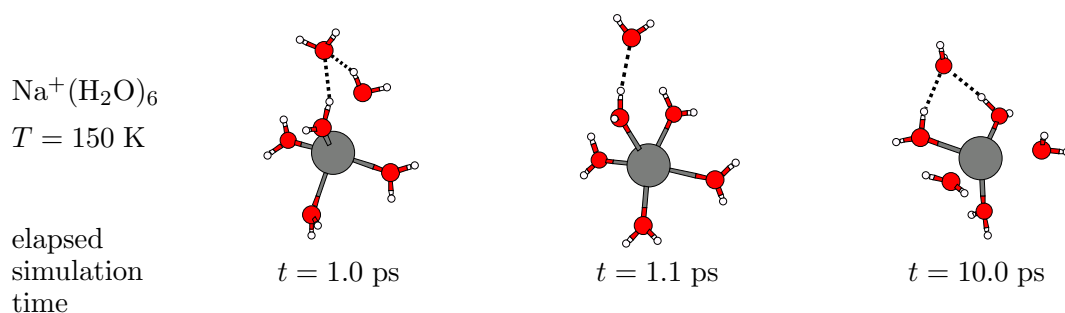
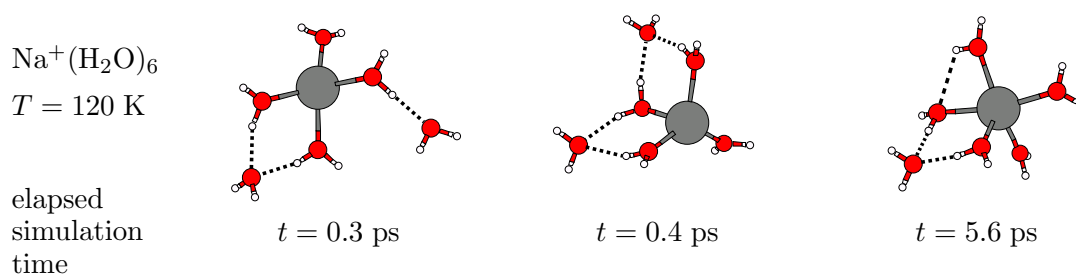
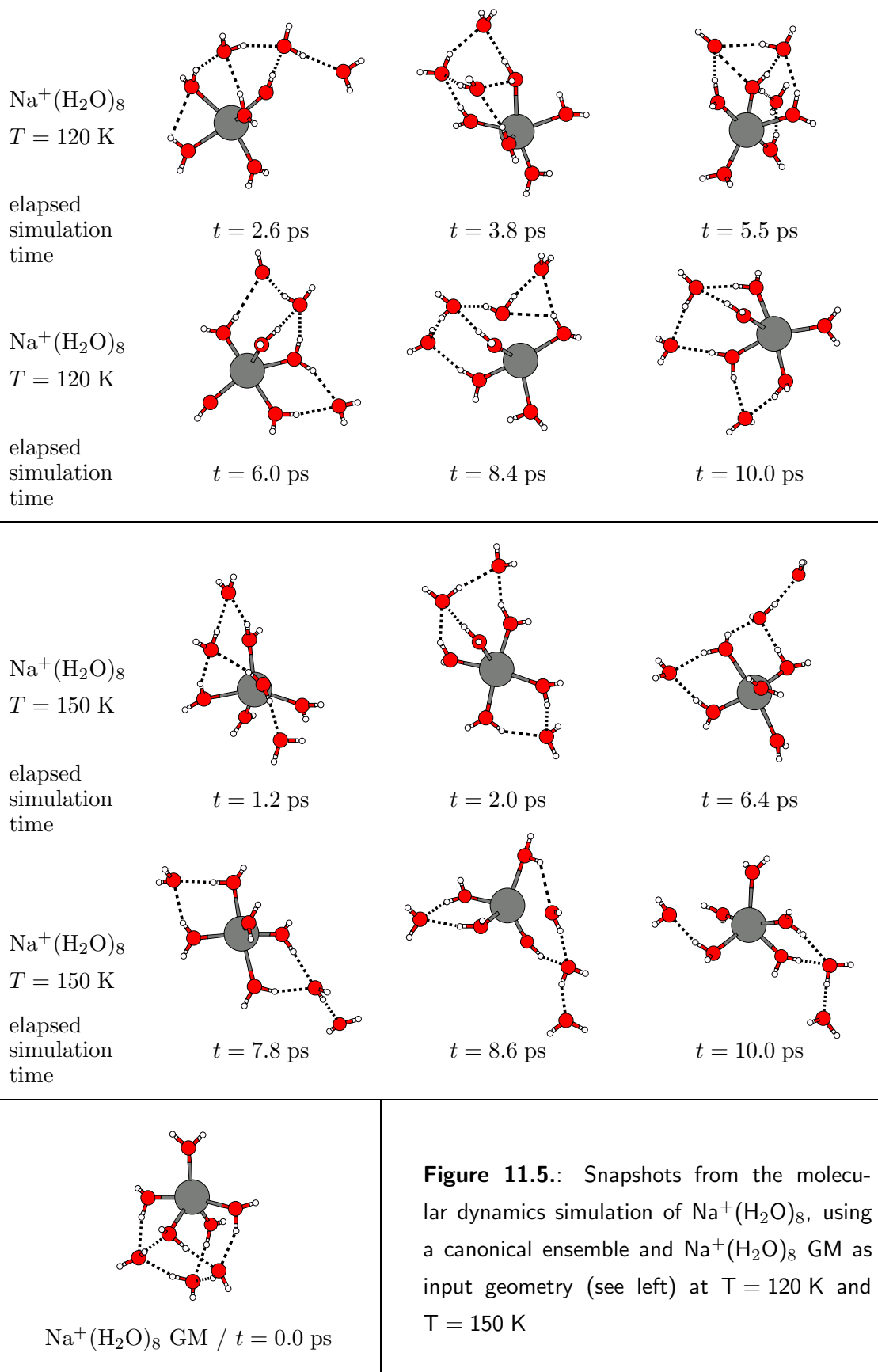


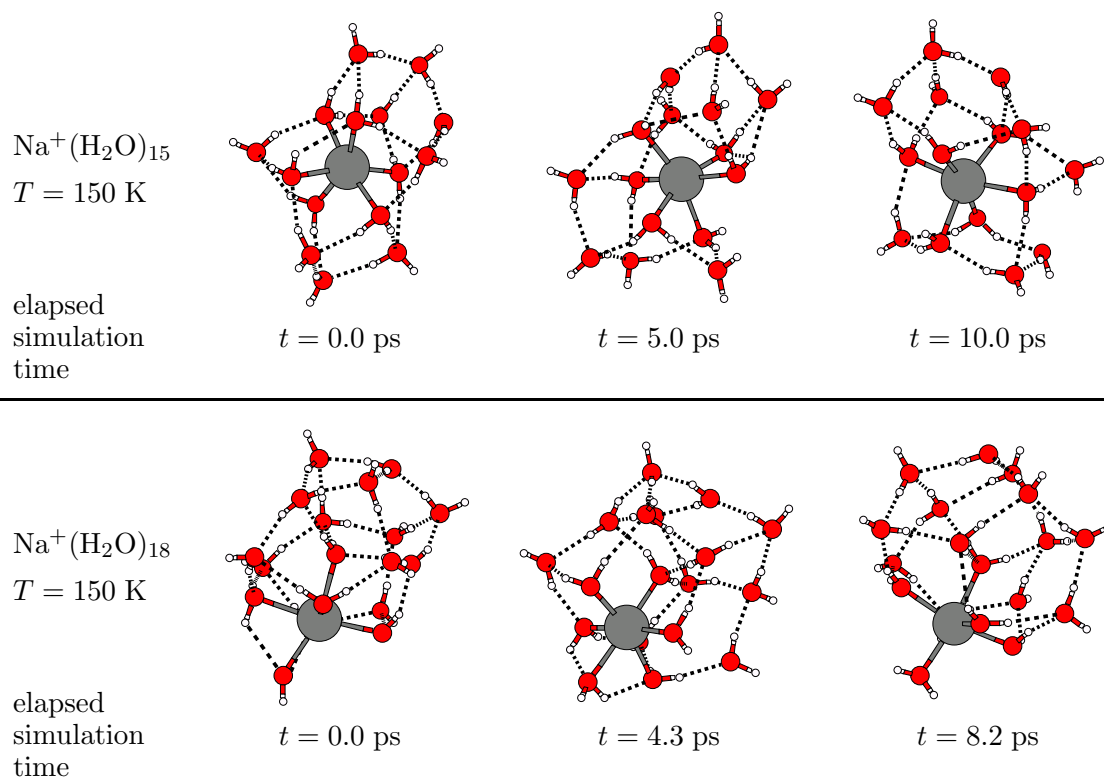
Figure 11.4.: Snapshots from the molecular dynamics simulation of $\text{Na}^+(\text{H}_2\text{O})_6$, using a canonical ensemble and $\text{Na}^+(\text{H}_2\text{O})_6 \text{ GM}$ as input geometry (see left) at $T = 120 \text{ K}$ and $T = 150 \text{ K}$



For structures around approximately $8 \leq n \leq 12$, the largest structural variety can be found. This is most probably due to the fact that with these numbers of water molecules no cohesive water network can yet be established and also due to the number of degrees of freedom still being moderate such that the available energy cannot be distributed over the network as extensively as for larger cluster sizes. Hence the water molecules can move relatively freely around the ion. It is important to note that no boundary box was implemented in the algorithm, hence leaving water molecules the possibility to completely abandon the ion and the other water molecules. One might expect this to happen for smaller clusters, as the water molecules are not yet connected by a cohesive water network. Nevertheless, this does not happen. Sometimes water molecules move farther away from the ion (as shown for $n = 5$ in figure 11.3), however, the influence of the ion and the other water molecules, respectively, is too high for the water molecule to depart. Similar to $n = 6$, structural changes begin to occur for $n = 8$ at $T = 120$ K correlating with the increased temperature. It is probably important to note that for cluster sizes of $8 \leq n \leq 12$, where the water molecules can move somewhat unhindered, the coordination number of 5 is favoured for $5 \leq n \leq 8$, which can be seen both in figure 11.4 for $n = 6$ where the simulation starts with a $(4 + 2)$ structure and proceeds on to different $(5 + 1)$ structures and in figure 11.5 for $n = 8$ where the simulation is started with a $(5 + 3)$ structure, varieties of which can be seen throughout the simulation. Cluster sizes of $9 \leq n \leq 12$ prefer the coordination number 6. The structures try to keep their preferred coordination number throughout the simulation. Hence, for numbers such as $5 \leq n \leq 8$ rather more hydrogen bonds to water molecules arranged in a 2^{nd} -shell are formed instead of forming structures with the coordination number 6 (see also section 4.1 for pair interactions of water molecules in different shells).

The effect of different starting conditions, i.e. different initial velocities per particle, is probably most pronounced for cluster sizes between $8 \leq n \leq 12$ as the structural variety is larger for these structures, as already mentioned above. This will change for medium to larger sized clusters, as due to the cohesive water network both translational and rotational motions are reduced.

Moving on from $n = 8$ to $n = 15$ (see figure 11.6), the cluster structures start to build up a cohesive water network on one side of the ion. Cohesive water networks which are formed only on one side of the ion are typical for $\text{Na}^+(\text{H}_2\text{O})_n$ cluster structures as already explained in section 4.4. As already mentioned, when advancing to medium and larger cluster sizes, i.e. $n \geq 17$, effects of employing different starting conditions become less pronounced, as the water network “forces” the water molecules to their positions. This does not mean that for higher temperatures, such as $T = 120$ K and $T = 150$ K, hydrogen bonds are not broken. Instead although hydrogen bonds are still broken from time to time, water molecules tend to move back to their original position. Water molecules at the “edge” of the water network are still allowed to move more freely, therefore these water molecules try to participate in



$\text{K}^+(\text{H}_2\text{O})_n$

In most aspects $\text{K}^+(\text{H}_2\text{O})_n$ clusters behave similarly to $\text{Na}^+(\text{H}_2\text{O})_n$ clusters. They exhibit little to none translational and only modest rotational movement for temperatures below $T = 80$ K. For increasing temperatures it is again mostly the small cluster structures that show very strong changes, compared to medium and larger cluster sizes where a cohesive water network tends to hinder the movements of the water molecules and where the available kinetic energy is distributed over more degrees of freedom. In contrast to sodium clusters, where the ion-water interactions dominate the cluster structure, the water networks of $\text{K}^+(\text{H}_2\text{O})_n$ cluster structures are more self-supported starting from $n = 16$ which is clearly reflected in the dynamics. Compared to $\text{Na}^+(\text{H}_2\text{O})_n$ clusters, the movements of $\text{K}^+(\text{H}_2\text{O})_n$ clusters below $T = 80$ K are less pronounced and also still slightly slower for $T = 120$ K, whereas at $T = 150$ K basically no difference is observable. As for $\text{Na}^+(\text{H}_2\text{O})_4$, no changes can be found for $\text{K}^+(\text{H}_2\text{O})_4$, not even for $T = 150$ K. For $\text{K}^+(\text{H}_2\text{O})_5$, a (4+1) structure has been found as global minimum. Upon increasing the temperature to $T = 120$ K, this structure no longer seems to be the preferred one (see figure 11.7). Rather a coordination number of 5 is favoured, similar to the structures found for $\text{Na}^+(\text{H}_2\text{O})_5$ which is most probably due to an entropy effect as (4+2) is more rigid than (5+1). The case for $n = 6$ is again comparable to $\text{Na}^+(\text{H}_2\text{O})_6$ (see figures 11.4 and 11.7). Advancing to $n = 7$, the choice of the coordination number 5 still seems to be in favour for $T = 80$ K and $T = 120$ K, though for $T = 150$ K the coordination number 6 can be found more often (see figure 11.8). Nevertheless, a clear preference of certain coordination numbers is less pronounced for the potassium case. For $\text{K}^+(\text{H}_2\text{O})_n$ the structural variety is probably largest for $7 \leq n \leq 9$.

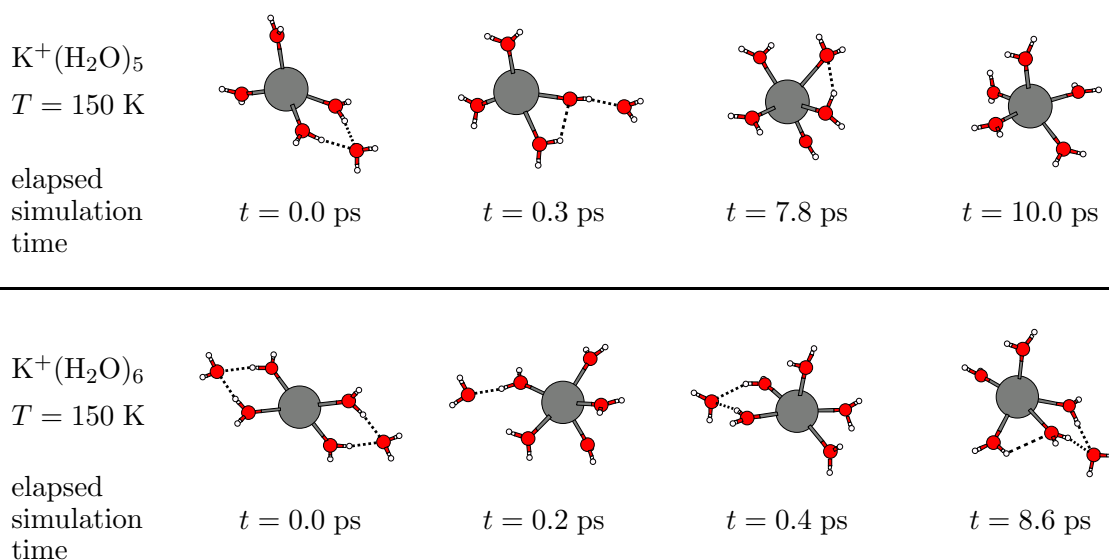
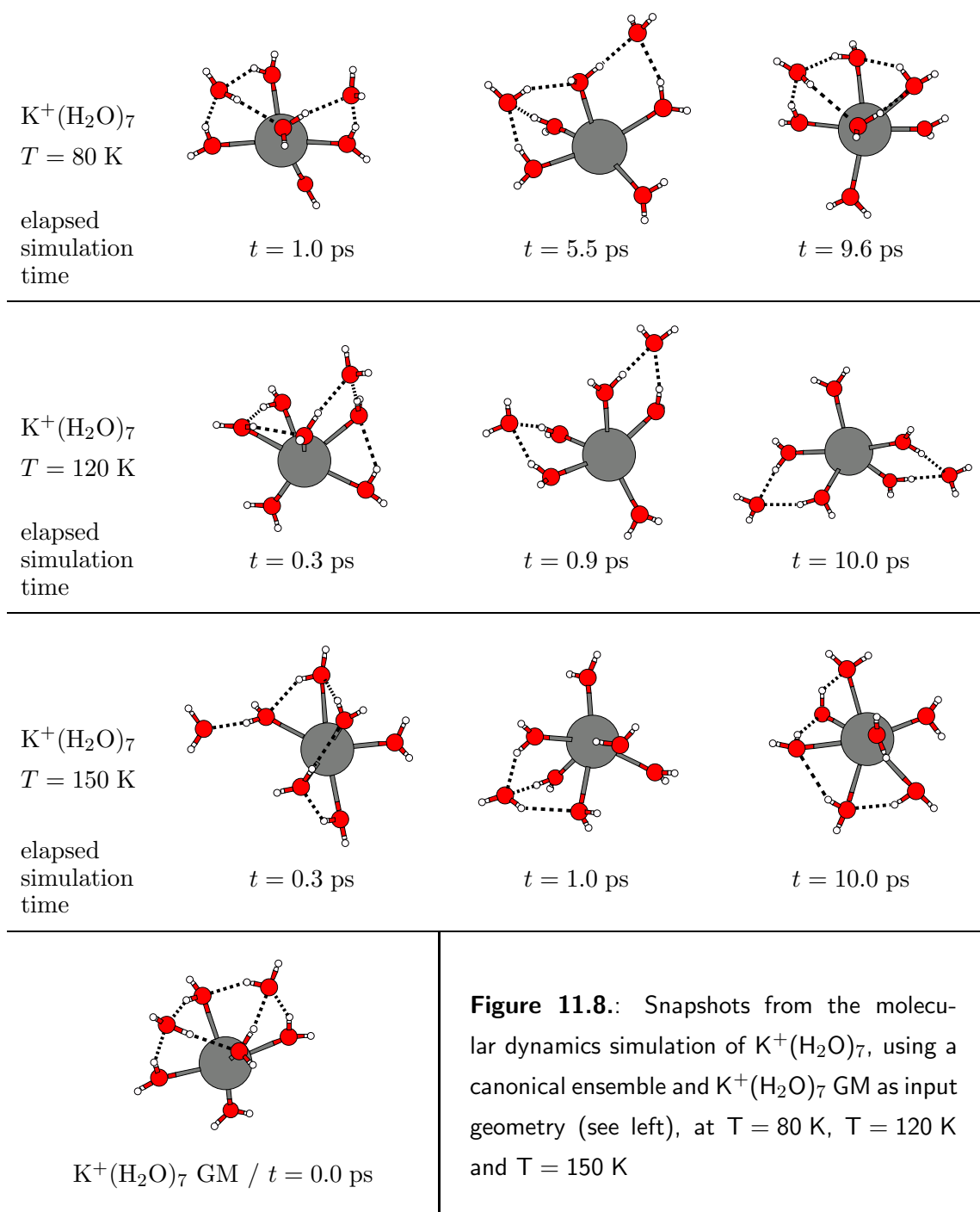


Figure 11.7.: Snapshots from the molecular dynamics simulation of $\text{K}^+(\text{H}_2\text{O})_5$ and $\text{K}^+(\text{H}_2\text{O})_6$, using a canonical ensemble at $T = 150$ K



Starting with $n = 9$, potassium cluster structures do not seem to be able to decide whether they should start preferring annealed rings or whether they should follow the path of sodium clusters. This trend of potassium taking an intermediate position between sodium and caesium clusters has already been explained in detail for static structures in section 4.4. This picture is also seen in the dynamics of cluster sizes around $9 \leq n \leq 14$, as during the total simulation time these cluster structures change back and forth between open structures and structures forming annealed rings, see for example figure 11.9 for $n = 10$: The simulation is

started with a structure which mostly contains annealed rings which are then broken apart during the simulation, as depicted for $t = 6.9$ ps and $t = 9.1$ ps, while in between the cluster tries to re-form new annealed rings.

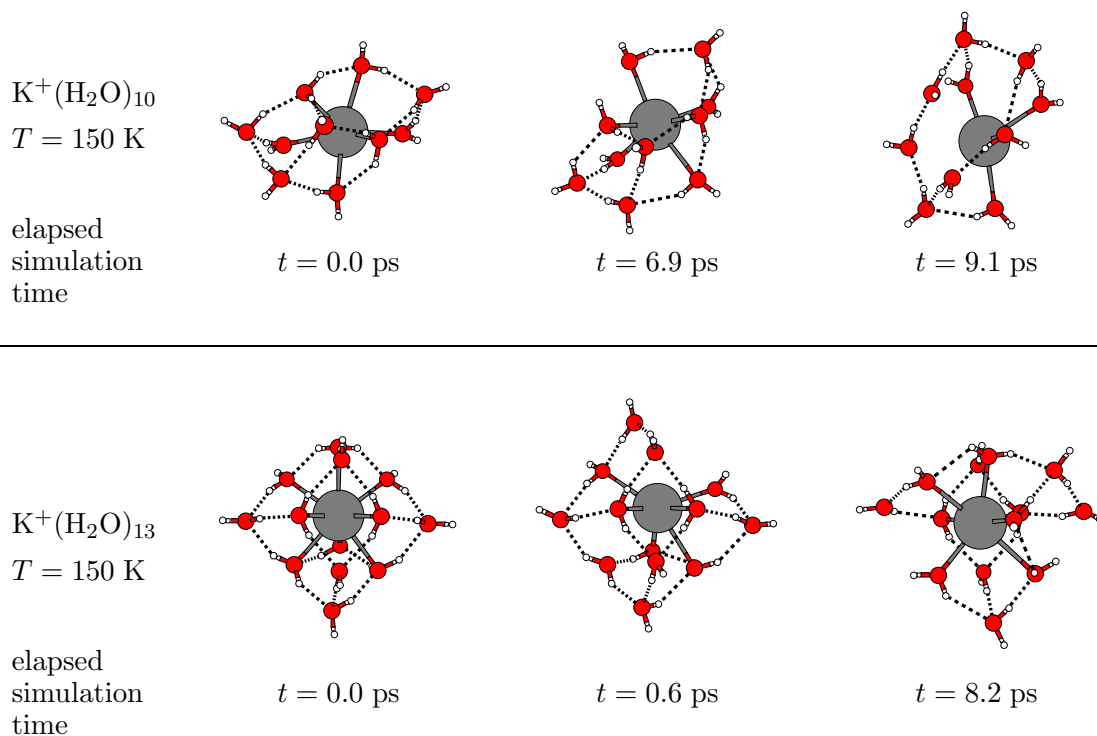


Figure 11.9.: Snapshots from the molecular dynamics simulation of $K^+(H_2O)_{10}$ and $K^+(H_2O)_{13}$, using a canonical ensemble at $T = 150$ K

Increasing the number of water molecules to $n = 16$, the first shell closure around the potassium ion can be observed (see section 4.4). For cluster sizes with $n \geq 16$, potassium clusters behave more like caesium clusters, i.e. preferring annealed rings over more open structures. Looking at the dynamics of these cluster sizes, different starting conditions again seem to have a lesser impact on the simulations, as already found for sodium clusters (see figure 11.10). The water network more or less keeps its shape, occasionally opening and closing one or the other hydrogen bond. Example snapshots which depict these bond-openings are given in figure 11.10 for $n = 16$ at $t = 3.1$ ps and for $n = 17$ at $t = 2.4$ ps, while the snapshots for $n = 16$ and $n = 17$ at $t = 10.0$ ps and $t = 9.9$ ps, respectively, show yet again closed water networks. $n = 16$ happens to be a magic number for $K^+(H_2O)_n$ and in section 4.4 it was assumed that maybe this magic number is due to a shell closure, thus exhibiting a stronger water network compared to its smaller relatives. In section 4.5.1 it was additionally speculated that magic numbers might be due to a structural pattern all magic numbers seem to have in common, namely exhibiting only water molecules which have a coordination number of either 3 or 4. Hence the dynamics of $K^+(H_2O)_{16}$ were compared to that of its immediate neighbours $K^+(H_2O)_{15}$ and $K^+(H_2O)_{17}$ bearing this pattern in mind. Although DA molecules seem to

be able to move more freely, as they are only bound to two other water molecules, so far no significant difference between the behaviours of the respective cluster hulls could be found. One simple reason may be that the results obtained here by no means represent a sufficient statistic. But then $n = 16$ is only a very weak magic number. Therefore this topic further shall not be explored any further at this stage. The more important magic number $n = 20$ is treated in a separate section (see section 11.2.3).

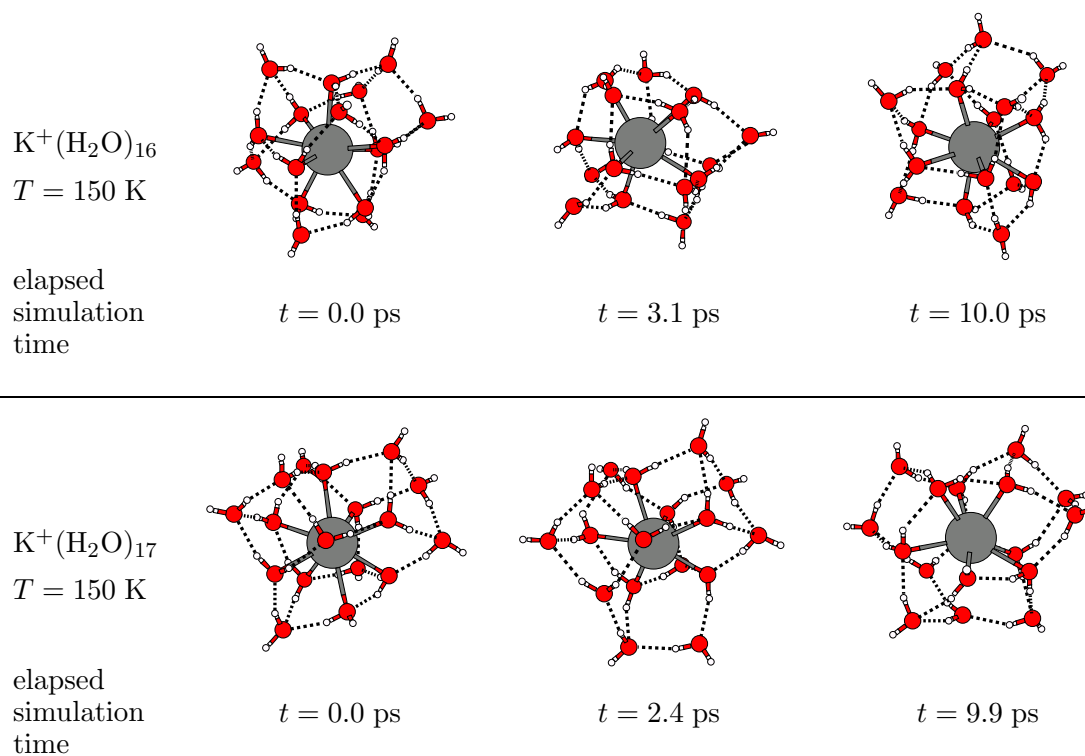
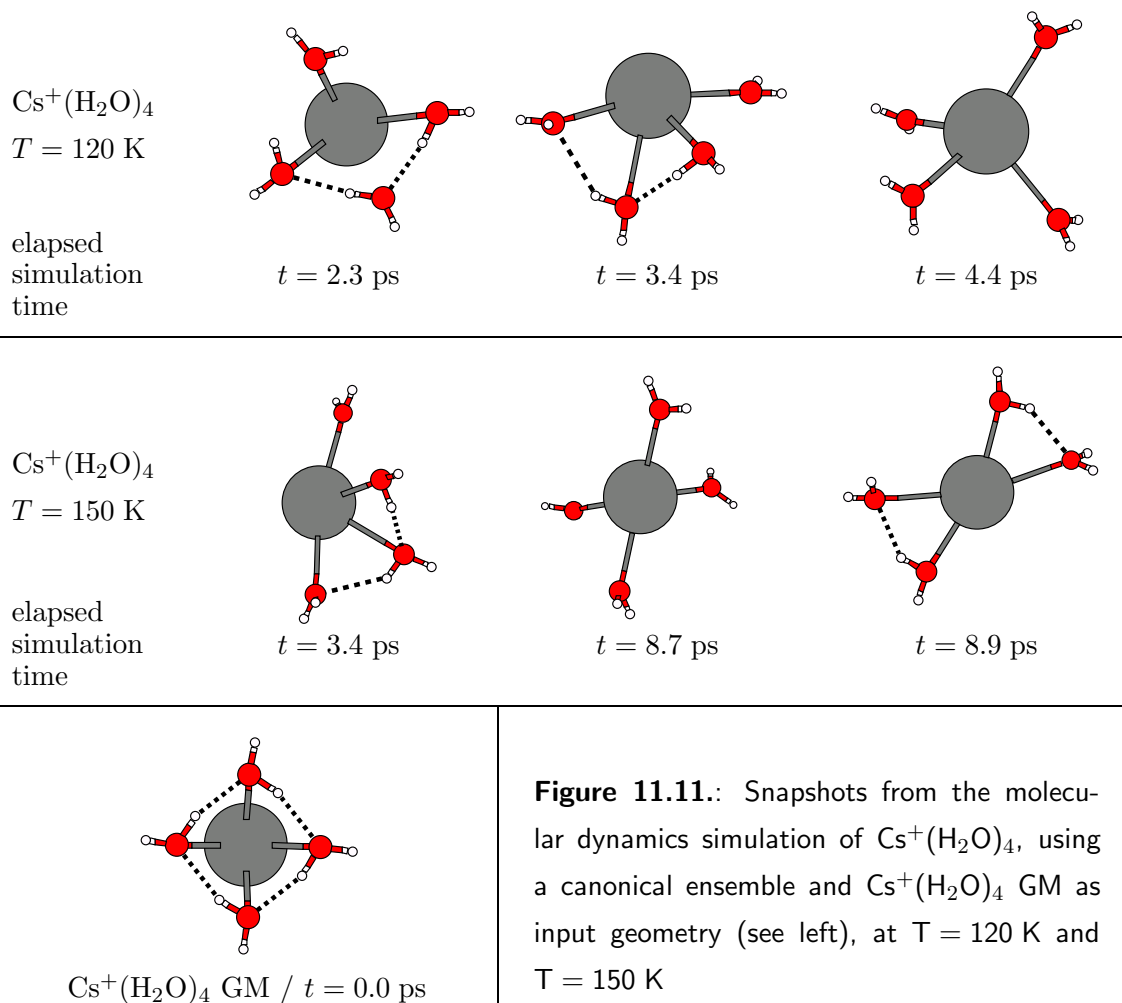


Figure 11.10.: Snapshots from the molecular dynamics simulation of $\text{K}^+(\text{H}_2\text{O})_{16}$ and $\text{K}^+(\text{H}_2\text{O})_{17}$, using a canonical ensemble at $T = 150 \text{ K}$

$\text{Cs}^+(\text{H}_2\text{O})_n$

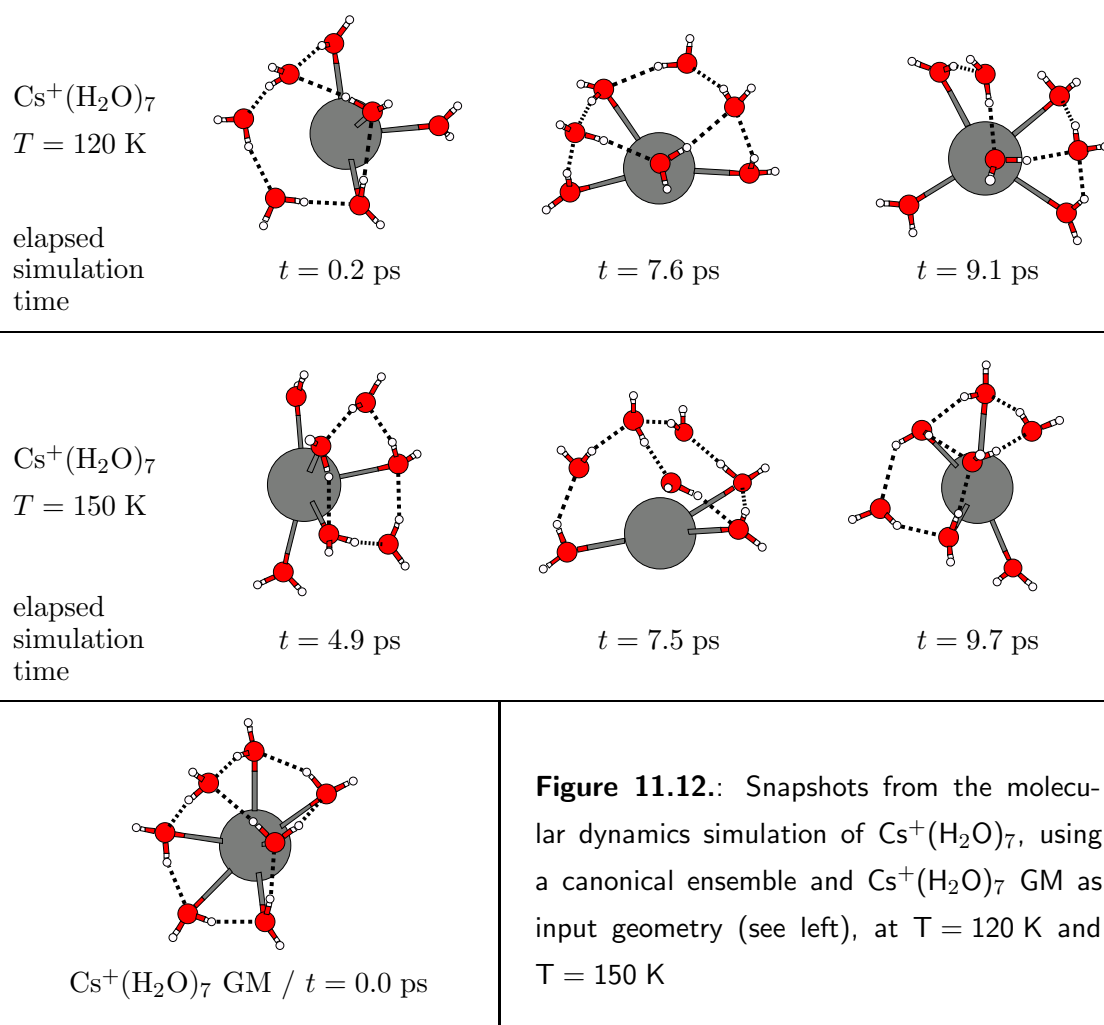
In some though not all aspects the dynamics of $\text{Cs}^+(\text{H}_2\text{O})_n$ is comparable to the dynamics of both $\text{Na}^+(\text{H}_2\text{O})_n$ and $\text{K}^+(\text{H}_2\text{O})_n$: The greatest number of changes in cluster structure and simultaneously the most serious changes are observed for small cluster sizes, whereas the bigger the clusters get, the less pronounced the movements become. The latter is again due to more degrees of freedom and to the movements being hindered by the water network surrounding the ion. As already observed when comparing potassium clusters with sodium clusters, the movements for caesium cluster structures below $T = 80 \text{ K}$ are even less pronounced than those observed for potassium clusters. In other words basically no translation is observed for $T = 40 \text{ K}$ and the rotational motion occurs rather slowly. For $T = 80 \text{ K}$, the translational movement becomes visible more easily, though it is still very small, whereas the rotational

movements become more distinct. Unlike both potassium and sodium clusters, for caesium clusters no opening of any of the hydrogen bonds could be observed below $T = 80$ K. However when increasing the temperature to $T = 120$ K movements become apparent and even more so for $T = 150$ K. The behaviour gap between $T = 80$ K and $T = 120$ K is quite outstanding for $\text{Cs}^+(\text{H}_2\text{O})_n$, though it is also present for the other two systems in an alleviated form. As the gap becomes larger when increasing the mass of the ion, very simply the ion mass may be responsible. An ion as light as sodium can experience stronger movements at lower temperature than the caesium ion, which would in turn also affect the water molecules.



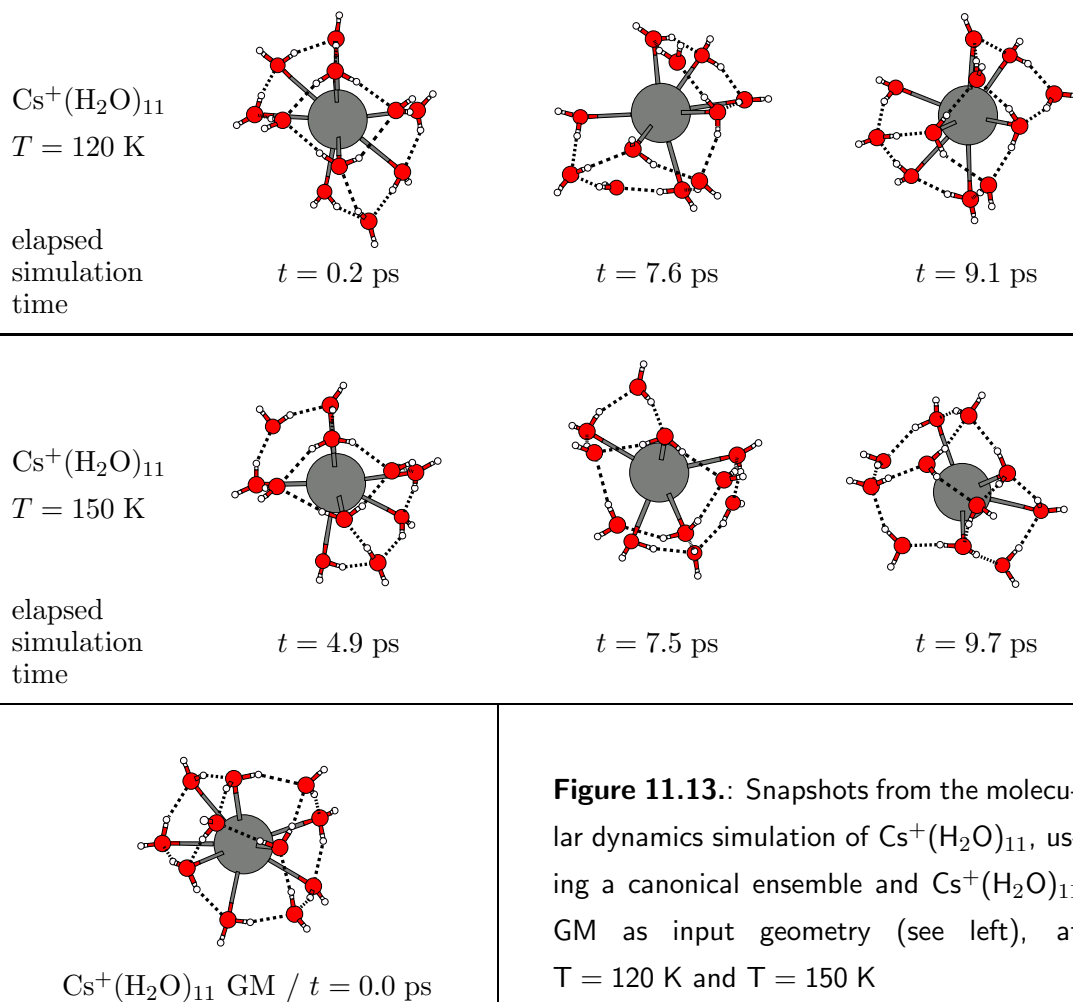
For small cluster sizes, i.e. up to approximately $n = 10$, $\text{Cs}^+(\text{H}_2\text{O})_n$ clusters tend to form rings as soon as possible compared to their relatives $\text{Na}^+(\text{H}_2\text{O})_n$ and $\text{K}^+(\text{H}_2\text{O})_n$. Looking at the dynamics of $\text{Cs}^+(\text{H}_2\text{O})_4$ at $T = 120$ K and $T = 150$ K (see figure 11.11), one observes that $\text{Cs}^+(\text{H}_2\text{O})_4$ readily opens up its four-membered ring. In the course of the simulation, the tetrahedron seems to be the preferred structure, as after the ring opening the structures interchange between the structures depicted in figure 11.11 and the tetrahedron. Once

the four-membered ring has been broken up, there is no difference observable regarding the swiftness of the movements of the molecules when comparing the two temperatures. For $T = 150$ K the four-membered ring is totally destroyed after approximately 0.3 ps. However, at $T = 120$ K it takes about 40 ps for the ring to be completely destroyed. Nevertheless, one already observes occasional bond openings in the four-membered ring for $t \leq 40$ ps (see for example figure 11.11 at $t = 2.3$ ps) which however are retracted again very fast until the movements finally become too strong (at around $t = 40$ ps) for a retraction of these openings which then results in the destruction of the ring. Again, as observed above for $\text{K}^+(\text{H}_2\text{O})_n$, it is likely that this preference of a LM over a GM is an entropy effect.



Moving on to $n = 7$, the picture changes slightly. Similar to the cluster structures of $\text{K}^+(\text{H}_2\text{O})_n$ with $9 \leq n \leq 14$, $\text{Cs}^+(\text{H}_2\text{O})_7$ tries a mixture between an open structure and structures where annealed rings are formed (see figure 11.12). For $n = 7$ the simulation is started with a structure consisting of two annealed rings, one five-membered and one four-membered ring. For $T = 120$ K snapshots where only the four-membered ring has been

destroyed are depicted for $t = 0.2$ ps and $t = 7.6$ ps. While at $t = 0.2$ ps only one water molecule is attached to the five-membered rings at $t = 7.6$ ps both remaining water molecules are attached to the five-membered ring again. For $t = 9.1$ ps a snapshot is depicted where all rings have been destroyed while the water molecules still try to preserve as many hydrogen bonds as possible. For $T = 150$ K the first two snapshots, i.e. at $t = 4.9$ ps and $t = 7.5$ ps, are comparable to the first two snapshots at $T = 120$ K, i.e. $t = 0.2$ ps and $t = 7.6$ ps, while the snapshot at $t = 9.7$ ps shows a structure where the cluster again managed to form two annealed four-membered rings. According to the observations made for $n = 4$, it takes comparatively longer to break up the rings at $T = 120$ K for the first time. Once the rings are open, changes occur more rapidly, now more comparable to the swiftness of the changes at $T = 150$ K. Compared to potassium clusters, caesium clusters still show their tendency to keep a large number of hydrogen bonds, sometimes resulting in a long chain of water molecules wrapped around the ion.



This trend continues for $7 \leq n \leq 11$ although it becomes less pronounced for $9 \leq n \leq 11$ as the water network already forms one half of a shell surrounding the central ion (see figure 11.13). In figure 11.13 the starting structure comprises a water network consisting of three

five-membered and one four-membered ring. At $T = 120$ K the structures at both $t = 0.2$ ps and $t = 9.1$ ps still form annealed rings while the snapshot at $t = 7.6$ ps depicts a structure where this annealed ring system is almost broken apart. For $T = 150$ K the snapshots at both $t = 4.9$ ps and $t = 9.7$ ps again depict structures where the water network is still almost intact while the structure obtained at $t = 7.5$ ps shows broken up rings. Also for $n = 11$ a clear difference can be seen between the two temperatures $T = 120$ K and $T = 150$ K, as the structure opens up even less readily for $T = 120$ K than for the case $n = 7$. The movements also become somewhat slower compared to the velocities at $T = 120$ K and $n = 7$. Hence at $n = 11$ and $T = 120$ K a tendency of the cluster to prefer a structure similar to the initial structure starts to be visible.

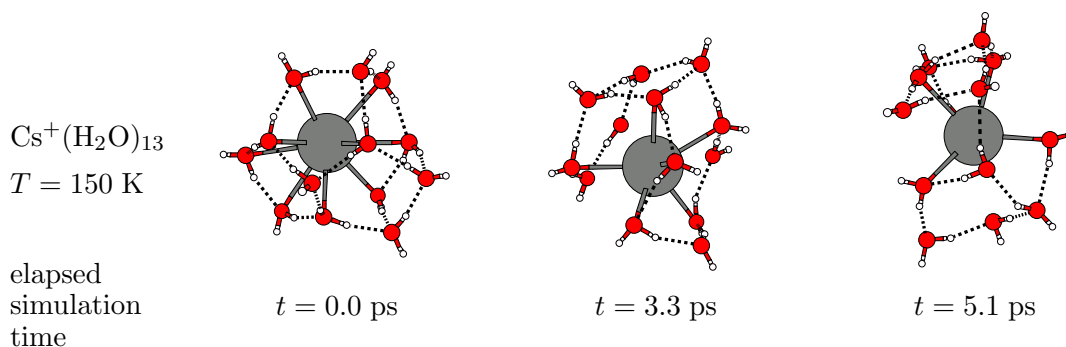


Figure 11.14.: Snapshots from the molecular dynamics simulation of $\text{Cs}^+(\text{H}_2\text{O})_{13}$, using a canonical ensemble at $T = 150$ K

Moving onwards to $n = 13$ (see figure 11.14) the cluster structures start to less readily open up also for $T = 150$ K, as already found for $n = 11$ and $T = 120$ K. The snapshots depicted in figure 11.14 give a rare example of a simulation in which the cluster structure still breaks. However, it takes less than 1 ps after the break-up for the cluster structure to obtain a shape similar to the initial structure, as the coherence of the water network starts to become stronger. This trend continues for even larger systems. Similar to $\text{K}^+(\text{H}_2\text{O})_{16}$, a first shell closure is observed at $n = 18$ for the case of caesium (see section 4.4), which again is a magic number. Comparing the dynamics of cluster structures with $17 \leq n \leq 19$, one observes that although the trend that the already rather cohesive water network hinders the movements of all three cluster sizes equivalently, cluster structures with $n = 18$ open up hydrogen bonds extremely seldom, even more seldom than $n = 17$ and $n = 19$. Again, it should be mentioned that the results presented here do by no means represent a sufficient statistic. Nevertheless, these findings indicate that $n = 18$ may be dynamically more stable than $n = 17$ and $n = 19$. In figure 11.15 an example is given of one of the rare occasions at $T = 150$ K where indeed hydrogen bonds are broken up for $\text{Cs}^+(\text{H}_2\text{O})_{18}$, see snapshots at $t = 0.2$ ps and $t = 5.2$ ps, respectively. The magic number $n = 20$ will be treated in a separate section (see section 11.2.3 below) as also for sodium and potassium clusters, as this number is considered to be more important according to the dodecahedron hypothesis proposed in the literature.

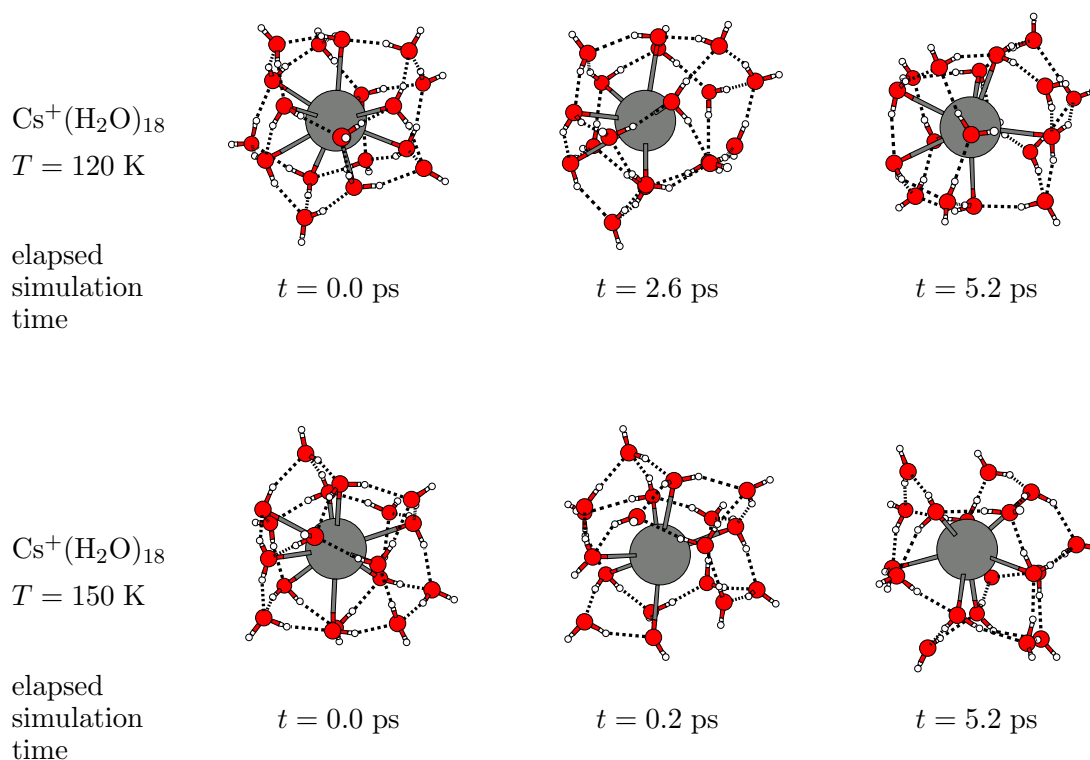


Figure 11.15.: Snapshots from the molecular dynamics simulation of $\text{Cs}^+(\text{H}_2\text{O})_{18}$, using a canonical ensemble at $T = 120 \text{ K}$ and $T = 150 \text{ K}$

11.2.3. Dynamics of dodecahedral cage structures

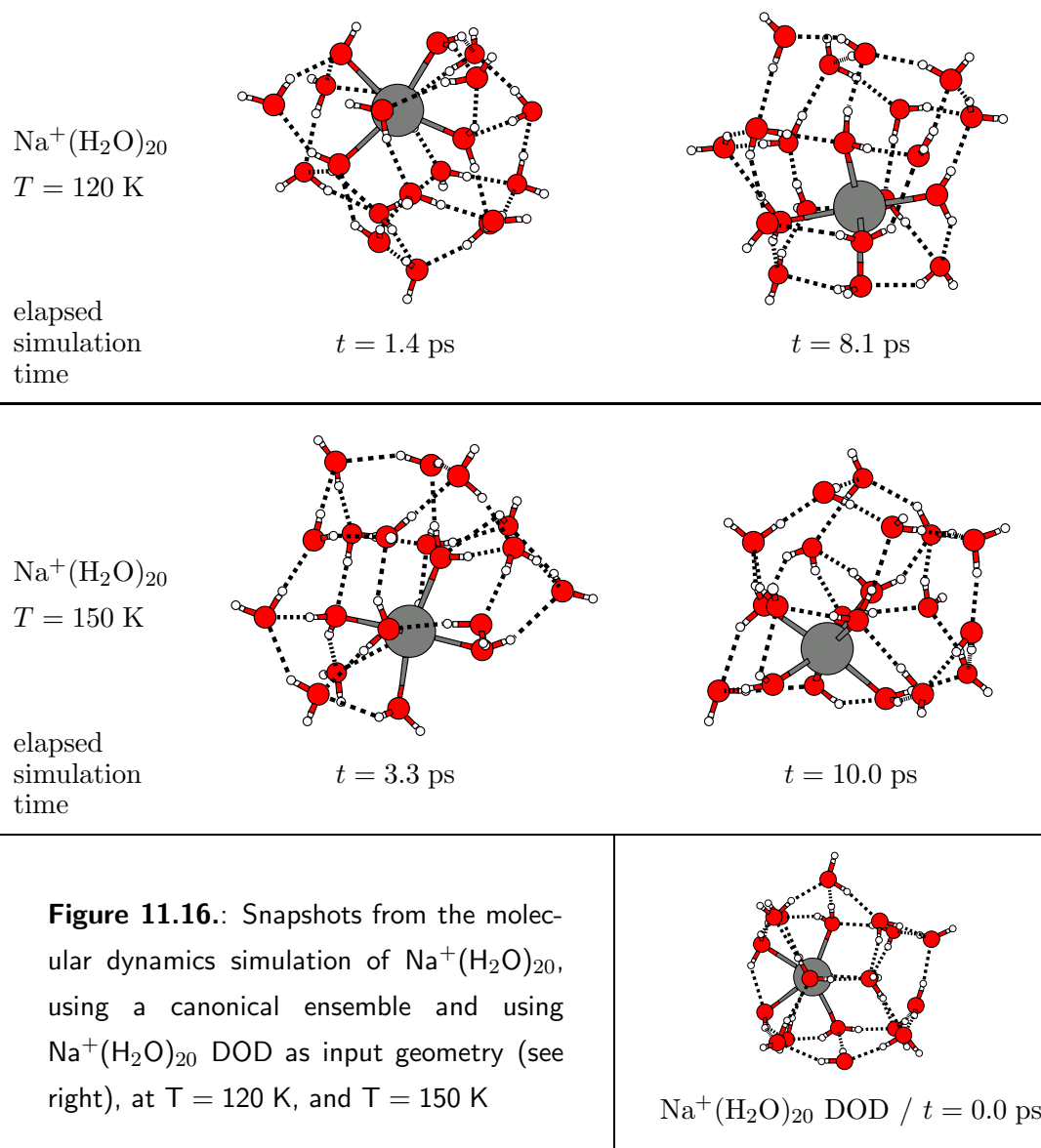
As already mentioned in section 4.5, in case of $\text{Cs}^+(\text{H}_2\text{O})_{20}$ the global minimum structure (dodecahedral) and the best non-dodecahedral structure are almost isoenergetic. The pair potential terms between the cation and all water molecules add up to 399.65 kJ/mol for the dodecahedron and 403.29 kJ/mol for the non-dodecahedron. Hence, the water network contributions appear to be better for the dodecahedral-like cage. However, this just barely over-compensates the better embedding of the ion in the non-dodecahedral cage structure to a final difference of not even 1 kJ/mol. As stated in section 4.5, a water hull consisting only of five-membered rings may have a kinetic advantage: It is speculated that sequential ring enlargement may be a preferred mode of water cluster growth, as seen in the experimental environment of helium droplets [45]. Also, for the pure water hexamer, a single six-membered ring is energetically less favourable than two annealed four-membered rings. Therefore, the dodecahedron may form a natural culmination point. Hence, to tackle the issue of magic numbers being due to a possible kinetic advantage, both structures were first submitted to cluster dynamics using a canonical ensemble and also to constrained dynamics in order to evaluate the free energy of the dissociation of single water molecules from both water hulls (see following section). For comparison canonical ensemble dynamics were also computed for

$\text{K}^+(\text{H}_2\text{O})_{20}$ and $\text{Na}^+(\text{H}_2\text{O})_{20}$ (see below).

When comparing the dynamics of both structures of $\text{Cs}^+(\text{H}_2\text{O})_{20}$, no difference whatsoever could be observed for temperatures $T = 40$ K, $T = 80$ K, and $T = 120$ K, respectively. Rather, both structures follow the trends given in section 11.2.2, namely no changes occur apart from small hindered rotational motion and even smaller hindered translational motion of individual molecules. When increasing the temperature to $T = 150$ K, again for the dodecahedron structure not even a single hydrogen bond opening could be observed, though the water molecules wiggle around a little more. This does not necessarily mean that bond openings do not occur at all for the dodecahedral structures as due to limited disk space not each time-step was recorded for the analysis. However, it is assumed that according to statistics at least one or two bond openings should have been visible in at least one of the movies. For the non-dodecahedral cage structure occasional bond openings between two annealed four- and six-membered rings were observed. Hence this might be a weak indication that indeed the overall dynamical stability of the dodecahedron structure is better compared to that of a non-dodecahedron.

For $\text{K}^+(\text{H}_2\text{O})_{20}$, the global minimum is also a dodecahedron shaped cluster structure (see section 4.5). Both the global minimum structure and the best non-dodecahedral structure were submitted to molecular dynamics simulation. Again, for $T = 40$ K and $T = 80$ K, apart from rotational and small translational motion nothing of importance occurs. For $T = 120$ K and $T = 150$ K occasional hydrogen bond openings were observable for both cluster structures. Hence from just comparing the dynamics of the two different structures no further insight into the status of the dodecahedron hypothesis could be gained in the case of $\text{K}^+(\text{H}_2\text{O})_{20}$.

In the case of $\text{Na}^+(\text{H}_2\text{O})_{20}$, the dynamics of a constructed and optimised dodecahedron shaped structure (see section 4.5) was compared to that of the global minimum structure. As already explained in section 11.2.2, for $T = 40$ K and $T = 80$ K apart from very small rotational and even smaller translational motion nothing much occurs in the case of the global minimum structure. Even when increasing the temperature to $T = 120$ K or $T = 150$ K, the water molecules of the water network only wiggle around their initial positions whereas the water molecules on the edges move between positions where they take up an active part in the water network and positions that allow the sodium ion to have its preferred coordination geometry. Overall the cluster structure stays the same and does not change its general appearance during the simulation. However, the behaviour of the dodecahedron shaped water hull is different. Similar to the dynamics of the global minimum structure, for temperatures of $T = 40$ K no structural changes or hydrogen bond openings occur, apart from water molecules wiggling around their positions, whereas, upon increasing the temperature to $T = 80$ K, the first serious changes can be observed. The dodecahedron structure of $\text{Na}^+(\text{H}_2\text{O})_{20}$ is extremely



distorted, as the sodium ion is simply too small to fill the cage. Hence the ion clings to one side of the dodecahedron hull (see figure 11.16) which leaves it “open” to one side. The number of water molecules arranged around the central ion in a 1st-shell (see also section 4.1) is equal to 6, however due to the cage-like structure of the water network they cannot be arranged in an octahedron shape which is the preferred coordination geometry of the global minimum structures of $n \geq 17$. This implicates that one of the 1st-shell water molecules that is nearby the “open side” of the ion will try to move into a position which allows the sodium ion to obtain an octahedral shaped 1st-shell coordination geometry. And indeed this is found to be the general procedure. One 1st-shell water molecule close to the “open side” of the sodium ion moves towards the centre of the clathrate cage which cannot be filled by the sodium ion alone. While this change occurs the dodecahedron hull starts to break apart such that the water molecule is allowed to move to its preferred position while maintaining as

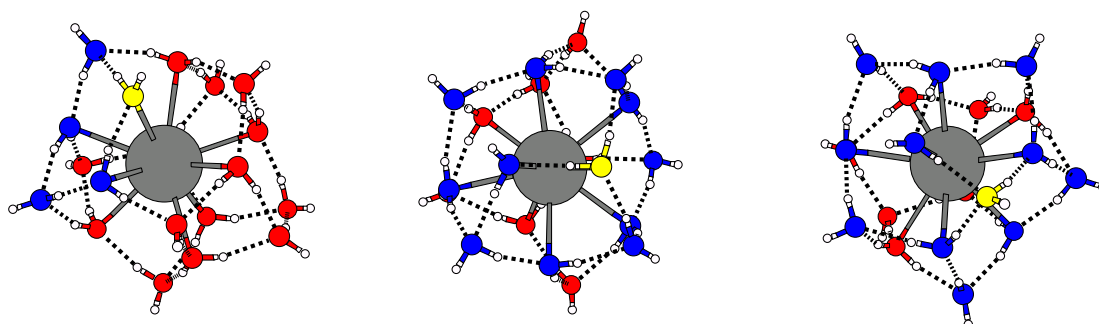
many hydrogen bonds as possible. In other words during the simulation the five-membered rings are broken apart and new rings are reformed as soon as possible though now also four- and six-membered in order to lessen the strain on the water network. Upon increasing the temperature to $T = 120$ K and $T = 150$ K, these changes are advanced even further as at $T = 150$ K the dodecahedron cluster structure arrives at a structure very similar to the global minimum structure by the end of the simulation. To ensure that this was not just plain coincidence, more simulations were run on this special case which confirmed the findings: In all simulations performed, the dodecahedron shaped structure changed, taking up forms which were equivalent or very close to the global minimum structure. This is indeed a very surprising result as the MD-simulations performed were just basic MD-simulations, merely enforcing a canonical ensemble, but by no means forcing any structural transformations. Also these structural transformations do not just occur occasionally but very frequently. However, barrier crossings usually are very rare occasions in MD, hence one would not expect the same things to happen too frequently. Also, as the energy landscape of systems of this size is extremely complex one could not expect this to happen in different trajectories. A possible explanation might be that the barriers are indeed relatively small, thus allowing frequent crossings, i.e. in other words allowing a simple deformation pathway connecting these two seemingly so different structures. Another possibility might be, that several different levels exist on the energy landscape resulting for example in a big funnel towards the global minimum on a large scale and on a smaller scale in a large number of smaller sub-minima of this structure which are only divided by low energy barriers. In any case these results underpin the fact that $\text{Na}^+(\text{H}_2\text{O})_{20}$ is not magic due to the fact that the water network is able to form a clathrate like structure (including the dodecahedron). Instead structures similar to the off-centred, non-dodecahedral global minimum structure are preferred.

These findings are not only important with respect to the fact that the non-existence of the magic number $n = 20$ could be clarified in the case of $\text{Na}^+(\text{H}_2\text{O})_{20}$, they also prove that indeed the use of global geometry optimisation is justified as a tool to circumvent the effort and expenses of full molecular dynamics simulation.

11.3. Constrained dynamics

As already mentioned several times, the magic number $n = 20$ is most prominent in the case of $\text{Cs}^+(\text{H}_2\text{O})_{20}$, rather weak for $\text{K}^+(\text{H}_2\text{O})_{20}$, and not observed to be a magic number for $\text{Na}^+(\text{H}_2\text{O})_{20}$. In the previous section, it was found that when submitting a dodecahedron shaped structure of $\text{Na}^+(\text{H}_2\text{O})_{20}$ to a molecular dynamics simulation using a canonical distribution, this structure will collapse during the simulation to a shape very close to that of the global optimum. The conclusion to be drawn was that the sodium ion is simply too small for $\text{Na}^+(\text{H}_2\text{O})_{20}$ to prefer a dodecahedron shaped structure or for that matter any clathrate

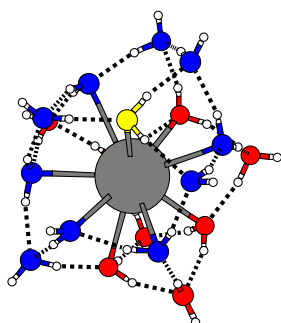
cage (see also section 4.5). It was also indicated in section 4.5 that the potassium ion still seems a little too small for the dodecahedron cage, as it also prefers to be located somewhat off-centred. In contrast, the caesium ion seems to perfectly fit a clathrate cage composed of 20 water molecules, both dodecahedral and non-dodecahedral. This section focuses on constrained dynamics and the free energies of the dissociation of single water molecules of $\text{Cs}^+(\text{H}_2\text{O})_{20}$ in order to further clarify the dodecahedron hypothesis. For this matter also $\text{Cs}^+(\text{H}_2\text{O})_{19}$ and $\text{Cs}^+(\text{H}_2\text{O})_{21}$ were investigated as maybe the explanation as to why $n = 20$ is magic lies in the difference between the nearest neighbours of $\text{Cs}^+(\text{H}_2\text{O})_{20}$ and itself. The aim of constrained dynamics was to investigate which of the two cluster structures could be dissociated more easily. One might argue that plain MD could also be used for this purpose, however, as already mentioned, usually activation energy barrier crossings are very rare in MD-simulations. Hence a very good statistic of very long MD-trajectories would be needed, which results in extremely long CPU-times. Therefore, the idea was to generate the same results in less time. One such possibility is to force the system along a single well-defined path. At the same time it turns out that this also allows the calculation of the free energy associated with this reaction path rather conveniently and directly. As for the case of $\text{Cs}^+(\text{H}_2\text{O})_{20}$ the ability of the water hull to dissociate was the most important question, the simplest of all dissociation reactions, namely that of one single water molecule was investigated. Hence it was sufficient to pull single water molecules from the water network to obtain the free energy of the dissociation of these water molecules. These water molecule were pulled from the water network step by step, while at each step they were constrained to a fixed distance r from the central ion. The average constrained force $\langle F \rangle$, i.e. the average force needed to keep the water molecule at this distance r , could then be integrated over r to yield the free energy ΔG of the dissociation of these water molecules. This is a standard procedure which is described in detail in references [105–107]. In practice, the obtained values for $\langle F \rangle$ were plotted vs. the distance r_i , averaged, and interpolated with a spline. This spline could then be integrated to yield the free energy of the dissociation of single water molecules. Due to limited time, the free energy of the dissociation of one water molecule could not be computed for all water molecules of each of the four structures, $\text{Cs}^+(\text{H}_2\text{O})_{19}$, $\text{Cs}^+(\text{H}_2\text{O})_{20}$ (dodecahedron/dod), $\text{Cs}^+(\text{H}_2\text{O})_{20}$ (best non-dodecahedron/bnd), and $\text{Cs}^+(\text{H}_2\text{O})_{21}$, respectively, hence water molecules were selected which are representative for several water molecules in similar surroundings. For $\text{Cs}^+(\text{H}_2\text{O})_{19}$ and $\text{Cs}^+(\text{H}_2\text{O})_{21}$, four water molecules were selected each. As one structural pattern all magic numbers have in common is that they do not contain water molecules which exhibit a coordination number smaller than three, see section 4.5.1, the first water molecule to be pulled from both $\text{Cs}^+(\text{H}_2\text{O})_{19}$ and $\text{Cs}^+(\text{H}_2\text{O})_{21}$ was a (or the) DA molecule, followed by its two adjacent molecules. The last molecule to be pulled from both structures was one that had a similar surrounding compared to the water molecules of both $\text{Cs}^+(\text{H}_2\text{O})_{20}$ structures. For the corresponding structures of $\text{Cs}^+(\text{H}_2\text{O})_{19}$ and $\text{Cs}^+(\text{H}_2\text{O})_{21}$ see figures 11.17 and 11.18.



Cs.019.a

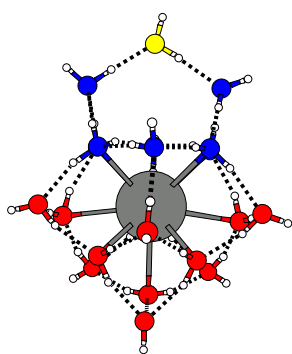
Cs.019.b

Cs.019.c

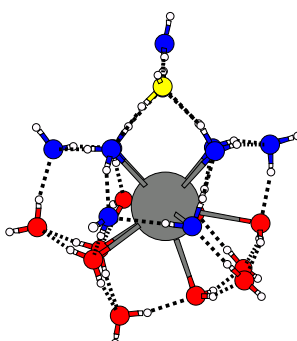


Cs.019.d

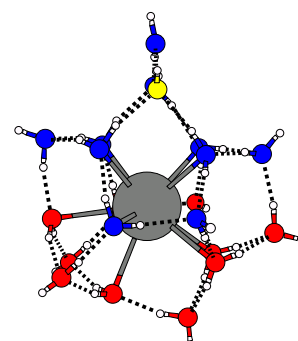
Figure 11.17.: Global minimum structure of $\text{Cs}^+(\text{H}_2\text{O})_{19}$ where the water molecules marked yellow indicate the pulled water molecules whereas the blue water molecules indicate annealed rings which contain the pulled water molecule.



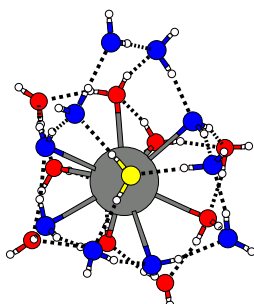
Cs.021.a



Cs.021.b



Cs.021.c



Cs.021.d

Figure 11.18.: Global minimum structure of $\text{Cs}^+(\text{H}_2\text{O})_{21}$ where the water molecules marked yellow indicate the pulled water molecules whereas the blue water molecules indicate annealed rings which contain the pulled water molecule.

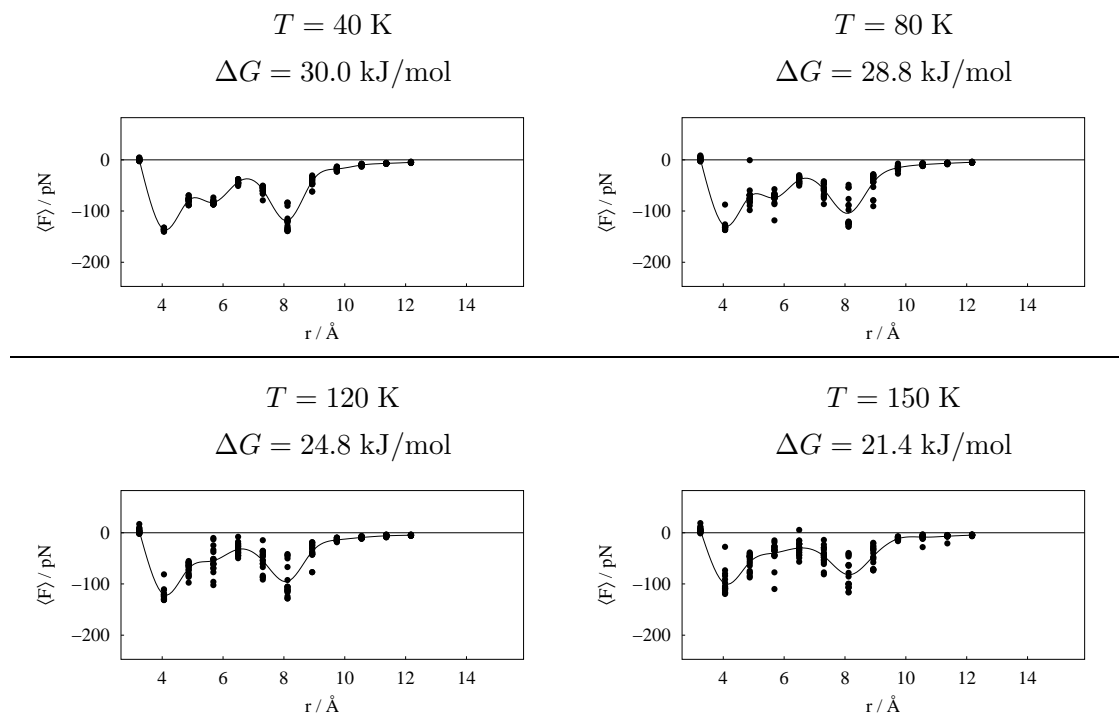


Figure 11.19.: Average constraint force $\langle F \rangle$ in pN vs. distance r in Ångström of pulled water molecules of structure $\text{Cs}^+(\text{H}_2\text{O})_{19}$ (Cs.019.d) for eighteen starting conditions per distance r each at $T = 40\text{ K}$, $T = 80\text{ K}$, $T = 120\text{ K}$, and $T = 150\text{ K}$, respectively

In figure 11.19 the average force vs. distance plots are displayed for Cs.019.d at the four different temperatures $T = 40\text{ K}$, $T = 80\text{ K}$, $T = 120\text{ K}$, and $T = 150\text{ K}$, respectively. Each point in one plot represents the average force computed from eighteen different starting conditions (hence a total of 198 simulations per plot were computed). When looking at the four plots in figure 11.19, one observes that the overall trend of the curve stays about the same, while maxima and minima become less pronounced for increasing temperatures. The free energy of the dissociation of one water molecule drops by 8.4 kJ/mol upon increasing the temperature from $T = 40\text{ K}$ to $T = 150\text{ K}$, from $\Delta G = 30.0\text{ kJ/mol}$ to $\Delta G = 21.4\text{ kJ/mol}$. Due to the fact that most structural changes appear to happen for temperatures $T \geq 120\text{ K}$ and that no fundamental changes in the average force vs. distance plots can be observed for different temperatures, in the course of this section only a selection of average force vs. distance plots at $T \geq 120\text{ K}$ will be described in detail (also for both $\text{Cs}^+(\text{H}_2\text{O})_{20}$ structures), whereas a full set of plots for all structures and all temperatures can be found in the appendix. Minima in the average force vs. distance plots correspond to distances where the pulled water molecule occupies a position of optimal “hydration shell” distance to the central ion and simultaneously also to the other water molecules in the network. These distances approximately correspond to the optimal distances given in section 4.1 when looking at pair interactions. Average force vs. distance plots for all structures of $\text{Cs}^+(\text{H}_2\text{O})_{19}$ and $\text{Cs}^+(\text{H}_2\text{O})_{21}$ at $T = 120\text{ K}$ are depicted in figure 11.20 as an example for the plots of these two structures. The full set of plots is depicted in the appendix, sections 15.1 and 15.2.

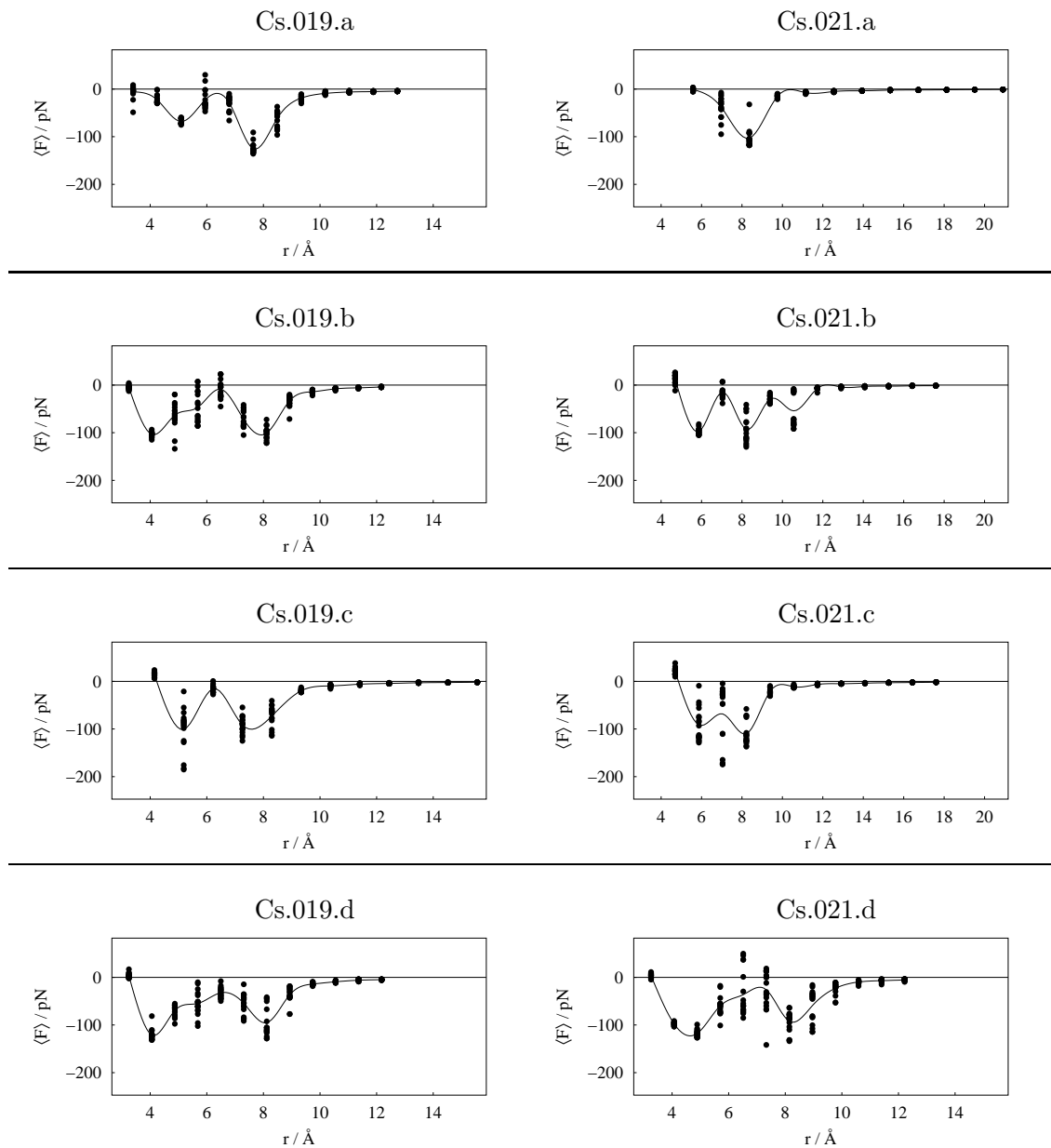


Figure 11.20.: Average constraint force $\langle F \rangle$ in pN vs. distance r in Ångström of pulled water molecules of structure $\text{Cs}^+(\text{H}_2\text{O})_{19}$ and $\text{Cs}^+(\text{H}_2\text{O})_{21}$ (for eighteen starting conditions per distance r each) at $T = 120$ K

Comparing the average force vs. distance plots of the same type of water molecule being pulled from the cluster such as for example Cs.019.c and Cs.021.c, which in both cases is a DAA molecule, one can observe subtle similarities between the plots, i.e. the trends of the curves are approximately the same, each exhibiting two minima and one maximum, though the intensity of the extrema vary. When looking more closely at the surroundings of these two DAA molecules one finds that they do not have an equivalent surrounding with respect to what types of water molecules donate or accept the hydrogen bonds. Comparing the average force vs. distance plots of the same type of water molecule exhibiting equivalent surroundings, such as Cs.019.d and Cs.021.d, one observes that both plots are indeed very

similar and also yield similar free energies (see table 11.2). Hence equivalent surroundings seem to be important for the actual comparison of values of the free energy of the dissociation of one water molecule.

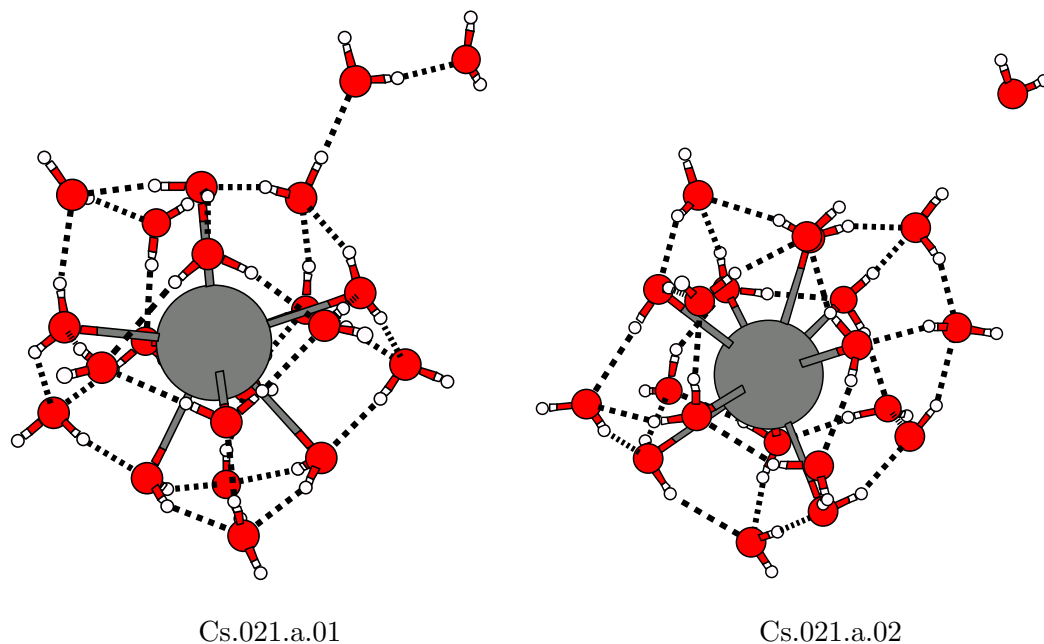


Figure 11.21.: Equilibrium structures of $\text{Cs}^+(\text{H}_2\text{O})_{21}$ for two different starting conditions with a distance r of 8.3 Ångström for the constraint molecule at $T = 120$ K

Another feature all plots have in common is that for larger distances of the pulled water molecule with respect to the central ion, the scatter of the points is smaller and vice versa. It was found that this scattering is due to different equilibrium structures obtained at the end of the simulation for the same input geometry but different starting conditions. See for example figure 11.21 where for Cs.021.a.01 the constrained water molecule is bound by one hydrogen bond to another water molecule which in turn is bound to the remaining water network which is forming a cage consisting of 19 water molecules by the end of the simulation, yielding an average force of -32.13 pN. For Cs.021.a.02, however, the constrained molecule does not have direct contact with the water network, while the water cage consists of a structure very close to that of the best non-dodecahedron for $\text{Cs}^+(\text{H}_2\text{O})_{20}$ yielding an average force -115.3 pN. In both cases the distance for the constrained molecule is equal to 8.3 Ångström. In case the difference between the two equilibrium structures is less pronounced, i.e. in case the constrained molecule can decide whether to function as a DDA or DAA in the water network, the average force still yields offsets though not as large.

Comparing the free energies obtained for the four different types of water molecules being pulled from the water network for $\text{Cs}^+(\text{H}_2\text{O})_{19}$ and $\text{Cs}^+(\text{H}_2\text{O})_{21}$ (see table 11.2), one observes that for all temperatures the free energy of the dissociation of the DA molecule of $\text{Cs}^+(\text{H}_2\text{O})_{19}$ is lower than the free energy of the dissociation of the other three. For $\text{Cs}^+(\text{H}_2\text{O})_{21}$, however,

T		40 K	80 K	120 K	150 K
structure	pulled H ₂ O	ΔG in kJ/mol			
Cs.019.a	DA	22.5	21.0	19.0	17.7
Cs.019.b	DDA	27.4	24.7	23.0	20.1
Cs.019.c	DAA	27.3	23.6	20.8	18.8
Cs.019.d	DDA	30.0	28.8	24.8	21.4
Cs.021.a	DA	28.9	19.8	15.1	14.2
Cs.021.b	DAA	27.5	25.6	22.2	19.7
Cs.021.c	DAA	25.2	25.0	22.9	21.4
Cs.021.d	DDA	30.6	28.5	26.4	24.5
Cs.020.dod.a	DDA	29.3	27.5	23.7	20.9
Cs.020.dod.b	DDA	29.4	27.2	23.9	19.7
Cs.020.dod.c	DDA	38.2	34.4	27.9	21.9
Cs.020.dod.d	DDA	35.6	32.0	28.3	25.3
Cs.020.dod.e	DAA	32.5	29.5	27.4	25.0
Cs.020.dod.f	DAA	27.6	25.4	23.4	20.9
Cs.020.dod.g	DAA	28.4	26.4	24.2	21.2
Cs.020.bnd.a	DDA	28.2	26.0	23.9	22.0
Cs.020.bnd.b	DDA	36.6	33.6	28.1	24.5
Cs.020.bnd.c	DDA	37.0	34.7	32.2	29.0
Cs.020.bnd.d	DDA	39.2	34.3	28.9	23.4
Cs.020.bnd.e	DAA	29.0	25.0	22.5	19.5
Cs.020.bnd.f	DAA	24.5	22.2	21.2	20.3
Cs.020.bnd.g	DAA	27.0	26.2	23.9	21.0

Table 11.2.: Free energy ΔG in kJ/mol for different water molecules being pulled from the cluster structures $\text{Cs}^+(\text{H}_2\text{O})_{19}$, $\text{Cs}^+(\text{H}_2\text{O})_{21}$, and $\text{Cs}^+(\text{H}_2\text{O})_{20}$ (dodecahedral/dod and non-dodecahedral/bnd), for corresponding structures see figures 11.17, 11.18 and 11.22, 11.23; for a selection of average force vs. distance graphs of $\text{Cs}^+(\text{H}_2\text{O})_{19}$ and $\text{Cs}^+(\text{H}_2\text{O})_{21}$ see figure 11.20 whereas for a complete set of all graphs of all systems see sections 15.1, 15.2, 15.3, and 15.4 in the appendix

the free energy of the dissociation of the DA water molecule is only lowest for temperatures of $T \geq 80$ K. Comparing the values obtained for the two DA molecules with the values obtained for the free energy of the dissociation of one water molecule of the dodecahedron and the non-dodecahedron, the DA molecules beat all other values with respect to being the lowest in energy, with the exception of $\text{Cs}^+(\text{H}_2\text{O})_{21}$ at $T = 40$ K. For temperatures of $T \leq 80$ K, the

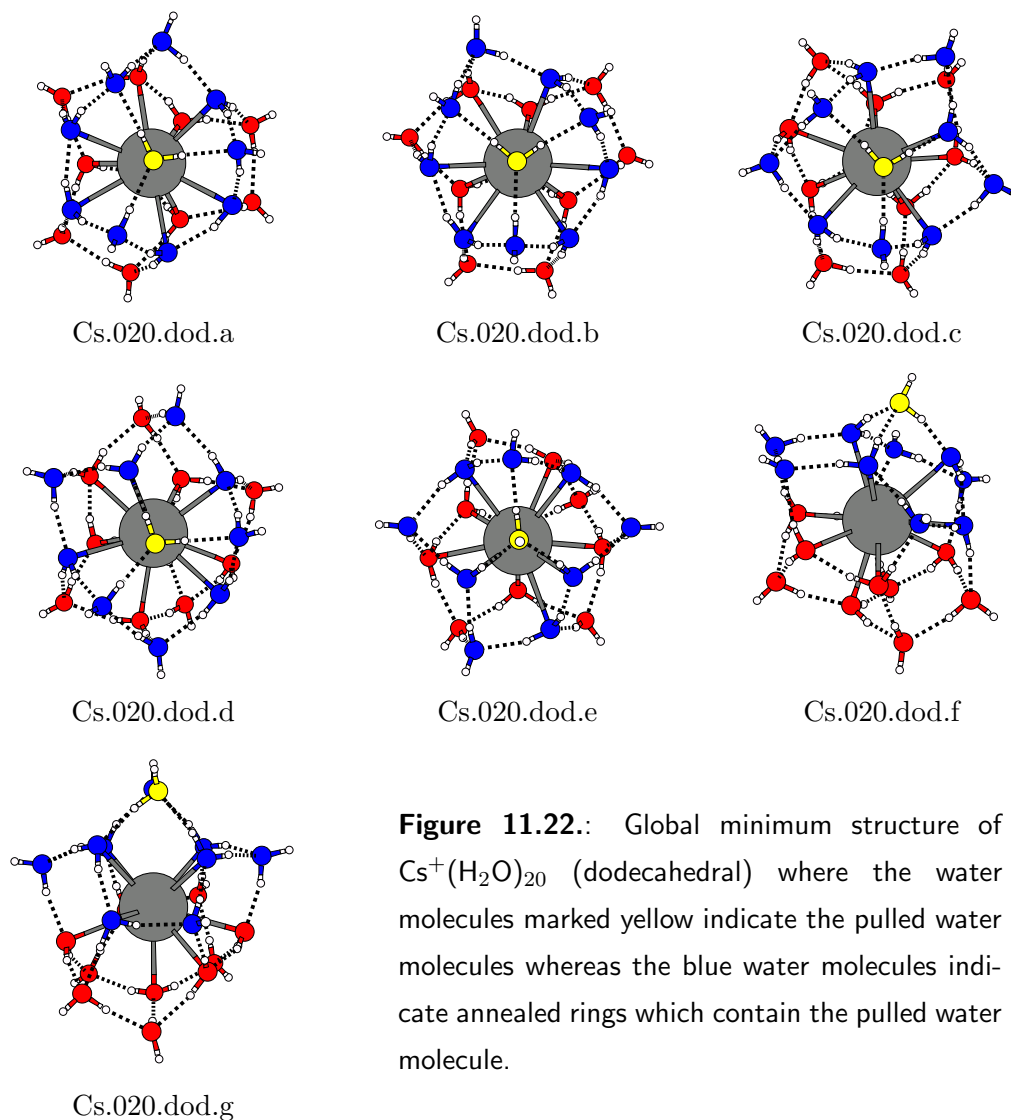


Figure 11.22.: Global minimum structure of $\text{Cs}^+(\text{H}_2\text{O})_{20}$ (dodecahedral) where the water molecules marked yellow indicate the pulled water molecules whereas the blue water molecules indicate annealed rings which contain the pulled water molecule.

free energy of the dissociation of DA molecules does not differ much from the values obtained for most of the three-coordinated molecules for $\text{Cs}^+(\text{H}_2\text{O})_{20}$, $\text{Cs}^+(\text{H}_2\text{O})_{21}$, and $\text{Cs}^+(\text{H}_2\text{O})_{19}$. However when looking at $T \geq 120$ K, especially the free energy of the dissociation of the DA molecule from for $\text{Cs}^+(\text{H}_2\text{O})_{21}$ is considerably lower compared to all others. The effect is also present for $\text{Cs}^+(\text{H}_2\text{O})_{19}$, though not as pronounced. Hence one can assume that it is indeed easier for a DA molecule to be dissociated from the water network. Comparing the values of the free energy of the dissociation of single water molecules of the dodecahedron with the non-dodecahedron, one observes for temperatures of $T \leq 80$ K that it is most of the time much harder to dissociate the water molecules from the non-dodecahedron especially for DDA molecules. If this trend would continue this would be the downfall of the dodecahedron hypothesis.

In the canonical ensemble structural changes were only observable for $\text{Cs}^+(\text{H}_2\text{O})_{20}$ at temperatures of $T \geq 120$ K. Hence these temperatures are more important with respect to possible

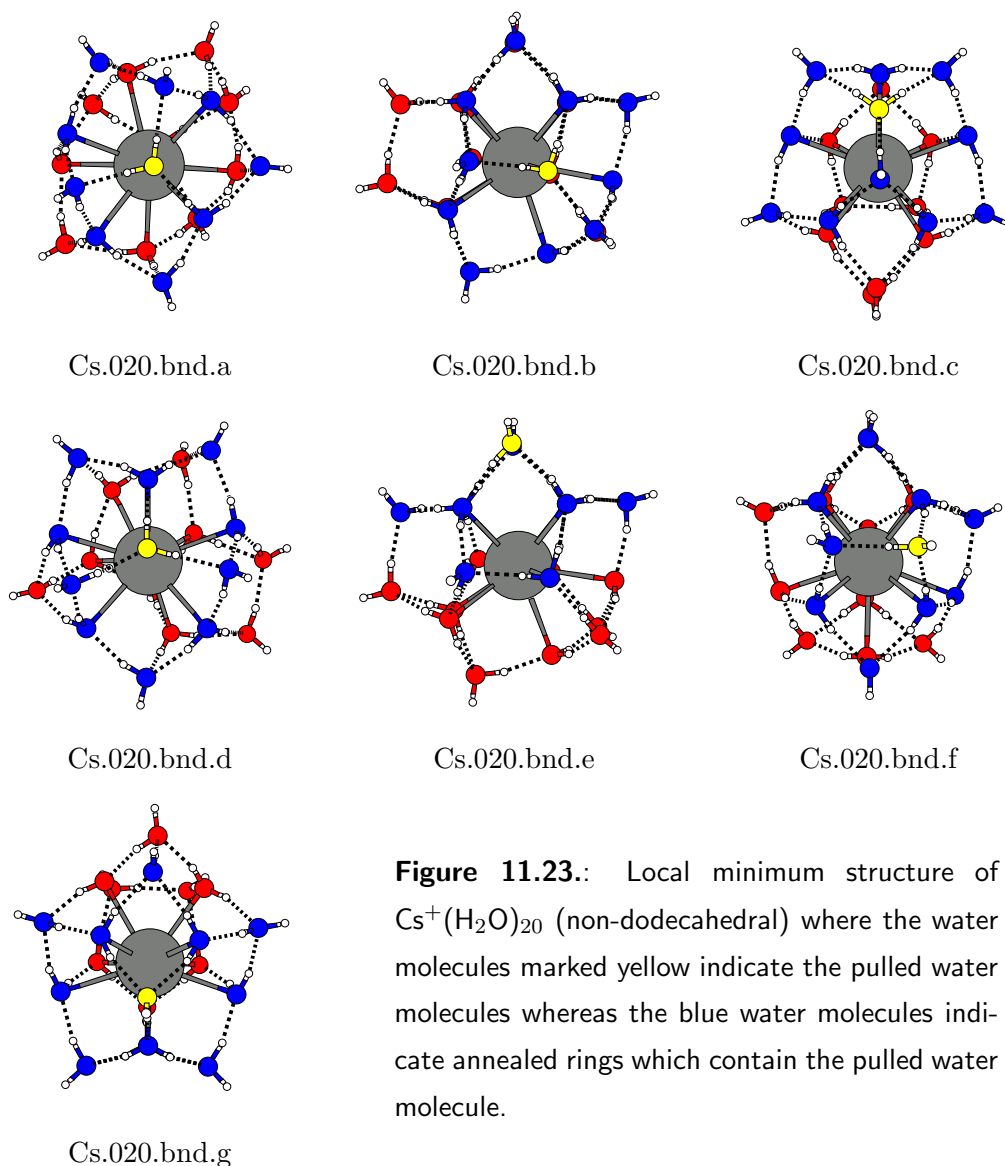


Figure 11.23.: Local minimum structure of $\text{Cs}^+(\text{H}_2\text{O})_{20}$ (non-dodecahedral) where the water molecules marked yellow indicate the pulled water molecules whereas the blue water molecules indicate annealed rings which contain the pulled water molecule.

explanations, therefore, the free energies of the dissociation of different water molecules with equivalent surrounding (already depicted in table 11.2) are shown also in a separate table for these temperatures for better comparison (see table 11.3). The according average force vs. field plots for $T = 120$ K can be found in figure 11.24 (for a full set of plots see appendix sections 15.3 and 15.4). The corresponding structures are depicted in figures 11.22 and 11.23. When looking at the average force vs. distance graphs for $T = 120$ K, one also observes that for similar water molecules being pulled from the water network the curves of both structures are similar although the respective maxima and minima in the curves differ by their depths as it was already found for the comparison of $\text{Cs}^+(\text{H}_2\text{O})_{19}$ and $\text{Cs}^+(\text{H}_2\text{O})_{21}$. Nevertheless, compared to average force vs. distance graphs of $\text{Cs}^+(\text{H}_2\text{O})_{19}$ and $\text{Cs}^+(\text{H}_2\text{O})_{21}$ the difference between the two plots of $\text{Cs}^+(\text{H}_2\text{O})_{20}$ is less pronounced.

T		120 K	120 K	150 K	150 K
		ΔG in kJ/mol	ΔG in kJ/mol	ΔG in kJ/mol	ΔG in kJ/mol
structure	pulled H ₂ O	DOD	BND	DOD	BND
Cs.020.dod.b/Cs.020.bnd.b	DDA	23.9	28.1	19.7	24.5
Cs.020.dod.d/Cs.020.bnd.d	DDA	28.3	28.9	25.3	23.4
Cs.020.dod.e/Cs.020.bnd.e	DAA	27.4	22.5	25.0	19.5
Cs.020.dod.f/Cs.020.bnd.f	DAA	23.4	21.2	20.9	20.3
Cs.020.dod.g/Cs.020.bnd.g	DAA	24.2	23.9	21.2	21.0

Table 11.3.: Free energy ΔG in kJ/mol for different water molecules being pulled from the cluster (for corresponding structures see figures 11.22 and 11.23 and for corresponding average force vs. distance graphs for $T = 120$ K see figure 11.24 and for $T = 150$ K see appendix sections 15.3 and 15.4, respectively)

In the case of the DAA molecules being pulled, the free energy of dissociation obtained for these water molecules is in all cases larger for the dodecahedron than for non-dodecahedron. However, the difference is not very significant, ranging between 0.2 kJ/mol and 5.5 kJ/mol at most. When looking at the two similar DDA molecules it is the other way round for $T = 120$ K, namely the free energies of dissociation of the water molecules pulled from the non-dodecahedron are higher by 4.2 kJ/mol and 0.6 kJ/mol, respectively. For $T = 150$ K the DDA of structure Cs.020.dod.d is better by 1.9 kJ/mol than that of the structure Cs.020.bnd.d, whereas for Cs.020.dod.b and Cs.020.bnd.b the non-dodecahedral structure beats the dodecahedral structure by 4.7 kJ/mol.

Hence neither the dodecahedron shaped structure nor the non-dodecahedron shaped structure was found to be better, as the differences between the two structures are far too small to allow any assumption and the differences would lead to conflicting conclusions anyway. Therefore it is impossible to ascribe the existence of the magic number $n = 20$ solely to the dodecahedron. However, it was found that it seems to be indeed easier to pull DA molecules from water networks compared to three-coordinated water molecules. As both the dodecahedron and the non-dodecahedron at $n = 20$ do not contain any of these DA water molecules in contrast to their immediate neighbours $n = 19$ and $n = 21$, this could lead to an explanation that $n = 20$ is magic due to cage inclusion compounds of various forms, exhibiting a water network of water molecules solely three- or four-coordinated (see also section 4.5.1).

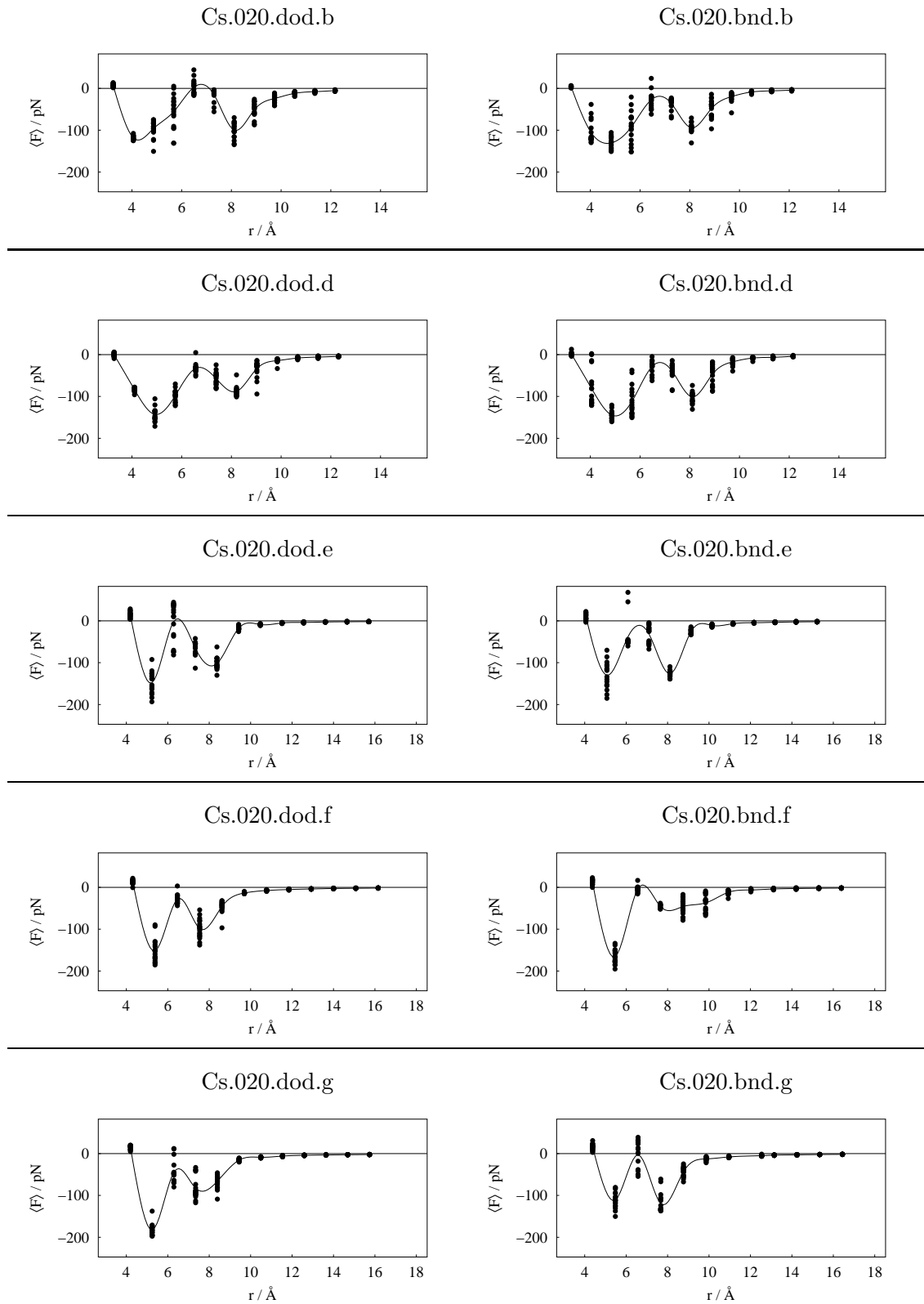


Figure 11.24.: Average constraint force $\langle F \rangle$ in pN vs. distance r in Ångström of pulled water molecules of structure Cs.020.dod.b for eighteen starting conditions per distance r at $T = 120$ K

12. Conclusions obtained from cluster dynamics

A molecular dynamics routine has been programmed from scratch for alkali cation microhydration clusters. As integration scheme, the velocity-Verlet was chosen for the translational motion and a velocity-Verlet-like rotational integrator for the rotational motion. The algorithm can generate microcanonical ensembles (default) and canonical ensembles via the Andersen thermostat. The algorithm also allows for a constraint, which forces a selected water molecule to stay at a fixed distance from the central ion.

All global minimum structures (see part I) were submitted to molecular dynamics simulations using the canonical ensemble and a total simulation time of 10 ps with a time-step of 0.1 fs. It was found that for temperatures of $T \leq 80$ K mostly hindered rotational motion and very little hindered translational motion occurred for all three systems $\text{Na}^+(\text{H}_2\text{O})_n$, $\text{K}^+(\text{H}_2\text{O})_n$, and $\text{Cs}^+(\text{H}_2\text{O})_n$. Upon increasing the temperature to $T = 150$ K, mostly the smaller cluster structures with $4 \leq n \leq 13$ exhibited strong structural changes. Once the water molecules start to form a cohesive network and the energy is distributed over more degrees of freedom, changes become less pronounced and also the effect of different starting conditions on structural variety decreases. For larger cluster sizes with $16 \leq n \leq 21$, mostly small rotational motion and to some extent also very small translational motion can be observed as the water molecules are hindered by the network to move freely. This is in stark contrast to the frequent assumption that these systems are so flexible that the concept of “structure” itself loses its meaning. For $n = 20$ it was found that when using the canonical ensemble and comparing non-dodecahedron shaped structures with dodecahedron structures for all three systems, most changes were observed in the case of sodium: The dodecahedron cluster structure collapsed during the simulations towards a cluster structure very close to that of the global optimum (non-dodecahedral). Hence it could be shown that for sodium $n = 20$ is not a magic number due to a possible cage formation, as clearly non-dodecahedral and non-clathrate structures are strongly preferred energetically and easily accessible dynamically. In the case of potassium, no information could be gained by this comparison, whereas in the case of caesium at least at $T = 150$ K a small difference was observable, i.e. it was found that for the dodecahedron structure no bond openings were visible, whereas they sometimes occurred for non-dodecahedron structures and then mostly between annealed four- and six- membered

rings. Hence this is a weak support of the dodecahedron hypothesis in case of $\text{Cs}^+(\text{H}_2\text{O})_{20}$. In the special case $\text{Cs}^+(\text{H}_2\text{O})_{20}$, and for that matter also $\text{Cs}^+(\text{H}_2\text{O})_{19}$ and $\text{Cs}^+(\text{H}_2\text{O})_{21}$, constrained dynamics simulations were run, i.e. where selected single water molecules were constrained to fixed distances from the central ion. This allowed for the computation of the free energy of the dissociation of these water molecules. The single water molecules to be pulled from the water network have been selected such that they were comparable to each other with respect to similar surroundings or equivalent coordination patterns. For the two structures $\text{Cs}^+(\text{H}_2\text{O})_{20}$, i.e. the dodecahedron and the non-dodecahedron, no significant differences could be observed for the free energies of dissociating single water molecules. In other words neither of the structures was less stable than the other. Hence no further proof could be gained that the magic number $n = 20$ is solely due to the formation of a dodecahedron shaped water network. However, when comparing the immediate neighbours of $\text{Cs}^+(\text{H}_2\text{O})_{20}$, i.e. $\text{Cs}^+(\text{H}_2\text{O})_{19}$ and $\text{Cs}^+(\text{H}_2\text{O})_{21}$, to $\text{Cs}^+(\text{H}_2\text{O})_{20}$ it was found that it was indeed easier to pull off the DA (single donor – single acceptor) molecules and for that matter also their two adjacent molecules, respectively, from the water networks. As both structures investigated for $n = 20$ do not contain any DA molecule, this is some support for the magic number 20 being due to clathrate like structures, in general, containing solely three or four coordinated water molecules. Therefore, we propose to replace the dodecahedron hypothesis by a simpler but possibly more robust hypothesis, namely that the magic number $n = 20$ (but also others) observed in $\text{K}^+(\text{H}_2\text{O})_n$ and $\text{Cs}^+(\text{H}_2\text{O})_n$ are due to several different lowest-energy cage structures that do not contain any weakly bound DA molecules that are susceptible to dissociation and association reactions. Due to the smallness and the stronger “structure breaking” effect of $\text{Na}^+(\text{H}_2\text{O})_n$, these cage structures collapse quickly to very different off-centred structures in the case of $\text{Na}^+(\text{H}_2\text{O})_n$. These three-dimensional networks follow totally different build-up principles and hence do not show the magic number pattern of the cage structures.

There are many ways to extend these investigations. At first one might stay within the given model potential and compute MD-simulations using other local minimum energy structures as input geometries as to be able to better compare different structures of one cluster size. Also a larger variety of different starting conditions should be tested. To further clarify the structural pattern found for magic number cluster structures it is also possible to force other dissociation reactions than that investigated in this work or for that matter also association reactions. This would also allow for comparisons between dissociation and association reactions. As the TIP4P/OPLS potential is not always reliable in producing correct energy differences between different isomers, it would also be necessary to employ better model potentials which allow for flexible water molecules and polarisation. Unfortunately model potentials employing flexible water molecules of this type are so far not available for alkali cation hydration clusters. Another possibility would be to use ab-initio potentials for the simulations, however, this is still too expensive to realise.

Part IV.

Summary

13. Final conclusions and future prospects

The purpose of this work was to obtain structural information about alkali cation microhydration clusters, i.e. $\text{Na}^+(\text{H}_2\text{O})_n$, $\text{K}^+(\text{H}_2\text{O})_n$, and $\text{Cs}^+(\text{H}_2\text{O})_n$ with $4 \leq n \leq 24$, both in general and also with a special focus on cage inclusion compounds and magic numbers. The problem was approached using a combination of global geometry optimisation, simulated anharmonic infrared spectra (partly in combination with recently available experimental data) and finally molecular dynamics simulation:

As a first step, an extensive global geometry optimisation study has been carried out for these systems. The results obtained constitute a first complete and systematic overview on structures of alkali cation microhydration clusters [57]. With a detailed analysis of pair interactions and many-body effects reasons for structural trends could be provided. This study is also the first unbiased check of the dodecahedron hypothesis. For a better understanding of these systems, and to provide data for direct comparison to the experiment, anharmonic infrared spectra for each global as well as some low-lying local minimum energy structures were calculated in the OH-stretch region within an empirical model by Victoria Buch [37]. At this point of the investigation, the model had been optimised for pure water clusters and ice only, however, it was found to produce qualitatively correct data also for the present systems. The spectra obtained with this model show characteristic correlations between cluster structures and certain spectral signatures which should make it possible to discern these cluster structures experimentally [82]. It has also been also shown that at temperatures up to 100 K global minimum structures (computed at 0 K) still dominate the spectra. Recently available experimental data was used for the fitting of the empirical model of Victoria Buch to alkali cation microhydration clusters in order to obtain quantitatively correct frequencies. Using the fitted version of the model, it was for the first time possible to assign peaks in the experimental spectrum to certain cluster structures which has been a significant progress, as experimentalists so far had been unable to assign any structure with certainty. In a final step, molecular dynamics simulations were applied to all global minimum energy and selected low-lying local minimum energy cluster structures at different temperatures, simulating a canonical distribution. As reactions are a rare event to observe in cluster dynamics, constrained dynamics was used to force a dissociation reaction as to be able to compare the dissociation behaviour of different water cages and to allow the computation of the free energies for the chosen dissociation reactions.

Conclusions to each method have already been given separately in the chapters 5, 9, and 12. The question now is what could be gained by the combination of the three methods.

For $M = \text{Na}$, the results obtained by global geometry optimisation suggest simple explanations for the absence of clearly discernible magic numbers, in particular for the missing magic number $n = 20$: Clathrate-like cage structures play no important role, and competition of two structural principles prevents obvious shell closures. This is consistent with the results obtained from molecular dynamics simulation, as the dodecahedron cluster structure was observed to collapse for $T \geq 80$ K during the simulations towards a cluster structure very similar to that of the global optimum. As already mentioned, the observation of reactions in molecular dynamics simulations is a rare event, and as this transformation has been observed in all trajectories for $T \geq 120$ K, this strongly underpins the static picture obtained from the global geometry optimisation and also clearly shows that the dodecahedron and for that matter obviously also other cage structures only play a very minor role in the case of $\text{Na}^+(\text{H}_2\text{O})_{20}$. Another aspect which is of importance to $\text{Na}^+(\text{H}_2\text{O})_n$ cluster structures in general is the coordination of the sodium ion in the 1st-shell. As a result of global geometry optimisation it is important for the overall potential energy that water molecules in the 1st-shell are orientated optimally with respect to the sodium ion due to the dominance of pair interactions between the sodium ion and water molecules. This behaviour, i.e. that both coordination numbers and the orientation of the water molecules are important for sodium clusters, was also observable in cluster dynamics of the global minimum energy structures of $\text{Na}^+(\text{H}_2\text{O})_n$ in a canonical ensemble. It was found that two different coordination numbers were favoured, namely five and six. The coordination number five was preferred for smaller cluster structures, whereas the coordination number six has been observed to be of importance for medium to larger sized cluster structures, almost always resulting in the formation of a slightly distorted octahedron around the sodium ion. Overall the static picture obtained by global optimisation could be underpinned by the cluster dynamics.

For $M = \text{K}$, it was found that the cluster structures seem to take an intermediate position between $\text{Na}^+(\text{H}_2\text{O})_n$ and $\text{Cs}^+(\text{H}_2\text{O})_n$ cluster structures, as smaller $\text{K}^+(\text{H}_2\text{O})_n$ cluster structures were found to be similar to equivalent $\text{Na}^+(\text{H}_2\text{O})_n$ cluster structures, whereas medium to larger sized $\text{K}^+(\text{H}_2\text{O})_n$ cluster structures appear to favour ring formations in a cohesive water network as well as clathrate like structures equivalent to $\text{Cs}^+(\text{H}_2\text{O})_n$ cluster structures. This behaviour has also been found in the dynamics of $\text{K}^+(\text{H}_2\text{O})_n$ clusters for the intermediate size region: On the one hand the clusters seemed to favour certain coordination numbers while on the other hand they also showed enhanced ring formation, switching back and forth between the two structural principles as both at the same time are not possible to realise. For $n = 20$, the global minimum appears to have a dodecahedral cage, but it is strongly distorted, and clearly non-dodecahedral minima are very close in energy. Comparing the dynamics of a $\text{K}^+(\text{H}_2\text{O})_{20}$ dodecahedron with the dynamics of a $\text{K}^+(\text{H}_2\text{O})_{20}$ non-dodecahedron, no signifi-

cant differences could be observed. It was found that magic numbers may have an extremely simple explanation as all magic number clusters of $\text{K}^+(\text{H}_2\text{O})_n$ and $\text{Cs}^+(\text{H}_2\text{O})_n$ seem to hold one structural pattern in common: namely the absence of water molecules which are not at least three or four coordinated in the water network.

$\text{M} = \text{Cs}$ exhibits a much clearer preference for water ring formation than the other two cases, leading naturally towards clathrate-like cage structures. Nevertheless, even here the dodecahedron does not dominate clearly for $n = 20$; other cages containing four- and six-membered rings are isoenergetic. Whereas in the case of $\text{K}^+(\text{H}_2\text{O})_{20}$ no information could be gained by this comparison, in the case of caesium at least at $T = 150$ K a difference was observable. It was found that for the dodecahedron structure no bond openings occurred, whereas they sometimes did occur for non-dodecahedron structures and mostly between annealed four- and six-membered rings (which are absent in the non-dodecahedron). Hence this is a weak support of the dodecahedron hypothesis in case of $\text{Cs}^+(\text{H}_2\text{O})_{20}$. In the special case $\text{Cs}^+(\text{H}_2\text{O})_{20}$ also constrained dynamics simulations were run, i.e. selected water molecules were constrained to fixed distances from the central ion to simulate a dissociation reaction of these water molecules, in order to compare the different water networks. For comparison also simulations on $\text{Cs}^+(\text{H}_2\text{O})_{19}$ and $\text{Cs}^+(\text{H}_2\text{O})_{21}$ were performed. It was found that indeed it seems to be easier to dissociate a two-coordinated water molecule from the water network as well as its two adjacent water molecules than any of the other three-coordinated water molecules present in the water network. Therefore, it was proposed to replace the dodecahedron hypothesis by a simpler but possibly more robust hypothesis, namely that the magic number $n = 20$ (but also others) observed in $\text{K}^+(\text{H}_2\text{O})_n$ and $\text{Cs}^+(\text{H}_2\text{O})_n$ are due to several different lowest-energy cage structures that do not contain any weakly bound two-coordinated water molecules that are susceptible to dissociation and association reactions.

Although the results obtained for both the global geometry optimisation and the molecular dynamics simulations are merely theoretical, they are very encouraging indeed, as they already explain both the absence of magic numbers in the mass spectrum of $\text{Na}^+(\text{H}_2\text{O})_n$ and the occurrence of the latter in both the mass spectra of $\text{K}^+(\text{H}_2\text{O})_n$ and $\text{Cs}^+(\text{H}_2\text{O})_n$. Especially the findings in the case of $\text{Na}^+(\text{H}_2\text{O})_{20}$ show that it is indeed justified to use a combination of global geometry optimisation and molecular dynamics simulation to circumvent the effort of full MD. Although these results are very consistent in themselves they are without experimental proof. So far, larger alkali cation microhydration clusters have been investigated experimentally mostly by mass spectrometry, yielding these magic numbers, but no structural information. It has been shown, however, that infrared spectra can contribute to obtaining structural information, even in the presence of several cluster isomers at non-zero temperatures. It has been possible to reproduce the experimental spectral data on alkali cation microhydration clusters so far available which in turn made it possible to actually assign cluster structures to the experiment – a task in which the experimentalists have failed

so far. Although the global optimisation results were computed at 0 K they again proved themselves to be most important for the comparison of theory and experiment. Even though the MD-simulations were not actually used for the interpretation of the spectra they still hold valuable information regarding the behaviour of the cluster structures at different temperatures and might become a useful tool for interpretation of the experimental spectra of medium and larger sized cluster structures.

Overall one can say that the combination of the three methods indeed proved to be very successful as it clearly produced more insight in these systems as when just using one method.

There are many ways to extend these investigations. For example the global optimisation results should be tested more thoroughly using either better model potentials which also allow for flexible water molecules and/or the polarisation of the water molecules and the ions or even ab-initio potentials. Unfortunately, model potentials which allow for flexible molecules, such as for example TTM2F, do not yet contain alkali cation modelling. Another possibility to check upon the results gained from the global geometry optimisation is to directly submit these cluster structures to ab-initio calculations, such as for example DFT or MP2. However, results obtained from DFT do not necessarily have to be more reliable than results obtained from model potentials, since DFT has known defects for long-range interactions. MP2/cc-pVTZ is generally accepted as minimum level for a quantitatively reliable description of such systems, however, this would be extremely expensive. For an extension of the molecular dynamics investigations one may at first stay within the given model potential TIP4P/OPLS and compute MD-simulations using other local minimum energy structures as input geometries as to be able to better compare different structures of one cluster size. Also a larger variety of different starting conditions should be tested. To further clarify the structural pattern found for magic number cluster structures it is also possible to force other dissociation reactions than that investigated in this work or for that matter also association reactions. This would also allow for comparisons between dissociation and association reactions. As the TIP4P/OPLS potential is not always reliable in producing correct energy differences between different isomers, again better model potentials which allow for flexible water molecules and polarisation should be employed. Another possibility would be to use ab-initio potentials for the simulations, however, this is far too expensive to realise on a statistically meaningful level. The experimental investigations are currently extended in two directions. The first aim is to further cool down the clusters as to obtain more distinct peaks while at the same time it is tried to obtain experimental data on cluster structures in the magic number region. We are confident that by continuing the present combination of the experiment and theory into this size-region, first direct and definite structural information on magic numbers of alkali cation microhydration clusters will be obtained.

Part V.

Appendix

14. Excerpts from the molecular dynamics routine used in this work

14.1. double precision function gauss

In this section the double precision function `gauss` [85] is depicted, which has been used to draw random velocities needed for the Andersen thermostat (see sections 10.4.1 and 11.2.1 and 14.2).

```
double precision function gauss ( iseed, sigma )

implicit none
real*8 r, v1, v2, fac, gset, ranf
real*8 sigma
real*8 ran0
integer iset
integer iseed
external ran0
save gset, iset
data iset/0/

ccc normally distributed Gauss function with variance sigma and
ccc mean zero

100 if (iset.eq.0) then
    v1 = 2.d0*ran0(iseed) - 1.d0
    v2 = 2.d0*ran0(iseed) - 1.d0
    r = v1*v1 + v2*v2
    if (r.ge.1) goto 100
    fac = sqrt(-2.d0*log(r)/r)
    gset = v1*fac
    gauss = v2*fac
    iset = 1
else
    gauss = gset
    iset = 0
end if

gauss = gauss*sigma

return
end
```

14.2. subroutine andersen

In this section the subroutine `andersen` is depicted, which has been used to ensure a correct canonical ensemble. The routine has been described in detail in sections 10.4.1 and 11.2.1.

```

subroutine andersen ()
implicit none
include 'parameter.h'      ! input parameter
real*8  vx(nmolmax)       ! initial velocity osc. in x
real*8  vy(nmolmax)       ! initial velocity osc. in y
real*8  vz(nmolmax)       ! initial velocity osc. in z
real*8  lx(nmolmax)       ! angular momentum in x
real*8  ly(nmolmax)       ! angular momentum in y
real*8  lz(nmolmax)       ! angular momentum in z
real*8  wx(nmolmax)       ! angular velocity in x
real*8  wy(nmolmax)       ! angular velocity in y
real*8  wz(nmolmax)       ! angular velocity in z
real*8  ixx, iyy, izz     ! principal moment of inertia of H2O
real*8  q0(nmolmax)       ! quaternion
real*8  q1(nmolmax)       ! quaternion
real*8  q2(nmolmax)       ! quaternion
real*8  q3(nmolmax)       ! quaternion
real*8  amass(nmolmax)    ! masses of water molecules
real*8  dt                ! time step integration
real*8  temper, colfrq    ! temperatur, collision frequency
real*8  qe(3,3)           ! quaternion matrix
real*8  iwx, iwy, iwz     ! counting variable
real*8  sigtrsw           ! sigma for translation of H2O
real*8  sigrotx, sigroty, sigrotz ! sigma for rotation in x, y, z
integer nmol              ! number of molecules
integer iseed             ! seed of random number generator
external gauss            ! function gauss distribution
external ran0             ! function random number generator

do i=1,nmol-1
  if (ran0(iseed).lt.colfrq*dt) then
    vx(i) = gauss(iseed,sigtrsw)
    vy(i) = gauss(iseed,sigtrsw)
    vz(i) = gauss(iseed,sigtrsw)
    wx(i) = gauss(iseed,sigrotx)
    wy(i) = gauss(iseed,sigroty)
    wz(i) = gauss(iseed,sigrotz)
    iwx  = ixx * wx(i)
    iwy  = iyy * wy(i)
    iwz  = izz * wz(i)
    qe(1,1) = q0(i)*q0(i)+q1(i)*q1(i)-q2(i)*q2(i)-q3(i)*q3(i)
    qe(1,2) = 2.d0*(q1(i)*q2(i)-q0(i)*q3(i))
    qe(1,3) = 2.d0*(q1(i)*q3(i)+q0(i)*q2(i))
    qe(2,1) = 2.d0*(q1(i)*q2(i)+q0(i)*q3(i))
    qe(2,2) = q0(i)*q0(i)-q1(i)*q1(i)+q2(i)*q2(i)-q3(i)*q3(i)
    qe(2,3) = 2.d0*(q2(i)*q3(i)-q0(i)*q1(i))
    qe(3,1) = 2.d0*(q1(i)*q3(i)-q0(i)*q2(i))
    qe(3,2) = 2.d0*(q2(i)*q3(i)+q0(i)*q1(i))
    qe(3,3) = q0(i)*q0(i)-q1(i)*q1(i)-q2(i)*q2(i)+q3(i)*q3(i)
    lx(i)  = qe(1,1)*iwx + qe(1,2)*iwy + qe(1,3)*iwz
    ly(i)  = qe(2,1)*iwx + qe(2,2)*iwy + qe(2,3)*iwz
    lz(i)  = qe(3,1)*iwx + qe(3,2)*iwy + qe(3,3)*iwz
  end if
end do

```

14.3. subroutine randimp

In this section the subroutine `randimp` is depicted, which has been used to draw the random velocities according to the description given in section 11.1.2.

```

subroutine randimp ( )

implicit none
include 'parameter.h'      ! input parameter
include 'random.h'        ! input parameters for velocity

real*8 xci, yci, zci      ! position of central ion
real*8 vxci, vyci, vzci  ! linear velocity of central ion
real*8 pxci, pyci, pzci  ! linear momentum of central ion
real*8 lxci, lyci, lzci  ! angular momentum of central ion
real*8 xx(nmolmax)       ! position in x
real*8 yy(nmolmax)       ! position in y
real*8 zz(nmolmax)       ! position in z
real*8 vx(nmolmax)       ! linear velocity in x
real*8 vy(nmolmax)       ! linear velocity in y
real*8 vz(nmolmax)       ! linear velocity in z
real*8 vrx(nmolmax)      ! rotational velocity in x
real*8 vry(nmolmax)      ! rotational velocity in y
real*8 vrz(nmolmax)      ! rotational velocity in z
real*8 vkx, vky, vkz     ! total velocity in x, y, z
real*8 vtot              ! total linear velocity ( = 0)
real*8 wx(nmolmax)       ! angular velocity in x
real*8 wy(nmolmax)       ! angular velocity in y
real*8 wz(nmolmax)       ! angular velocity in z
real*8 wtot              ! total angular velocity ( = 0)
real*8 ixx, iyy, izz     ! principal moment of inertia
real*8 q0(nmolmax)       ! quaternion
real*8 q1(nmolmax)       ! quaternion
real*8 q2(nmolmax)       ! quaternion
real*8 q3(nmolmax)       ! quaternion
real*8 lx(nmolmax)       ! angular momentum in x
real*8 ly(nmolmax)       ! angular momentum in y
real*8 lz(nmolmax)       ! angular momentum in z
real*8 lkx, lky, lkz    ! total angular momentum
real*8 ltot              ! total angular momentum
real*8 scalev            ! scaling factor for kinetic energy
real*8 px(nmolmax)       ! momentum in x
real*8 py(nmolmax)       ! momentum in y
real*8 pz(nmolmax)       ! momentum in z
real*8 pkx, pky, pkz    ! known total momentum for n = nmol-3
real*8 ptot              ! total momentum (has to be = 0)

```

```

real*8 amass(nmolmax) ! mass of water molecules
real*8 cmass          ! mass of central ion
real*8 k1, k2, k3    ! constants
real*8 dx, dy, dz    ! difference -> x(nmol) - x(n1) ; ...
real*8 ddx, ddy, ddz ! difference -> x(n2) - x(n1) ; ...
real*8 limes         ! to ensure that vx .. isn't too big
real*8 temper        ! temperature in Kelvin
real*8 sigtrsi, sigtrsw ! sigma for translation
real*8 sigrotx, sigroty, sigrotz ! sigma for rotation
real*8 qe(3,3)       ! quaternion matrix
real*8 iwz, iwz      ! principal moment of inertia
integer i, ireject   ! counting variables
integer n3, n2, n1   ! nmol - 3, nmol - 2, nmol - 1
integer nmol         ! number of molecules
integer izeed        ! random seed
external ran0        ! function random number generator
external gaussrot    ! function gauss-distribution

cccc !-----!
cccc ! get scaling factor for kinetic energy: scalev !
cccc !-----!

cccc get scaling factor scalev for velocities (depends on the kinetic
cccc energy and hence the temperature, which can be chosen in
cccc parameter.in)

cccc NOTE (units of variables):
cccc - temperature [ K ] = temper
cccc - boltzmann-constant [ J / K ] = kb
cccc - scalev (scaling factor for linear velocity -> translation)

      scalev = sqrt(3.d0*kb*temper*jtoh/amass(1))*2.d0

cccc !-----!
cccc ! compute velocities (hence kinetic energy) using scalev !
cccc !-----!

cccc first calculate random velocity/momentum for all atoms but the three
cccc last ones -> do i=1,nmol-3

      limes = ulimes * 2.d0
      ireject = 1

      n3 = nmol - 3
      n2 = nmol - 2
      n1 = nmol - 1

      do i=1,nmol
        vx(i) = 0.d0
        vy(i) = 0.d0
        vz(i) = 0.d0
        px(i) = 0.d0
        py(i) = 0.d0
        pz(i) = 0.d0
        lx(i) = 0.d0
        ly(i) = 0.d0
        lz(i) = 0.d0
      end do

cccc do momentum in x-direction

      vxci = (ran0(izeed) - (ulimes/2.d0))*2.d0
      pxci = cmass * vxci
      pkx = pxci
      do i=1,n3
        vx(i) = (ran0(izeed) - (ulimes/2.d0))*2.d0
        px(i) = amass(i) * vx(i)
        pkx = pkx + px(i)
      end do

```

```

cccc do momentum in y-direction

vyci = (ran0(iseed) - (ulimes/2.d0))*2.d0
pyci = cmass * vyci
pky = pyci
do i=1,n3
  vy(i) = (ran0(iseed) - (ulimes/2.d0))*2.d0
  py(i) = amass(i) * vy(i)
  pky = pky + py(i)
end do

cccc do momentum in z-direction

vzci = (ran0(iseed) - (ulimes/2.d0))*2.d0
pzci = cmass * vzci
pkz = pzci
do i=1,n3
  vz(i) = (ran0(iseed) - (ulimes/2.d0))*2.d0
  pz(i) = amass(i) * vz(i)
  pkz = pkz + pz(i)
end do

ptot = pkx + pky + pkz

cccc calculate angular momentum for i=1,nmol-3 for known velocities

lxc_i = ( yci*pzci - zci*pyci )
lyc_i = ( zci*pxci - xci*pzci )
lzc_i = ( xci*pyci - yci*pxci )
lkx = lxc_i
lky = lyc_i
lkz = lzc_i
do i=1,n3
  lx(i) = ( yy(i)*pz(i) - zz(i)*py(i) )
  ly(i) = ( zz(i)*px(i) - xx(i)*pz(i) )
  lz(i) = ( xx(i)*py(i) - yy(i)*px(i) )
  lkx = lkx + lx(i)
  lky = lky + ly(i)
  lkz = lkz + lz(i)
end do

cccc calculate angular momentum of the remaining particles

k1 = - lkx - ( pky*zz(n1) - pkz*yy(n1) )
k2 = - lky - ( pkz*xx(n1) - pkx*zz(n1) )
k3 = - lkz - ( pkx*yy(n1) - pky*xx(n1) )

dx = xx(nmol) - xx(n1)
dy = yy(nmol) - yy(n1)
dz = zz(nmol) - zz(n1)
ddx = xx(n2) - xx(n1)
ddy = yy(n2) - yy(n1)
ddz = zz(n2) - zz(n1)

vx(n2) = (ran0(iseed) - (ulimes/2.d0))*2.d0
vy(n2) = (ran0(iseed) - (ulimes/2.d0))*2.d0
vx(nmol) = (ran0(iseed) - (ulimes/2.d0))*2.d0
px(n2) = amass(n2) * vx(n2)
py(n2) = amass(n2) * vy(n2)
px(nmol) = amass(nmol) * vx(nmol)

py(nmol) = (1.d0/dx) *
& (px(nmol)*dy + ddy*px(n2) - ddx*py(n2) + k3)
pz(nmol) = (1.d0/(dy*ddx-dx*ddy)) *
& (- dz*ddy*px(nmol) + dz*ddx*py(nmol)
& - ddx*ddy*px(n2) + ddz*ddx*py(n2) + k1*ddx + k2*ddy )
pz(n2) = (1.d0/ddy) *
& (dz*py(nmol) - dy*pz(nmol) + ddz*py(n2) + k1)

px(n1) = - pkx - px(n2) - px(nmol)
py(n1) = - pky - py(n2) - py(nmol)
pz(n1) = - pkz - pz(n2) - pz(nmol)

```

```
do i=n2,nmol
  lx(i) = ( yy(i)*pz(i) - zz(i)*py(i) )
  ly(i) = ( zz(i)*px(i) - xx(i)*pz(i) )
  lz(i) = ( xx(i)*py(i) - yy(i)*px(i) )

  lkx  = lkx + lx(i)
  lky  = lky + ly(i)
  lkz  = lkz + lz(i)
end do

pkx = pkx + (px(n2) + px(n1) + px(nmol))
pky = pkx + (py(n2) + py(n1) + py(nmol))
pkz = pkz + (pz(n2) + pz(n1) + pz(nmol))

ptot = pkx + pky + pkz
cccc calculate velocities from momentum
vtot = 0.d0

vxci = pxci / cmass
vyci = pyci / cmass
vzci = pzci / cmass

vkx = vxci
vky = vyci
vkz = vzci

do i=1,nmol
  vx(i) = px(i) / amass(i)
  vy(i) = py(i) / amass(i)
  vz(i) = pz(i) / amass(i)

  vkx = vkx + vx(i)
  vky = vky + vy(i)
  vkz = vkz + vz(i)
end do

vxci = vxci * scalev
vyci = vyci * scalev
vzci = vzci * scalev

vkx = vxci
vky = vyci
vkz = vzci

pxci = cmass * vxci
pyci = cmass * vyci
pzci = cmass * vzci

pkx = pxci
pky = pyci
pkz = pzci

lxci = ( yci*pzci - zci*pyci )
lyci = ( zci*pxci - xci*pzci )
lzci = ( xci*pyci - yci*pxci )

lkx = lxci
lky = lyci
lkz = lzci
```

```

do i=1,nmol
  vx(i) = vx(i) * scalev
  vy(i) = vy(i) * scalev
  vz(i) = vz(i) * scalev
  vkx  = vkx + vx(i)
  vky  = vky + vy(i)
  vkz  = vkz + vz(i)
  px(i) = amass(i) * vx(i)
  py(i) = amass(i) * vy(i)
  pz(i) = amass(i) * vz(i)
  pkx  = pkx + px(i)
  pky  = pky + py(i)
  pkz  = pkz + pz(i)
  lx(i) = ( yy(i)*pz(i) - zz(i)*py(i) )
  ly(i) = ( zz(i)*px(i) - xx(i)*pz(i) )
  lz(i) = ( xx(i)*py(i) - yy(i)*px(i) )
  lkx  = lkx + lx(i)
  lky  = lky + ly(i)
  lkz  = lkz + lz(i)
end do

vtot = vkx + vky + vkz  ! total velocity of whole cluster
ltot = lkx + lky + lkz  ! total angular momentum of whole cluster
ptot = pkx + pky + pkz  ! total linear momentum of whole cluster

cccc compute the angular velocity for the rotation of the water
cccc molecules (at random) and from there get the angular momenta
cccc in the molecular frame

sigrotx = sqrt( kb * temper * jtoh / ixx )
sigroty = sqrt( kb * temper * jtoh / iyy )
sigrotz = sqrt( kb * temper * jtoh / izz )

do i=1,nmol
  wx(i) = gaussrot(iseed,sigrotx)
  wy(i) = gaussrot(iseed,sigroty)
  wz(i) = gaussrot(iseed,sigrotz)

  qe(1,1) = q0(i)*q0(i)+q1(i)*q1(i)-q2(i)*q2(i)-q3(i)*q3(i)
  qe(1,2) = 2.d0*(q1(i)*q2(i)-q0(i)*q3(i))
  qe(1,3) = 2.d0*(q1(i)*q3(i)+q0(i)*q2(i))
  qe(2,1) = 2.d0*(q1(i)*q2(i)+q0(i)*q3(i))
  qe(2,2) = q0(i)*q0(i)-q1(i)*q1(i)+q2(i)*q2(i)-q3(i)*q3(i)
  qe(2,3) = 2.d0*(q2(i)*q3(i)-q0(i)*q1(i))
  qe(3,1) = 2.d0*(q1(i)*q3(i)-q0(i)*q2(i))
  qe(3,2) = 2.d0*(q2(i)*q3(i)+q0(i)*q1(i))
  qe(3,3) = q0(i)*q0(i)-q1(i)*q1(i)-q2(i)*q2(i)+q3(i)*q3(i)

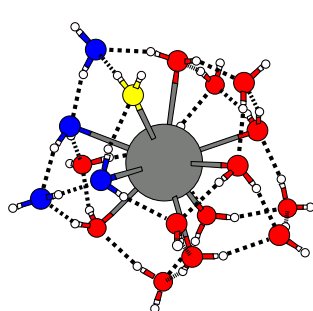
  iwz = izz * wz(i)
  iwx = ixz * wx(i)
  iwz = iyz * wy(i)
  lx(i) = qe(1,1)*iwx + qe(1,2)*iwy + qe(1,3)*iwz
  ly(i) = qe(2,1)*iwx + qe(2,2)*iwy + qe(2,3)*iwz
  lz(i) = qe(3,1)*iwx + qe(3,2)*iwy + qe(3,3)*iwz
end do

return
end

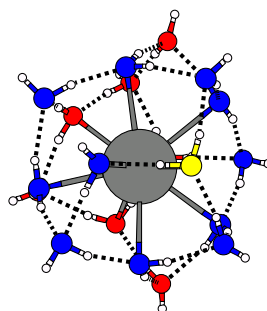
```


15. Additional figures

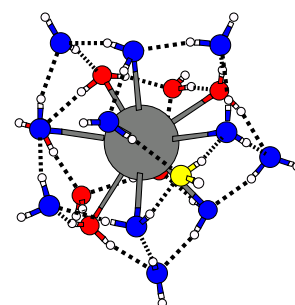
15.1. Figures for constrained dynamics of $\text{Cs}^+(\text{H}_2\text{O})_{19}$



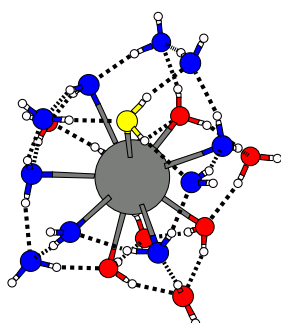
$\text{Cs}^+(\text{H}_2\text{O})_{19}$
Cs.019.a



$\text{Cs}^+(\text{H}_2\text{O})_{19}$
Cs.019.b



$\text{Cs}^+(\text{H}_2\text{O})_{19}$
Cs.019.c



$\text{Cs}^+(\text{H}_2\text{O})_{19}$
Cs.019.d

Figure 15.1.: Global minimum structure of $\text{Cs}^+(\text{H}_2\text{O})_{19}$ where the water molecules marked yellow indicate the pulled water molecules whereas the blue water molecules indicate annealed rings which contain the pulled water molecule.

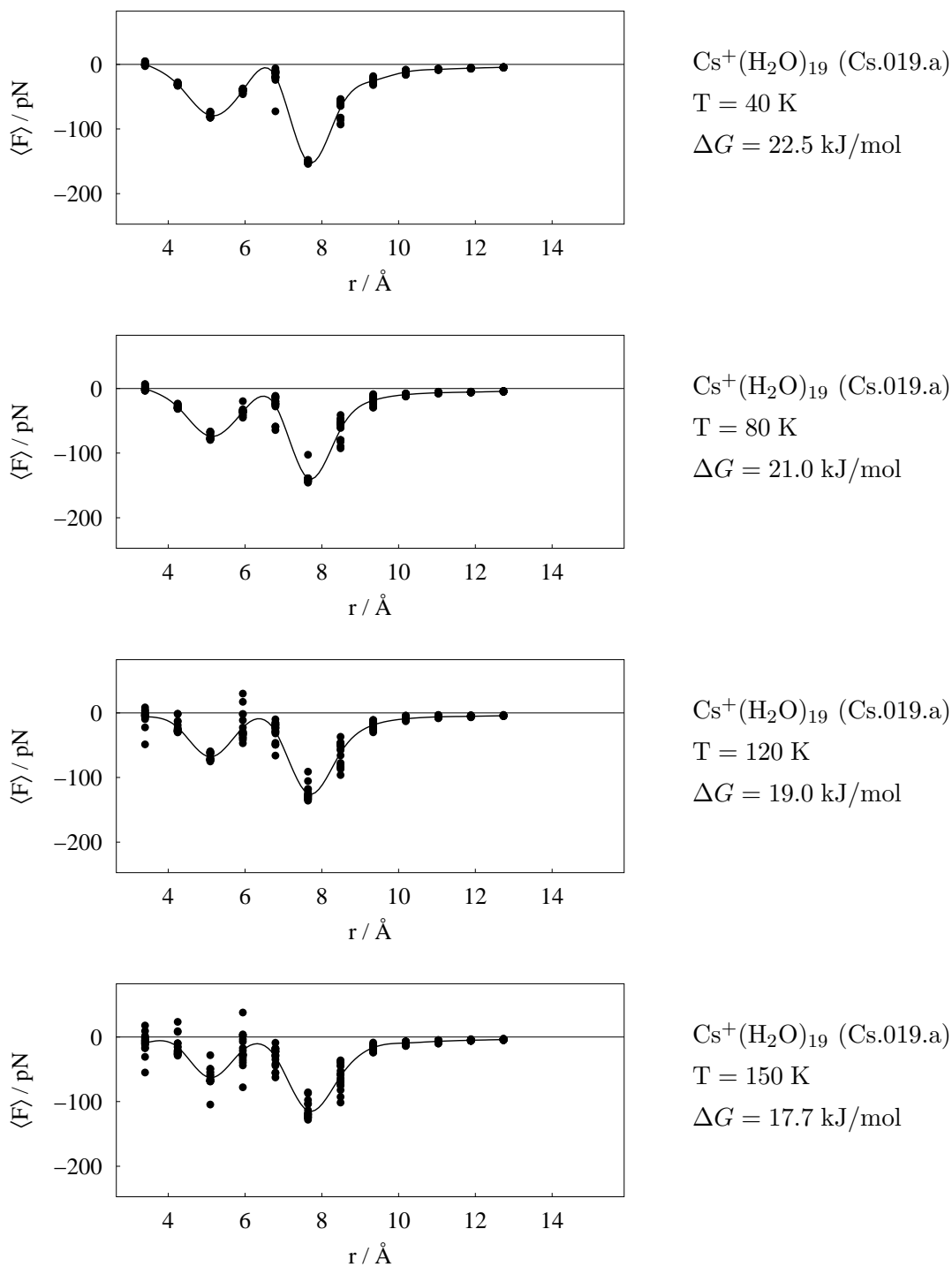


Figure 15.2.: Average constraint force $\langle F \rangle$ in pN vs. distance r in Ångström of pulled water molecules of structure Cs.019.a for eighteen starting conditions per distance r at $T = 40$ K, $T = 80$ K, $T = 120$ K, and $T = 150$ K, respectively, and corresponding free energy ΔG in kJ/mol

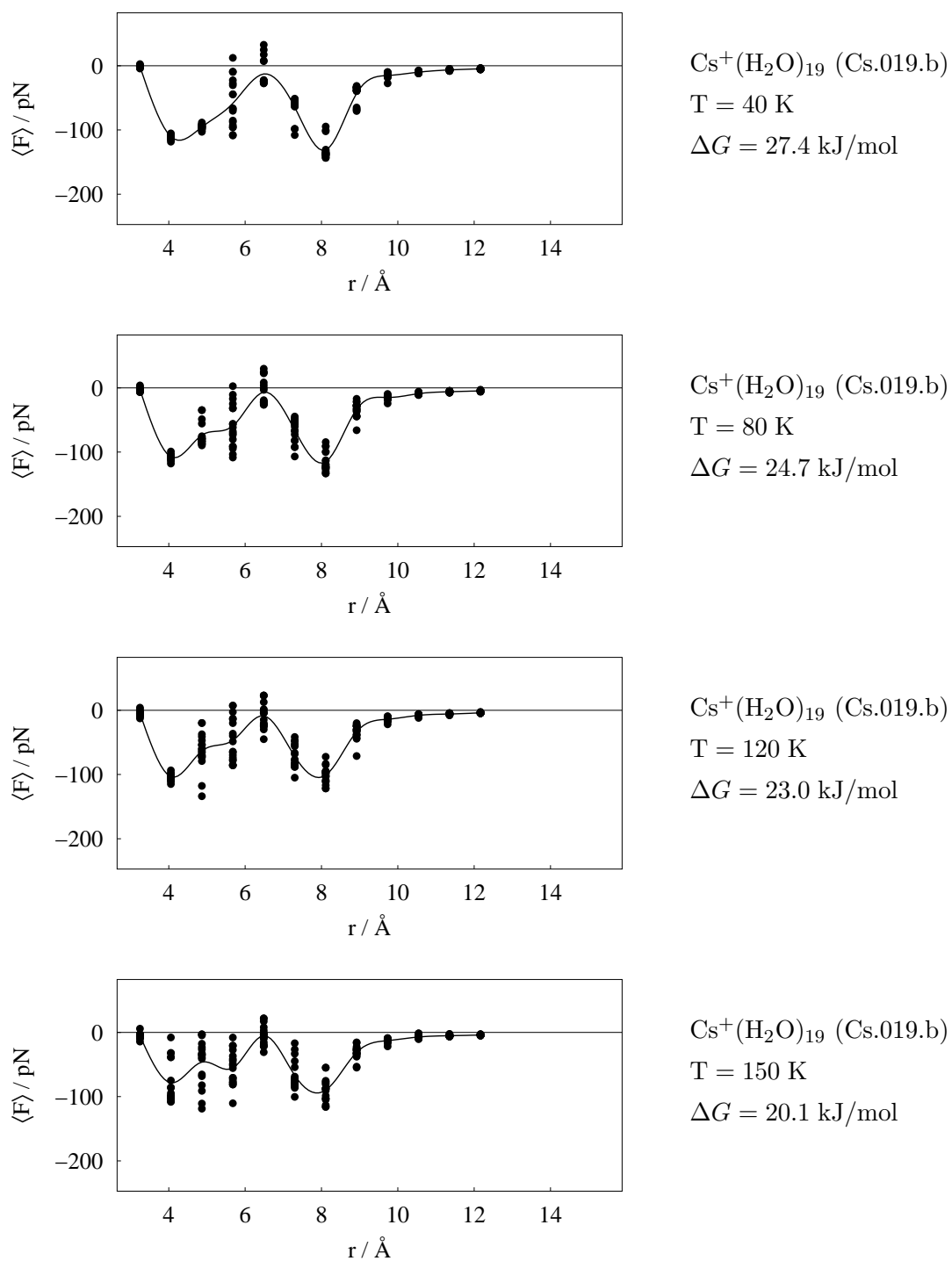


Figure 15.3.: Average constraint force $\langle F \rangle$ in pN vs. distance r in Ångström of pulled water molecules of structure Cs.019.b for eighteen starting conditions per distance r at $T = 40$ K, $T = 80$ K, $T = 120$ K, and $T = 150$ K, respectively, and corresponding free energy ΔG in kJ/mol

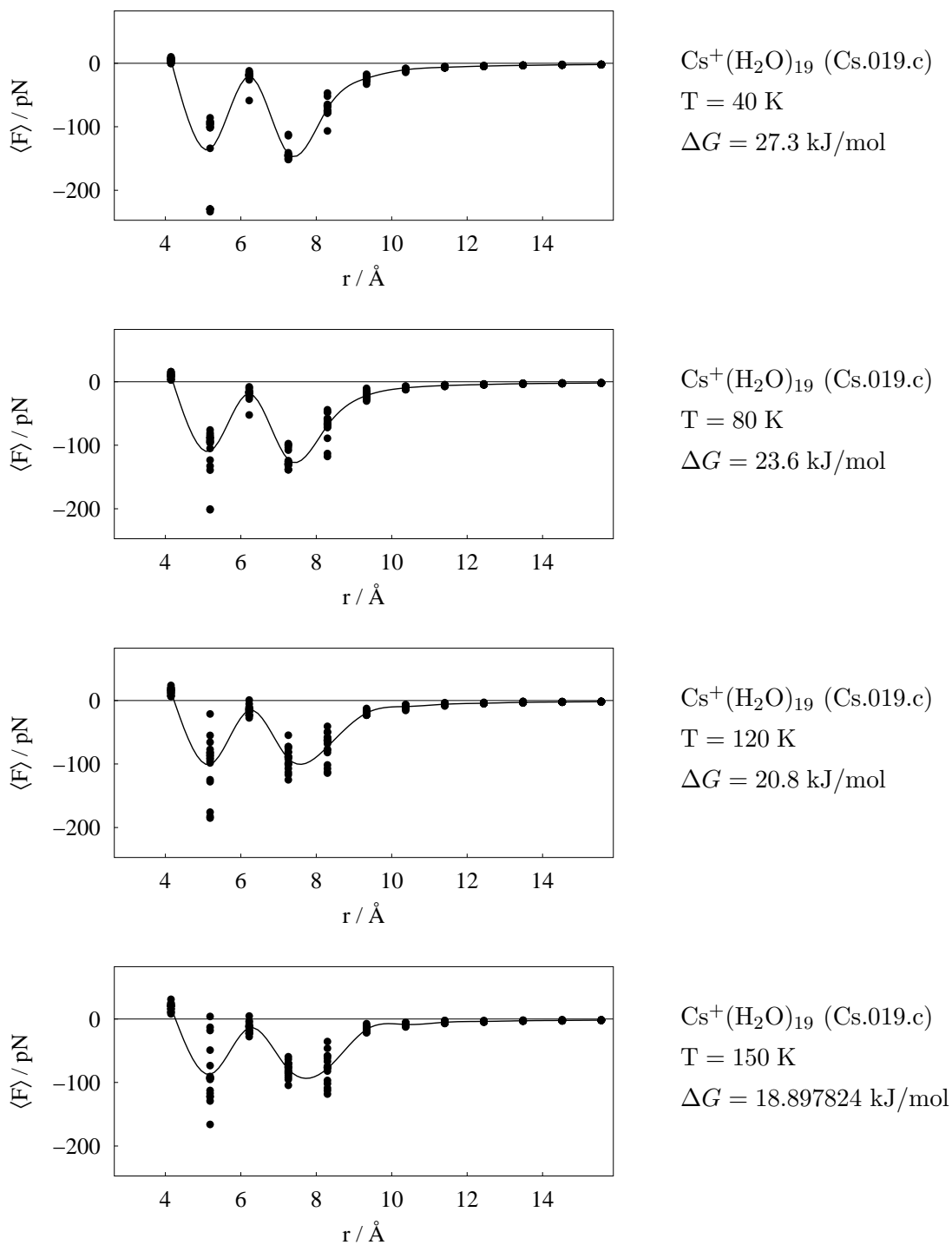


Figure 15.4.: Average constraint force $\langle F \rangle$ in pN vs. distance r in Ångström of pulled water molecules of structure Cs.019.c for eighteen starting conditions per distance r at $T = 40$ K, $T = 80$ K, $T = 120$ K, and $T = 150$ K, respectively, and corresponding free energy ΔG in kJ/mol

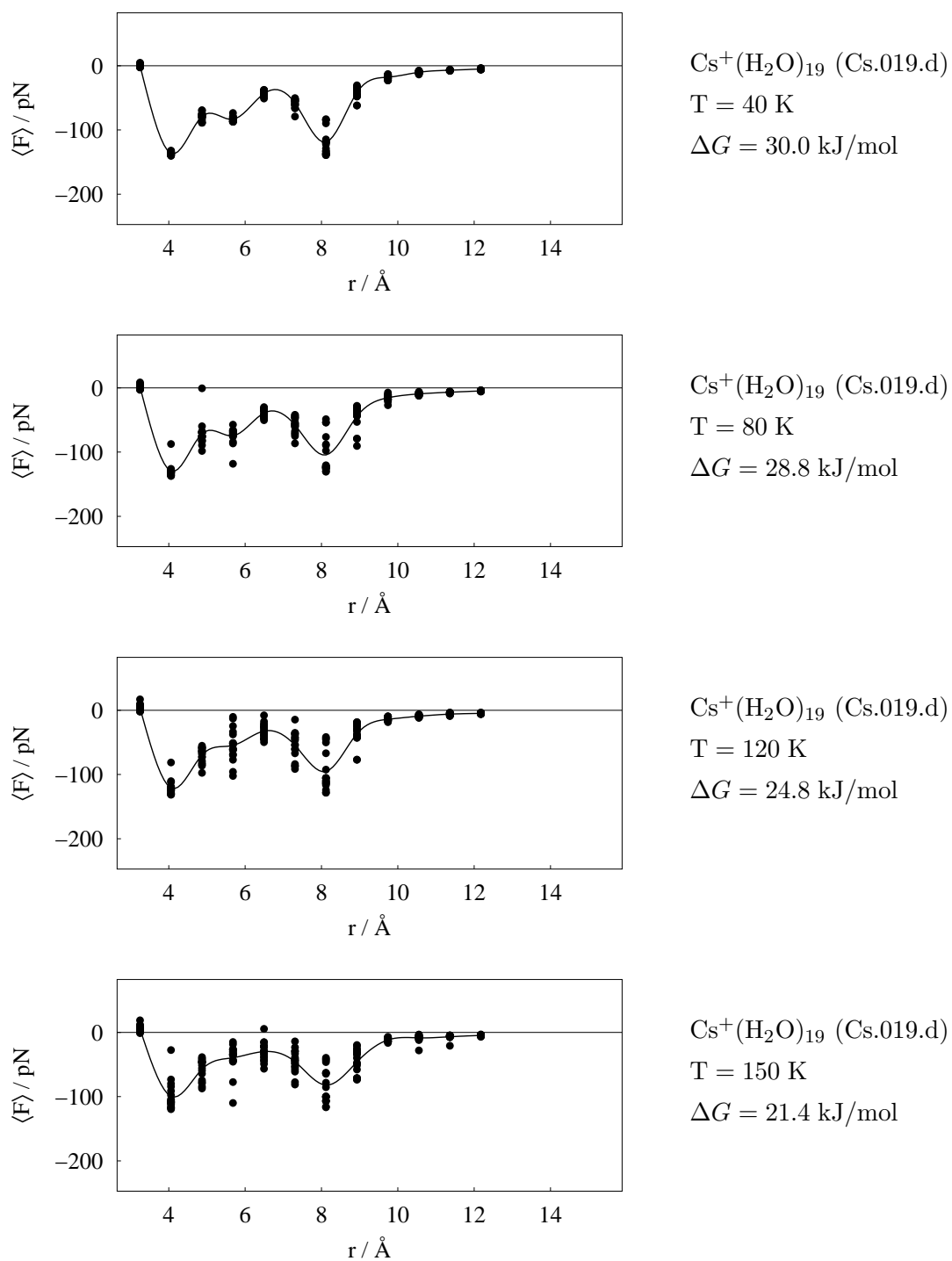
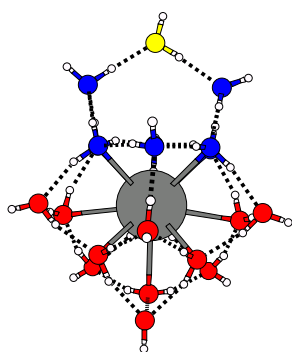
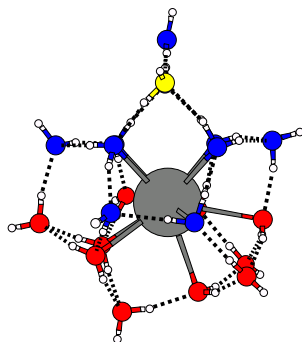


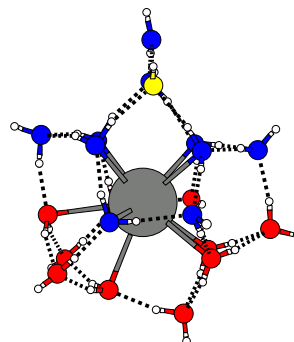
Figure 15.5.: Average constraint force $\langle F \rangle$ in pN vs. distance r in Ångström of pulled water molecules of structure Cs.019.d for eighteen starting conditions per distance r at $T = 40$ K, $T = 80$ K, $T = 120$ K, and $T = 150$ K, respectively, and corresponding free energy ΔG in kJ/mol

15.2. Figures for constrained dynamics of $\text{Cs}^+(\text{H}_2\text{O})_{21}$ 

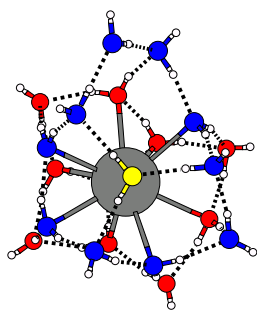
$\text{Cs}^+(\text{H}_2\text{O})_{21}$
Cs.021.a



$\text{Cs}^+(\text{H}_2\text{O})_{21}$
Cs.021.b



$\text{Cs}^+(\text{H}_2\text{O})_{21}$
Cs.021.c



$\text{Cs}^+(\text{H}_2\text{O})_{21}$
Cs.021.d

Figure 15.6.: Global minimum structure of $\text{Cs}^+(\text{H}_2\text{O})_{21}$ where the water molecules marked yellow indicate the pulled water molecules whereas the blue water molecules indicate annealed rings which contain the pulled water molecule.

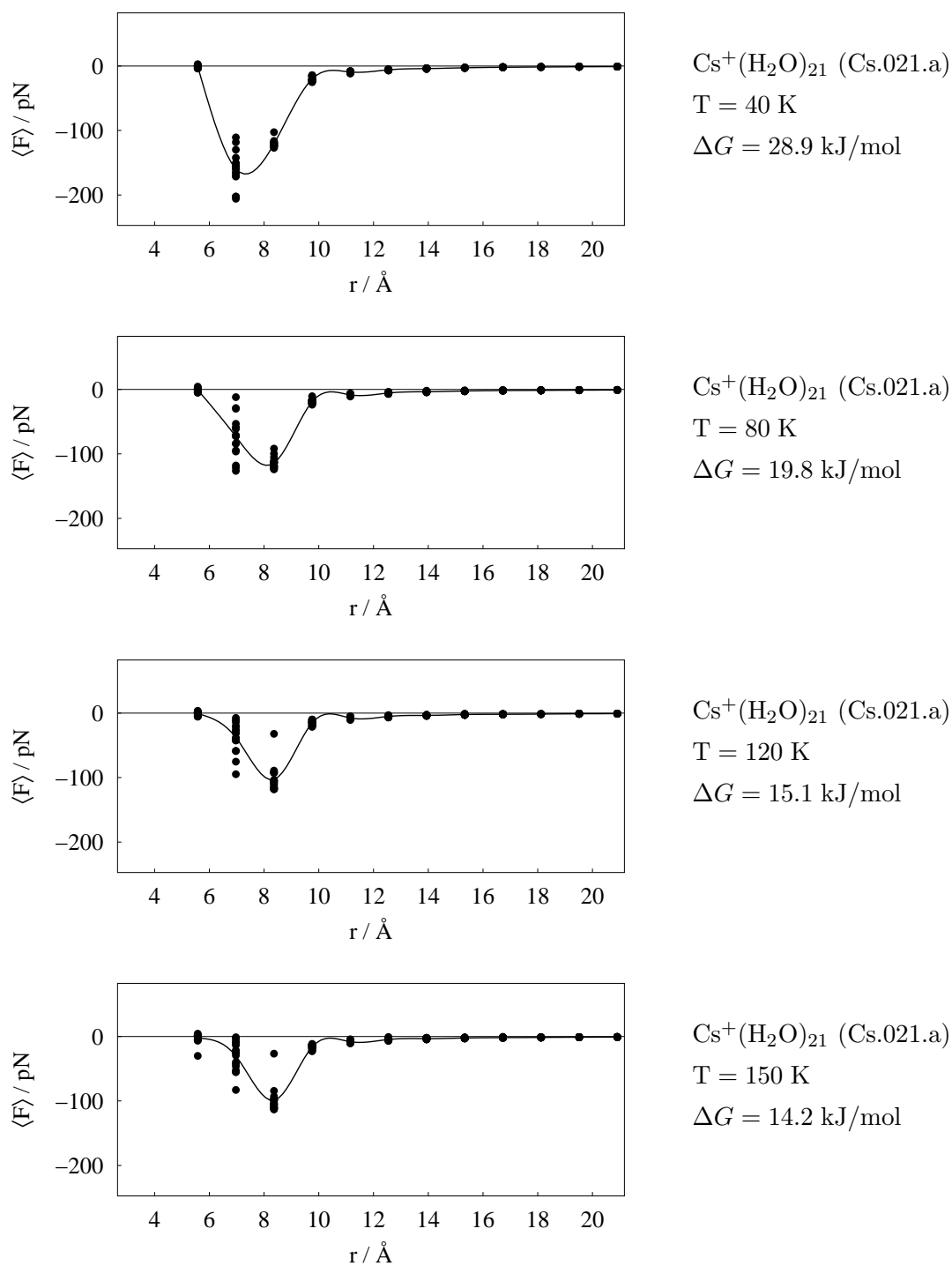


Figure 15.7.: Average constraint force $\langle F \rangle$ in pN vs. distance r in Ångström of pulled water molecules of structure Cs.021.a for eighteen starting conditions per distance r at $T = 40$ K, $T = 80$ K, $T = 120$ K, and $T = 150$ K, respectively, and corresponding free energy ΔG in kJ/mol

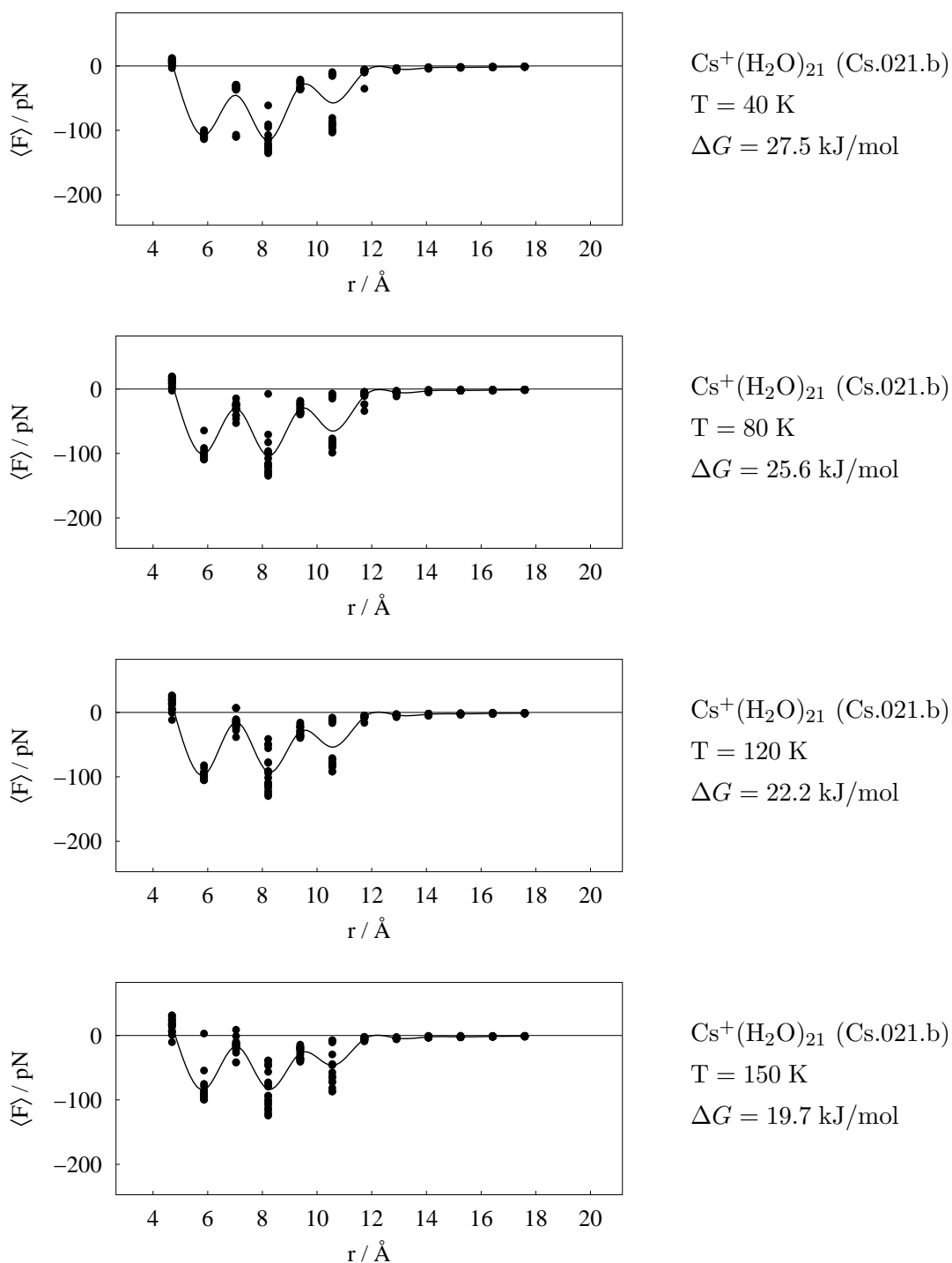


Figure 15.8.: Average constraint force $\langle F \rangle$ in pN vs. distance r in Ångström of pulled water molecules of structure Cs.021.b for eighteen starting conditions per distance r at $T = 40$ K, $T = 80$ K, $T = 120$ K, and $T = 150$ K, respectively, and corresponding free energy ΔG in kJ/mol

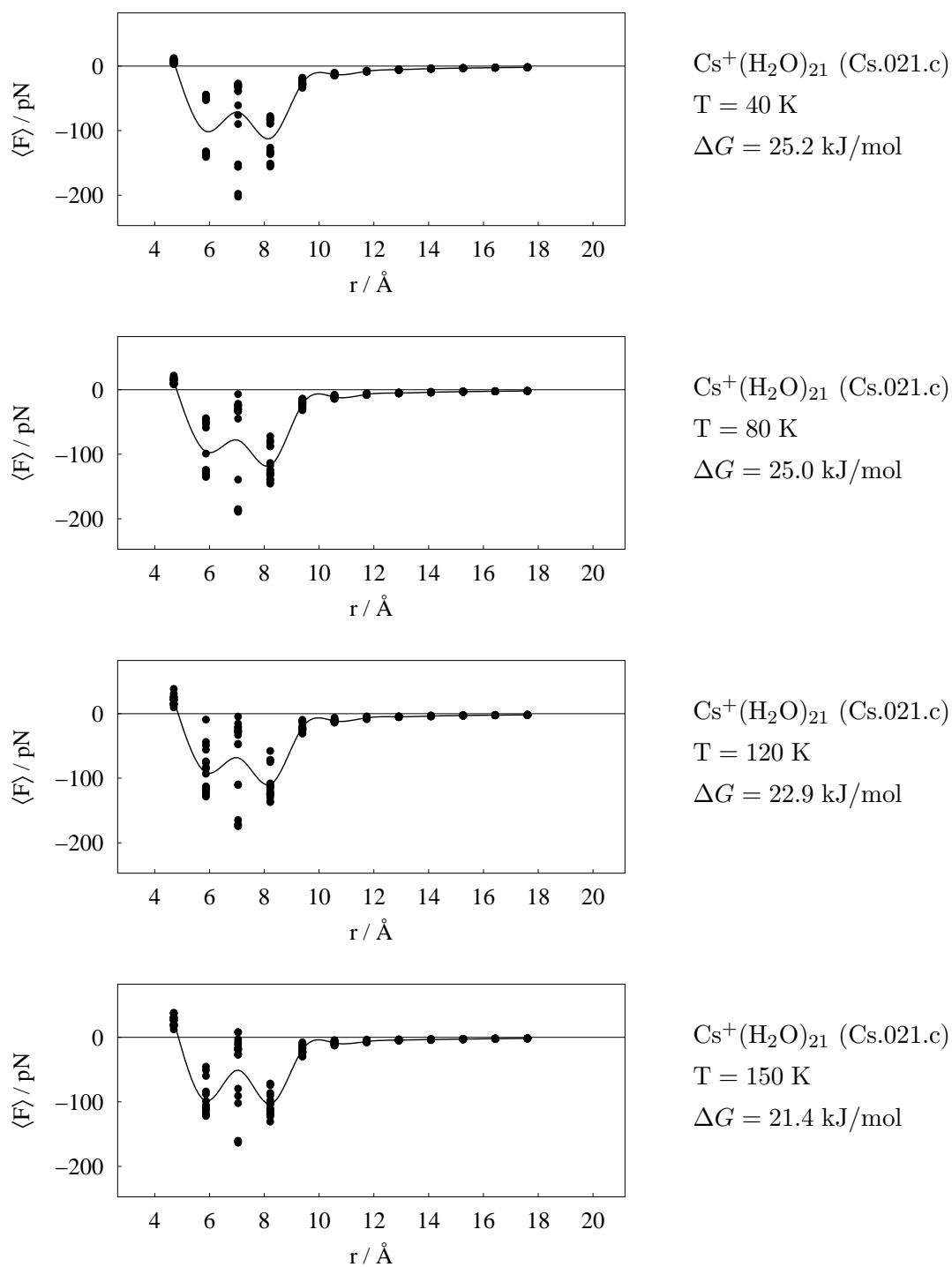


Figure 15.9.: Average constraint force $\langle F \rangle$ in pN vs. distance r in Ångström of pulled water molecules of structure Cs.021.c for eighteen starting conditions per distance r at $T = 40$ K, $T = 80$ K, $T = 120$ K, and $T = 150$ K, respectively, and corresponding free energy ΔG in kJ/mol

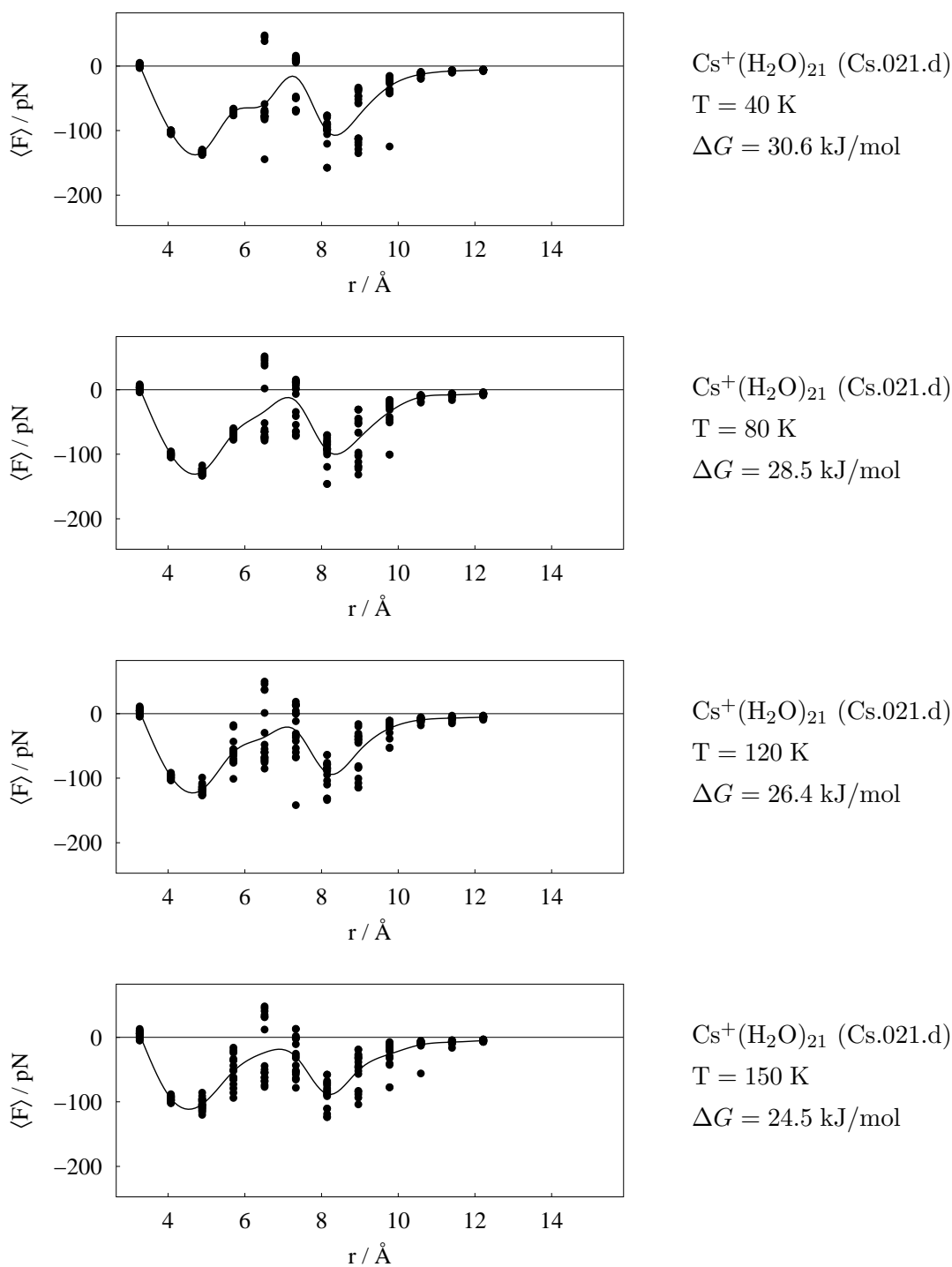
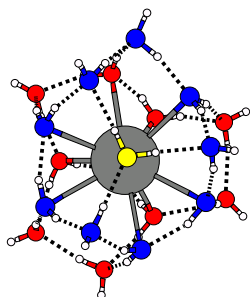
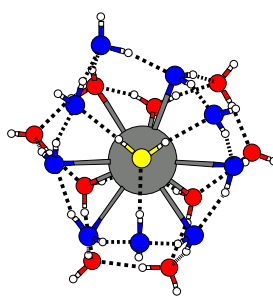


Figure 15.10.: Average constraint force $\langle F \rangle$ in pN vs. distance r in Ångström of pulled water molecules of structure Cs.021.d for eighteen starting conditions per distance r at $T = 40 \text{ K}$, $T = 80 \text{ K}$, $T = 120 \text{ K}$, and $T = 150 \text{ K}$, respectively, and corresponding free energy ΔG in kJ/mol

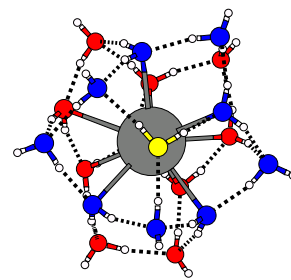
15.3. Figures for constrained dynamics of $\text{Cs}^+(\text{H}_2\text{O})_{20}$ DOD – dodecahedral



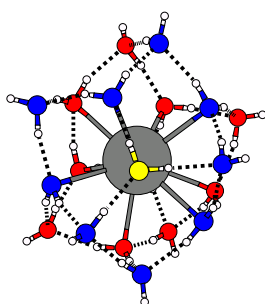
$\text{Cs}^+(\text{H}_2\text{O})_{20}$
Cs.020.dod.a



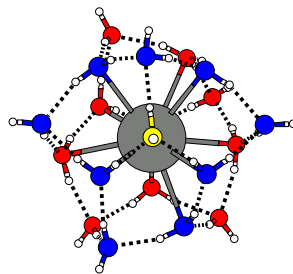
$\text{Cs}^+(\text{H}_2\text{O})_{20}$
Cs.020.dod.b



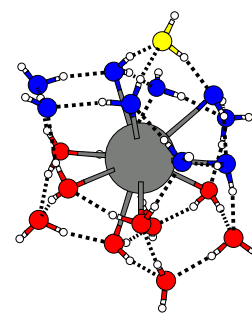
$\text{Cs}^+(\text{H}_2\text{O})_{20}$
Cs.020.dod.c



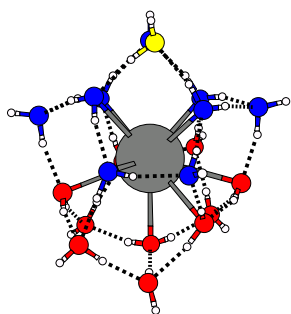
$\text{Cs}^+(\text{H}_2\text{O})_{20}$
Cs.020.dod.d



$\text{Cs}^+(\text{H}_2\text{O})_{20}$
Cs.020.dod.e



$\text{Cs}^+(\text{H}_2\text{O})_{20}$
Cs.020.dod.f



$\text{Cs}^+(\text{H}_2\text{O})_{20}$
Cs.020.dod.g

Figure 15.11.: Global minimum structure of $\text{Cs}^+(\text{H}_2\text{O})_{20}$ (DOD – dodecahedral) where the water molecules marked yellow indicate the pulled water molecules whereas the blue water molecules indicate annealed rings which contain the pulled water molecule.

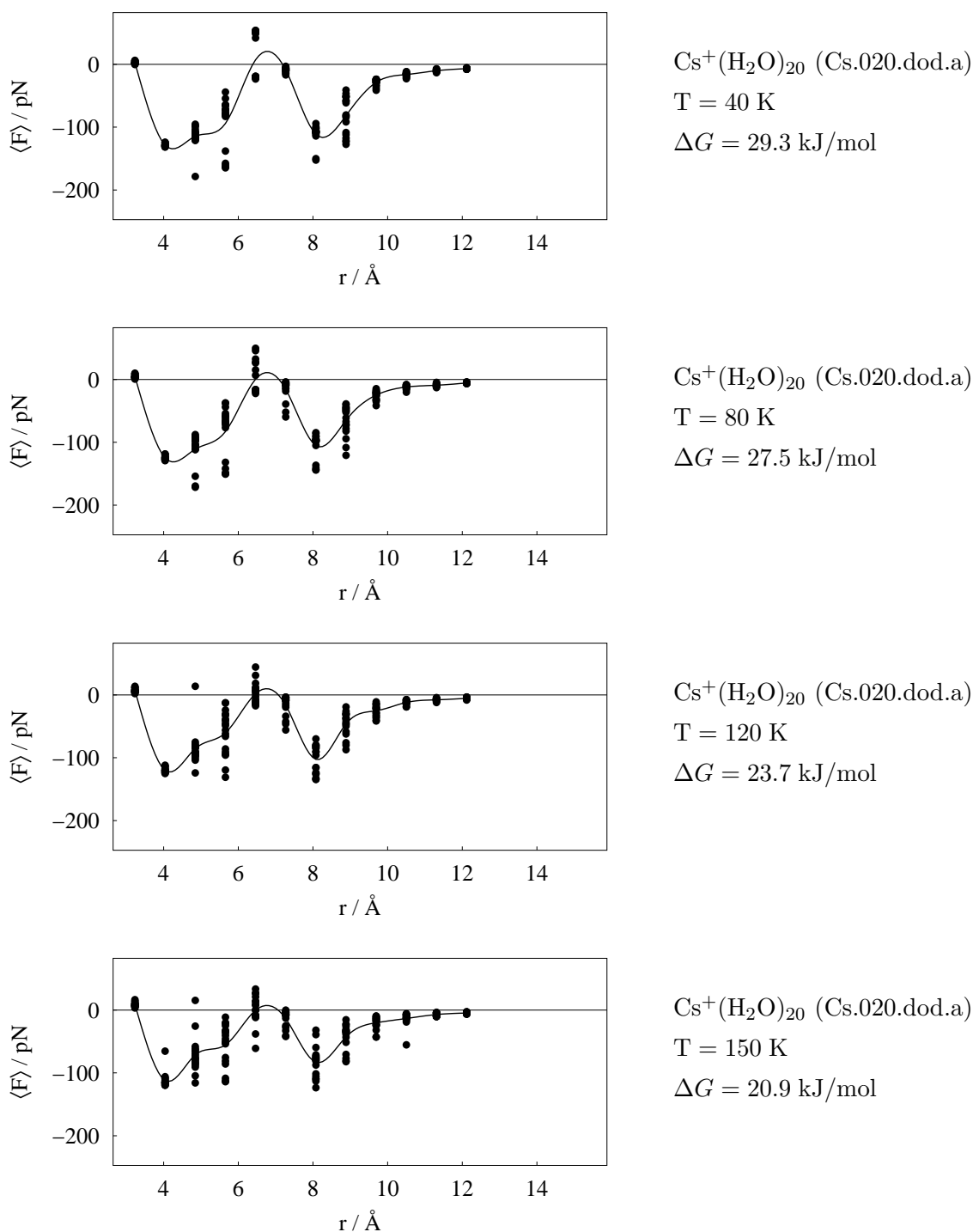


Figure 15.12.: Average constraint force $\langle F \rangle$ in pN vs. distance r in Ångström of pulled water molecules of structure Cs.020.dod.a for eighteen starting conditions per distance r at $T = 40 \text{ K}$, $T = 80 \text{ K}$, $T = 120 \text{ K}$, and $T = 150 \text{ K}$, respectively, and corresponding free energy ΔG in kJ/mol

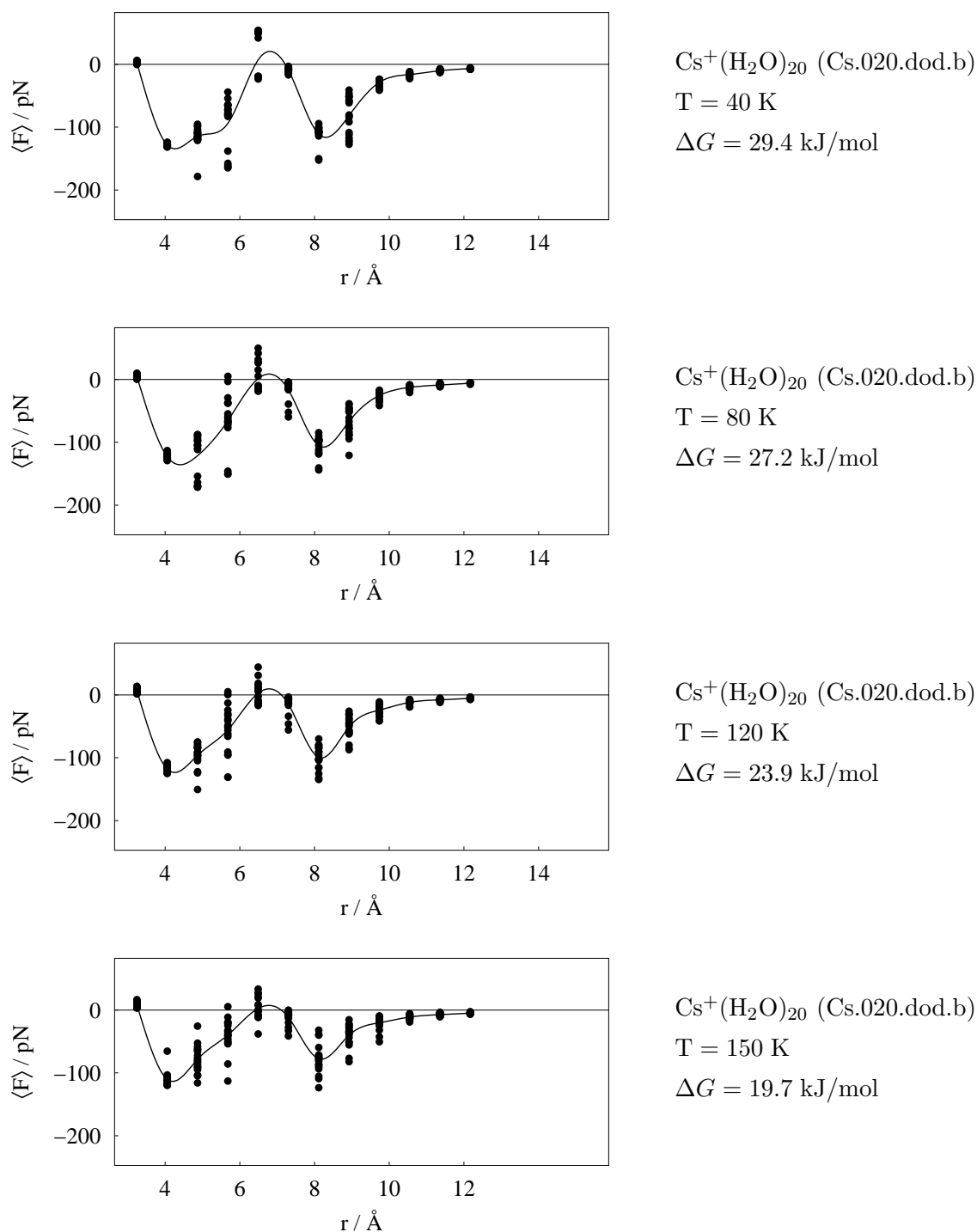


Figure 15.13.: Average constraint force $\langle F \rangle$ in pN vs. distance r in Ångström of pulled water molecules of structure Cs.020.dod.b for eighteen starting conditions per distance r at $T = 40$ K, $T = 80$ K, $T = 120$ K, and $T = 150$ K, respectively, and corresponding free energy ΔG in kJ/mol

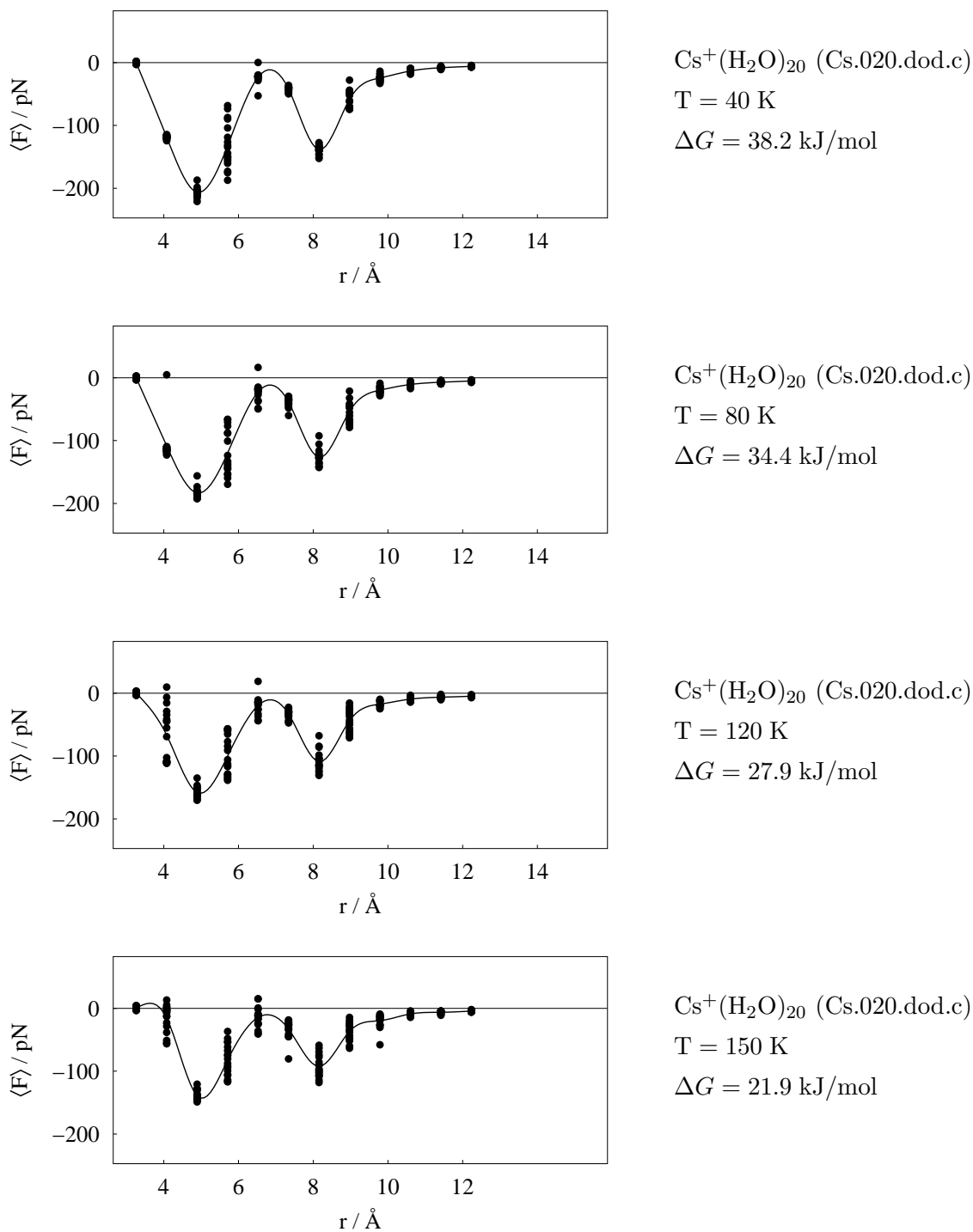


Figure 15.14.: Average constraint force $\langle F \rangle$ in pN vs. distance r in Ångström of pulled water molecules of structure Cs.020.dod.c for eighteen starting conditions per distance r at $T = 40$ K, $T = 80$ K, $T = 120$ K, and $T = 150$ K, respectively, and corresponding free energy ΔG in kJ/mol

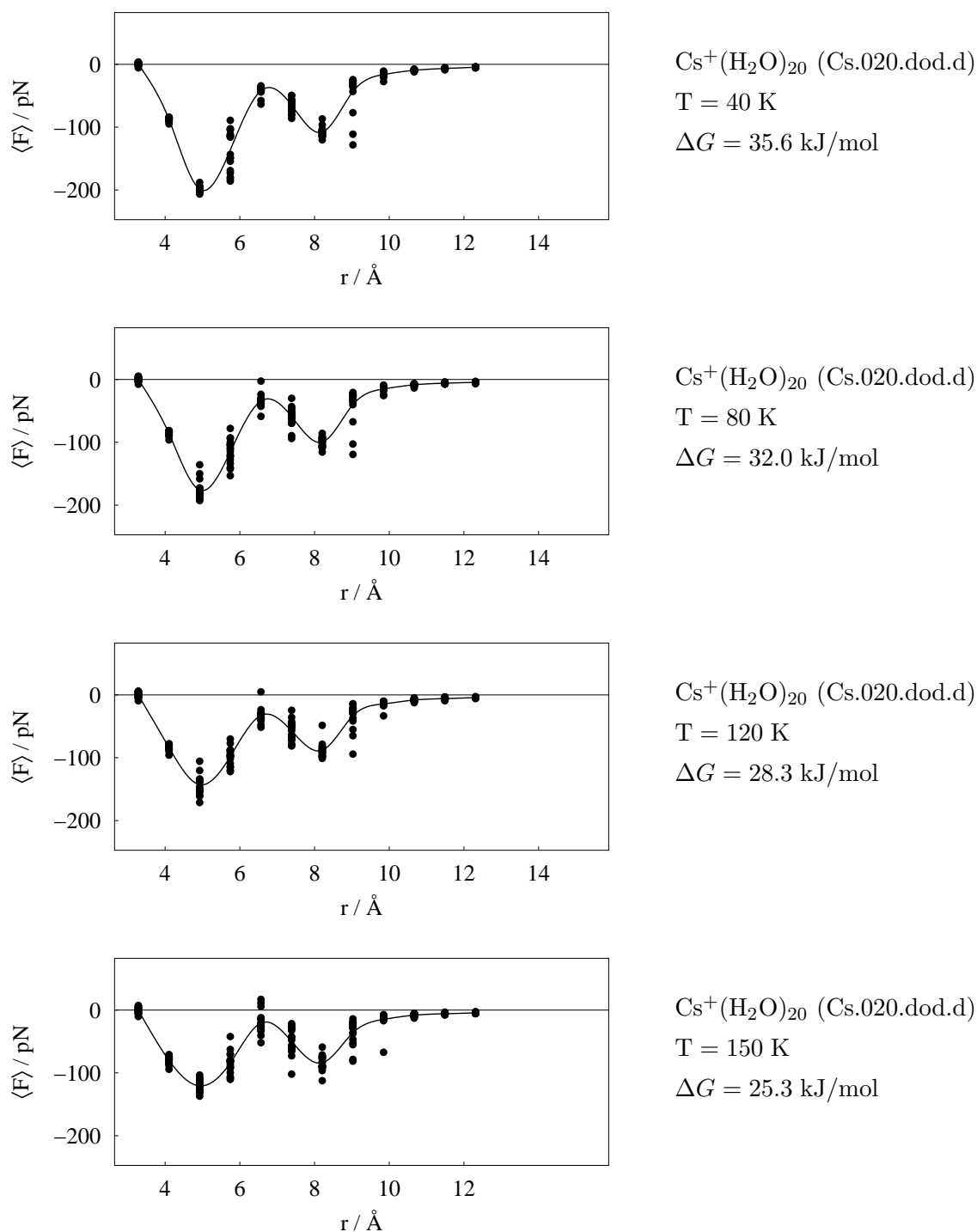


Figure 15.15.: Average constraint force $\langle F \rangle$ in pN vs. distance r in Ångström of pulled water molecules of structure Cs.020.dod.d for eighteen starting conditions per distance r at $T = 40$ K, $T = 80$ K, $T = 120$ K, and $T = 150$ K, respectively, and corresponding free energy ΔG in kJ/mol

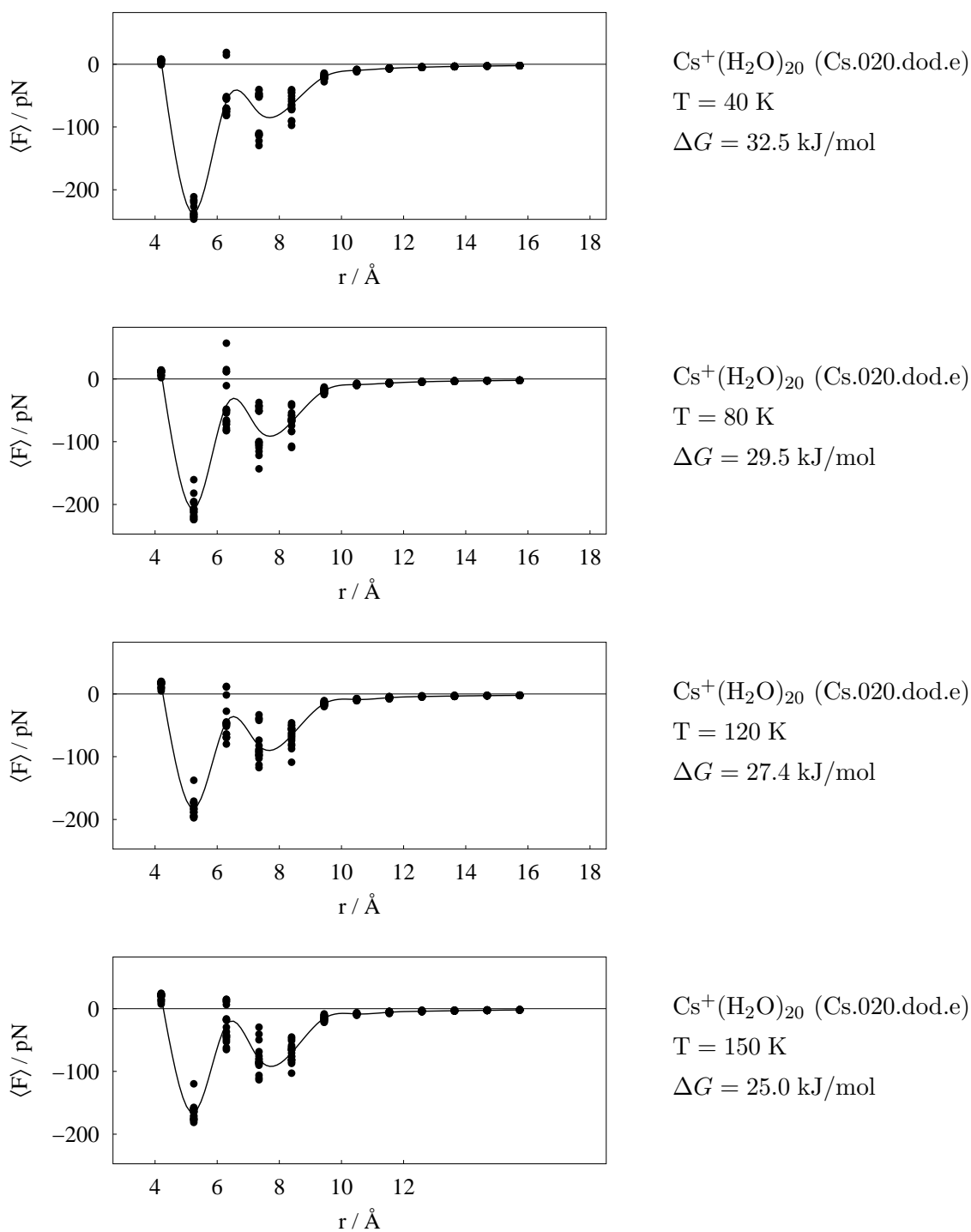


Figure 15.16.: Average constraint force $\langle F \rangle$ in pN vs. distance r in Ångström of pulled water molecules of structure Cs.020.dod.e for eighteen starting conditions per distance r at $T = 40$ K, $T = 80$ K, $T = 120$ K, and $T = 150$ K, respectively, and corresponding free energy ΔG in kJ/mol

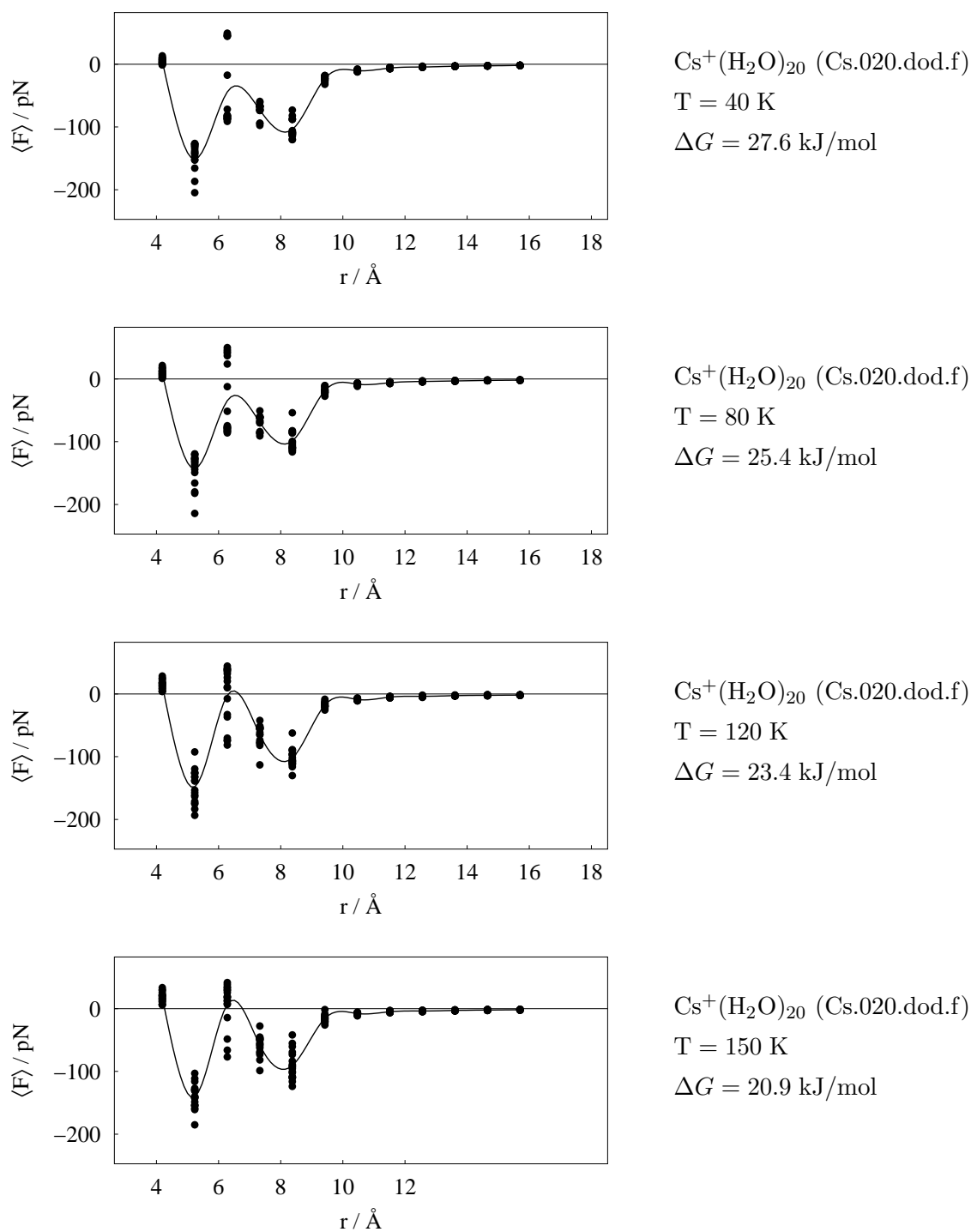


Figure 15.17.: Average constraint force $\langle F \rangle$ in pN vs. distance r in Ångström of pulled water molecules of structure Cs.020.dod.f for eighteen starting conditions per distance r at $T = 40$ K, $T = 80$ K, $T = 120$ K, and $T = 150$ K, respectively, and corresponding free energy ΔG in kJ/mol

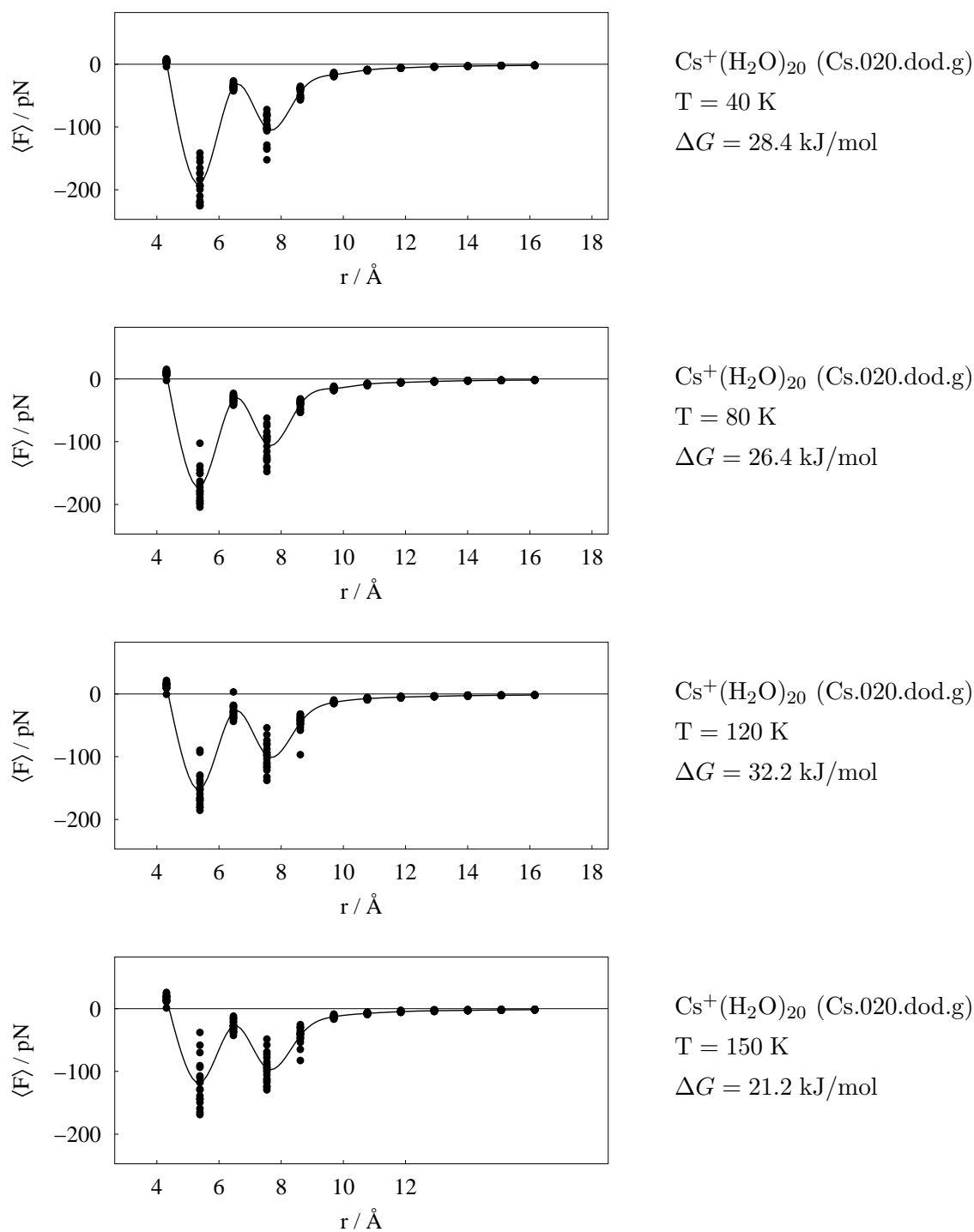
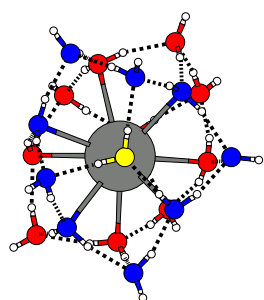
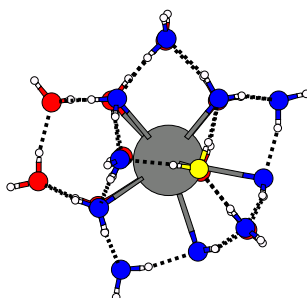


Figure 15.18.: Average constraint force $\langle F \rangle$ in pN vs. distance r in Ångström of pulled water molecules of structure Cs.020.dod.g for eighteen starting conditions per distance r at $T = 40$ K, $T = 80$ K, $T = 120$ K, and $T = 150$ K, respectively, and corresponding free energy ΔG in kJ/mol

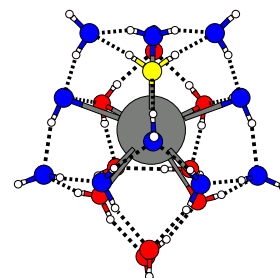
15.4. Figures for constrained dynamics of $\text{Cs}^+(\text{H}_2\text{O})_{20}$ BND – non-dodecahedral



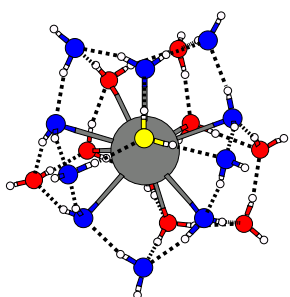
$\text{Cs}^+(\text{H}_2\text{O})_{20}$
Cs.020.bnd.a



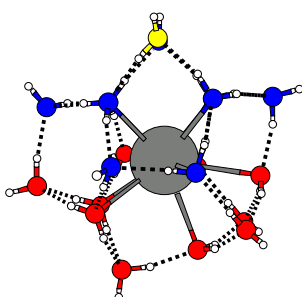
$\text{Cs}^+(\text{H}_2\text{O})_{20}$
Cs.020.bnd.b



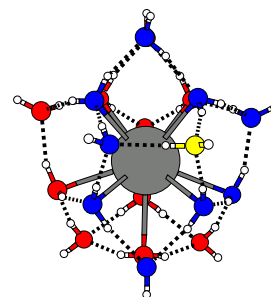
$\text{Cs}^+(\text{H}_2\text{O})_{20}$
Cs.020.bnd.c



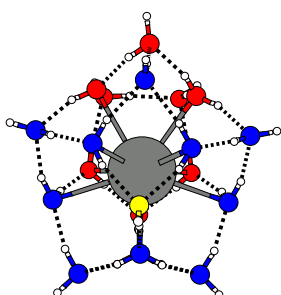
$\text{Cs}^+(\text{H}_2\text{O})_{20}$
Cs.020.bnd.d



$\text{Cs}^+(\text{H}_2\text{O})_{20}$
Cs.020.bnd.e



$\text{Cs}^+(\text{H}_2\text{O})_{20}$
Cs.020.bnd.f



$\text{Cs}^+(\text{H}_2\text{O})_{20}$
Cs.020.bnd.g

Figure 15.19.: Local minimum structure of $\text{Cs}^+(\text{H}_2\text{O})_{20}$ (BND – non-dodecahedral) where the water molecules marked yellow indicate the pulled water molecules whereas the blue water molecules indicate annealed rings which contain the pulled water molecule.

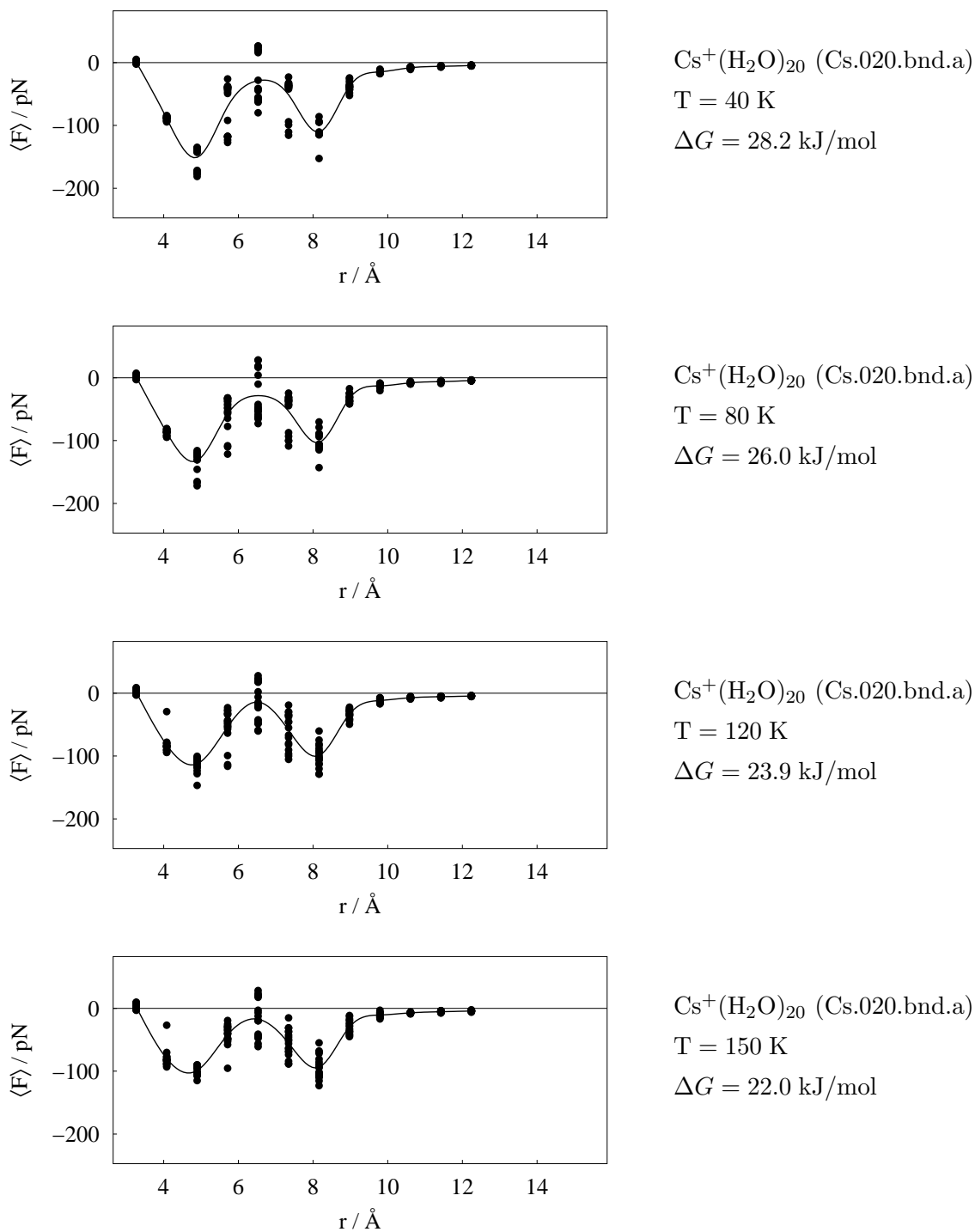


Figure 15.20.: Average constraint force $\langle F \rangle$ in pN vs. distance r in Ångström of pulled water molecules of structure Cs.020.bnd.a for eighteen starting conditions per distance r at $T = 40$ K, $T = 80$ K, $T = 120$ K, and $T = 150$ K, respectively, and corresponding free energy ΔG in kJ/mol

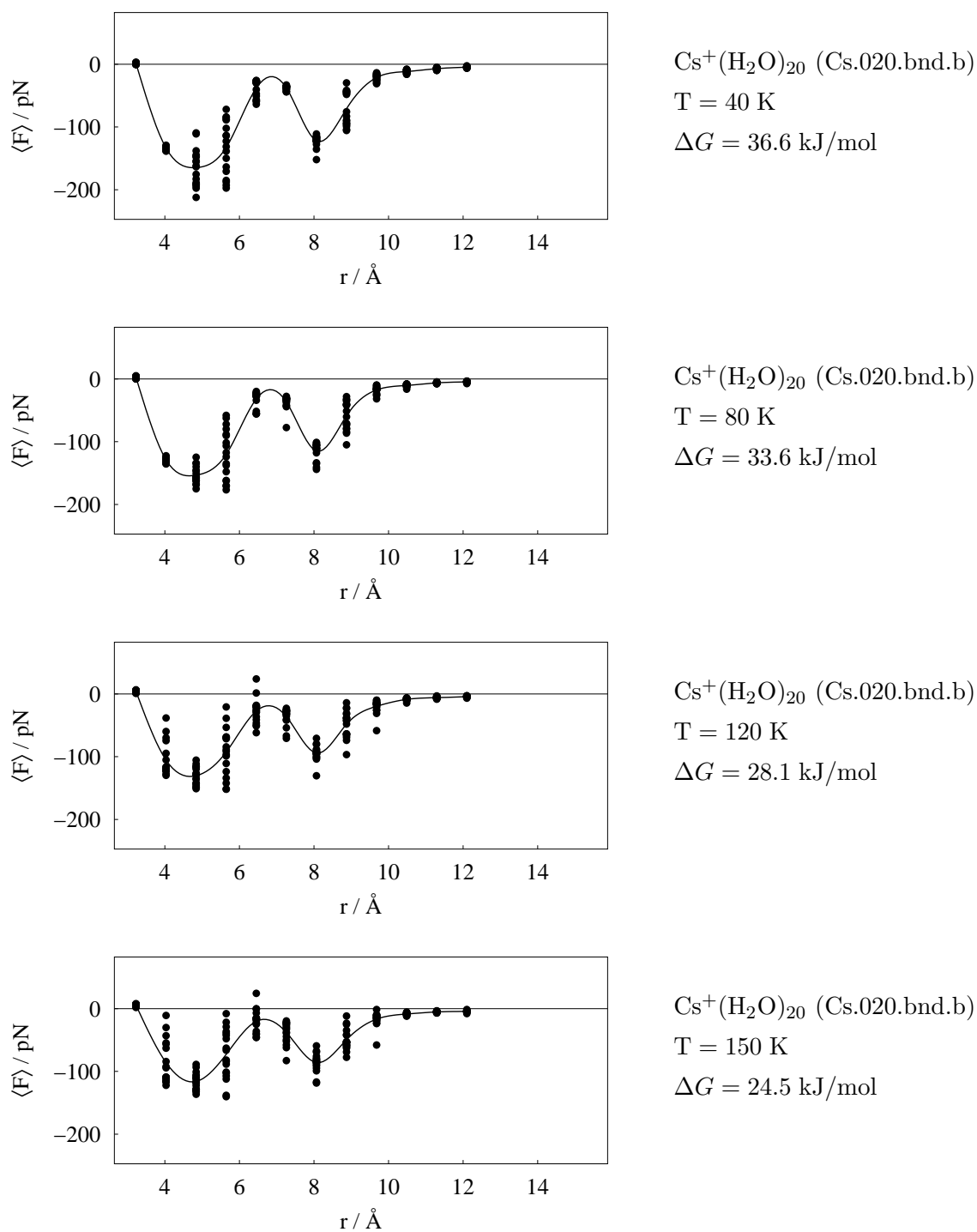


Figure 15.21.: Average constraint force $\langle F \rangle$ in pN vs. distance r in Ångström of pulled water molecules of structure Cs.020.bnd.b for eighteen starting conditions per distance r at $T = 40$ K, $T = 80$ K, $T = 120$ K, and $T = 150$ K, respectively, and corresponding free energy ΔG in kJ/mol

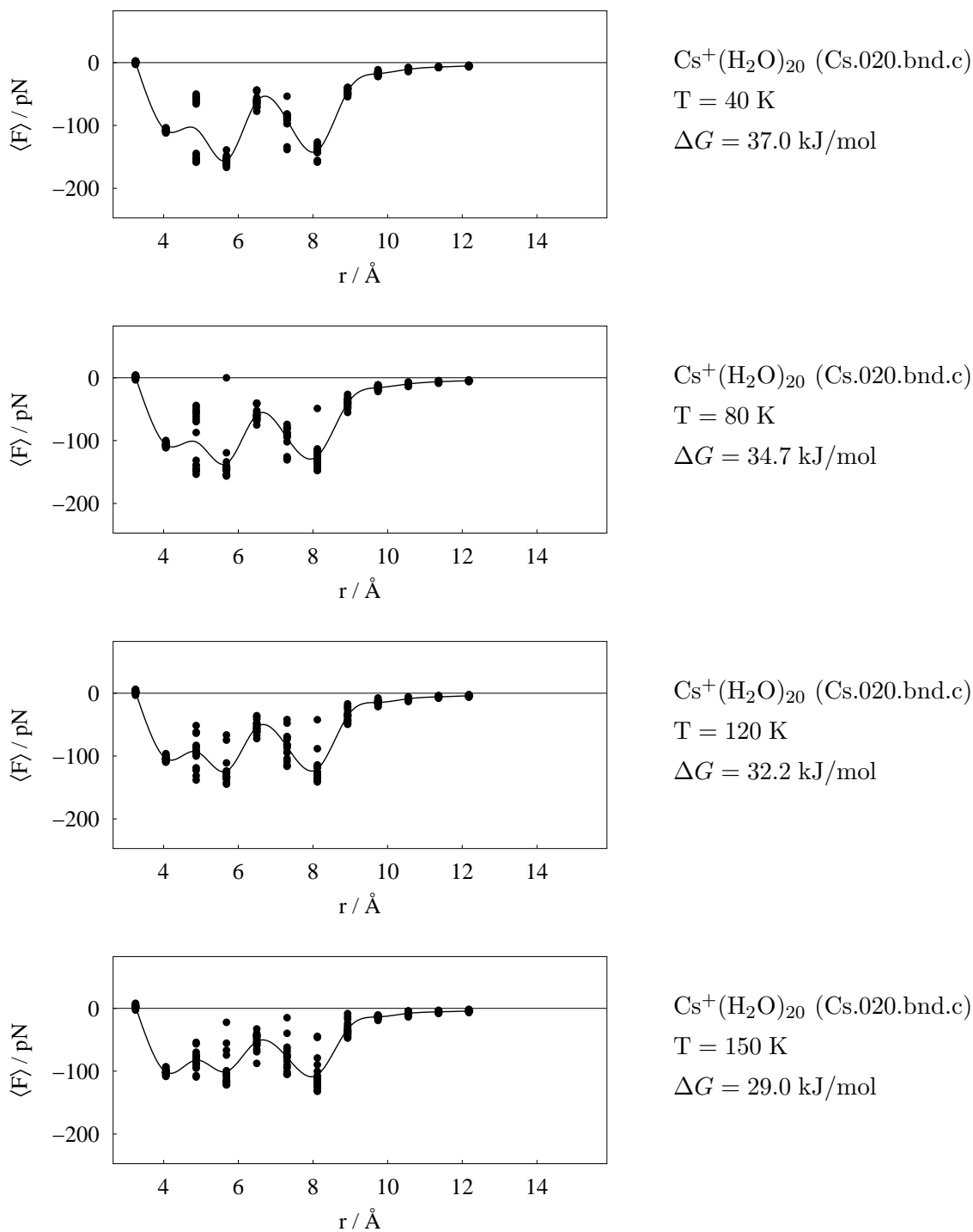


Figure 15.22.: Average constraint force $\langle F \rangle$ in pN vs. distance r in Ångström of pulled water molecules of structure Cs.020.bnd.c for eighteen starting conditions per distance r at $T = 40$ K, $T = 80$ K, $T = 120$ K, and $T = 150$ K, respectively, and corresponding free energy ΔG in kJ/mol

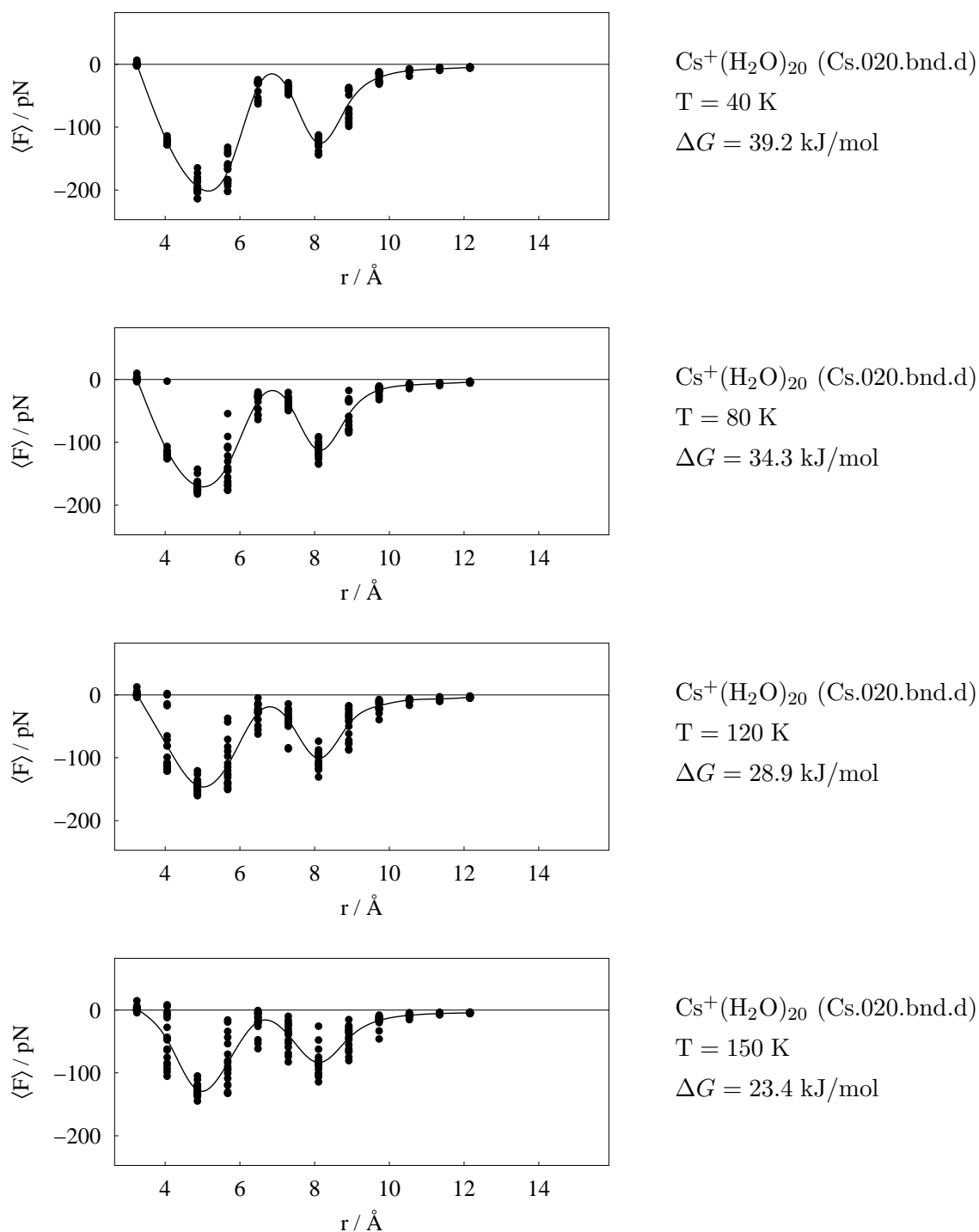


Figure 15.23.: Average constraint force $\langle F \rangle$ in pN vs. distance r in Ångström of pulled water molecules of structure Cs.020.bnd.d for eighteen starting conditions per distance r at $T = 40$ K, $T = 80$ K, $T = 120$ K, and $T = 150$ K, respectively, and corresponding free energy ΔG in kJ/mol

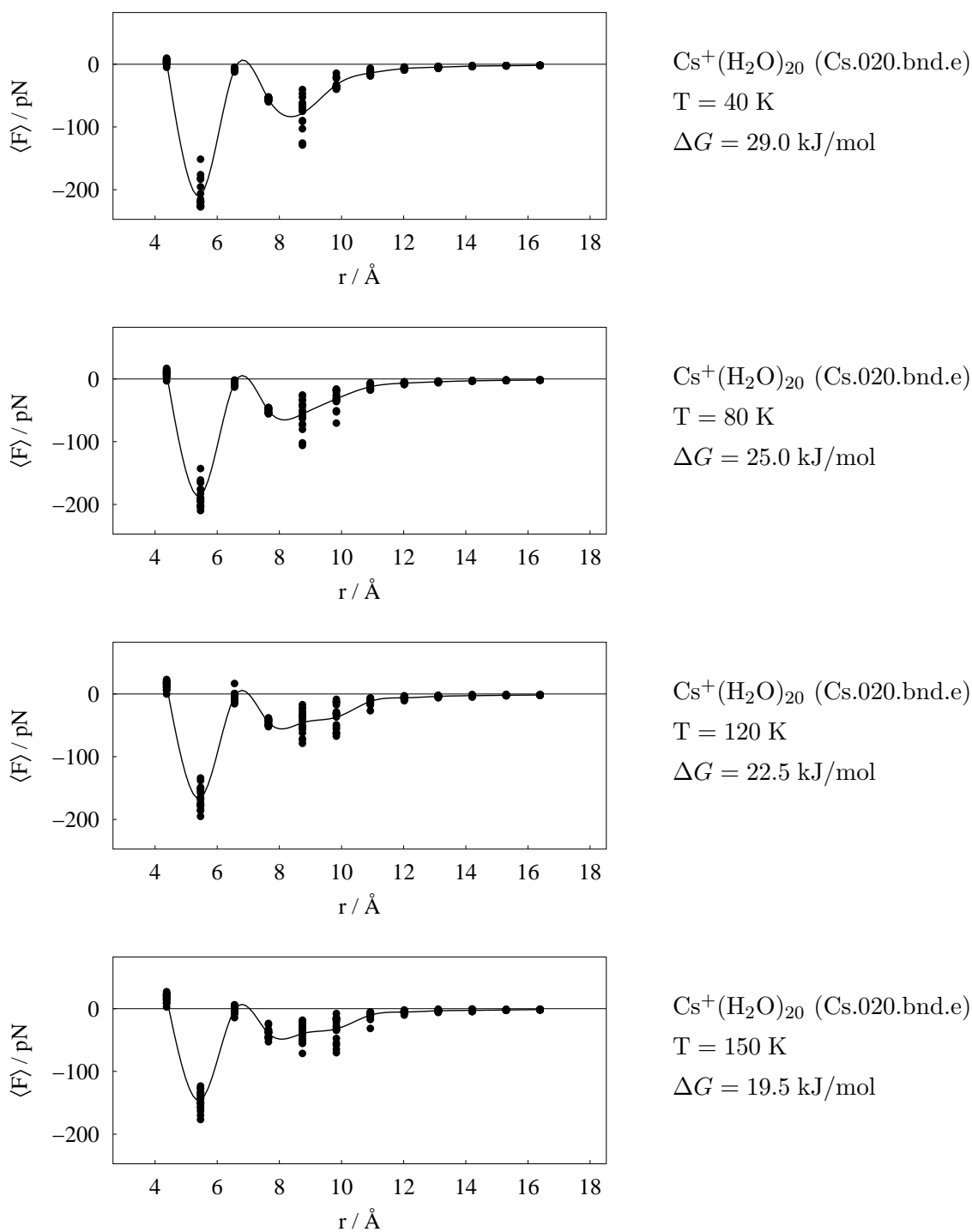


Figure 15.24.: Average constraint force $\langle F \rangle$ in pN vs. distance r in Ångström of pulled water molecules of structure Cs.020.bnd.e for eighteen starting conditions per distance r at $T = 40$ K, $T = 80$ K, $T = 120$ K, and $T = 150$ K, respectively, and corresponding free energy ΔG in kJ/mol

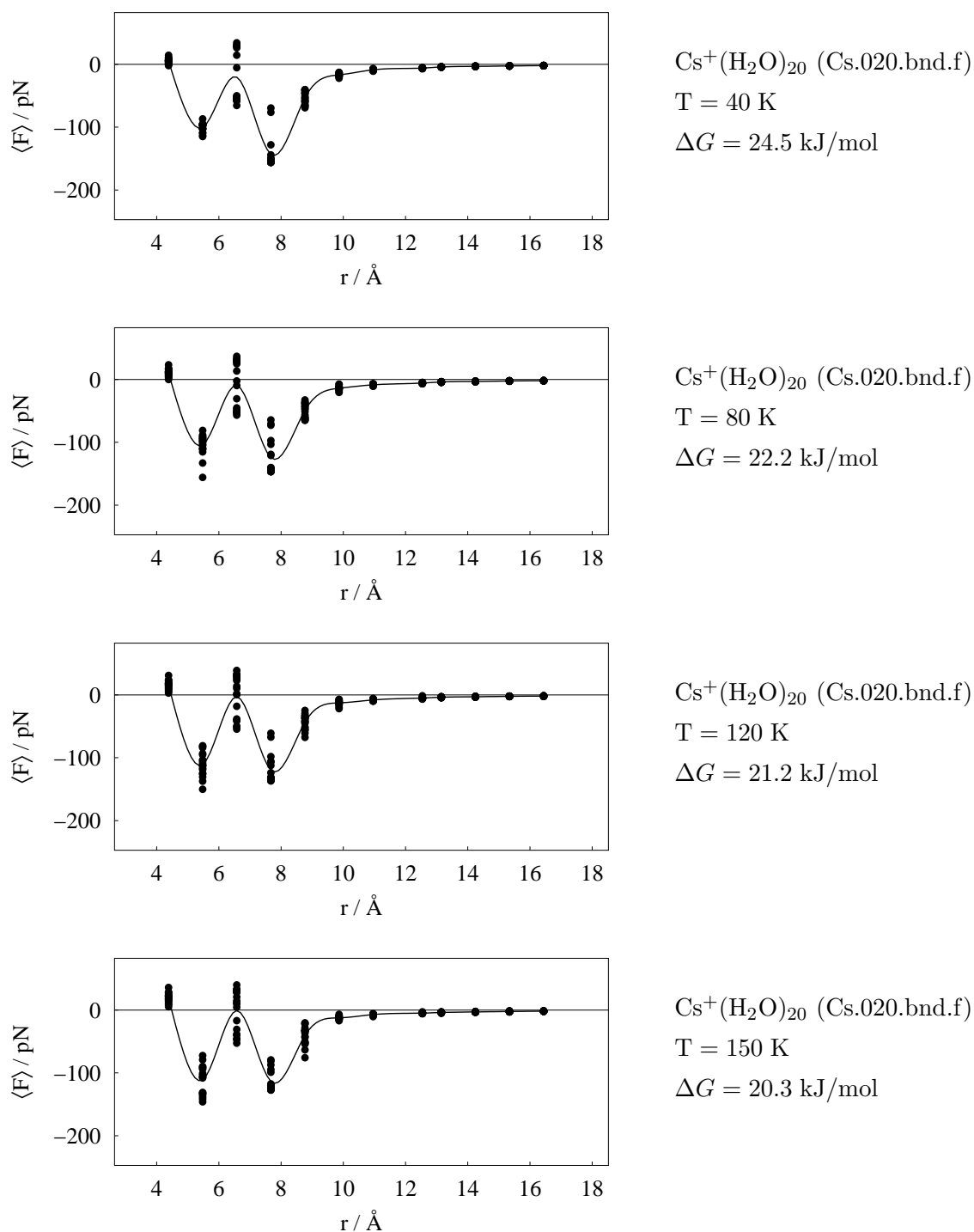


Figure 15.25.: Average constraint force $\langle F \rangle$ in pN vs. distance r in Ångström of pulled water molecules of structure Cs.020.bnd.f for eighteen starting conditions per distance r at $T = 40$ K, $T = 80$ K, $T = 120$ K, and $T = 150$ K, respectively, and corresponding free energy ΔG in kJ/mol

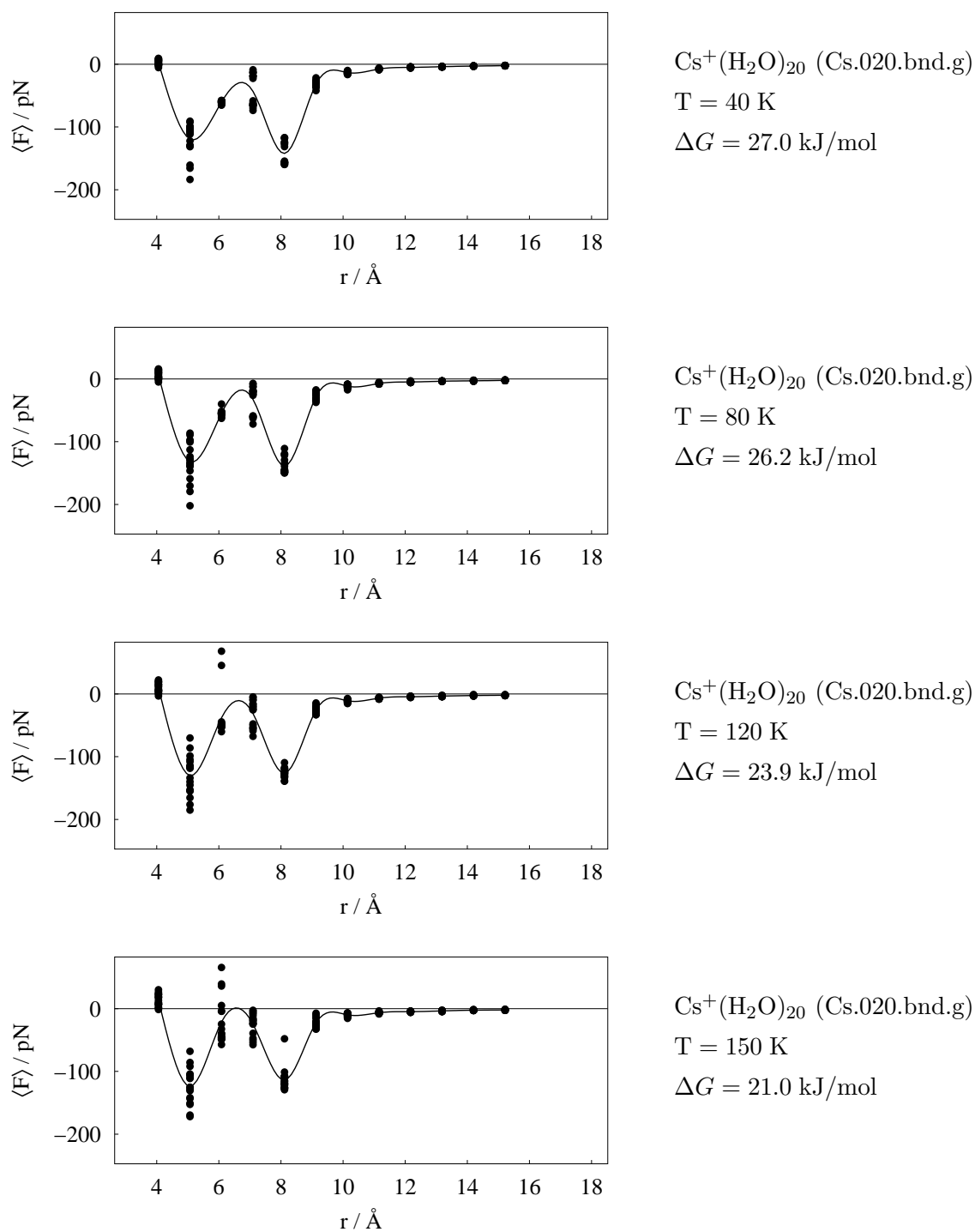


Figure 15.26.: Average constraint force $\langle F \rangle$ in pN vs. distance r in Ångström of pulled water molecules of structure Cs.020.bnd.g for eighteen starting conditions per distance r at $T = 40 \text{ K}$, $T = 80 \text{ K}$, $T = 120 \text{ K}$, and $T = 150 \text{ K}$, respectively, and corresponding free energy ΔG in kJ/mol

Bibliography

- [1] K. Liu, J.D. Cruzan, and R.J. Saykally, *Science* **271**, 929 (1996).
- [2] Jr. A.W. Castleman and K.H. Bowen, *J. Phys. Chem.* **100**, 12911 (1996).
- [3] M.A. Duncan, *Annu. Rev. Phys. Chem.* **48**, 69 (1997).
- [4] J.M. Lisy, *Int. Rev. Phys. Chem* **16**, 267 (1997).
- [5] U. Buck and F. Huisken, *Chem. Rev.* **100**, 3863 (2000).
- [6] G. Niedner-Schatteburg and V.E. Bondybey, *Chem. Rev.* **100**, 4059 (2000).
- [7] F. Sobott, A. Wattenberg, H.-D. Barth, and B. Brutschy, *Intern. J. Mass Spectroscopy* **185/186/187**, 271 (1998).
- [8] S.-W. Lee, P. Freivogel, T. Schindler, and J.L. Beauchamp, *J. Am. Chem. Soc.* **120**, 11758 (1998).
- [9] J. Kim, S. Lee, S.J. So, B.J. Mhin, and K.S. Kim, *J. Chem. Phys.* **102**, 839 (1995).
- [10] H.M. Lee, J. Kim, S. Lee, B.J. Mhin, and K.S. Kim, *J. Chem. Phys.* **111**, 3995 (1999).
- [11] T. Lybrand and P.A. Kollman, *J. Chem. Phys.* **83**, 2923 (1985).
- [12] P. Cieplak, P. Kollman, and T. Lybrand, *J. Chem. Phys.* **86**, 6393 (1987).
- [13] P.B. Balbuena, L. Wang, T. Li, and P.A. Dorosa, *Molecular Dynamics From Classical Quantum Methods*, (Theoretical and Computational Chemistry Vol. 7, P.B. Balbuena and J.M. Seminario (Ed.); S.431, Amsterdam, 1999).
- [14] J.L. Kassner, Jr., and D.E. Hagen, *J. Chem. Phys.* **64**, 1860 (1976).
- [15] G.A. Jeffrey, *Inclusion Compounds, Vol.1*, (J.L. Atwood, J.E.D. Davies, D.D. MacNiol, Academic Press, New York, chapter 5, 1984).
- [16] J. Lipkowski, *Annual Reports on the Progress of Chemistry, Section C, Vol.96*, (G.A. Webbs, The Royal Society of Chemistry, Cambridge, Chapter 10, 1996).

- [17] C.A. Koh, R.P. Wisbey, X. Wu, R.E. Westacott, and A.K. Soper, *J. Chem. Phys.* **113**, 6390 (2000).
- [18] O.K. Førrisdahl, B. Kvamme, and A.D.J. Haymet, *Mol. Phys.* **89**, 819 (1996).
- [19] A. Khan, *Chem. Phys. Lett.* **217**, 443 (1994).
- [20] G. Hulthe, G. Stenhagen, O. Wennerström, and C.-H. Ottosson, *J. Chem. Phys.* **777**, 155 (1997).
- [21] W. Blokzijl and J.B.F.N. Engberts, *Angewandte Chemie* **105**, 1610 (1993).
- [22] T. Head-Gordon, *Biophysics* **92**, 8308 (1995).
- [23] M.P. Hodges and D.J. Wales, *Chem. Phys. Lett.* **324**, 279 (2000).
- [24] A. Khan, *Chem. Phys. Lett.* **319**, 440 (2000).
- [25] S. Wei, Z. Shi, and Jr. A.W. Castleman, *J. Chem. Phys.* **94**, 3268 (1991).
- [26] A. Tongraar, K.R. Liedl, and B.M. Rode, *J. Phys. Chem.* **102**, 10340 (1998).
- [27] B. Hartke, *Chem. Phys. Lett.* **258**, 144 (1996).
- [28] R. Horst, P.M.Pardalos, and N.V. Thoai, *Nonconvex Optimization and its Applications*, (Kluwer, Dordrecht, 2000).
- [29] L.T. Wille, *Annual Reviews of Computational Physics VII*, (D. Stauffer (Ed.), World Scientific, Singapore, 2000).
- [30] B. Hartke and E.A. Carter, *Chem. Phys. Lett.* **216**, 324 (1993).
- [31] S.K. Gregurick, M.H. Alexander, and B. Hartke, *J. Chem. Phys.* **104**, 2684 (1996).
- [32] B. Hartke, *J. Comput. Chem.* **20**, 1752 (1999).
- [33] B. Hartke, *Z. Phys.Chem.* **1251**, 214 (2000).
- [34] B. Hartke, M. Schütz, and H.-J. Werner, *Chem. Phys.* **239**, 561 (1998).
- [35] B. Hartke, *Angewandte Chemie* **114**, 1534 (2002).
- [36] B. Hartke, A. Charvat, M. Reich, and B. Abel, *J. Chem. Phys.* **216**, 3588 (2002).
- [37] J. Sadlej, V. Buch, J.K. Kazimirski, and U. Buck, *J. Chem. Phys.* **103**, 4933 (1999).
- [38] A.R. Bandy and J.C. Ianni, *J. Phys. Chem.* **102**, 6533 (1998).
- [39] R.W. Siegel, *Nanostruct. Mater.* **3**, 1 (1993).

-
- [40] K. Liu, M.G. Brown, C. Carter, R.J. Saykally, J.K. Gregory, and D.C. Clary, *Nature* **381**, 501 (1996).
- [41] J. Kim and K.S. Kim, *J. Chem. Phys.* **109**, 5886 (1998).
- [42] D.J. Wales, *Energy Landscapes: With Applications to Clusters, Biomolecules and Glasses*, (Cambridge Molecular Science, Cambridge, 2003).
- [43] C.S. Maranas and C.A. Floudas, *J. Glob. Opt.* **4**, 135 (1994).
- [44] D.J. Wales and M.P. Hodges, *Chem. Phys. Lett.* **286**, 65 (1998).
- [45] K. Nauta and R.E. Miller, *Science* **287**, 293 (2000).
- [46] J.C. Culberson, *Evolutionary Comput. Journal* **6**, 109 (1998).
- [47] J.D. Pintér, *Global Optimization in Action*, (Kluwer, Dordrecht, 1996).
- [48] S. Kirkpatrick, C.D. Gelatt, Jr., and M.P. Vecchi, *Science* **220**, 671 (1983).
- [49] Z. Li and H.A. Scheraga, *Proc. Natl. Acad. Sci. USA* **84**, 6611 (1987).
- [50] E. Fontain, *Anal. Chim. Acta* **265**, 227 (1992).
- [51] P. Tuffery, C. Etchebest, S. Hazout, and R. Lavery, *J. Biomol. Struct. Dyn.* **8**, 1267 (1991).
- [52] W. Linert, P. Margl, and I. Lukovits, *Comput. Chem.* **16**, 61 (1992).
- [53] R.S. Judson, *Rev. Comput. Chem.* **10**, 1 (1997).
- [54] L. Davis (Ed.), *Genetic Algorithms and Simulated Annealing*, (Pitman, London, 1987).
- [55] L. David (Ed.), *Handbook of Genetic Algorithms*, (Van Nostrand Reinhold, New York, 1991).
- [56] D.E. Goldberg, *Genetic Algorithms in Search, Optimization, and Machine Learning*, (Addison-Wesley, Reading, Massachusetts, 1989).
- [57] F. Schulz and B. Hartke, *Chem. Phys. Chem.* **3**, 98 (2002).
- [58] P.M. Holland and A.W. Castleman, *J. Chem. Phys.* **72**, 5985 (1980).
- [59] W.L. Jorgensen, *J. Chem. Phys.* **77**, 4156 (1982).
- [60] W.L. Jorgensen, J. Chandrasekhar, J.D. Madura, R.W. Impey, and M.L. Klein, *J. Chem. Phys.* **79**, 926 (1983).
- [61] J. Chandrasekhar, D.C. Spellmeyer, and W.L. Jorgensen, *J. Am. Chem. Soc.* **106**, 903 (1984).

- [62] S.H. Lee and J.C. Rasaiah, *J. Chem. Phys.* **101**, 6964 (1994).
- [63] M.R. Reddy and M. Berkowitz, *J. Chem. Phys.* **88**, 7104 (1998).
- [64] D.J. Tobias, P. Jungwirth, and M. Parrinello, *J. Chem. Phys.* **114**, 7036 (2001).
- [65] O. Borodin, R.L. Bell, Y. Li, D. Bedrov, and G.D. Smith, *Chem. Phys. Lett.* **336**, 292 (2001).
- [66] C.J. Burnham, J. Li, S.S. Xantheas, and M. Leslie, *J. Chem. Phys.* **110**, 4566 (1999).
- [67] E.D. Isaacs, A. Shukla, P.M. Platzman, D.R. Hamann, and B. Barbiellini, *Phys. Rev. Lett.* **82**, 600 (1999).
- [68] M. Bräuchler, S. Lunell, I. Olovsson, and W. Weyrich, *Int. J. Quantum Chem.* **35**, 895 (1989).
- [69] W. Klopper and H.P. Luethi, *Mol. Phys.* **96**, 559 (1999).
- [70] J. Jortner, *Z. Phys. D – Atoms, Molecules and Clusters* **24**, 247 (1992).
- [71] R.L. Johnston, *Phil. Trans. R. Soc. London* **356**, 211 (1998).
- [72] M.P. Hodges, *program xmakemol*, (<http://www.nongnu.org/xmakemol/>, latest version, 2004).
- [73] A. Selinger and Jr. A.W. Castleman, *J. Phys. Chem.* **95**, 8442 (1991).
- [74] K. Kim, K.D. Jordan, and T.S. Zwier, *J. Am. Chem. Soc.* **116**, 11568 (1994).
- [75] J. Brudermann, M. Melzer, U. Buck, J.K. Kazimirski, J. Sadlej, and V. Buch, *J. Chem. Phys.* **110**, 10649 (1999).
- [76] U. Buck, I. Ettischer, M. Melzer, V. Buch, and J. Sadlej, *J. Chem. Phys.* **103**, 4933 (1999).
- [77] A. Lüchow, D. Spangenberg, C. Janzen, A., Jansen, M. Gerhards, and K. Kleinermanns, *Phys. Chem. Chem. Phys.* **3**, 2771 (2001).
- [78] V. Buch, J.P. Devlin, and C. Joyce, *J. Phys. Chem.* **104**, 1974 (2000).
- [79] V. Buch and J.P. Devlin, *J. Phys. Chem.* **110**, 3437 (1999).
- [80] M. Sage, *Chem. Phys.* **35**, 357 (1978).
- [81] K. Hermansson, J. Lindgren, and M.M. Probst, *Chem. Phys. Lett.* **233**, 371 (1995).
- [82] F. Schulz and B. Hartke, *Phys. Chem. Chem. Phys.* **5**, 5021 (2003).

-
- [83] R.N. Pribble and T.S. Zwier, *Science* **265**, 75 (1994).
- [84] J.M. Lisy, *Personal Correspondence*, (Department of Chemistry, University of Illinois at Urbana Champaign, Illinois/USA, 2004).
- [85] D. Frenkel and B. Smit, *Understanding Molecular Simulation*, (Academic Press, 2002).
- [86] M.P. Allen and D.J. Tildesley, *Computer Simulation of Liquids*, (Clarendon Press, Oxford, 1987).
- [87] L. Verlet, *Phys. Rev.* **159**, 98 (1967).
- [88] W.C. Swope, H.C. Andersen, P.H. Berens, and K.R. Wilson, *J. Chem. Phys.* **76**, 637 (1982).
- [89] H. Goldstein, *Classical Mechanics*, (Addison Wesley 2nd Edition, 1980).
- [90] D. Evans and S. Murad, *Mol. Phys.* **34**, 327 (1977).
- [91] H. Friedmann, *Mol. Phys.* **29**, 1533 (1975).
- [92] G. Gaberoglio, *PhD Thesis: Dynamical properties of H-bonded liquids: A theoretical and computer simulation study*, (Università Degli Studi di Trento, Trento/Italy, 2001).
- [93] H.C. Andersen, *J. Chem. Phys.* **72**, 2384 (1980).
- [94] N.G. van Kampen, *Stochastic Processes in Physics and Chemistry*, (North-Holland, Amsterdam, 1981).
- [95] W. Feller, *An Introduction to Probability Theory and its Applications, Volume 1*, (Wiley, New York, 1957).
- [96] W. Feller, *An Introduction to Probability Theory and its Applications, Volume 2*, (Wiley, New York, 1966).
- [97] S. Nose, *J. Chem. Phys.* **81**, 511 (1984).
- [98] S. Nose, *Mol. Phys.* **52**, 255 (1984).
- [99] W.G. Hoover, *Phys. Rev. A* **31**, 1695 (1985).
- [100] W.G. Hoover, *Phys. Rev. A* **34**, 2499 (1986).
- [101] G.J. Martyna, *J. Chem. Phys.* **97**, 274 (1992).
- [102] R. Kutteh and T.P. Straatsma, *Reviews in Computational Chemistry, volume 12, pp. 75*, (K.B. Lipkowitz and D.B. Boyd, editors, Wiley-VCH, New York, 1998).
- [103] H.C. Andersen, *J. Comput. Phys.* **52**, 24 (1983).

- [104] F. Baletto, C. Mottet, and R. Ferrando, *Surface Science* **446**, 31 (2000).
- [105] T. Mülders, P. Krüger, W. Swegat, and J. Schlitter, *J. Chem. Phys.* **104**, 4869 (1996).
- [106] J. Schlitter, W. Swegat, and T. Mülders, *J. Mol. Model.* **7**, 171 (2001).
- [107] W. Swegat, J. Schlitter, P. Krüger, and A. Wollmer, *Biophysical Journal* **84**, 1493 (2003).

16. Acknowledgements

First of all I would like to express my gratitude to my supervisor Prof. Dr. Bernd Hartke. He has always been very generous regarding his time and knowledge and has also always allowed me great freedom in my research. I very much enjoyed the research topic I was given and also the time I spent for the studies.

I would also like to thank Prof. Dr. F. Temps for becoming my co-referee.

Thanks go to my former colleagues in Stuttgart, as they provided a very nice working atmosphere, and we often had great fun especially when visiting the “Unithekle”. Special thanks go to PD Dr. Guntram Rauhut who has always been very helpful and patient in answering questions, especially “stupid” questions regarding Gaussian. I would also like to thank Dr. Andreas Nicklass for the fun we had at lunch times. Finally, I would also like to acknowledge Klaus Pflüger for introducing me to L^AT_EX.

Upon moving to Kiel, I experienced a really warm welcome. I want to thank everyone at the Institute, especially those who have contributed to various parts of my research and every day life in all kinds of ways. To name but a few, Prof. Dr. H. Mäder, Dipl.-Chem. Ingo Berndt, Dr. Kai Brendel, Dipl.-Chem. Simmy Jacobsen, Dipl.-Chem. Stefan Schweiger, and Thorben Starck.

I am very grateful to Dipl.-Chem. Alexandra Kulle, as during my stay in Kiel, she became a true friend. Thank you!

After moving to Kiel, our group steadily grew. Thanks go to everybody in the group. Special thanks go to Rungtiva Palangsuntikul, I shared my office with, who always spread good mood. I would also like to mention Dipl.-Phys. Bernhard Bandow whom I have to express my gratitude for very good discussions on Molecular Dynamics. I would also like to thank Dipl. Phys. Frank von Horsten who provided me with essential music during the time of writing. For one year our group had support from Dipl.-Inf. André Janz, which had been more than helpful. Thank you for always helping out (and not just during the time you worked with our group, but) whenever I had problems with “Mozart” (my computer). I would also like to thank our newest group member, Florian Koskowski, for his help during the last weeks before finishing the thesis.

On a more private note, I want to acknowledge the Judo-Klub-Kiel, as I experienced a very

warm welcome which made me feel at home in Kiel very soon. I especially would like to mention the Jujutsu division for the great times I had with Martina, Hilde, Karsten, Carsten, Karsten (yes, there are three K/Carstens), Martin, Herbert, and Heiko. The training always provided a great place to work off frustrations due to bug searches in my molecular dynamics routine. Heiko, thanks for also always listening to my complaints ;-), for always cheering me up, and last but not least also for becoming a great friend.

A very nice aspect of moving to Kiel was that part of my mother's family lived in this region. They supported me a great deal, especially in the last couple of weeks of writing the thesis. Thank you, Claas, Jane, and Gerd.

I am grateful for finding a great partner in André Janz. Thank you for always being there for me! I was also always supported from his family, which is why I would like to express my gratitude to his parents as well.

Finally, I want to thank the people who have been and always will be most important in my life: my parents Angela and Hermann, my brother Leonhard and also my grandmother Gertrud. My deepest thanks for your permanent support and encouragement during my entire life.

17. Curriculum Vitae

Personal data

name: Franziska Schulz
date of birth: 28th of September 1975
place of birth: Böblingen
nationality: German
parents: Angela Schulz and Dr. Hermann Schulz
brother: Leonhard Schulz

Academic Record

1982 – 1986 attendance of the Pfalzgraf-Rudolph-Grundschule Herrenberg
1986 – 1995 attendance of the Andrae-Gymnasium Herrenberg
Abitur: Allgemeine Hochschulreife (1.6)
WS 1995 begin of chemistry studies at the University of Stuttgart
1997 Vordiplom: gut (1.6)
15/05/2001 Diplom: gut (1.6)
title of the diploma thesis:
“Globale Geometrieoptimierung von Alkali-Kation-
Mikrohydratations-Clustern auf TIP4P / OPLS Niveau
mittels eines genetischen Algorithmus”
06/2001 – 02/2002 begin of PhD studies with PD Dr. B. Hartke at the
Institute of Theoretical Chemistry at the University of
Stuttgart
since 03/2002 continuation of the PhD studies with Prof. Dr. B. Hartke
at the Institute of Physical Chemistry at the
Christian-Albrechts-University of Kiel

Work experience

- 07/1995 – 10/1995 temporary nursing at the Kreiskrankenhaus Böblingen at the gynaecological department
- 02/2001 – 05/2001 undergraduate assistant at the Institute of Theoretical Chemistry at the University of Stuttgart
- 06/2001 – 12/2001 graduate assistant at the Institute of Theoretical chemistry at the University of Stuttgart
- 01/2002 – 03/2002 research associate at the Institute of Theoretical Chemistry at the University of Stuttgart
- since 04/2002 research associate at the Institute of Physical Chemistry at the Christian-Albrechts-University of Kiel

Stay abroad

- 01/1993 – 07/1993 attendance of the Presbyterian Ladies College Armidale in NSW, Australia, year 12
- 08/1998 – 08/1999 exchange student at the University of Cincinnati in OHIO/USA
exam: Master of Science (organic chemistry)
title of the thesis:
“Synthesis of precursors for the preparation of 1,4-Dihydrodioxins as masked DNA-cleaving agents via an intramolecular Schoenberg reaction”

18. Erklärung

Diese Arbeit wurde am Institut für Theoretische Chemie der Universität Stuttgart im Juni 2001 begonnen und am Institut für Physikalische Chemie der Christian-Albrechts-Universität zu Kiel ab März 2002 weitergeführt.

Hiermit erkläre ich an Eides Statt, daß die vorliegende Dissertation – abgesehen von der Beratung durch meinen Betreuer Herrn Prof. Dr. Hartke – nach Inhalt und Form meine eigene Arbeit ist.

Diese Arbeit hat weder in Auszügen noch in ganzer Form einer anderen Stelle im Rahmen eines Prüfungsverfahrens vorgelegen.

Kiel, den 17.12.2004